THE APPLICATION OF MODELLING AND SIMULATION TO SHIP DESIGN FOR HELICOPTER OPERATIONS

Thesis submitted in accordance with the
requirements of the University of Liverpool
for the degree of Doctor in Philosophy

By

Paul Michael Scott

School of Engineering
University of Liverpool
December 2017

Abstract

Modern combat ships, such as frigates and destroyers, routinely operate with maritime helicopters. The challenge of landing the helicopter in bad weather is acknowledged as being both demanding and dangerous; moreover, if the flying conditions are too difficult the helicopter will not be cleared to take off, and an important component of the ship's capability will be lost. The unsteady air flow over the ship, particularly in the vicinity of the flight deck, is a significant factor that limits the helicopter's operational envelope. The characteristics of the air flow, known as the ship's airwake, depend on the wind speed and direction relative to the ship, and the geometry of the ship's superstructure. The aerodynamics of the ship's superstructure does not receive much attention at the design stage, compared to, for example, its radar cross-section. This thesis presents an investigation where modelling and simulation has been used to assess and inform the aerodynamic design of a modern warship. The modelling techniques that have been applied are time-accurate computational fluid dynamics, to compute the complex three-dimensional unsteady flow field over the full-size ship, and the mathematical modelling of a helicopter's flight dynamics, to compute how a helicopter will respond to the unsteady air flow. These modelling techniques have then been used in two simulation applications; one is the Virtual AirDyn, to assess the unsteady loads applied to the helicopter by the ship's airwake, and the second is piloted flight simulation in a motion-base flight simulator, to assess the effect of the airwake on a pilot's workload while conducting a deck landing. Collectively the modelling and simulation techniques have been used to assess different design options for a ship's superstructure. The techniques have also been applied investigate how the ship's size affects the airwake and the ship's motion, and how these affect the helicopter and the pilot workload when operating over the landing deck. Air flow modelling has also been used to predict how a ship's hot engine exhaust gases mix with the airwake to cause fluctuating elevated temperatures over and around the flight deck.

It has been demonstrated how relatively small changes to the geometry of the ship's superstructure ahead of the flight deck can affect the aerodynamic loads on the helicopter, and that these effects can be detected and quantified to provide guidance to the ship designer. It has also been shown that while larger ships create larger and more aggressive airwakes that perturb the helicopter and increase the pilot workload during a landing. Smaller ships, on the other hand, have a more dynamic motion in rough seas, and smaller decks with a closer superstructure. Simulation has been used to show how these different effects combine and how ship size affects the pilot workload during a deck landing. The study has also identified that while offshore oil rig helicopter operators have clear guidelines on limits for air temperature increases, there are no such guidelines when operating a helicopter to a ship, and that the range of temperature increases that can occurs over the flight deck are sufficient to affect the helicopter performance.

A significant contribution made by this study has been to inform the design of a real ship, so demonstrating the potential of modelling and simulation in the design of ships for helicopter operations.

Acknowledgements

There are many people who have contributed to the success of the research reported in this thesis, and many more who have contributed to the experiences I have gained.

I would like to thank my supervisors, Prof Ieuan Owen and Dr Mark White, not just for their supervision and guidance, but also their encouragement and support throughout the project and whose selfless time and care where sometimes all that kept me going. I'd also like to note their efforts which have contributed enormously to this work. Through them I have had the opportunity to meet others involved in the naval aerodynamics research community and providing me the opportunity to travel and present work.

The financial support of BAE Systems, Naval Ships, is acknowledged, specifically the technical input facilitated by Niven McDowell, Kevin Brown and Geoff Roach. As well as the continued support from ANSYS.

My fellow PhD students working in ship aerodynamics have provided help, particularly Rebecca Mateer, Michael Kelly who also provided the ship motion analysis, and Thomas Fell who has provided a great deal of guidance with flight simulation and FLIGHTLAB. They have not only supported me academically but have been extremely supportive, providing friendship and help outside of our research.

The contributions of test pilots Andy Berryman and Charlie Brown are acknowledged, as is their expertise and their practical knowledge of helicopter-ship operations that they have shared with me.

I'd like to thank my family, especially my parents who have supported me in more ways than I can recall, and their encouragement despite my many disturbances while working into the small hours. Their unwavering belief that I was able to continue when times were hard has helped me more than I can express on paper.

Contents

Nomenclature

ABL	Atmospheric Boundary Layer
C_{DES}	DES length-scale constant
E_i	Specific internal energy (J/kg)
K_{eff}	Effective thermal conductivity (W/(m.K))
L_t	Turbulent length scale
Re	Reyonolds number
Si	Source term for internal energy (J)
T	Temperature of fluid (K)
k	Turbulent kinetic energy per unit mass (m^2/s^2)
l_s	Ship length (m)
n	Number of time steps
p	Pressure (N/m^2)
q_i'	Fluctuating velocity (m/s)
$\overline{q_\iota}$	Mean flow velocity (m/s)
$q_i q_j$	Reynolds stress
u	Longitudinal velocity (m/s)
v	Lateral velocity (m/s)
v_f	Freestream velocity (m/s)
v_{max}	Maximum velocity (m/s)
v_{ref}	Reference velocity (m/s)
w	Vertical velocity (m/s)
x	Longitudinal distance (m)
y	Lateral distance (m)
z	Vertical distance (m)
z_h	Hangar height (m)

z_{ref}	Reference height (m)
α	Surface roughness constant
Δ_0	Target grid spacing in focus region
Δt	Time step (s)
ρ	Fluid density (kg/m^3)
μ	Coefficient of viscosity (kg/(s.m))
ν	Kinematic eddy viscosity (m^2/s)
φ	Wind over deck angle (°)

Operators

∇	Differential operator

Acronyms

ACP	Airload Computational Points
AFCS	Automatic Flight Control System
CFD	Computational Fluid Dynamics
CFL	Courant-Friedrichs-Lewy
DES	Detached Eddy Simulation
DIPES	Deck Interface Pilot Effort rating Scale
dstl	Defence Science and Technology Laboratory
FSC	Future Surface Combatant
FOCFT	First Of Class Flight Trials
GUI	Graphical User Interface
HPC	High Performance Computing
JSHIP	Joint Shipboard Helicopter Integration Process

LES	Large Eddy Simulation
MTE	Mission Task Element
NRC	National Research Council
PBNS	Pressure Based Navier-Stokes
PISO	Pressure Implicit with Splitting of Operator
PSD	Power Spectral Density
RANS	Reynolds Averaged Navier-Stokes
SAIF	Ship-Air Interface Framework
SAS	Stability Augmentation System
SHOL	Ship-Helicopter Operating Limit
SFS	Simple Frigate Shape
SST	Shear Stress Transport
TTCP	Technical Cooperation Program
URANS	Unsteady Reynolds Averaged Navier-Stokes
WOD	Wind Over Deck

CHAPTER 1

INTRODUCTION

This thesis presents a detailed and extensive study of how particular aspects of a ship's superstructure geometry affect the operation of the ship's helicopter, in particular the superstructure geometry ahead of the landing deck, the hot exhaust gases discharged from the ship's engines, and the overall size of the ship. Modelling and simulation has been used to create the unsteady airflow over the ship and to apply it to a flight dynamics model of a helicopter. In this chapter the background to the research will be presented and the aim of the research will be established.

1.1 Background

Modern combat ships, e.g. frigates and destroyers, routinely operate with maritime helicopters. The challenge of landing the helicopter in bad weather is acknowledged as being both demanding and dangerous; moreover, if the flying conditions are too difficult the helicopter will not be cleared to take off, and an important component of the ship's capability will be lost [1]. The maritime helicopter is often regarded as one of the most important tactical systems on the ship and is used to perform a variety of different roles, including anti-submarine warfare, surveillance, troop-transfer and supply replenishment at sea. While these operations are now considered routine, the ship-helicopter dynamic interface still presents one of the most challenging environments in which a helicopter pilot will operate. As well as a restricted landing area and a pitching, rolling and heaving deck, the pilot must also contend with the presence of a highly dynamic airflow over the flight deck. This phenomenon, known as the ship's “airwake”, is caused by the air flowing over and around the ship's superstructure as a result of the combined effect of the prevailing wind and the forward motion of the ship.

There has been considerable research into understanding the ship's airwake and how it affects a helicopter's handling qualities, predominantly through modelling and simulation – both computer-based and experimental. A major contributor to this international effort has been the Flight Science and Technology Research Group at the University of Liverpool, which has led the UK's development of modelling and simulation of the helicopter-ship dynamic interface [e.g. 2-5].

As outlined above, the task of landing a helicopter to a ship in bad weather is both dangerous and difficult. Ship-Helicopter Operating Limits (SHOL) for a given ship and helicopter combination are normally determined during the ship's First of Class Flight Trials (FOCFT) in which the ship and the helicopter are put to sea and test pilots perform numerous launch and recovery tasks for winds of different strength and direction. Figure 1.1 shows an example SHOL diagram where the limits of wind strength and direction, relative to the deck, are indicated on a polar chart. This chart highlights wind direction, or azimuth, as a set of radial lines while the magnitude of the wind speed is described by concentric lines; azimuth and speed are spaced 10° and 10 knots apart, respectively, in this example. By joining the test points carried out during SHOL testing an area on the chart can be produced, inside of which define the safe operating limits for the particular ship-helicopter combination tested.

The chart is for a UK standard port-side landing manoeuvre, Fig. 1.2, where the pilot first positions the helicopter parallel to and alongside the port side of the ship, matching the ship's speed. The aircraft is then translated sideways across the deck, with the pilot's eye-line at about hangar height until positioned above the landing spot; during a quiescent period in the ship's motion the pilot will descend to the deck and land the aircraft. It can be seen for the SHOL diagram shown in Fig. 1.1 that for a headwind the helicopter is still able to operate with a relative wind speed up to 50 knots, while this reduces to some 20-30 knots for oblique winds, partly because of the complex unsteady flows being shed from the ship's superstructure and partly because of the control authority required to overcome the side winds. The lower permissible winds from astern are because they push the helicopter towards the hangar and they also reduce the effectiveness of the tail rotor. The asymmetry in the SHOL is partly due to the landing being from the port side regardless of whether the winds are from the starboard (Green) or port (Red). In practice it is very difficult in a FOCFT to obtain a full range of wind over deck (WOD) conditions in the chosen trial period and the costly and time-consuming trails are often incomplete. While various techniques can be used to fill the gaps in the SHOLs, these normally err on the conservative side and lead to a restricted SHOL. More recently, a method of using shore-based hover trials and ship airwake data to construct a "candidate flight envelope" that can be assessed in shorter at-sea trials has been developed to support the Dutch navy [6].

Significant research into the air flow over ship superstructures and the effect on maritime helicopter operations began to emerge in the mid-1990s, e.g. [7]. In the US, the Joint Shipboard Helicopter Integration Process (JSHIP) was established to support the interoperability of helicopters from the US Navy, Army and Air Force with a range of ships [8,9]. Conducting the at-sea trials for the multiplicity of possible ship/helicopter combinations is prohibitively expensive and time-consuming, so a major task of JSHIP was to develop a high-fidelity simulation capability, including use of the NASA Ames Vertical Motion Simulator, to demonstrate that realistic piloted launch and recovery missions could be conducted for different aircraft and ship combinations and simulated SHOLs could be determined. Meanwhile, in 2003 the UK Ministry of Defence began funding a project to develop a simulation capability for predicting SHOLs using the Merlin helicopter training simulator at the Royal Navy Air Station in Culdrose, Cornwall [10]. The Ship/Air Interface Framework (SAIF) project, as it was called, created a federated computer architecture where the different elements specific to ship operations (e.g. motion, visuals and airwake for different ships, and different aircraft types) could be flexibly used with the Merlin simulator. The SAIF project has conducted simulated SHOL trials for a Merlin operating to a Type 23 frigate and a Type 45 Destroyer [11].

Separately, within the UK, the Flight Science and Technology Research Group at The University of Liverpool was established in 2000, central to which was research into rotorcraft flight dynamics and control, including flight simulation using a motion-base. Flight simulation research began with a single-seat, full motion flight simulator, HELIFLIGHT [12] which was built with a technical and functional specification that would allow research into flight handling qualities, flight mechanics, flight control system design, aircraft design concepts and cockpit technologies. Being a research simulator it provided greater availability and flexibility than a qualified naval training simulator and also allowed access to the simulator’s motion system controllers. In 2008 a second, larger and more capable simulator, HELIFLIGHT-R, was installed [13] by Advanced Rotorcraft Technology (ART), shown in Fig. 1.3 (the smaller single-seat HELIFLIGHT simulator can be seen in the background).

Amongst the flight simulation projects that were initiated at Liverpool in the mid 2000’s was research into the ship-helicopter dynamic interface, with a particular focus on including the effect of the ship’s airwake. Figure 1.4 shows the mean air flows over three ship geometries for a headwind, generated using Computational Fluid Dynamics (CFD). The ships are a Type 23 frigate (133m long), a Type 45 destroyer (152m) and a Wave Class Tanker (197m). For each ship the path lines show the chaotic air flow over the aft landing deck and it should also be noted that these flows are highly unsteady.

Early research at Liverpool used steady-state CFD airwakes, and the challenge was to integrate the velocity field with the helicopter flight mechanics model so that the aerodynamic loadings could be applied correctly, and then implemented in a piloted flight simulation facility. This PhD research was undertaken by Roper [14] who successfully integrated the time-averaged ship airwakes with the single-seat HELIFLIGHT simulator to conduct piloted deck landings. The ship model was a simplified frigate known as the Simple Frigate Shape-2, Fig. 1.5 (SFS-1 was a simpler block without a representative bow as indicated in Fig. 1.5). The SFS ship geometries were defined by The Technical Cooperation Programme (TTCP) [15] for comparative experimental and CFD studies. TTCP has research partners in the UK, Canada, Australia and the USA with a common interest in modelling and simulation of the helicopter-ship dynamic interface. However, while the pilots reported a more realistic flying experience when conducting simulated deck landings when the steady airwake was included, they also reported that the fidelity was compromised by not having the ‘bumping’ associated with unsteady aerodynamic loads.

As more powerful computing resources become available, unsteady CFD was used to create the ship airwakes, and more realistic and complex ship geometries were employed; this PhD research was carried out by Forrest [16] who developed the CFD capability, and Hodge [17] who developed the simulation environment. A challenge for the CFD was not just to create the unsteady velocity field as the air flows over the ship superstructure, but also to maintain the unsteadiness in the ship airwake as it passes over the ship. The turbulence modelling technique that has been adopted for the airwake simulation is Detached Eddy Simulation (DES) [18], which will be described in more detail in Chapter 2. DES is particularly effective for bluff bodies with sharp edges, such as a ship’s superstructure, where the edges from which the flow separates from the superstructure are well-defined. Figure 1.6, extracted from [16] shows how the velocity in the flow at a particular point over the landing deck changes with time; one trace has been computed using a less sophisticated Unsteady Reynolds-Averaged Navier Stokes (URANS) approach to CFD, and the other has been computed using DES. As can be seen, the DES solution is able to maintain the unsteadiness in the flow, while the velocity produced by the URANS solution is damped out and converges onto a steady-state solution.

The development and validation of the DES technique applied to ship airwakes was a significant step forward and led to simulated SHOLs being produced; an example is shown in Fig. 1.7 for a SH-60B SeaHawk landing on a Type 23 frigate, extracted from Forrest et al [5]. It also became apparent from Forrest’s work, where flying trials were used to create SHOLS for different ships, that the helicopter loads and the pilot experience were different for different ship geometries. This observation led to the development of an instrument called the Airwake Dynamometer which is effectively a model scale helicopter that is immersed in the flow over and around the landing deck of a ship to measure the unsteady loads imparted by the ship's wake [19]. The model helicopter, with a main rotor diameter of about 300 mm, was based on a Merlin AW 101 and was mounted on a six-axis force balance (Fig. 1.8). Since the helicopter is effectively an instrument for measuring the loads arising from the airwake, it is an airwake dynamometer and has been called the AirDyn. The advantage of the AirDyn is that it integrates most of the effects of the airwake on the aircraft and, because the main rotor is motored, it also includes the rotor/airwake interaction. There are clearly scale limitations such as rigid blades and incompressible flow, but scaling parameters such as thrust coefficient and rotor tip/speed ratio are well matched, and Reynolds number matching is improved by conducting the experiment in a water tunnel.

The AirDyn was therefore an instrument for evaluating the effect of ship geometries on a helicopter, and this concept was applied by Kaaria in his PhD studies [20], where the AirDyn was used to evaluate various design modifications to a simplified frigate [21]. Between Forrest's work on using computational modelling and simulation to apply CFD-generated airwakes to a helicopter flight model, and Kaaria's work into using the experimental AirDyn to assess the effect of different ship geometries on a helicopter, emerged the recognition that the AirDyn methodology could be reproduced using CFD-generated airwakes in place of experimental flows, and using a helicopter flight model instead of an experimental helicopter. The resulting software-based technique was called the Virtual AirDyn [22] and this simulation tool has been used extensively in the research being reported in this thesis.

The research was funded by BAE Systems Surface Ships. It was conducted at the same time that BAE were developing the design for a future surface combatant ship and the simulation tools and methodologies that have been developed by the research was being applied to aspects of the ship design as it evolved. Therefore some of the work cannot be reported in this thesis but, when practical, the same techniques and analysis were applied to a fictitious ship with a generic geometry representative of a modern warship, thereby avoiding any issues arising from confidentiality. During the course of the work the importance of the hot exhaust gas from the ships' engines was identified, by the author, as an issue and so a significant amount of effort has been dedicated to this aspect of airwake modelling. It is worthy of note that this thesis is reporting on aspects of a wider programme of research in which a Royal Navy ship has, for the first time ever, undergone a significant aerodynamic analysis as part of its design process, with a specific aim of improving the flying environment for the ship's helicopter.

The overall aim of the research was therefore to apply simulation and modelling to the design of a combat ship with the specific aim of improving the operational envelope and safety of the ship's helicopter. In order to fulfil these aims the following objectives are required:

- Aerodynamic data will be generated through use of ANSYS-Fluent CFD simulations for various ship geometries.
- Data will be extracted from these unsteady data sets to show the content of the flow field in the regions around the ship, highlighting dominant flow features.
- The inclusion of hot exhaust gas emanating from the ship will be included within CFD simulations.
- The feasibility of scaling previously computed CFD data to account for changes in geometric scale will be confirmed.
- A qualitative assessment of the changes to a ship's superstructure on helicopter performance will be carried out using off-line flight simulations.
- Piloted flight simulation will be conducted within the HELIFLIGHT-R simulator using unsteady CFD data.
- Flight trails data will be analysed to identify potential issues through scrutiny of pilot comments, control activities, and rating scores.

Chapter 2 will describe the simulation and modelling processes that have been applied in this research, namely CFD and flight simulation, both with a piloted motion-base and with the computer-based Virtual AirDyn. The number and complexities of the ship geometries and the fidelity required of the CFD created new challenges, particularly the handling of very large multiple data sets and the streamlining of data processing, so significant effort was dedicated to these areas.

Chapter 3 will describe how the Virtual AirDyn was used to assess a number of design variants of a future surface combatant ship. Four design evolutions were considered, all of which had superstructure geometry changes just ahead of the flight deck. Although the design changes are not major, differences are detected on the unsteady loading expected to be experienced by the helicopter, leading to one design configuration being favoured. The helicopter loads imposed by the airwake from the future ship are also compared with those from the airwake of a smaller Type 23 frigate. The smaller ship is shown to have a less aggressive airwake.

Chapter 4 presents a systematic study into how a ship’s size affects the characteristics of the airwake and how this, in turn, affects the aerodynamic loads and handling qualities of the helicopter. The study has considered ship sizes ranging from those of a small helicopter-enabled offshore patrol vessel at 100m, to a large destroyer at 200m, as well as a frigate size ship at 150m. Over this size range not only will the aerodynamics of the ship be affected, but so too will the motion of the different sized ships in the same seaway. The study therefore includes simulated flight trials in which both the airwake and ship motion was modelled.

Chapter 5 uses CFD to model how the hot exhaust gases from the ship’s gas turbine and Diesel exhausts are dispersed in the ship’s airwake. Hot gases can affect the helicopter performance through reduced main rotor lift and a reduction in engine power. This air temperature effect on helicopter performance and safety has been recognised by the offshore oil and gas industry, where well-defined guidance is provided; in contrast, no such guidance is provided for shipborne helicopters. The prediction of ship exhaust gas dispersion has been considered in the light of the offshore oil and gas guidelines.

The main contributions and conclusions from the research are presented in Chapter 6, along with recommendations for future work.

The research has led to the publishing of six refereed conference papers, authored or co-authored by this thesis author; they are included in the Appendix.

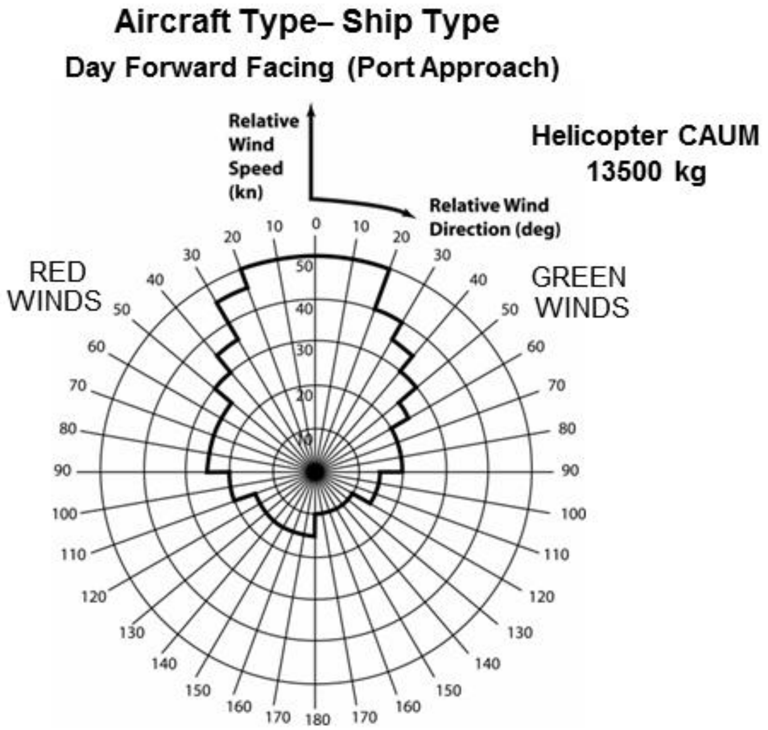

Max Pitch	Max Roll
±2°	±6°

Figure 1.1 Example SHOL showing wind over deck envelope for a UK port-side landing manoeuvre

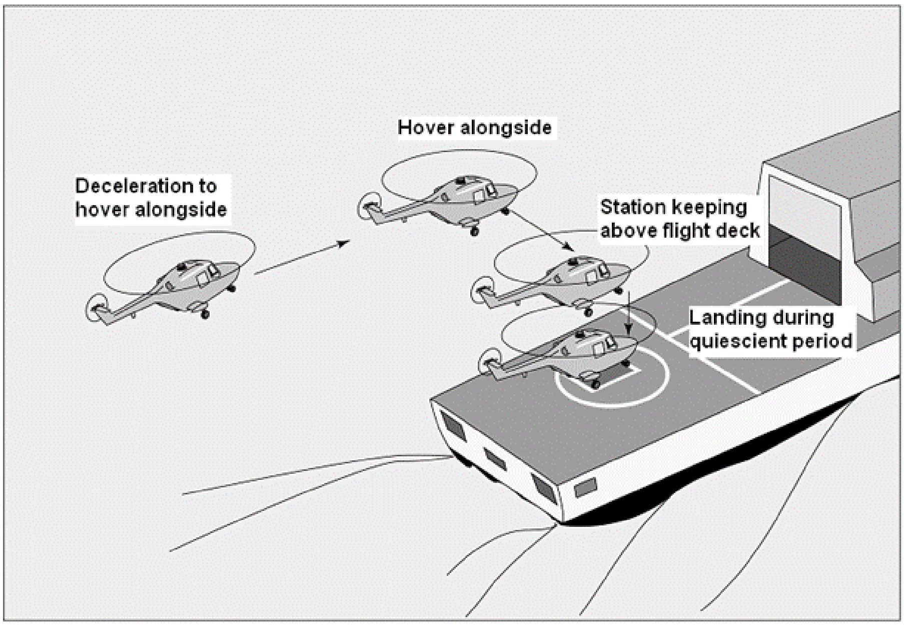

Figure 1.2 Final stages of the recovery of a Royal Navy helicopter to a single-spot frigate

Figure 1.3 The HELIFLIGHT-R flight simulator

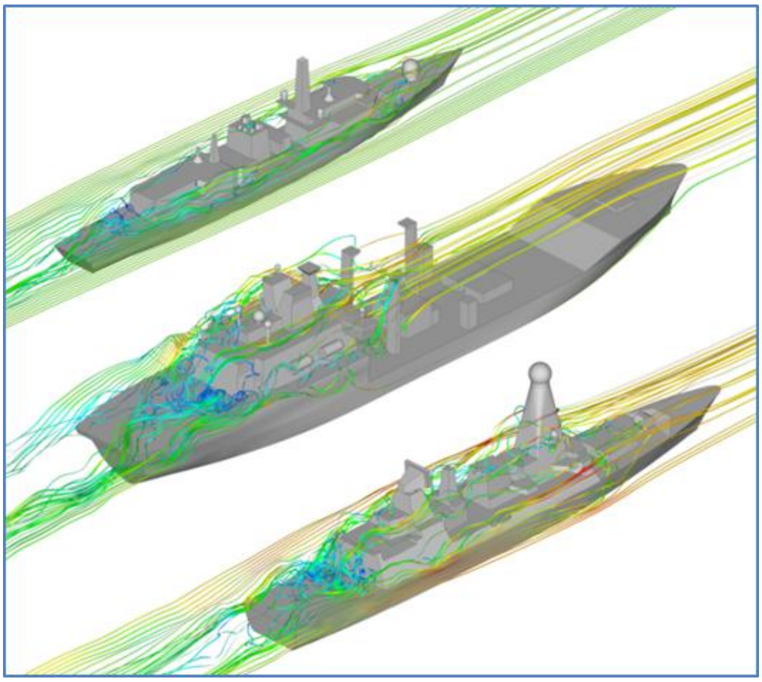

Figure 1.4 Mean pathlines over (from top) Type 23 Frigate, Wave Class Tanker, Type 45 Destroyer.

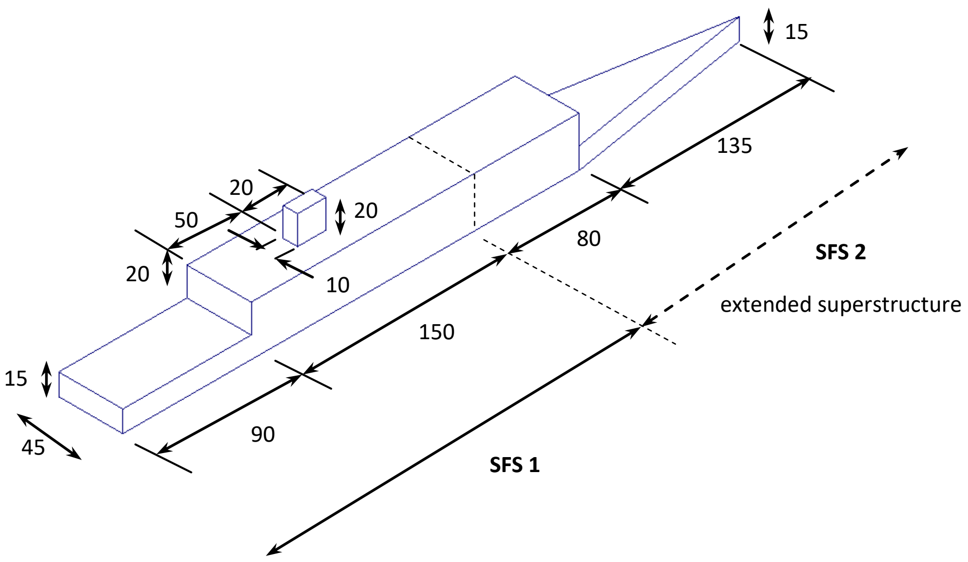

Figure 1.5 The SFS1 &SFS2 geometry (extended & pointed bow).
All dimensions in feet.

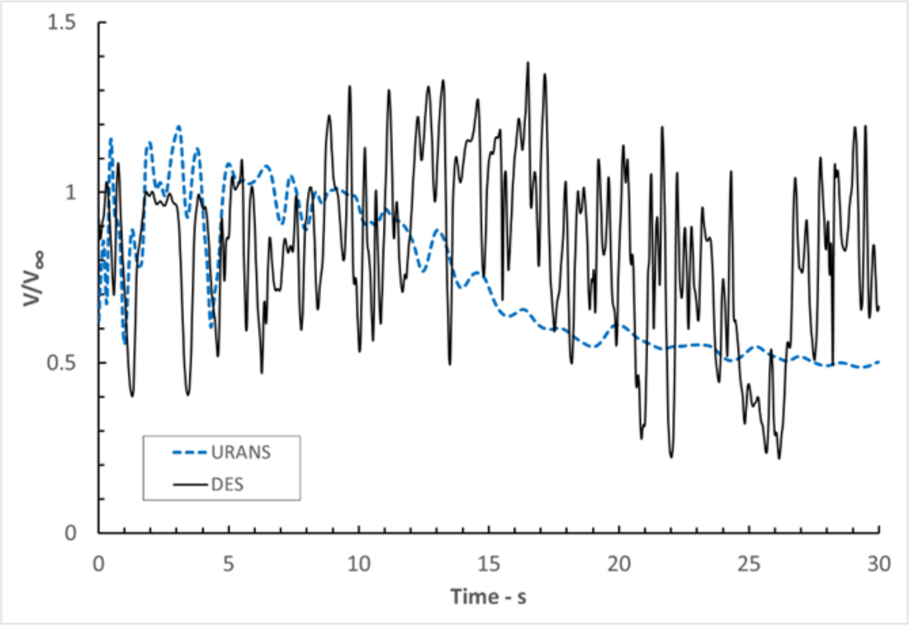

Figure 1.6 Time history of velocity at a point in the flow above the flight deck using URANS and DES [16]

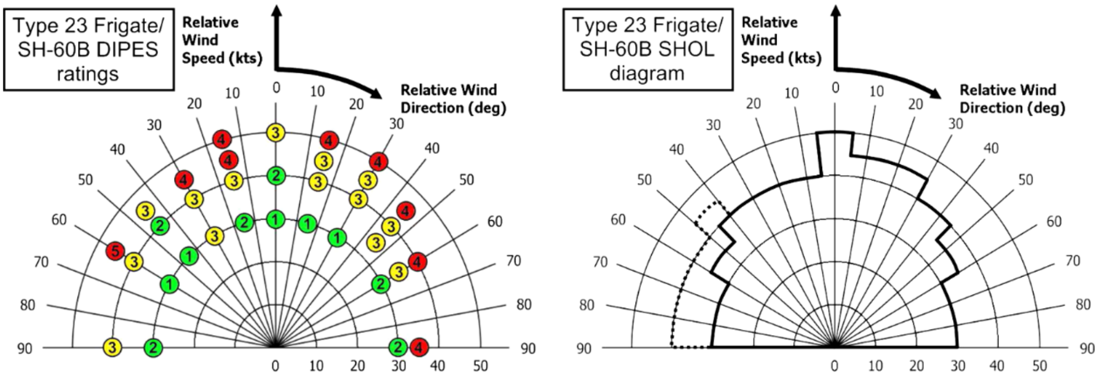

Figure 1.7 DIPES ratings and simulated SHOL envelop [5].

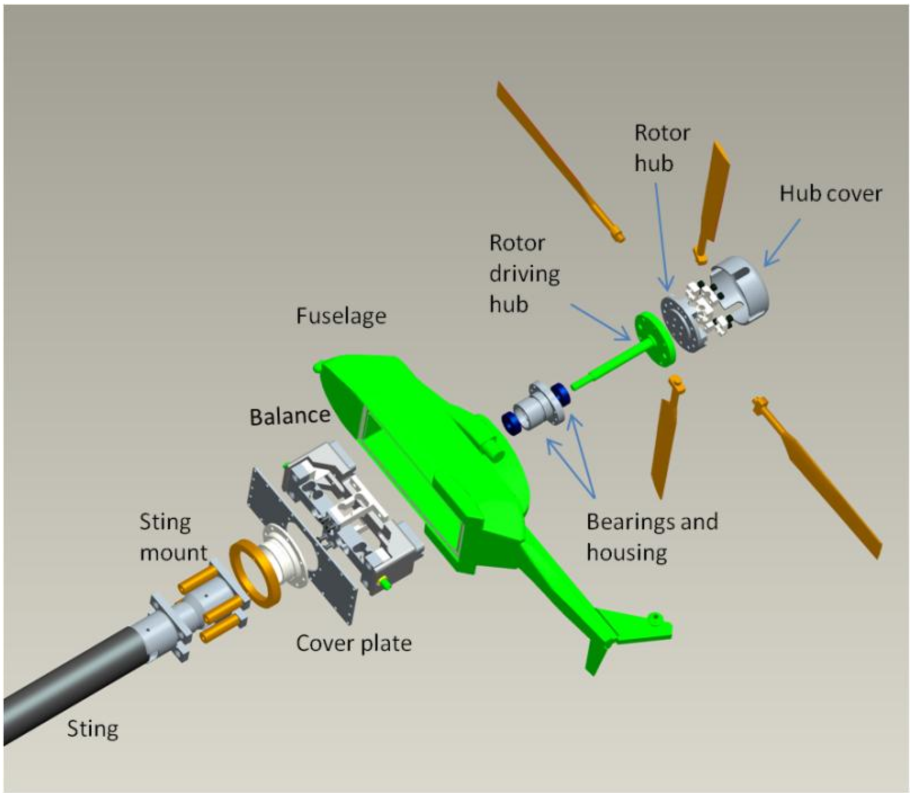

Figure 1.8 An exploded view of the AirDyn [19]

CHAPTER 2

MODELLING AND SIMULATION TECHNIQUES

For the purpose of this study Modelling and Simulation (M&S) is the use of physical and mathematical models that represent a system or a process as a basis for simulations to predict the behaviour and performance of the process or system.

More specifically, the research reported in this thesis is concerned with fluid flow modelling and flight dynamics modelling, and their integration in a flight simulation environment. Each of these elements will be introduced in this chapter.

2.1 CFD Methodology

The following sections describe the methods used to compute the unsteady flow field over and around different ship geometries through use of CFD, along with the techniques used to generate the complex computational meshes required for the flow solver.

2.1.1 Introduction to the Use of CFD for the Simulation of Ship Airwakes

Wind tunnels have traditionally been used to measure the unsteady air flow around a ship's superstructure; however the technique is both time consuming and costly. It is also difficult to obtain dynamic flow similarity through Reynolds number matching. Reducing a ship to a model of a size suitable for wind tunnel testing would require high speed flows which in turn would result in a high Mach number and compressible. While it is possible to adjust the fluid density to obtain Reynolds number matching, even that is impractical in most circumstances. However, CFD is emerging as a tool to investigate this problem at full scale and is becoming a practical alternative, particularly as high performance computing power has become more readily available in recent years.

As previously discussed in Chapter 1, the use of CFD for computing ship airwakes at the University of Liverpool began with the work of Roper [14] using the ANSYS Fluent flow solver to produce steady state simulations of the flow around the Simple Frigate Shape (SFS) and a modified version (SFS2) ship geometries. A database of steady state airwakes were created for a variety of wind over deck (WOD) angles for use within a flight simulation environment. The results from a number of simulated sea trials with piloted flight simulation to perform deck landings were used to generate a SHOL envelope for a hypothetical SFS2-Lynx helicopter combination [5]. Although the resulting SHOL was found to have the main characteristics typically expected over the range of wind magnitudes and azimuths simulated, the levels of pilot workload were found to be lower than expected due to the absence of turbulent perturbations in the airwake. Further work by Roper, reported in Hodge et al [23], later improved on this through use of unsteady CFD simulations and showed that the level of pilot workload reported was considerably affected by the turbulence generated by the ship, although the use of CFD was constrained by the computational hardware available at the time, giving only a few seconds of unsteady flow data.

The fidelity of modelling the airwake around a ship was further improved by Forrest [16] using Detached Eddy Simulation (DES) to produce unsteady ship airwakes. DES is a CFD method first developed by Spalart et al [18] for computing highly separated flows around bluff-bodies. In the flow region adjacent to a solid boundary, where the turbulent length scale is less than the maximum local grid spacing, the turbulence is modelled; but as the turbulent length scale begins to exceed the local grid size the solver switches to a Large Eddy Simulation (LES) mode and starts to explicitly resolve the turbulent eddies. This hybrid method requires a less demanding grid resolution, improves the computational cost of the simulation, and has been proven to be an effective approach for use with the separation that occurs over sharp-edged bluff bodies [24] such as those found on the superstructure of a typical ship.

Forrest was able to compare his DES calculations with experimental data by comparing time-averaged flow statistics and velocity spectra from CFD simulations of both a simplified frigate and a full-scale realistic ship geometry for a number of WOD conditions. Wind tunnel data for the SFS2, obtained by hot wire anemometry, was provided by the National Research Council (NRC) Canada, and full scale data for a Type 23 frigate, measured by ultrasonic flowmeters assembled over the ship's flight deck, was provided by the Defence Science & Technology (dstl) of the UK MoD. A detailed presentation of the experimental and CFD comparisons can be found in Forrest's PhD thesis [16], and in Forrest & Owen [3]. A sample of the mean and turbulent flow characteristics over the flight deck of the SFS2, extracted from [16] can be seen in Fig. 2.1.

The current research has adopted the CFD methodology developed by Forrest and therefore it can be used with the same degree of confidence.

2.1.2 CFD – The Navier-Stokes Equations

Newton's Laws of Motion, applied to an incompressible Newtonian fluid can be expressed in terms of the Navier-Stokes equations. The three-dimensional equations, in the x, y, z directions, together with the conservation of mass equation, provide a complete mathematical description of the fluid flow [25].

The three Navier-Stokes equations of motion can be expressed as a single vector equation:

$$\rho \frac{Dq}{Dt} = -\underline{\nabla} p + \mu \underline{\nabla}^2 \underline{q} + \frac{1}{3}\mu \underline{\nabla}\left(\underline{\nabla} \cdot \underline{q}\right) + p\underline{B} \qquad (2.1)$$

Where $\underline{q} = (u, v, w)$ represents the x, y, z components of velocity, ρ is the density of the fluid, μ is the coefficient of the fluid viscosity, p is the pressure, $\underline{B} = (x, y, z)$ defines the body force vector, and ∇ is the differential operator: $\frac{D}{Dt} = \frac{\partial}{\partial t} + u\frac{\partial}{\partial x} + v\frac{\partial}{\partial y} + w\frac{\partial}{\partial z}$

The mass continuity equation in similar notation is given by:

$$\underline{\nabla}\rho \cdot \underline{q} + \frac{D\rho}{Dt} = 0 \qquad (2.2)$$

In addition to the previous equations it is also necessary to define the thermal interaction within the model for simulations involving the dissipation of hot gases within the flow. Within the ANSYS Fluent flow solver this requires solving the energy equation:

$$\frac{\partial(\rho E_i)}{\partial t} + \underline{\nabla} \cdot \left(\rho \underline{q} E_i\right) = \underline{\nabla \mathrm{p}} \cdot \underline{q} + \underline{\nabla} \cdot \left(\underline{\nabla} T K_{eff}\right) + \Phi + S_i \qquad (2.3)$$

Where T is the temperature of the fluid, E_i is the specific internal energy, S_i is a source term for the internal energy, Φ is the dissipation of internal energy, while K_{eff} is the effective thermal conductivity, which considers turbulent thermal conductivity in addition to the thermal conductivity of the fluid.

Due to the complexity of these non-linear partial differential equations, there are only a limited number of trivial flow problems for which analytical solutions can be found. For more complicated simulations the equations need to be solved numerically through a process called discretisation, where the equations are transformed through use of finite-volume or finite-difference methods in order that they can applied to a number of discrete points within the volume of the fluid.

For steady-state flow problems only spatial-discretisation is required, however for unsteady flow problems the governing equations must be discretised both spatially and temporally using implicit or explicit time integration. The implicit method finds a solution to the governing equations by solving for both the current state of the system and the later one, explicit methods calculate a solution at a time ahead of the current state of the system.

As such, a CFD simulation becomes an iterative process requiring some initial values at each of the discrete locations in order to begin the process of finding a solution, often requiring a large number of iterations to achieve convergence. This is defined as the point at which the ‘residual error’ has fallen below a level that is deemed acceptable and is typically a drop in several orders of magnitude.

2.1.3 ANSYS Flow Solver

The unsteady ship airwake computations carried out for this work were each implemented using ANSYS Fluent, a general purpose, finite-volume CFD solver [25]. ANSYS Fluent accepts both structured and unstructured meshes and has extensive physical modelling capabilities, such as the ability to model steady-state or transient simulations, multi-phase flows, heat transfer from natural, forced and mixed convection. The ability to use parallel processing allows for computationally demanding simulations to be carried out by enabling the simulation to be shared among many CPU’s, reducing the time required to complete a simulation.

The Pressure-Based Navier-Stokes solver (PBNS) within Fluent was used for all computations, second order discretisation was used in time and space to enhance the level of numerical accuracy of the solution and a blended upwind-central differencing scheme was used for the connective terms. Pressure-velocity coupling was resolved through use of the PISO scheme (Pressure Implicit with Splitting of Operator), see Fig. 2.2.

Instability of the solution can occur between each iteration due to fluctuations in the magnitudes of the flow variables. This can be avoided by limiting the amount a flow variable can change with each iteration through use of Under-Relaxation, although this can impact on the convergence rate, potentially leading to increases in overall computational time. The Under Relaxation factor is defined as a constant between 0 and 1, with values approaching 0 leading to no change between iterations and conversely values approaching 1 allowing the maximum possible change in the flow variables. Values between 0.2 and Fluent's default value of 0.75 were used for both the momentum and pressure during the initialisation of the simulation, to prevent divergence of the solution.

The use of the PBNS solver in ANYSYS Fluent requires that only implicit time integration is used, where a number of sub-iterations are computed for each time-step. During the initial time-steps of an unsteady simulation up to 20 sub-iterations were required to achieve acceptable levels in the solution residuals. However, once stabilised this could be reduced to 10 sub-iterations for the remainder of the computations, leading to only a minor decrease in convergence but a significant reduction in the computational time.

2.1.4 Time Step

The choice of time step used for the CFD simulations should be carefully considered to reduce the possibility of not fully resolving the development of turbulent structures within the unsteady flow field. Too large a time-step will result in loss of the dominant frequencies captured, while too small a time-step will lead to an overall increase in the computational time required to complete a simulation.

Spalart et al [26] suggest a method where the Courant-Friedrichs-Lewy (CFL) number is set equal to unity at the smallest cell dimension within the computational domain, such that the smallest eddy structures are convected by the time-marching scheme, leading to error levels close to the spatial discretisation error. The time-step is determined using the following expression, where Δ_0 is the grid spatial dimension in the refined areas of the computational domain, v_{max} is the maximum velocity likely to occur within this region, generally regarded in this study as 1.5 times the freestream velocity of 40knts. This gives a suggested time-step of 0.01 seconds, or a computational frequency of 100Hz.

$$\Delta t = \frac{\Delta_0}{v_{max}} \qquad (2.4)$$

2.1.5 Turbulence Modelling

As discussed in Chapter 1, the level of pilot workload during the launch and recovery of a helicopter to the deck of a ship is often dominated by the unsteady turbulent structures that are continually shed from the ship's superstructure. Viscous flows at large Reynolds numbers are generally turbulent in nature, therefore to accurately represent the airwake produced by the ship, a CFD solution must be capable of capturing both the mean and time-varying characteristics within the flow-field through use of a turbulence model as will be described later.

2.1.5.1 Reynolds-Averaged Navier-Stokes

Turbulent flow is characterised by fluctuating velocities in each direction with infinite degrees of freedom. Directly solving the Navier-Stokes equations for turbulent flow fields is very difficult as the governing equations are non-linear, elliptic, with the pressure coupled with velocity; the flow can be described as chaotic, three-dimensional and diffusive. One solution to this problem is through use of Reynolds decomposition where the instantaneous flow variables are described by a separate mean and fluctuating element such that the velocity components are described thus:

$$q_i = \overline{q}_i + q'_i \tag{2.5}$$

Where $\overline{q}_i$ is the mean flow velocity and q'_i is the fluctuating velocity.

Substitution of this equation into the Navier-Stokes equations and taking a time average will generate the Reynolds-Averaged Navier-Stokes (RANS) equations. However Reynolds decomposition introduces new unknowns (such as turbulent stresses and fluxes) therefore the RANS model describes an open set of equations that require these unknowns to be modelled to achieve closure.

A commonly used method within CFD modelling is to use the Boussinesq method. For turbulent flow fields, Boussinesq proposed that the Reynolds stresses are proportional to the rates of strain with a proportionality coefficient that describes the eddy-viscosity of the fluid. This is shown below in tensor notation:

$$-\overline{q_i q_j} = \nu \left(\frac{\partial q_i}{\partial x_j} + \frac{\partial q_j}{\partial x_i} \right) - \frac{2}{3} \delta_{ij} k \tag{2.6}$$

Where $\overline{q_i q_j}$ is the Reynolds stress, ν is the kinematic eddy viscosity, k is the turbulent kinematic energy, $q = (u, v, w)$ is the velocity vector, $x = (x, y, z)$ is the directional vector and δ_{ij} is the Kronecker delta function.

Therefore if the kinematic and turbulent eddy viscosities are parameterised then the unknown terms can be approximated, allowing closure of the RANS model. However, turbulence modelling based on this method depends on the assumption that eddy viscosity is isotropic and can lead to errors as the model does not account for anisotropic effects. Furthermore, it fails to represent the complexity of the interactions between the mean flow field and the Reynolds stresses, for example large turbulent structures which can perturb a significant portion of the bulk flow.

Using time-averaged RANS can be considered a relatively computationally inexpensive method, as the variables for the mean flow and turbulent quantities can be found through an iterative process to achieve steady-state conditions.

2.1.5.2 Unsteady Reynolds-Averaged Navier-Stokes

As discussed above, the RANS model equations describe the mean flow field with the turbulence derived from the turbulent kinetic energy within the flow, although the time averaging of the RANS equations requires the time differential to be deleted. However if the time derivative is retained and the equations solved in a time-accurate manner, turbulent flow features that develop can be resolved; this practice is known as the Unsteady Reynolds-Averaged Navier-Stokes (URANS) method.

URANS has previously been used to simulate the turbulent airwakes of ships and other large surface vessels [27], although issues have arisen with the suitability of URANS as a means by which to simulate such flows due to the simulations converging to approximate a steady-state solution, despite the use of an unsteady-flow solver [28,29]. Forrest suggests [16] that high levels of dissipative eddy-viscosity generated by the RANS turbulence model further combined with use of dissipative upwind schemes, result in the solution damping the turbulent velocity fluctuations, as demonstrated earlier in Fig. 1.6. Figure 2.3, extracted from [16], shows a comparison of the airwake of SFS2 produced by a URANS simulation and that generated through use of DES demonstrating that while the few vortical structures present in the URANS solution are representative of a quasi-steady-state flow field, the DES solution presents a richer, more chaotic and unsteady turbulent flow field.

2.1.5.3 Large Eddy Simulation

Large Eddy Simulation (LES) has gained popularity for the CFD simulation of turbulence for flows with large Reynolds numbers. It was initially proposed by Smagorinski [30] for the purpose of modelling atmospheric turbulence, including the atmospheric boundary layer, as well as modelling a wide range of engineering flows including combustion and acoustics. The principle of LES is to approach the modelling of turbulence by considering that the large vortical structures created by the geometry contain the majority of the energy within the bulk flow and negate the small scale turbulence length scales, as this improves computational efficiency. The small turbulent length scales are removed through low-pass filtering of the Navier-Stokes equations, using the local grid spacing to define the turbulent scale to be filtered, while the large scale turbulent structures are explicitly resolved by the grid [31]. This process, however, results in temporal and spatial averaging of the numerical solution, similar to Reynolds-Averaging, and the introducing of unknown terms which require a model to account for the sub-grid scale turbulence.

When using LES, careful consideration with respect to the grid spacing is needed, particularly in regions close to wall boundaries as the eddies produced in these regions are typically small in comparison with the vortical structures which go on to develop downstream from the walls. This requirement for high spatial resolution near walls in order to produce accurate LES simulations results in computational volumes with large cell counts. For example, an estimate of the cell count needed to fully resolve an LES simulation for a flow with Reynolds numbers greater than $Re = 10^7$ would be approximately 10^{11} cells [31]. This would be clearly impractical for the current work and, furthermore, the storage and analysis of datasets generated by using such large cell counts would present a significant practical problem.

2.1.5.4 Detached Eddy Simulation

As the main disadvantage for the use of LES for high Reynolds number flows is the requirement of very fine grids in the near-wall regions of the flow domain, hybridisation of LES with RANS has been developed to remove this limiting factor. This allows for the use of URANS in the near wall regions to model small-scale eddy structures without the need for extremely high grid spatial fidelity, while being able to resolve the large scale turbulence explicitly with the grid in the far field regions.

One such popular hybrid LES/RANS model is Detached Eddy Simulation (DES), developed by Spalart et al [31], with the original DES model originating as a modification to the Spalart-Allmaras turbulence model. Within the original Spalart-Allmaras model, the term governing the elimination of eddy-viscosity is dependent on the distance from the wall and is proportional the following expression: $(\tilde{v}/d)^2$, where $\tilde{v}$ is the eddy-viscosity and d is the unit distance to the wall. The modification required for DES involves the substitution of the wall distance, d, with the modification given below in equation (2.7); where C_{DES} is a constant, typically around 0.65, and the local grid spacing is defined by Δ.

$$\tilde{d} = min(d, C_{DES}\Delta) \tag{2.7}$$

This modified term prevents the damping of velocity fluctuations by limiting eddy-viscosity where the local grid spacing is small allowing eddies to propagate and turbulent structures to form which are larger than the grid spatial resolution, these can then be resolved directly through the mesh.

Due to the requirement to accurately capture the turbulent flow structures generated by a complex ship geometry, the work presented in this thesis has made use of the DES methodology as developed by Forrest [16] using the Shear-Stress-Transport (SST) $k-\omega$ model. The DES is applied to the SST $k-\omega$ model through a modification of the term governing the dissipation of turbulent kinetic energy, k. This term involves the parameter f_{B^*} and whereas in the standard model it is equal to unity, in the DES model it is modified according to equation (2.8) in which L_t is the local turbulent length scale, Δ defines the local mesh size and C_{DES} is a constant within the DES model with the value 0.61 (changed from the 0.65 value used in the Spalart-Allmaras model previously). Consequently when the local grid size falls below the local turbulent length scale, the parameter f_{B^*} increases above unity, resulting in an increase in the dissipation of turbulent kinetic energy. It is this reduction in eddy-viscosity which prevents turbulent structures suffering from the effects of damping within the turbulence model.

$$f_{B^*} = max\left(\frac{L_t}{C_{DES}\Delta}, 1\right) \tag{2.8}$$

2.1.6 Boundary Conditions

The ANSYS Fluent solver requires that all the surfaces within the mesh are defined with a specified boundary type along with any data or conditions that govern the behaviour of the boundary. The surface of the ship is modelled as a series of walls with a zero-slip condition, setting the velocity at the surface as zero allowing for the formation of a boundary layer. The sea surface was also set as a wall but with zero shear stress as this allows Fluent to apply a specified velocity profile to represent the atmospheric boundary layer and for it to propagate unchanged through the domain. The top of the computational domain was set to a symmetry condition, which within Fluent assumes there is zero flux across the boundary, while specifying a zero shear condition.

The overall domain, as will be explained later, is a squat circular cylinder, and the outer circumference of the domain is set as a 'pressure far field' which models the free stream conditions at infinity. The use of a pressure-far-field boundary condition requires that the freestream Mach number is defined along with the components of the flow direction. The direction of the flow or WOD angle, shown in Fig. 2.4, is specified in terms of the unit vectors shown in the following expressions; where the term ψ denotes the desired WOD angle, relative to the ship's longitudinal axis.

$$\hat{u}_x = \cos\psi$$

$$\hat{u}_y = \sin\psi$$

$$\hat{u}_z = 0$$

2.1.6.1 Atmospheric Boundary Layer

While the Earth's atmosphere is more than 100 km thick, it is the behaviour of the region immediately adjacent to the surface which provides the greatest influence on the operation of aircraft to and from ships. Both local and global variations in convection and stratification lead to changes in local pressure gradients that result in the formation of winds. These winds can then be further affected by land masses, prevailing winds and surface elements, such as urban environments, forests, and hills, to form a velocity gradient that varies with altitude called the Atmospheric Boundary Layer (ABL).

There has been an intensive undertaking into the modelling and understanding of the ABL and its influence when modelling bluff-body aerodynamics [32,33], including the importance of the ABL profile when performing unsteady ship CFD simulations [34]. Using a power law to describe the boundary layer profile has become a commonly used method by which to apply an ABL as an inlet boundary condition within CFD simulations. This power law, shown below, is based on the work carried out by Counihan [35].

$$v = v_{ref}\left(\frac{z}{z_{ref}}\right)^{\alpha} \tag{2.9}$$

Where v_{ref} is the reference velocity at the reference height, z_{ref} and the exponent α is a constant that describes the surface roughness of the local terrain. The profile of the ABL is dependent on the thickness of the wind layer being considered, the surface roughness and the atmospheric stability. A typical value of α for an ocean surface is given as 0.13 [35] while for the purposes of this study where complex ship designs are investigated, the reference speed and height were set to 50 knots and 100 metres respectively, the inlet profile used is shown in Fig. 2.5.

Although the power law has been shown to give a good approximation of the ABL, this model only holds for neutral conditions and is liable to vary over time for real-world conditions at sea due to the instability of the atmosphere [36]. However accounting for the variation in this exponent value would introduce another degree of complexity, as such a constant value that is representative a typical sea-surface was considered to be sufficient.

2.1.6.2 Exhaust Modelling

To model the mixing of hot exhaust gases from the ship's engines into the airwake, the energy equation was activated within ANSYS Fluent, along with the solution of additional transport equations to account for the buoyancy of the plume. Although the efflux has both momentum and buoyancy, in the near field where the exhaust is injected into highly disturbed air the plume is momentum-dominated rather than buoyancy-dominated as observed by Ergin et al [37], amongst others.

To model the exhaust flows, which is presented in Chapter 5, the boundaries of both the Diesel and gas turbine exhausts, an example of which is shown in Fig. 2.6, were designated as mass flow inlets. However, to give a representation of the velocity profile of the exhaust flow, the exhaust ducting within the ship was also included in the model so that the injected mass flow was allowed to develop from a uniform velocity profile for 5 duct diameters. The gas turbine and Diesel exhaust uptake boundary were circular surfaces with specified mass flow rates and temperatures using values typical for ship engines used in modern frigates that do not utilise waste heat recovery systems. The individual exhaust gas species were not specified and the exhaust was simply defined as air. For the purposes of this study, the Diesel and gas turbine engines were considered to be operating simultaneously.

2.1.7 Settling Time

The process of undertaking a transient CFD simulation requires that a steady-state solution is first carried out to provide a set of conditions in each cell so that the flow solver can start the iterative process with an initial 'guess' at the solution of the unsteady flow-field. Furthermore, when creating an unsteady flow simulation, a number of time steps must elapse before the solution can be considered 'settled' and reliable data gathered, giving a true reflection of the unsteady velocity perturbations in the flow field.

Previous work by Roper [14] and Forrest [16] and later by Kelly et al [38] relied on the time it would take for the flow to cover a distance of at least twice the length of the ship, through the flow domain using the following equation:

$$t_{sett} = \frac{2l}{v_{fs}} \tag{2.10}$$

Where l is the ship length and v_{fs} is the freestream velocity.

Determining the point at which an unsteady simulation of a ship airwake can be considered 'settled' is not straightforward, particularly as the airwake in the region of interest typically covers the flight deck. In this region, the complexities of the ship's superstructure create an airwake containing a broad spectrum of frequencies due to the chaotic nature of the flow and so the time for the unsteady flow field to settle needs careful consideration. Whereas equation (2.10) works well for a headwind flow along the length of the ship, it is not so obvious for investigating oblique WOD conditions, as a beam wind may present a case where the simulation does not adhere to the method shown in equation (2.10). Another way to assess whether the unsteady flow has settled is to monitor the unsteady velocity components at a specific point for each time-step during the simulation and taking the approach that as a simulation progresses, the cumulative moving average of the unsteady velocities will approach the true time-average magnitude of the unsteady velocity perturbations seen at that point. This can be expressed in the form shown below:

$$\frac{1}{n}\sum_{i=\Delta t}^{n} v_t \longrightarrow \overline{v}_t \pm \sigma \tag{2.11}$$

Where n is the number of time steps, Δt is the time step, v_t is the unsteady velocity and $\overline{v}_t$ is the time-averaged velocity. The time-averaged velocity is found using the most current half of the unsteady values and the simulation can be considered settled when the cumulative mean falls with the bounds of one standard deviation of the time average value, as seen in Fig.2.7.

The graph shown in Fig. 2.7 was generated using data sampled from the start of an unsteady CFD simulation of a 'frigate like' ship geometry, whose total length was

200 metres, for a 40 knot Green 45° WOD condition. Using equation (2.10) to estimate the settling time gives a value of 20 seconds, however the data in Fig. 2.7 shows the simulation could be assumed to be settled at 15 seconds, equivalent to 500 time steps for this case. Therefore when dealing with computationally expensive simulations it is worth taking into account the effects the ABL, WOD conditions, and ship size have on the time required to transition to a fully resolved, unsteady CFD solution.

2.1.8 Parallel Processing and High Performance Computing with ANSYS Fluent

The generation of time-accurate unsteady CFD simulations of ship airwakes requires the use of High-Performance-Computing (HPC) and the use of parallel processing to deal with issues arising from large cell counts, computationally expensive processes, and large data sets.

2.1.8.1 The Chadwick Compute Cluster

The Chadwick compute cluster is a parallel Unix-based HPC facility which came online in 2014 and provided a marked step in computational power available to researchers at the University of Liverpool, previously airwakes were computed using the ULGBC5 compute cluster. Both facilities make use of the Infinipath interconnect between each individual computer (node) within the cluster to increase the speed of communication between nodes during the simulation. All the 118 nodes in the Chadwick HPC are connected by InfiniBand connection operating at speeds of 40 Gigabits per second, each node has 16 Sandy Bridge quad-core processors each with 64 Gb of RAM, enabling parallel computations that require large amounts of memory.

2.1.8.2 Parallel Processing In ANSYS Fluent

The parallel solver within ANSYS Fluent allows for a solution to be handled by multiple processors, reducing the overall computational time needed to perform a complex simulation by using either multiple processors on a single computer or multiple computers connected over a network. Parallel processing in ANSYS Fluent involves the solver managing and interacting with the Host process and a set of compute nodes in the HPC. It should be noted that although the time required to compute will decrease as the number of compute nodes is increased, there comes a point at which the parallel compute efficiency begins to suffer as the time taken to communicate data between nodes increases.

Before the solver can begin, the grid and data required to initialise the simulation is split into multiple partitions, each of which is then shared amongst the compute nodes while the Host process is allocated a node to itself and designated 'compute-node-0'. This process is carried out automatically as part of the parallel solver as any imbalance between each of the partitions will result in the nodes being used unequally so creating a local bottleneck where some nodes are over-used, increasing computational time.

Figure 2.8 shows a flow diagram for a typical Fluent computation using four cores [25]. One node is chosen as the host process and this node then schedules the computations and communicates with the others over the network through compute node 0. Communication between nodes is performed using a message passing library, in this case the Message Passing Interface (MPI).

2.1.8.3 Scripting

ANSYS Fluent makes use of a Graphical User Interface (GUI) through which a user sets up the various parameters required to carry out the simulation. However when using a remote HPC facility to carry out a CFD simulation the GUI is not available so the simulation must be implemented through the use of text-based commands using the scripting language Scheme, which is native to ANSYS Fluent. A single, text based script file was created to carry out each CFD simulation from start to finish.

2.1.8.4 Overall Solution Strategy

This section presents a general overview of the method used to create time-accurate unsteady ship airwake computations at the University of Liverpool, and is based on the validated approach developed by Forrest [16]:

- Iterate the RANS solution to achieve steady-state using the steady state solver with the standard k-ε turbulence model (typically around 1000 iterations).
- Use the results from the steady state flow field to initialise the unsteady flow field.
- Activate the unsteady solver in DES mode and switch to SST k-ω turbulence model.

- Compute a number of time steps, to allow flow to transition from steady state to unsteady as described in section 2.1.7 (typically around 1500 time steps which are later discarded).

- Compute a further 3000 time steps, while sampling data from the entire flow-field at a rate every fourth time step for use within flight simulation. For particular points of interest in the flow, e.g. an anemometer position, data sampling should also be carried out at this point.

- Save case and data files and exit the solver.

While the simulation is underway, a dump file is constantly updated by the solver with values of the residual error of the governing calculations. These outputs are closely monitored to ensure that convergence has occurred and that an adequate reduction in the magnitude of the residuals has taken place; the continuity residual values were typically below 1×10^{-3}. Simulations were carried out using up to 128 cores, giving an average computation time of about 3 days to produce 45 seconds of unsteady simulation data for a mesh containing $\sim10 \times 10^{6}$ cells.

2.1.9 Meshing Techniques

The ship geometry was placed within a cylindrical domain with the centre of the hangar face, level with the flight deck being designated the datum point where the geometrical coordinates $(x, y, z) = 0$. The radius of the domain was set to $r = 4.5l_s$ and a total height of $z = 0.9l_s$, where l_s is the length of the ship, as shown in Fig. 2.9. This method was originally developed by Forrest [16] and allows a single mesh file to be used for an unlimited number of WOD azimuths by varying the horizontal u and v inlet velocity components.

2.1.10 Frigate Geometries

The use of realistic ship geometries, which reflect those currently in use by navies around the world, favours the use of an unstructured meshing approach. Modern naval ship design is now focused on the minimisation of radar cross-sectional area which produces topside geometries composed of sharp-edged, bluff-body structures. The complexity and intricacies of the superstructure found on a modern naval frigate would necessitate a convoluted and laborious effort to produce a hexahedral, block-structured grid. For simple geometries, such as aerofoils, a structured grid will be both more computationally efficient as convergence is achieved sooner while also producing a more accurate result. However the nature of unstructured meshing means that for a complex geometry a mesh can be generated much more quickly than a structured mesh. For more complex and turbulent flows, the adaptivity facilitated by an unstructured mesh may also give an increase in the accuracy of the solution, especially when using DES due to the isotropic nature of the tetrahedral cells away from walls [39,40].

For the purposes of this study a generic frigate geometry was created and called the ‘Future Surface Combatant’ (FSC) which is representative of a modern, single-spot naval frigate. The baseline geometry, termed FSC1 was used to identify the potential impact that various design features have on the ship-helicopter interface. This baseline variant of the FSC is shown in Fig. 2.10.

A second, different, ship geometry, was used for the investigation of the effects of scaling CFD airwake data. This Generic Naval Frigate (GNF) geometry presented a symmetrical superstructure, particularly in the regions which dominate the airflow over the flight deck. This symmetrical geometry was selected so that winds coming from the Port or Starboard would create symmetrical airwakes. The matrix below, Table 1, shows which ship geometry was used for each study.

Table 1.1 Ship geometries investigated

Ship Model	**Chapter 3**	**Chapter 4**	**Chapter 5**
Type 23	✓	-	-
GNF	-	✓	-
FCS0	✓	-	-
FCS1	✓	-	-
FCS2	✓	-	-
FCS3	✓	-	-
FCS4	✓	-	✓

2.1.11 Meshing Approach and Optimisation

The ANSYS meshing tool ICEM is an advanced geometry acquisition, mesh generation and optimising tool which was used to 'clean' the surface topology and produce meshes. ICEM supports a wide range of digital CAD model formats and as such provides some degree of flexibility when importing complex CAD geometries. Before meshing can commence, the geometry will often require some degree of attention to remove small features, such as narrow masts, railings, small ship-fittings etc, as the influence of these small objects would be negligible on the overall flow field but would need a very fine degree of meshing, driving up the cell count and impacting on the solution Courant Number (CFL condition). However due to read-write errors in the translation between CAD formats some distortion of the geometry may occur requiring the use of the Build-Topology tool within ICEM to align curves and ensure surfaces conform to the curves to yield a geometry which can be considered 'watertight'. Gaps or missing surfaces can provide routes through which the meshing tool may leak, creating a spurious volume mesh inside the ship model. Figure 2.11 shows an example of a ship superstructure geometry as supplied where the small features and the panels that make up the superstructure can be seen.

Once a suitable geometry has been created, the surface of the ship and flow domain are meshed with triangular elements. The surfaces of each ship were meshed with surface elements equivalent to a target spatial grid dimension of $\Delta_0 = 0.05z_h$, typically 0.3m, where z_h is the hangar height, in accordance with the validation and grid dependence work carried out by Forrest [16]. A growth rate of 1.3 away from the walls was used to ensure a smooth transition into the far-field regions to a maximum cell size of 3m in the extreme far-field. Regions of interest within the volume mesh, typically around the superstructure and the areas above the flight deck, require refinement to fully resolve the turbulence within the airwake. This can be achieved by carefully controlling the growth rate away from the surfaces and by the insertion of 'density boxes'. Within a density box, the cell size remains constant, allowing for regions of small, uniformly sized, isotropic cells which can make maximum use of DES.

To produce the surface mesh, as seen in Fig. 2.12, the Octree volume meshing tool was invoked in ICEM, this may seem counterintuitive but the Octree tool contains a powerful surface wrapping function that produces good quality surface elements from complex, underlying topological features. This is known as a 'top-down' approach, conversely the 'bottom-up' approach starts by splitting edges, then meshing surfaces before growing into the volume. The corresponding Octree volume mesh is not used and can be discarded. The Octree form of volume meshing is relatively inefficient and can often lead to cell counts double that of other volume meshing methods. Once the volume mesh is removed the remaining surface mesh can then be refined to both improve the overall quality without the volume elements to slow down and restrict the smoothing process. This removes any anisotropic triangular elements and will smooth the transition between the elements as the cells growth rate increases away from walls. Once smoothed and of sufficient quality, a Delaunay volume mesh is grown from the surface mesh, which is again smoothed to improve poor quality cells.

Twelve layers of prism cells were grown from the ship wall surfaces to efficiently resolve the viscous boundary layer; prism cells were also grown from the floor of the domain to help maintain the profile of the ABL as it moves through the domain. The prism layer mesh was generated by the initial insertion of four layers, each of which were further split into three layers. This approach reduces the amount of poor quality cells and the formation of pyramidal elements occurring due to the complex nature of the superstructure geometries used. The wall adjacent grid height was set to give $y^+ = \mathcal{O}(10)$ and the prism layers were grown into the tetrahedral cells using an expansion rate of ~1.3. It is important to note that the y^+ parameter is used to describe how fine or coarse a surface mesh is for a particular flow solution. Larger values of y^+ indicate that the flow within these layers of cells are turbulent, finer cells and thus smaller y^+ values indicate laminar flow regions in the sub-layers within the boundary flow. The value of y^+ was chosen such that the first cell height was beyond this laminar region.

The total cell counts were of the order of 8 million to 18 million cells, with the density regions, such as that shown over the deck in Fig. 2.12, being responsible for much of the variation in cell counts due to the large number of small cells occupying these boxes. Compared with the validation work carried out by Forrest [16], the higher cell counts used for the work carried out in this thesis differ only in the refinement levels of the volume mesh to make use of improvements in computational power available.

2.2 Helicopter Flight Dynamics Modelling

The simulation of a helicopter flying to the deck of a ship requires a mathematical flight dynamics model of the helicopter. The model will also need to interact with the CFD-generated airwake to appropriately perturb the aircraft while it is immersed in the unsteady air flow. The modelling was realised by using a commercially available software tool known as FLIGHTLAB®, which is a multi-body modelling and simulation environment [41]. Within FLIGHTLAB a helicopter flight model can be constructed from a library of predefined components such as those identified in Fig. 2.13.

High fidelity flight models of operational aircraft are generally unavailable as they are commercially sensitive. A natural choice for the helicopter models that might be used in this study were those of a AW101 Merlin and a AW159 Wildcat, as operated by the UK Royal Navy. However, due to the unavailability of these flight models, the approach taken was to adopt the Generic Helicopter Model within the FLIGHTLAB library and to configure it to represent a Sikorsky SH-60B SeaHawk, Fig. 2.14. The advantages of using this model is that it has been well validated using publically available flight data [42]. The flight model comprises the following major subsystem components, as identified in Fig. 2.13:

Main Rotor Model

A blade element theory model is used to model the helicopter main rotor. Using the blade element approach, each rotor blade is divided up into a series of contiguous elements, 10 in the case of the SH-60B model. The airspeed and incidence angle at each blade element are then calculated, and look-up tables of non-linear lift, drag and pitching moment coefficients are used to find the aerodynamic forces and moments at each blade element [43].

Rotor Inflow Model

The inflow model simulates the flow field induced by the rotor blades at the rotor disc. This flow field changes the local blade incidence and dynamic pressure, and consequently the aerodynamic forces and moments at the blade elements. A finite state Peters-He dynamic wake model is used in the SH-60B helicopter simulation [44].

Fuselage and Empennage Aerodynamic Models

Separate look-up tables are used to model the aerodynamics of the fuselage, vertical tail, and port and starboard horizontal stabilators. The aerodynamic forces and moments for each airframe component are modelled as coefficients derived from wind tunnel data, and stored in look-up tables as non-linear functions of incidence and sideslip [45].

Tail Rotor Model

A simple rotor model based on the theory described by Bailey [46] is used to model the helicopter tail rotor. The Bailey model uses linearised closed form expressions for the rotor thrust and torque, which have been obtained analytically by integrating the airloads over the rotor blade span and averaging over the disc azimuth. The cant angle of the SH-60B tail rotor, shown in Fig. 2.14 as 20°, is also included in the model [45].

Flight Control System

The SH-60B flight control system consists of a primary mechanical flight control system and an Automatic Flight Control System (AFCS) [42]. The AFCS model includes the analogue and digital channels of the Stability Augmentation System (SAS) and models of the sensors and actuators. The SAS provides rate damping and short-term dynamic stability in the roll, pitch, yaw and vertical control axes.

Engine Model

The engine is modelled as a simple turbo-shaft engine with a rotor speed governor [47].

Landing Gear Model

The landing gear model [48] provides reaction cues on touchdown during the deck landing task. The normal force developed by the oleo (strut/damper) and tyre combination is modelled as a spring and damper system. The tyre longitudinal and lateral forces are modelled as frictional forces that are proportional to the tyre normal force scaled by constant coefficients. In the longitudinal direction, the landing gear model has two coefficients of friction; rolling friction and braking friction.

The helicopter subsystem models listed above are integrated within FLIGHTLAB together with the relevant equations of motion. The total forces and moments produced by the integrated model are then applied at the helicopter's centre of gravity and are used to solve the six degrees-of-freedom rigid-body equations of motion to calculate the helicopter's state vector.

Later in the thesis the flight dynamics modelling described above will be used in flight simulation to assess the effect of ship airwakes on a helicopter's handling qualities and the pilot workload. It is therefore important for the reader to have a basic understanding of helicopter flight controls. The lower half of Fig. 2.15, extracted from [47], identifies three controllers: cyclic, collective and pedals which, in an advanced aircraft like a helicopter, operate with an automatic flight control system (AFCS).

Cyclic Controller

The cyclic, often called the 'stick' by pilots, is a control normally positioned vertically in front of, and between the legs of the pilot. It is used to change the attitude and airspeed of the helicopter. The cyclic does this by altering the attitude of what is called the rotor disc, i.e., the hypothetical 'disc' the rotors make when they are turning. The disc and hence the helicopter then moves in the direction of tilt. Moving the cyclic forward causes the rotor disc, and the helicopter, to tilt forward. The helicopter pitches nose down, and also speeds up, due to the effects of gravity. Moving the cyclic aft has the opposite effect, and moving it sideways causes the aircraft to turn.

Collective Controller

The collective is on the pilot's left side, and looks rather like an old-fashioned handbrake in a car. It is used to enable the helicopter to climb and descend. It does this by altering the pitch of the rotor blades together, or 'collectively'. Raising the lever increases the rotor pitch and causes the helicopter to climb; lowering it puts the aircraft into a descent.

Engine Throttle

The throttle, which controls the power of the engine, is integrated with the collective. While lifting the collective up and down alters the pitch of the rotor blades, twisting the handgrip adjusts the engine power. Raising the lever and increasing the pitch would cause more drag on the rotor, so more power is needed for lift to initiate a climb. The collective and throttle need to be carefully coordinated, although in modern helicopters there is an electronic governor which senses the position of the collective and adjusts the power accordingly.

Pedal Controls

The pedals are at the pilot’s feet and cause the helicopter to yaw, or turn about a vertical axis by altering the thrust of the tail rotor. Increasing thrust using the left pedal will turn the helicopter to the left, and decreasing it with the right pedal will turn it to the right.

2.3 The HELIFLIGHT-R Flight Simulator

The HELIFLIGHT-R, shown earlier in Fig. 1.3, is a full-motion research flight simulator which has a three channel 220 x 70 degree field of view computer visual system, a six-degree of freedom motion platform, a four-axis force-feedback control loading system and an interchangeable crew station. Flight mechanics models are developed in either FLIGHTLAB or Matlab/Simulink and the current aircraft library features a range of fixed wing, rotary wing and tilt-rotor aircraft. The outside world imagery is generated using Presagis’ Creator Pro software to produce either geo-specific or custom visual databases. Using Presagis’ VEGA Prime software, the Liverpool group has generated its own run-time environment, LIVE, which allows the simulator operator to change environmental effects such as daylight, cloud, rain and fog, along with maritime effects such as sea state, ship exhaust and rotor downwash on the sea surface. A heads-up display can either be generated using an LCD screen with a beam splitter located above the instrument panel or projected directly onto the inside surface of the dome. The motion and visual cues, together with realistic audio cues, provide a powerful immersive environment for a pilot. Data from the flight models, e.g. aircraft position, accelerations, attitudes etc., together with pilot control inputs can be monitored in real-time and recorded for post-flight data analysis, while in-cockpit cameras provide audio and video recordings of a flight, together with computer-generated “chase” views of the aircraft.

2.3.1 Helicopter Flight Simulation at the Ship-Helicopter Dynamic Interface

The creation of a full-motion flight simulation environment for a helicopter operating to a ship requires: a simulator, in this case the HELIFLIGHT-R; a helicopter flight dynamics model; a ship visual model such as that shown in Fig. 2.10 but with realistic rendered surface to give a ship model visual details such as doors, lights, paint, deck markings etc to improve the visual aspects for the pilot. Also required are an unsteady CFD-generated airwake; a ship motion model and a visual scene as can be seen in Fig. 2.16.

The FLIGHLTAB modelling and simulation software has a library with a number of flight models for both rotary and fixed wing aircraft. Figure 2.17 shows the FLIGHTLAB Generic Rotorcraft which, for this work, has been configured to represent a Sikorsky SH-60B Seahawk helicopter model that was used, for example, by Hodge et al [4]. The SH-60B was selected because of the availability of engineering data in the open literature for that type of helicopter [45]. The FLIGHTLAB Generic Rotorcraft model is made up of the major sub-system models described above in section 2.2.

The Airload Computation Points (ACP) indicated in Fig. 2.17 are where the three-dimensional velocity components of the air flow are applied to the helicopter model to create the forces and moments that are imposed on the aircraft by the unsteady airwake. The velocity components (u,v,w) created by the CFD are stored in a lookup table at fixed positions in space (x,y,z) and at different times (t). The x,y,z locations in the lookup table have to be translated, by FLIGHTLAB, to the locations of the ACPs shown in Fig. 2.17, including those along the rotating blades of the main rotor. There are 46 ACPs on the helicopter flight model.

2.4 Integration of CFD-Generated Airwakes into Flight Simulation

As outlined in Chapter 1, there are two flight simulation techniques that have been applied in the research being reported in this thesis: piloted motion-base flight simulation, and the Virtual AirDyn (VAD) which is a computer-based offline non-piloted simulation technique. The following sections will give more detail of the two techniques.

2.4.1 Motion-Base Flight Simulation

The simulation process begins with a solid model of the ship under consideration. The full-scale model is placed within the CFD domain discussed above and illustrated in Fig. 2.9. The digital drawing is also used for the visual scene so that the ship to which the pilot is flying represents the ship for which the CFD has been generated. The CFD-generated airwakes are created as described above and then they are integrated with the FLIGHTLAB simulation environment using the processes described in Fig. 2.18. As shown in Fig. 2.18 the unsteady CFD is created using Fluent, at a frequency of 100 Hz, and on an irregular unstructured grid. Using an interpolation routine within Fluent the u,v,w velocity components at positions x,y,z are then interpolated onto a rectangular regular grid of mesh size 1m; it is also down-sampled to 25Hz by only recording every 4th time step due to data size limit constraints; 25 Hz is more than adequate for realistic piloted flight simulation. The rectangular domain, as illustrated in Fig. 2.18, only encompasses the three-dimensional space in which the helicopter will be expected to fly and the 1m grid size is consistent with the spacing of the Airload Computation Points in the flight model shown in Fig. 2.17. This process significantly reduces the data file size and assists the data processing capacity of FLIGHTLAB. The Fluent data files are then processed in Matlab and are made available to FLIGHTLAB as a set of lookup tables where u,v,w velocity components are stored in x,y,z locations at every 0.025 seconds. There are 30 seconds of airwake data and this is looped with a smoothing function, so that an infinite loop of airwake data is constantly available and the change between the start and end points of the airwake data are imperceptible to the pilot. The spatial positioning of the velocity components and the integrity of the fluctuating velocities are checked by comparing the original CFD data with that which is finally used by FLIGHTLAB. The data is always nearly identical, with some minor smoothing of velocity perturbations due to spatial interpolation, showing that it has not been adversely affected by the process.

Separate ship airwakes are generated for every wind angle of interest, but at only at one velocity. Because of the bluff body aerodynamics of the ship, the structure of the flow field of the airwake does not change with the upstream velocity. Therefore if the airwake is computed for a 40 knots wind, it can be scaled down to 20 knots by halving all the velocity components and, from Strouhal scaling (frequency of vortex shedding is proportional to velocity), as the velocity is halved from 40 to 20 knots, the time step between components is doubled. This principle is discussed in greater detail in Chapter 4, where its validity will be demonstrated.

Ship motion is also required for the simulation, so the pilot has to contend not just with the unsteady forces and moments on the helicopter, but also the landing spot moving in roll, pitch and heave. Ship motion is determined by the ship design, the sea surface waves and the relative motion of the two. A ship does not therefore have a particular defined motion so what is required for the simulation is a motion that is representative of a particular ship and sea state, and is realistic when viewed by the pilot. While ship motion can be calculated by bespoke software models, the approach used most often at Liverpool has been a more pragmatic one, to take a recorded motion for a ship and to scale it according to the ship size and sea state so it has representative displacements and frequency and, importantly, has the naturally occurring quiescent periods when the motion subsides somewhat [4]. An example of ship motion data in the roll, pitch and heave axes measured at the ship's centre of gravity is shown in Fig. 2.19. The motion can be seen to have the naturally occurring quiescent period and it is this that the pilot waits for to execute the final landing phase. However, as part of the research being reported in this thesis, and presented in Chapter 4, it was also necessary to generate ship motions for different ship sizes in different sea states. The motion was computed for using ShipMo3D, a ship motion code developed by the Canadian Department of National Defence [49], and made available to the University of Liverpool.

Having created a simulation environment in which the airwake, ship motion, flight model and visual scene have been implemented in the motion base simulation environment via FLIGHTLAB, piloted flight tests can be conducted. A simulated flight test programme typically consisted of a series of approach and deck landing tasks for different winds over deck, usually in increments of 15° and 5 knots. During each experiment an experienced (former) Royal Navy (RN) test pilot is instructed to fly the deck landing task using the standard RN technique shown previously in Fig. 1.2. This involves flying the helicopter to a stabilised hover on the port side of the ship, then manoeuvring sideways across the deck to a position above the landing spot and waiting there for a quiescent period in the ship's motion before executing a vertical landing. Three Mission Task Elements (MTEs) can be identified from this description of the deck landing mission: (i) Sidestep manoeuvre; (ii) Station keeping (precision hover) above the flight deck; and (iii) Vertical landing.

During the test programme the pilot is asked to award ratings for the difficulty of carrying out the assigned task, which can be the full deck landing, or the individual MTEs described above. For the complete landing task the pilot uses the Deck Interface Pilot Effort Scale (DIPES), Fig. 2.20, which is the same 5-point rating scale that is used during FOCFT [50]. On completion of the landing the test pilot uses the chart in Fig. 2.20 to award a rating based on workload (or pilot compensation), performance, accuracy and consistency; the pilot makes this subjective judgement based on what would be expected of an average fleet pilot. On the DIPES scale a numerical rating of 3 or less indicates that deck landings can be repeatedly achieved with precision and safety, under the conditions being tested. A rating of 4 or 5 indicates the contrary and places that condition outside of the SHOL, thus prohibiting deck landings under those conditions. In addition to the detailed comments given by the pilot, a number of letter suffixes can also be assigned to each rating, to describe the cause of increased workload (e.g. ‘T’ for turbulence or ’D’ for deck motion). Of these suffixes, only spray (S) which reduces the pilots visibility, and funnel exhaust (E) which affects engine performance if ingested, are not currently modelled in the simulator. Figure 1.7, seen earlier in Chapter 1, shows a set of DIPES ratings awarded by the pilot, and the resulting simulated SHOL diagram.

Although the DIPES scale has clearly been optimised for the purpose for which it was devised (i.e. qualification and clearance of SHOL envelopes), it is too coarse a scale for assessing what can often be fairly subtle variations in pilot workload, resulting from changes in simulator modelling and cueing fidelity. Therefore, in the simulator, pilot workload ratings were also taken from the 10-point Bedford workload rating scale, Fig. 2.21. A questionnaire study, carried out by Roscoe and Ellis during development of the scale, found that pilots naturally think in terms of spare capacity when considering workload [51]. In the Bedford scale spare capacity is defined as the pilot’s ability to perform secondary tasks, such as maintaining mission awareness, monitoring aircraft systems or listening to radio communications, the primary task being to fly the aircraft through a particular manoeuvre or mission. The higher the workload generated by the primary task, the less spare capacity there is for attention to these secondary tasks.

How the piloted flight simulation and the two rating scales are applied in practice will be demonstrated in Chapter 4.

2.4.2 The Virtual AirDyn

Chapter 1 briefly described how the Virtual AirDyn (VAD) is a software-based derivative of the experimental AirDyn, where a model helicopter with a motored rotor and mounted on a six-axis force block is placed into the wake of a model ship and measures the unsteady loads imparted by the ship’s airwake. In the VAD, the airwake is generated by unsteady CFD, and the experimental model is replaced with the FLIGHTLAB UH-60B flight model [22,52].

As with the motion-base simulation described above, the simulation begins with the ship solid model; a 30 second airwake is created and interpolated onto the rectangular regular grid and is formatted and integrated into FLIGHTLAB. The method by which the VAD has been employed to compare ship airwakes is to carry out a translational approach beginning with the helicopter's rotor hub located at the ship's hangar height, one beam width from the landing spot, off the port edge of the ship. The helicopter is then held stationary with the rotor hub at several positions over the flight deck as shown in Fig. 2.22. If the helicopter was not held in a fixed position then it would move under the action of the unsteady aerodynamic forces and the pilot would counteract the displacements through the controls. By fixing the helicopter in one location the aircraft then has unsteady forces imposed by the airwake; the larger and more unsteady the forces are, the more aggressive the airwake is.

As with the application of FLIGHTLAB within the HELIFLIGHT-R flight simulator, the unsteady CFD airwake velocities are imposed onto the helicopter model at the 46 ACPs shown earlier in Fig. 2.17. At each of the sampling locations over the ship, Fig. 2.22, the helicopter is held stationary and the time histories of the unsteady forces and moments at the helicopter's centre of gravity are recorded over the full 30 seconds of airwake data. The unsteady loads are then time-averaged to provide the mean forces and moments acting on the helicopter at each of the test points.

Figure 2.23 shows plots of the unsteady thrust forces imposed on the helicopter flight model while in a headwind positioned off the port side, over the port edge and over the landing spot of a ship. The average of the loads represents the thrust provided by the helicopter main rotor. When the ship is off the port side and in relatively 'clean' air the thrust will equal the weight of the aircraft. As the helicopter moves into the airwake it experiences a greater downflow as the air flows over the hangar roof and downwards towards the deck. The thrust forces generated by the main rotor therefore decrease, in practice the pilot would increase the main rotor thrust but in the VAD the helicopter now experiences a net unbalanced thrust load. The average load is therefore a measure of how much control power is being applied.

Looking now at the fluctuations in the loads in Fig. 2.23, it can be seen that they increase as the helicopter moves from the freestream into the unsteady wake of the ship. If the pilot is trying to hold the aircraft steady, then it is these fluctuations that would need to be counteracted in order to maintain heading and altitude and which therefore dominate the pilot's workload. However, high frequency loads will be resisted by the helicopter's inertia and may only be felt as a vibration; low frequency loads will cause the helicopter to move about but below a certain frequency this drifting can easily be counteracted by the pilot with little effort.

It is known that disturbances in the frequency range 0.2–2 Hz have the most significant impact on helicopter handling qualities and pilot workload [53]; this frequency range is often called the Closed Loop Pilot Response Frequency Range. Therefore, when performing statistical analysis of unsteady loading, the usual definition of root-mean-square (RMS) of the deviations from the mean is not the ideal way to quantify the impact of the airwake as it includes fluctuations at frequencies outside the bandwidth known to be responsible for airwake-induced pilot workload. Instead, adopting the approach recommended by Lee and Zan [54],Power Spectral Density (PSD) plots are derived from the force and moment time-histories and the square root of the integral between the limits 0.2–2 Hz (shown schematically in Fig. 2.24) has been used as a measure of the RMS loading in this frequency bandwidth. This quantity is therefore referred to as the RMS loading of the particular force or moment in question (e.g. RMS yawing moment). The VAD provides RMS loading in each of the 6 degrees-of-freedom to characterize the unsteady aerodynamic loading of the helicopter as a result of the ship's airwake.

How the VAD has been used in this research will be demonstrated in Chapter 3 and Chapter 4.

2.5 Chapter Summary

This chapter has described the simulation tools used in this research: the CFD that has been used to create unsteady time-varying ship airwakes, including the dispersion of the hot exhaust gases from the ship's engine; the FLIGHTLAB flight dynamics modelling software that has been used with the ship airwakes to simulate helicopter flight during launch and recovery; the implementation of the integrated FLIGHTLAB/airwake models in the motion base flight simulator, HELIFLIGHT-R; and the implementation of the integrated FLIGHTLAB/airwakes in the computer-based Virtual AirDyn. The following chapters will consider particular applications of these simulation tools.

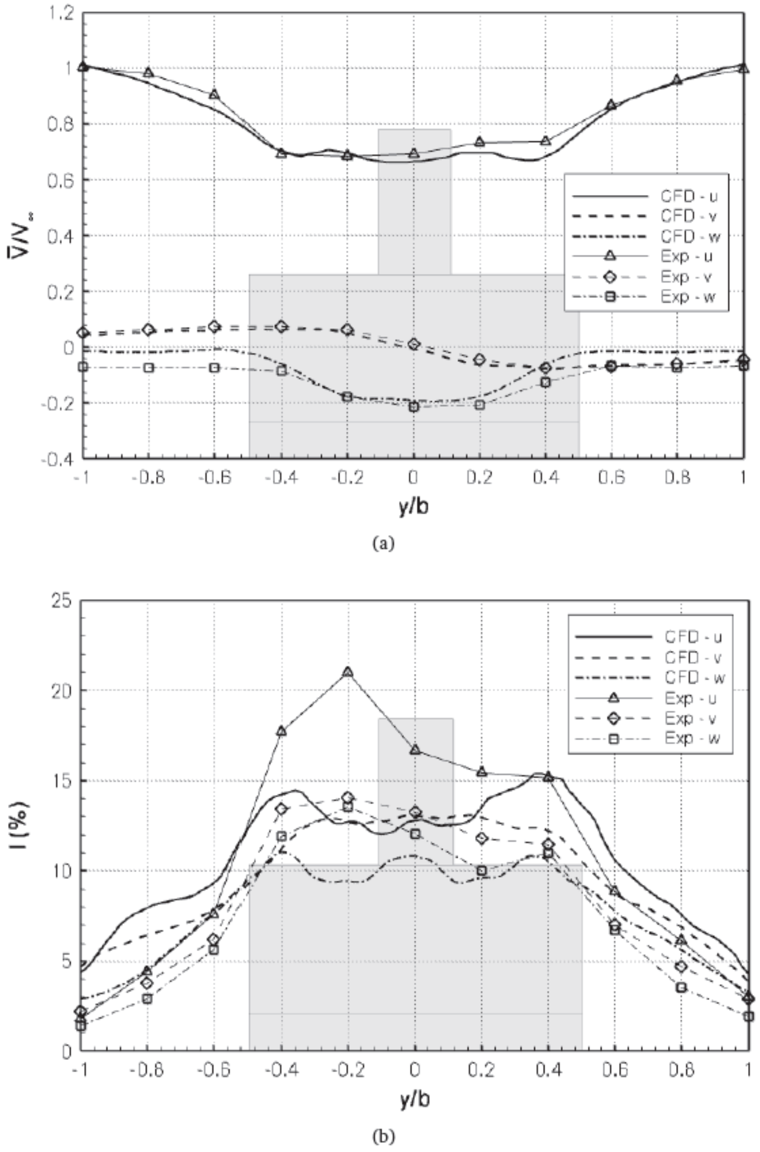

(a)

(b)

Figure 2.1 Headwind mean velocities (a) and turbulence intensities (b) for the SFS2 at 50 % deck length, plotted at hangar height. Lateral position normalised by ship beam; relative location of ship shown by shading [16].

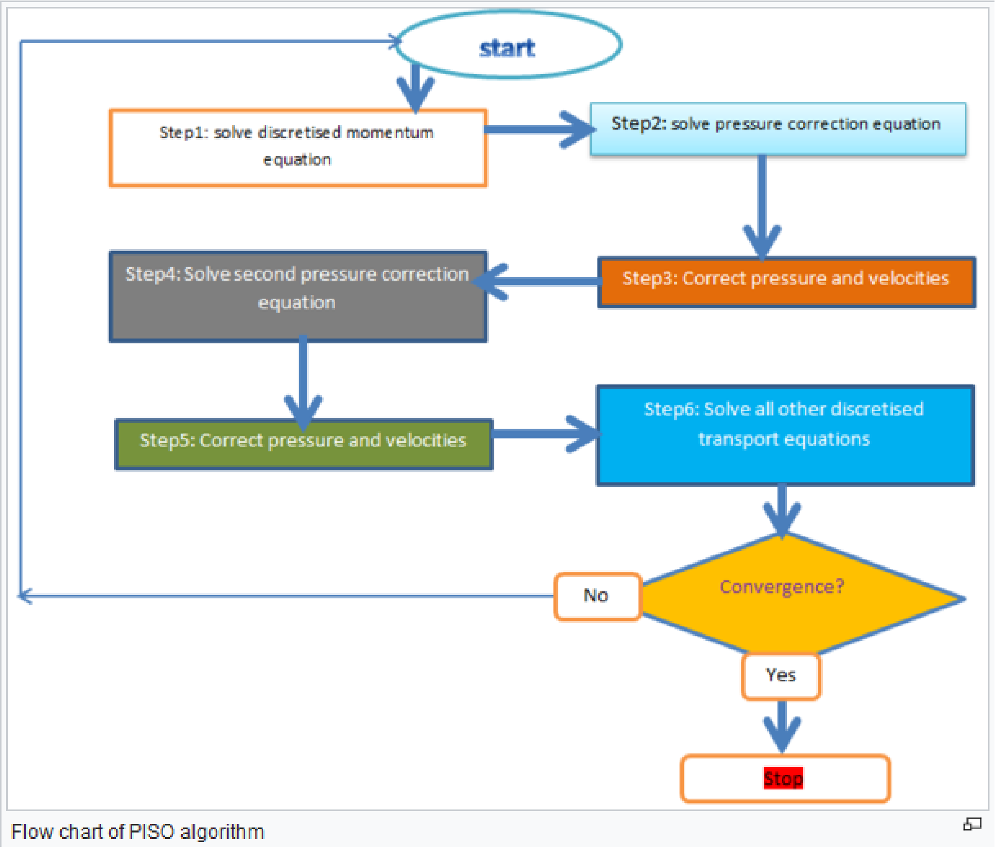

Figure 2.2 Flow chart of PISO algorithm [anon]

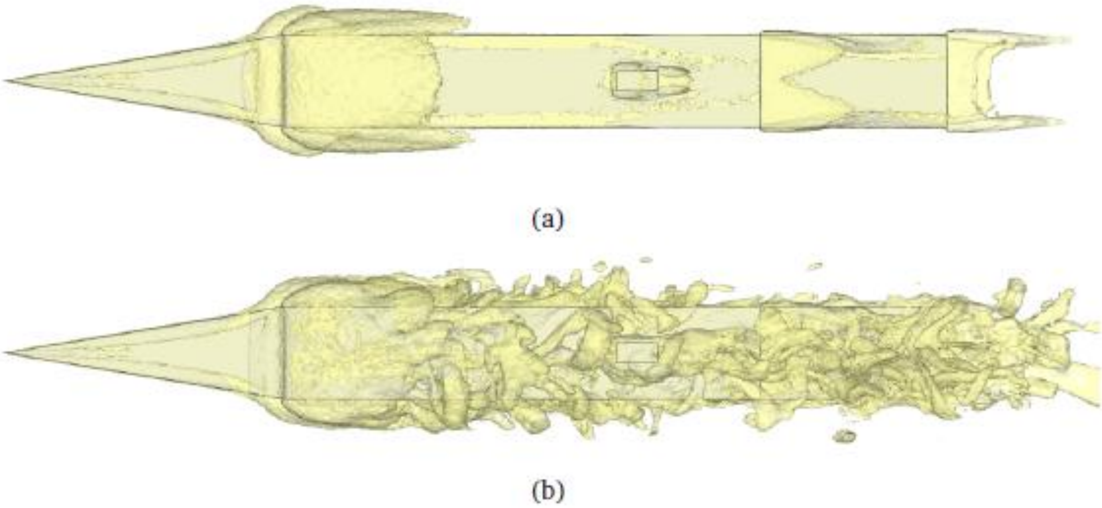

Figure 2.3 Instantaneous iso-surfaces of vorticity for (a) URANS and (b) DES computations [16]

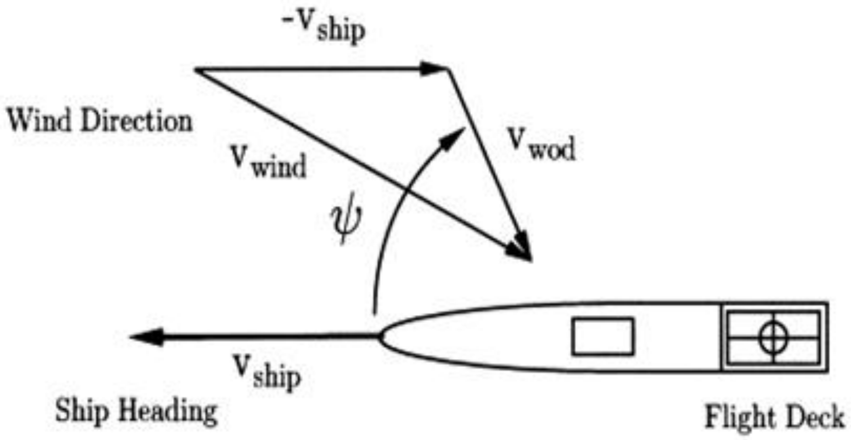

Figure 2.4 True wind and wind-over-deck

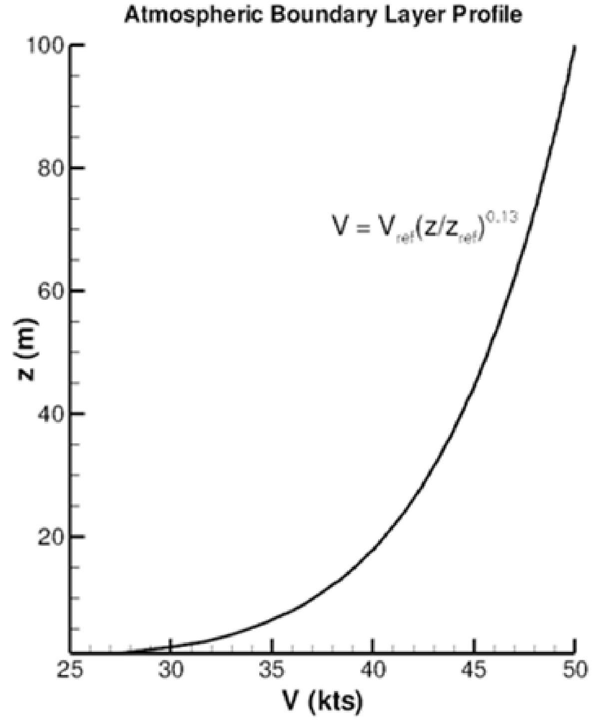

Figure 2.5 Atmospheric boundary used in airwake CFD computations

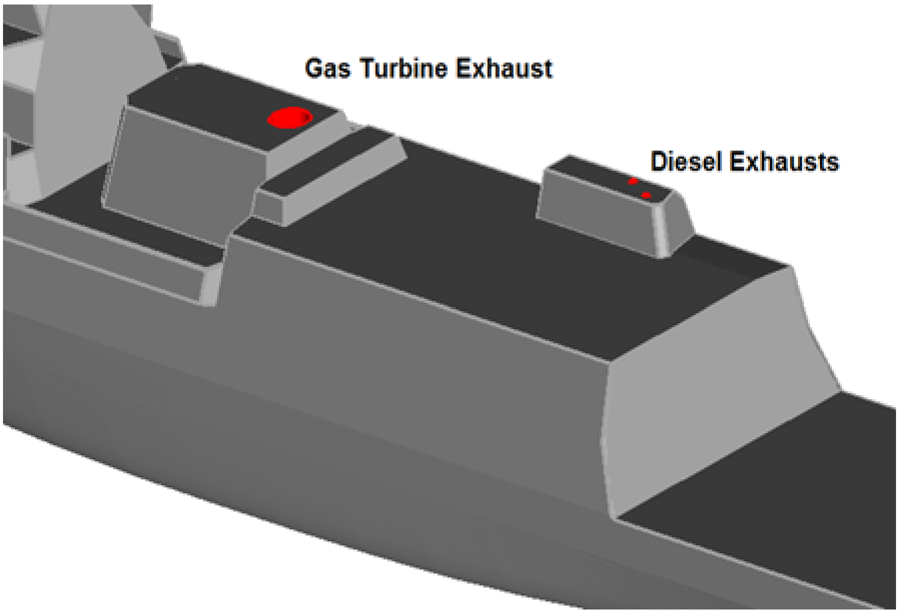

Figure 2.6 Ship engine exhaust uptakes

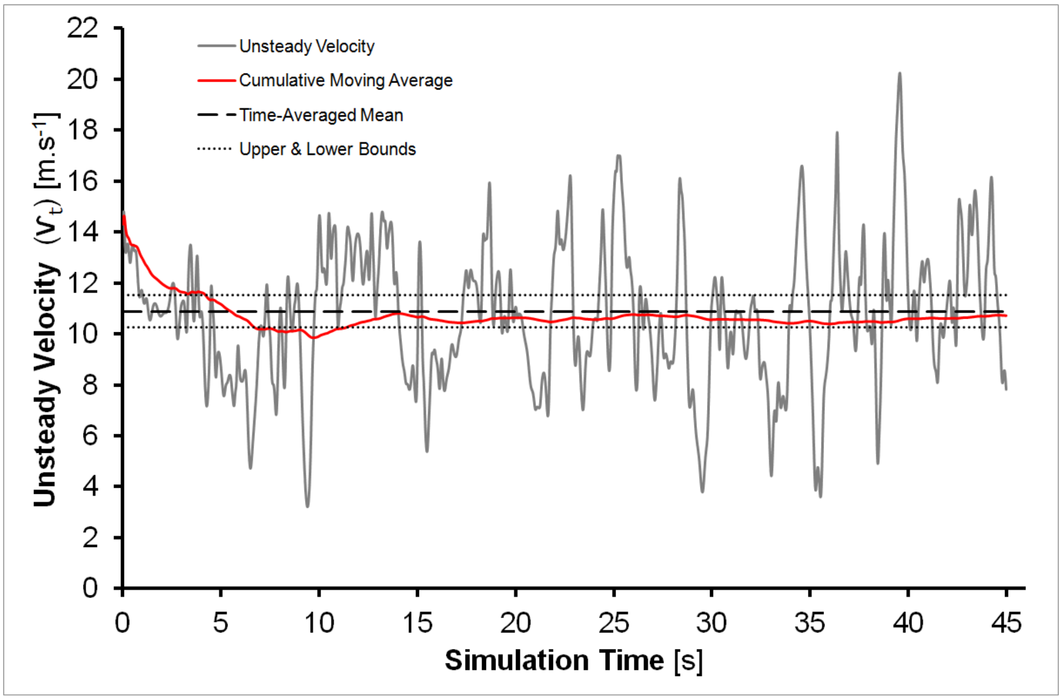

Figure 2.7 Settling time for unsteady airwake calculations

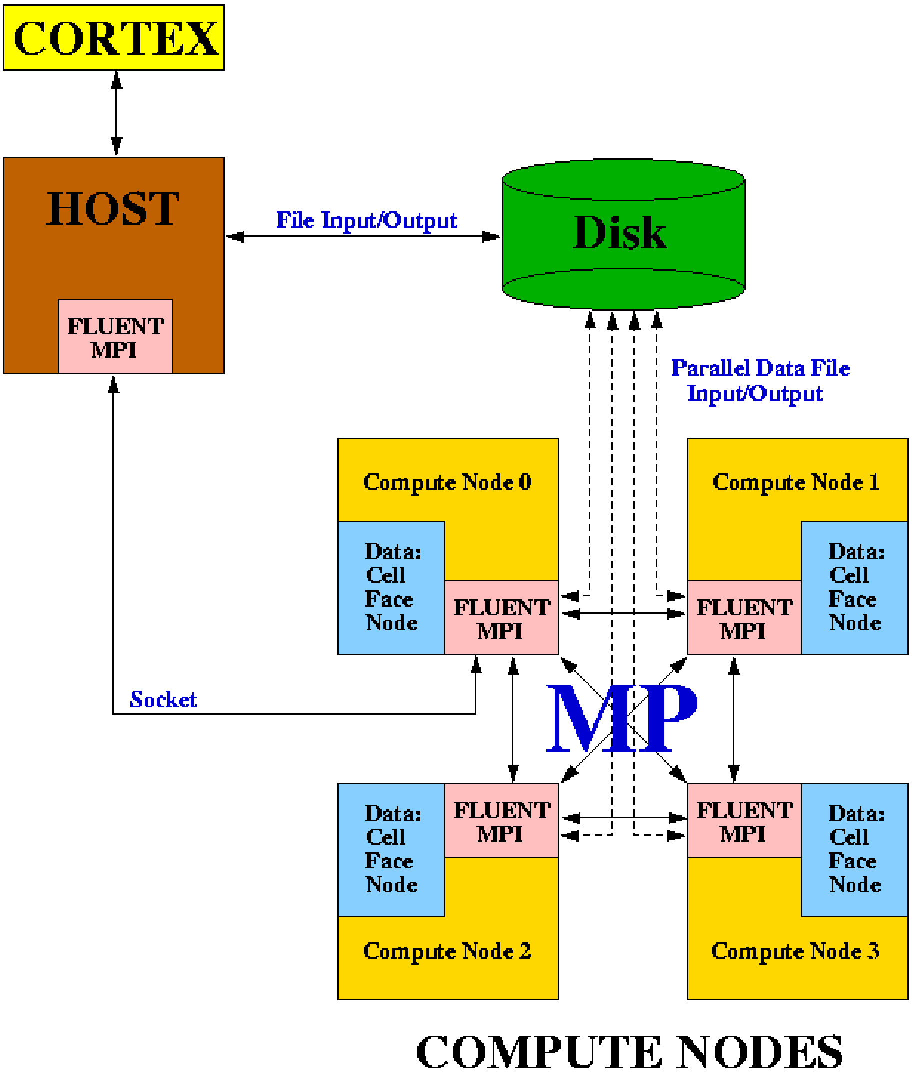

Fig 2.8 Schematic showing parallel Fluent architecture [25]

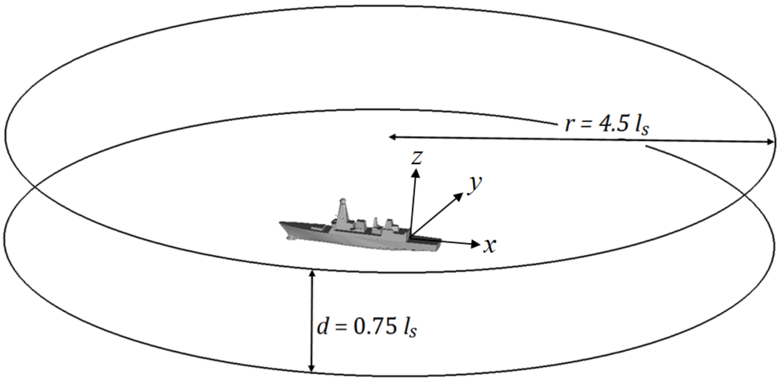

Figure 2.9 CFD domain for computing ship airwakes

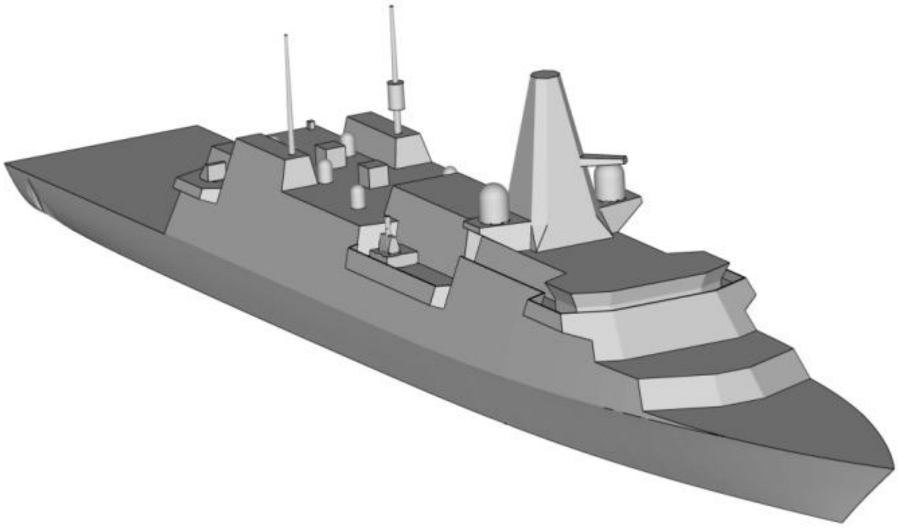

Figure 2.10 Generic Future Surface Combatant frigate 150m long, 21 m beam

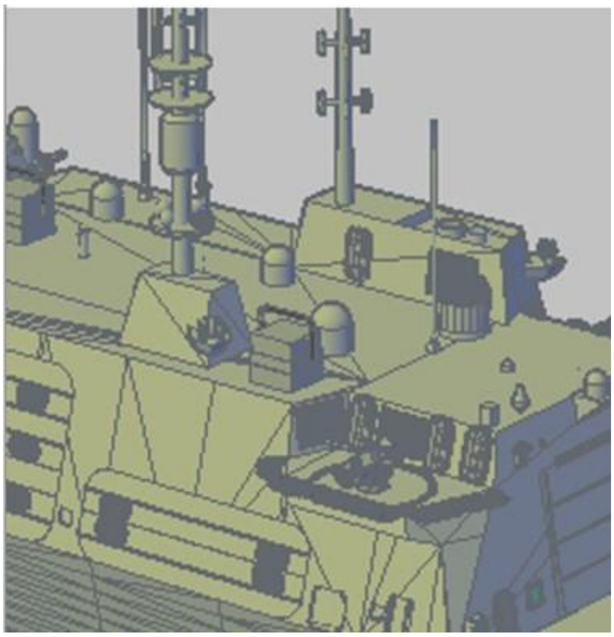

Figure 2.11 Example of ship digital drawing as supplied

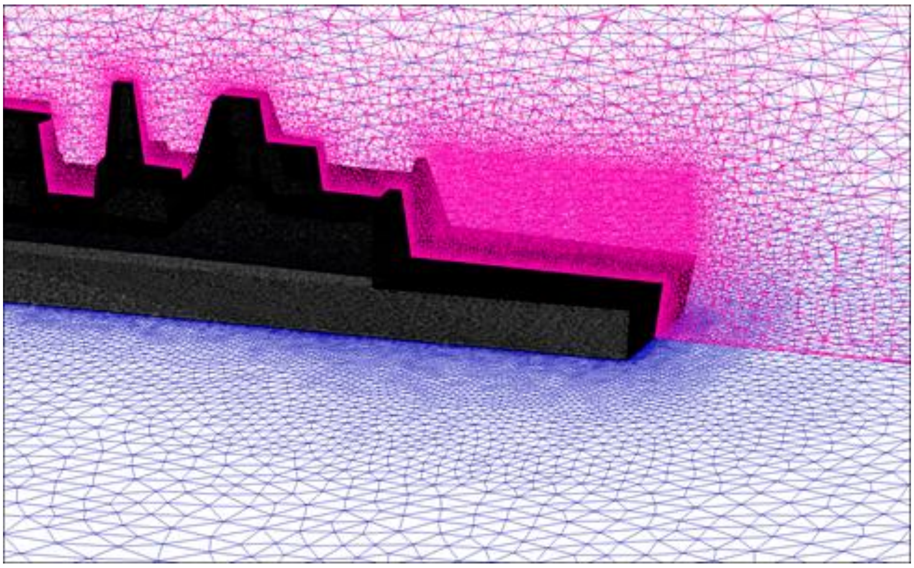

Figure 2.12 Computational mesh used to produce the CFD simulations, note the density box over the flight deck

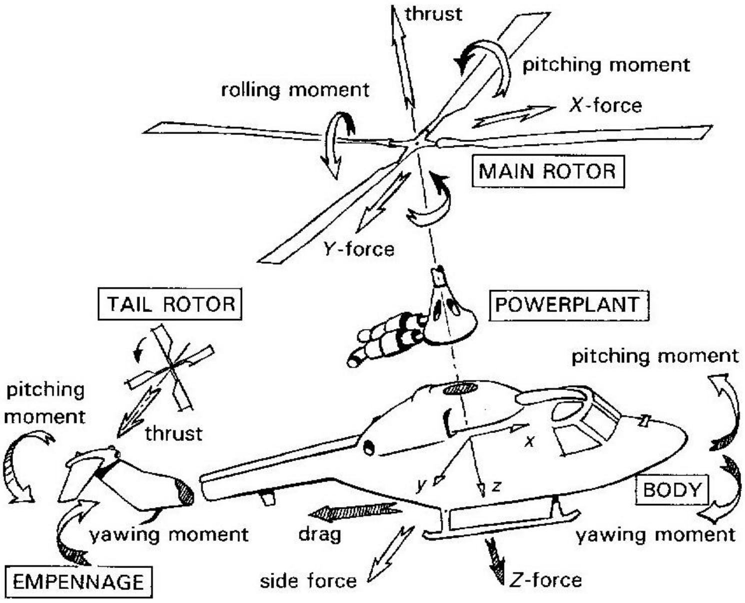

Figure 2.13 Components of a helicopter mathematical model [47]

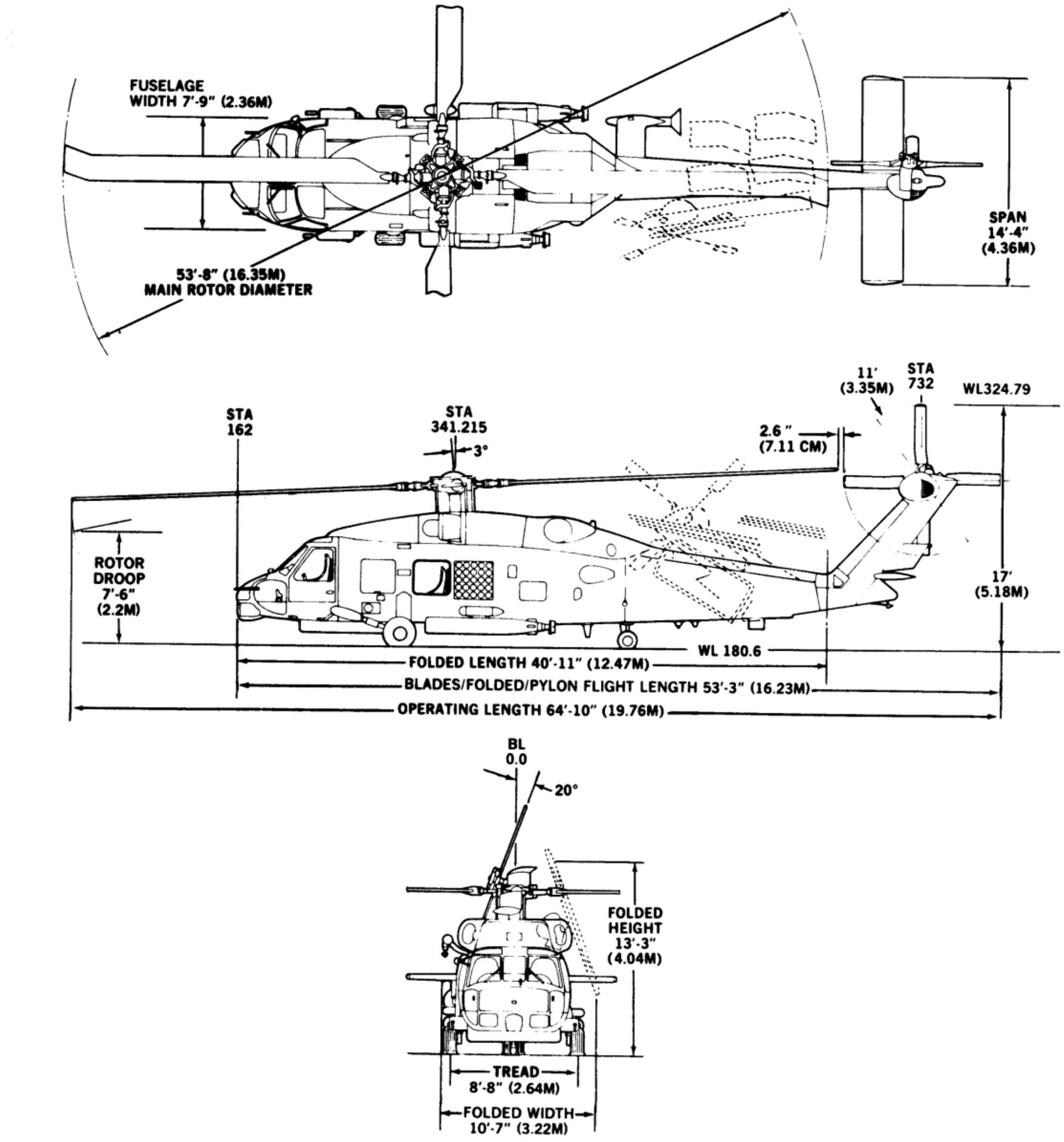

Figure 2.14 Sikorsky SH-60B SeaHawk helicopter used in flight simulation

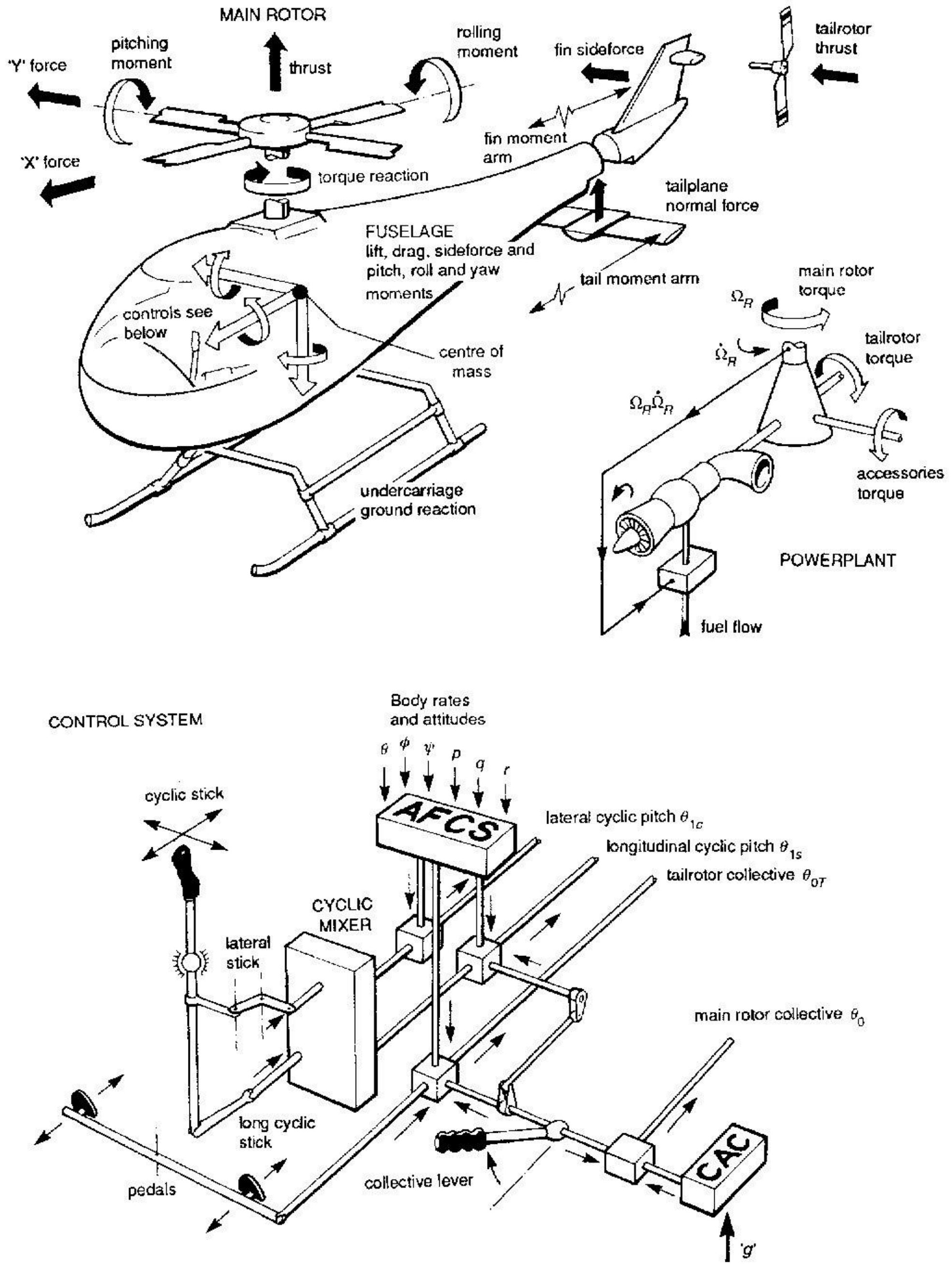

Figure 2.15 The helicopter as an arrangement of interacting subsystems and controls [47]

Figure 2.16 View of the pilot’s controls and the ’outside world’ view of a ship’s landing deck

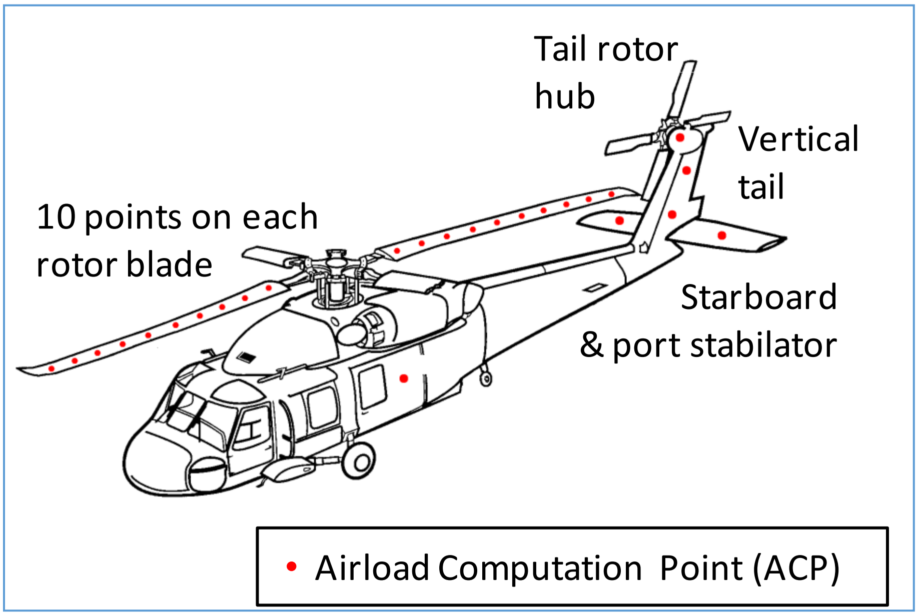

Figure 2.17 Seahawk helicopter model showing location of Airload Computation Points

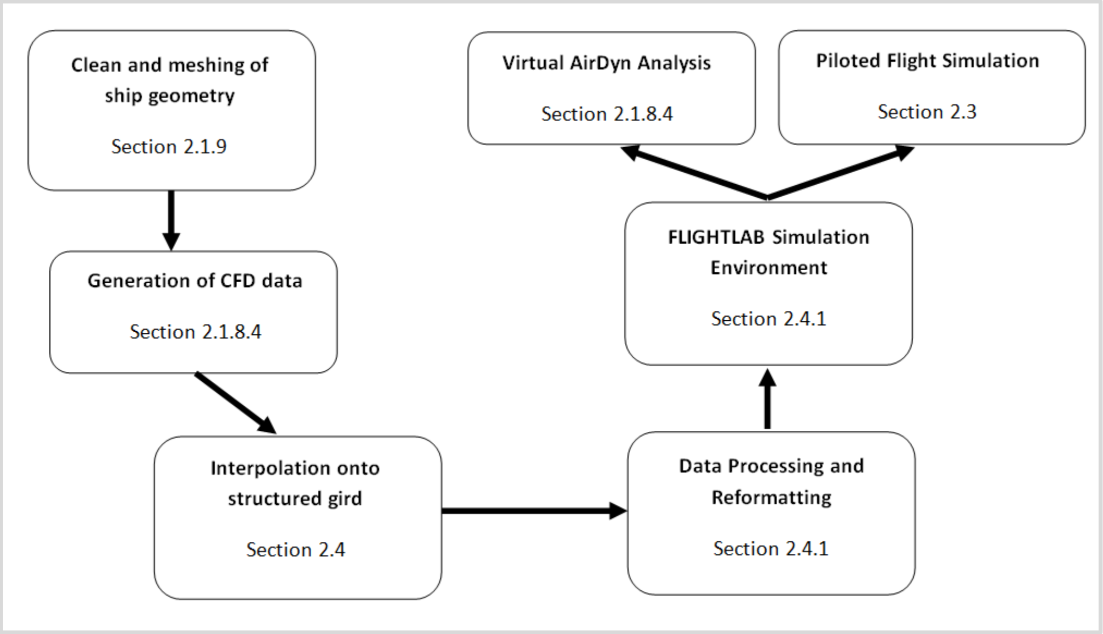

Figure 2.18 Schematic showing integration of unsteady CFD airwakes into FLIGHTLAB simulation environment

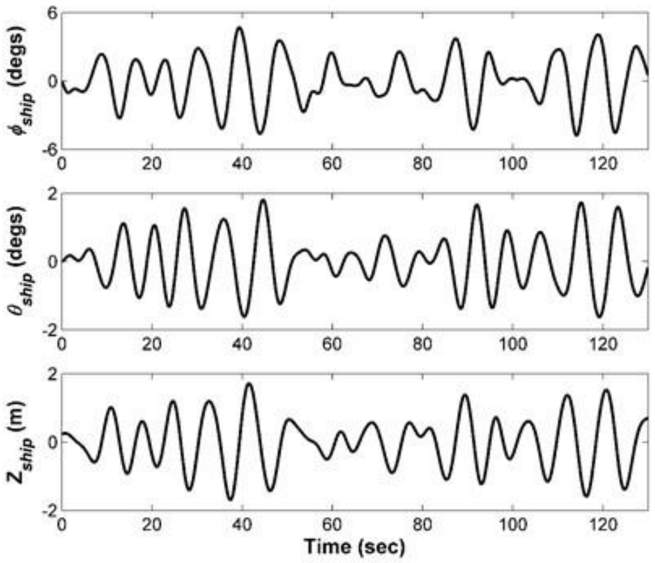

Figure 2.19 Example of simulated ship motion in sea state six conditions measured at the ship’s centre of gravity [4]

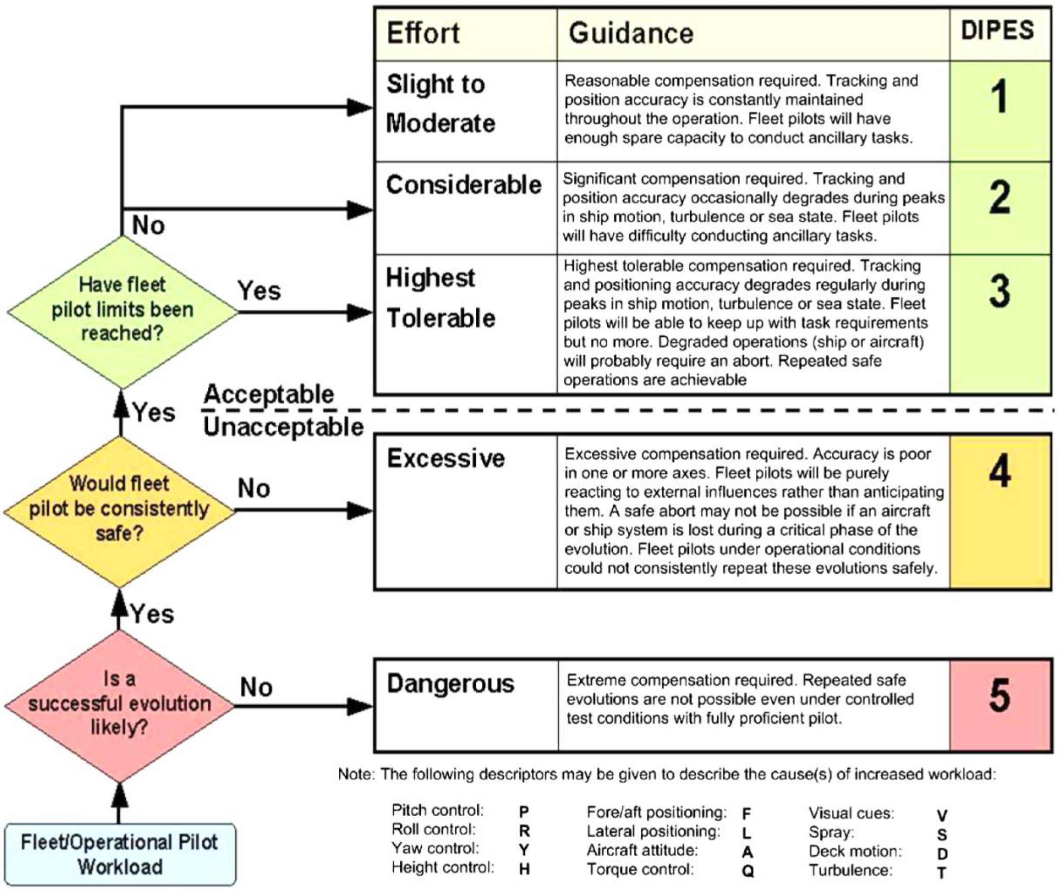

Effort	Guidance	DIPES
Slight to Moderate	Reasonable compensation required. Tracking and position accuracy is constantly maintained throughout the operation. Fleet pilots will have enough spare capacity to conduct ancillary tasks.	1
Considerable	Significant compensation required. Tracking and position accuracy occasionally degrades during peaks in ship motion, turbulence or sea state. Fleet pilots will have difficulty conducting ancillary tasks.	2
Highest Tolerable	Highest tolerable compensation required. Tracking and positioning accuracy degrades regularly during peaks in ship motion, turbulence or sea state. Fleet pilots will be able to keep up with task requirements but no more. Degraded operations (ship or aircraft) will probably require an abort. Repeated safe operations are achievable	3
Excessive	Excessive compensation required. Accuracy is poor in one or more axes. Fleet pilots will be purely reacting to external influences rather than anticipating them. A safe abort may not be possible if an aircraft or ship system is lost during a critical phase of the evolution. Fleet pilots under operational conditions could not consistently repeat these evolutions safely.	4
Dangerous	Extreme compensation required. Repeated safe evolutions are not possible even under controlled test conditions with fully proficient pilot.	5

Note: The following descriptors may be given to describe the cause(s) of increased workload:

Pitch control:	P	Fore/aft positioning:	F	Visual cues:	V
Roll control:	R	Lateral positioning:	L	Spray:	S
Yaw control:	Y	Aircraft attitude:	A	Deck motion:	D
Height control:	H	Torque control:	Q	Turbulence:	T

Figure 2.20 The Deck Interface Pilot Effort Scale (DIPES)

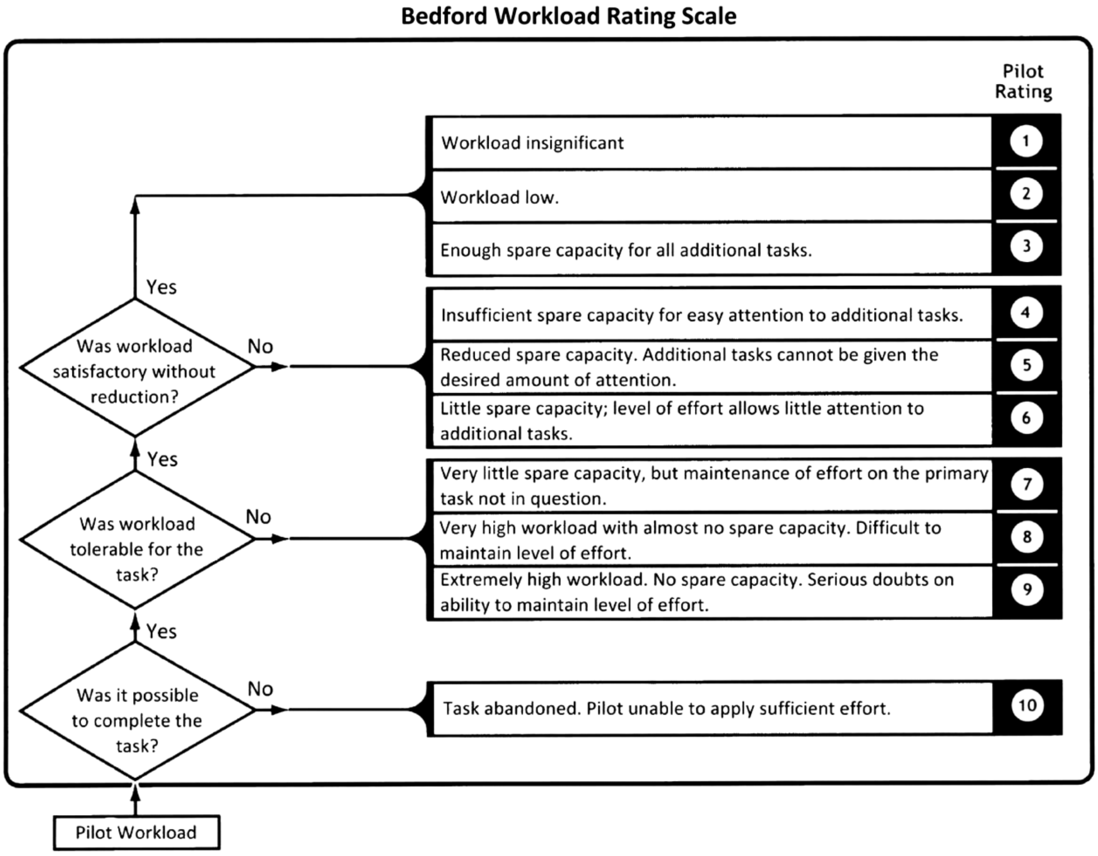

Figure 2.21 The Bedford Workload Rating Scale

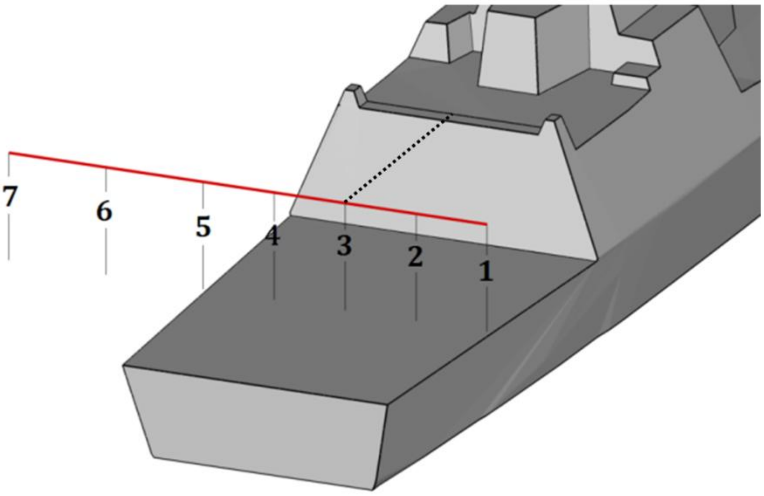

Figure 2.22 Rotor hub fixed positions used to investigate ship airwakes with the Virtual AirDyn, at 100% hangar height.

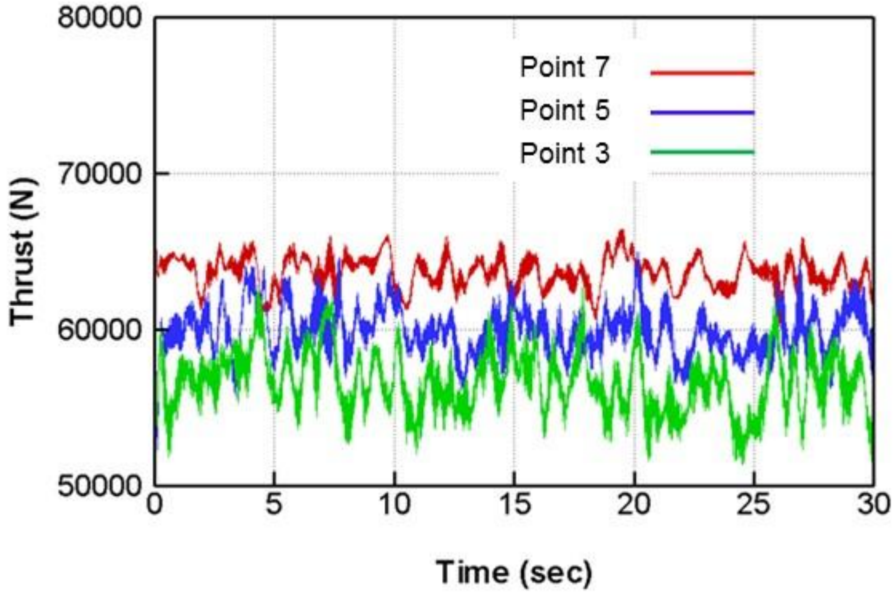

Figure 2.23 Time history of thrust load in a headwind at points 7, 5 & 3 corresponding to Fig. 2.22

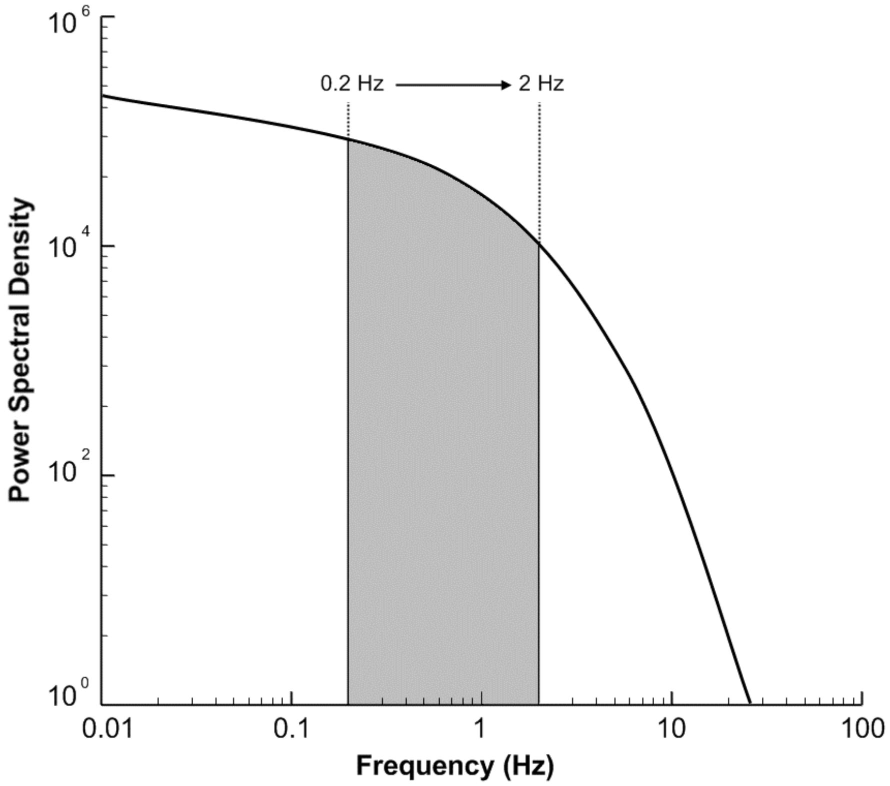

Figure 2.24 Closed-loop pilot response frequency bandwidth used to define RMS loads [53]

CHAPTER 3

VIRTUAL AIRDYN ANALYSIS OF SHIP GEOMETRY

This chapter presents a study in which the Virtual AirDyn (VAD) has been used to assess different ship design configurations. There are four configurations of what has been called a 'Future Surface Combatant', or FSC. CFD has been used to create unsteady airwakes for the different ships; for a headwind and for two oblique winds coming from the starboard side. The airwakes have then been used with the VAD to evaluate the unsteady loads imparted by the different ships' airwakes onto the SH-60B helicopter. To provide a reference to an existing ship with a known SHOL envelope, the same analysis has been applied to a Type 23 frigate.

3.1 Introduction

Figure 3.1 shows the five ship geometries under consideration; the four versions of the Future Surface Combatant are identified as FSC 0 to 4, while the sixth ship is a Type 23 frigate, a Duke Class ship that is presently in service with the Royal Navy. The FSC is 150m long and has a beam of 21m, while the Type 23 is 133m long and has a beam of 16m. The most striking difference between the FSC variants and the Type 23 is that the superstructure of the FSC has a continuous flat surface running the full length of the deck house, while the Type 23 superstructure is made up of different modules. The reason for this 'cleaner' slab-sided design of the FSC is to reduce radar reflections. The greatest above-water vulnerability of a warship comes from enemy radar beams originating near or slightly above the horizon coming from distant patrol aircraft, other ships or sea-skimming anti-ship missiles with active radar seekers. The FSC therefore has no vertical surfaces to reflect incoming radar signals, and instead the sloping surfaces, particularly the large surface area of the tumblehome, to deflect the incoming radar signal upwards.

Close inspection of the five versions of the FSC will reveal that the differences are in the geometries just ahead of the flight deck, on the roof of the hangar. FSC0 has long rectangular funnel casings on both sides of the hangar roof. There are also two platforms (sponsons), one either side of the hangar just ahead of the flight deck; these are gun platforms. The FSC1 is similar to the previous variant, however the gun platforms either side of the hangar have been reduced to 'shelf' like structures. On FSC2 the port (left) funnel is smaller; on FSC3 the gun platforms have been lowered; and on FSC4 the gun platform is at an intermediate height and the port funnel casing has been extended slightly. These are not major design changes so the challenge for the VAD was to evaluate which one, if any, causes the least unsteady loading on the helicopter.

The most common Wind Over Deck (WOD) on a ship is from the front, either head-on or oblique, because the ship will generally be moving forwards. Clearly if the wind is from astern and has a speed greater than that of the ship the statement above will not be true. Nevertheless, to restrict the number of WOD angles that need to be considered it was therefore decided to use Headwind, Green 30 and Green 45; i.e. a wind, relative to the ship, from an angle of 0°, 30° from the starboard, and 45° from the starboard. The selection of Green winds is because these are the winds that cause the highest workload for helicopter pilots and the reason for this is the port-side landing approach used by UK pilots (and other nations) as shown earlier in Fig. 1.2.

Bearing Fig. 1.2 in mind, consider an oblique wind coming from the starboard side, such as that shown for the simplified ship geometry in Fig. 3.2 [55]. A fluctuating shear layer caused by the flow separating from the hangar vertical edge can be clearly seen. The other dominant features in the figure are the numerous vortical structures caused by the flow 'rolling up' and shedding from the sharp edges, for example at the horizontal leading edge of the hangar. Both the vertical and horizontal edge flow separations are highlighted in Fig 3.2). More importantly for the helicopter, particularly while off the port side and translating across the deck, are the large vortex structures being shed from the upper horizontal edges on the starboard side of the hangar; the significance of these is that they pass above the path taken by the helicopter and get drawn into the helicopter's main rotor, causing significant unsteady moments. These flow features contribute significantly to the high pilot workload in Green winds. Considering the FSC and Type 23 geometries in Fig. 3.1 it can be expected that oblique winds will flow unimpeded along the sides of the FSC so that the flow separation from the vertical hangar edges will be more energetic than that from the Type T23 where the wind will have been broken up more by the fragmented superstructure. It can also be expected that the starboard funnel casing on the FSC will also affect the vortices being shed from the top of the hangar. Incidentally, if possible, naval helicopter pilots will land in Red winds if the captain can turn the ship to the appropriate heading, thus avoiding much of the chaotic flow shown in Fig. 3.2. Although Red winds may be preferred by pilots for being more benign than similar strength Green wind conditions, they still may cause issues at higher WOD speeds, this can be seen in a typical SHOL Fig 1.1.

3.2 Creating the Ship Airwakes

The methodology for creating CFD airwakes described earlier in Chapter 2 was followed. Figure 3.3 shows a part of the surface mesh on the geometry of FSC1 and from this a volume mesh was grown into the cylindrical domain as described earlier. An atmospheric boundary layer was applied with a speed of 40 knots at the height of the ships' anemometers. A steady state solution was first obtained and this was used as the initial condition for the unsteady calculations. The first 15 seconds of unsteady airwake was discarded and the next 30 seconds were recorded.

To provide an overview of the ship aerodynamics, and to aid the later discussion on the AirDyn results, Figs. 3.4 to 3.8 show mean streamlines of the flow over FSC1 and FSC4 versions of the ship. The lines are coloured by turbulence intensity and they enable the mean flow to be visualised while the colouring allows areas of high/low turbulence to be identified. The streamlines are shown for a headwind and Green 45° for just the two variants of the ship design because they represent the designs with the large and small port funnels which have the greatest effect on the flow. The headwind flow over FSC1 in Fig. 3.4 shows how flow is channelled between the two funnel casings and then separates off the top of the hangar. This flow reattaches to the deck about half way along, forming a recirculation zone behind the centre of the hangar face. The flow diverted around the outside of the funnel casings then appear to be drawn in towards the ship's centreline over the deck. For the helicopter, the unsteady wake will impose unsteady forces and moments that the pilot will have to counteract; behind the hangar the down-flow will reduce the main rotor lift and the recirculation zone will draw the aircraft into the hangar face as it descends to land. The headwind flow over FSC4, in Fig. 3.5, shows a similar air flow with some asymmetry due to the shorted port-side funnel casing.

The mean streamlines shown in Fig. 3.6 illustrate how the flow passes over the ship when the wind is coming from 45° off the starboard. The unsteady flow off the port side of the ship alongside the landing deck will affect the helicopter throughout its lateral translation over the deck during the landing task. Figures 3.7 and 3.8 show that the flow over the funnel casings are different when the port-side casing is of a different size; the significance of this will be discussed later in light of the VAD results.

With six ship variants and three wind angles, a very large amount of CFD data was generated. Figures 3.16 to 3.48 contain a complete set of CFD data presented as a series of contour plots showing longitudinal, lateral and vertical mean velocities and turbulence intensities. Each plot is shown as either a cross sectional slice at the landing spot on the vertical y-z plane or in the horizontal x-y plane at hangar height. Even though not all of these figures will be referred to in the discussion to follow, the decision was made not to place the figures in an appendix, but to include the complete data set in the thesis to provide a comprehensive record of the data; the reader will therefore be directed to a selection of figures to aid the discussion. Figs. 3.16 to 3.22 show the three velocity components (u, streamwise; v, lateral/transverse; w, vertical) as both mean and turbulence intensities for the headwind condition on a horizontal plane at hangar height, while Figs. 3.23 to 3.26 show just the turbulence intensities on a lateral vertical plane through the landing spot. The same components are shown for a Green 30 wind in Figs. 3.27 to 3.33 on a horizontal plane at hangar height, and in Figs. 3.34 to 3.37 on a lateral vertical plane through the landing spot. Finally for the Green 45 winds the same velocity data is shown in Figs. 3.38 to 3.44 and Figs. 3.45 to 3.48 for the horizontal and vertical planes respectively. This data is just a summary of all the different CFD plots that were produced to examine the airwake and to explain the loads measured by the VAD.

3.3 AirDyn Analysis Overview

The results from the VAD analysis were used to evaluate each ship design and to identify any potential adverse features within the airwake which may impact on pilot workload. The VAD data is presented as mean and RMS forces (Heave/Lift, Side, Drag) and moments (Roll, Pitch Yaw) at different lateral positions in line with the landing spot and presented in terms of ship beam widths, b, from the landing spot as illustrated earlier in Fig. 2.22. Figure 3.9 shows a view from astern of the rotor hub positions on the FSC. The landing spot is at y/b= 0, and the port and starboard deck edges are at y/b= ±0.5. The start of the translation used in the VAD occurs at one beam width from the landing spot, i.e. y/b = -1. Because pilot workload is associated with the unsteady RMS loads, the discussion in the following sections will concentrate more on this data.

The mean and RMS loads are shown for headwind, Green 30 and Green 45 in Figures 3.10 and 3.11, Figures 3.12 and 3.13, and Figures 3.14 and 3.15 respectively. To give some context to the magnitudes of the forces on the graphs, in Fig. 3.10 the value of Fz at y/b = -1 is 69 kN, i.e. the weight of the aircraft. This is because Fz is the mean lift force and, because the helicopter is in the undisturbed freestream, the lift from the rotor equals the helicopter's weight. When the helicopter is positioned above the spot, at y/b = 0, its rotor is now in the wake of the hangar and experiences a slower moving airflow that has a downward component, as shown in Fig. 3.4. The lift created by the rotor, Fz, has now decreased in Fig. 3.10 and in practice this would mean that the pilot would have to increase the lift to maintain the aircraft's height. However, in the VAD the helicopter is held in place and no corrective inputs are made, hence the aircraft is out of equilibrium and it is the non-equilibrium forces that quantify the effect of the airwake on the helicopter. It can also be seen in Fig 3.10 that the drag and side forces, Fx and Fy respectively, are much smaller than Fz, as would be expected. The magnitudes of these forces are not easily interpreted in isolation, as their importance is their effect on the helicopter in the flight mechanics model FLIGHTLAB and to fully experience this requires the helicopter to be 'flown' by a pilot in the simulator. For the purpose of interpreting the mean forces and moments in Figs. 3.10, 3.12 and 3.14 it is sufficient to look at whether these loads increase or decrease as this corresponds to the pilot needing to increase or decrease inputs through the cyclic, collective and pedal controls.

Interpreting the values of the unsteady RMS loads in Figs. 3.11, 3.13 and 3.15 also has to be done on a comparative basis. So, for example, in Fig. 3.11, as the helicopter moves from the undisturbed freestream off the port-side, y/b = -1, to a position above the landing spot at y/b = 0, all the unsteady forces and moments are seen to increase as the aircraft is now in the unsteady airwake in the lee of the hangar. At this stage of analysis the RMS loads are able to identify when the aircraft is experiencing more or less unsteady loading and therefore pilot workload. For the purpose of this study, the information to be taken from Figs. 3.11, 3.13 and 3.15 are whether the ship geometry is causing the RMS loads to increase or decrease as this translates into increased or decreased pilot workload.

3.4 FSC and Type 23 Data Comparison

The operational limits of a Merlin and Wildcat helicopter landing on a type 23 frigate are known; the data, however, are restricted and not openly available. Neither does a SeaHawk operate to British ships. Nevertheless, the inclusion of the Type 23 as a comparison is very useful as it provides a reference against which to judge the airwake of the FSC.

3.4.1 Headwind

For the headwind case the flow over the flight deck for all variants of the FSC and the Type 23 is dominated by the separation from the hangar's vertical sides and horizontal edges with subsequent reattachment approximately halfway along the flight deck. Figures 3.4 and 3.5 show the recirculation aft of the hangar for both the FSC4 and the FSC1 designs through a series of streamlines placed at equal points over the superstructure of each ship. As noted above, the streamlines indicate some modification to the recirculation of flow aft of the hangar face due to the reduction in the port funnel size and its position in comparison to the starboard funnel. This has the effect of reducing the mean vertical component of the flow immediately above the landing spot just below hangar height. However, although the streamlines can illustrate the mean flow, it is not easy to make a judgement on how each of these unsteady flows will affect the helicopter. It is for this reason that the VAD is used as the diagnostic tool, and that turbulence plots are used to differentiate between the different flows.

Looking at the mean streamwise velocity in Fig. 3.16 and the general turbulence intensity in Fig. 3.19, it can be seen that, relative to the size of the ship’s beam, at hangar height the FSC airwake is narrower than that of the Type 23, probably due to the smoother sides of the FSC. It can be expected, therefore, that the airwake will begin to impact on the helicopter sooner for the Type 23 than for the FSC as it translates from the port-side towards the deck. This is confirmed in Figs. 3.10 and 3.11 where the mean and unsteady loads for the all the FSC variants converge to consistent values in the freestream at $y/b = -1$, whereas at $y/b = -1$ for the Type 23 the helicopter is experiencing different loads, i.e. it is in disturbed air flow. Also in Fig. 3.10, it can be seen that in the lee of the hangar the reduction in lift over the FSC is less than over the Type 23, probably because the higher and wider hangar of the FSC means a greater down-draught over a greater area.

Figure 3.11 shows a comparison of the unsteady RMS forces and moments generated by the VAD in the headwind. It can be seen that although there are differences in the profiles of the unsteady loads they are broadly similar in magnitude for all the FSC designs across the translational path. All ship designs show comparable magnitudes of unsteady loads at one beam width from the landing spot, off the port side, except for the side force (F_y), rolling (M_x) and yawing (M_z) moments, for which the FSC designs slightly outperform the Type 23. Due to the asymmetry present in the Type 23 hangar design the turbulent wake is slightly skewed to the port side of the ship, Fig. 3.19(f), slightly extending the wake further from the port edge of the ship. The gun platforms on either side of the hangar edges for the FSC variants 1 - 4 appear to modify the flow such that they slightly reduce the width of the turbulent ship wake, Fig. 3.19(a - e), as observed in the previous paragraph. The protrusions formed by the gun platforms on FSC0 create high levels of turbulence, particularly the lateral components, as expected from the shedding created by the vertical edges, that propagate over both deck edges for the headwind WOD condition, Fig 3.20(a). This is reflected in the RMS loading on the helicopter Fig 3.11 while positioned over the deck edges, especially the vertical component (F_z). As can be seen in Fig. 3.11, all the variants of the FSC show higher RMS forces and moments over the starboard edge of the ship compared with the Type 23.

In the headwind, as the helicopter translates from off the port-side to over the landing spot, the differences in the RMS loads between the FSC variants and the Type 23 designs are not significant and it is expected that the pilot workload experienced during an approach to the FSC4 would be comparable to the Type 23 for this WOD. However, although the differences in the RMS loads for the different variants of the FSC do not favour a particular design as the helicopter translates across the deck, FSC4 does more consistently have lower unsteady loads above the spot, which is significant as the pilot will hover at this position for a period before descending to land.

3.4.2 Green 30°

Streamlines of the mean flow are not presented for this WOD as the observations are similar to those for the Green 45° wind. The flow at Green 30° is primarily influenced by the separation from the starboard hangar edges and the edges of the gun platforms, creating a flapping shear layer that cuts across the flight deck. This can be seen best in the lateral turbulence intensities in Fig. 3.32. Overall the turbulence levels for each FSC variant are greater than the Type 23, which is expected due to the larger beam width, length and height of the FSC. The superstructure of the FSC will also experience slightly higher freestream velocities in comparison to the Type 23, due to the height of the ship in the atmospheric boundary layer. The increase in hangar size of the FSC ship design means turbulence persists at heights well above the hangar, as turbulent structures within the flow are carried vertically by the mean vertical velocity component of the airwake. These features can be seen in the general turbulence intensities in Fig. 3.34.

As the WOD angle moves from headwind to Green 30°, the vertical hangar edge and gun platform on the windward side of the hangar of the FSC creates increased turbulence in the flow, particularly in the lateral component, in a region of the flight deck which the helicopter will encounter during a translational manoeuvre; for example Fig. 3.32(a - e) shows the lateral turbulence intensity at 100% hangar height for the five FSC variants. However the FSC4 variant produces the least impact in this respect, this is also reflected within the VAD results where the unsteady loads are generally lower as the helicopter translates from off the port side to the landing spot, Fig. 3.13.

The cross-sectional contour plot of lateral turbulence intensity for FSC4 shows the effects of the flow separating from the vertical edge beneath the gun platform, Fig. 3.36(e). The shear layer emanating from this vertical hangar edge in particular will impact on the pilot workload. The lateral turbulence component generated from the flow around the platform can reveal itself as an increase in the side force, yawing and pitching moments as the flow interacts with the fuselage, tail rotor and main rotor disc respectively. These trends are also reflected in the RMS results of the VAD, Fig. 3.13, showing higher values over the port half of the deck.

As observed in the headwind condition, for Green 30° winds there is, in general, not much difference between the unsteady loads for the different FSC variants although for much of the translation from off the port side to the landing spot the FSC4 imposes lower unsteady moments than the other variants. Unlike in the headwind, however, the FSC will impose greater unsteady loads than will the Type 23, as expected for a larger ship.

Furthermore, the effect of the smooth sides on the airwakes of the FSC ships compared with the Type 23 can be seen in Fig. 3.27 where the flow along the starboard face of the ships is less affected for the smooth-sided FSC. For all variants of the FSC, the CFD data in Fig 3.27 shows a larger recirculation zone in the hangar wake over the landing deck compared with the Type 23. This is further emphasised in Fig 3.34 where a cross section of the wake in the vertical plane across the centre of the landing deck shows much larger and more energetic wakes over the FSC variants.

3.4.3 Green 45°

Figure 3.6 shows the mean streamlines over FSC4 for a Green 45° wind. Other than showing the complexity of the airwake in the lee of the ship, it is difficult to draw any conclusions for the helicopter loads. It can be expected, however, that the large port-side funnel will shed turbulence, particularly in the Green winds.

An evaluation of the differences in the port funnels for the FSC1 and FSC4 designs show that the decrease in the starboard funnel size of the FSC4 compared with FSC1 has an effect at this WOD condition. Comparing Fig. 3.7 with Fig. 3.8 shows how the larger port-side funnel interferes with some of the flow and deflects it down onto the deck; the starboard funnel also has a radome on top. The combination of increased port funnel size and surface clutter, such as radomes, between the funnels of the FSC1 serve to disrupt the flow which is fed onto the flight deck. The arrangement of the superstructure in the FSC4 design appears to reduce this effect and the turbulent structures are now carried away with the freestream wind and may reduce the impact of the airwake on helicopter operations.

The Green 45° WOD condition has similar flow characteristics to the Green 30° case where the flow separation from the windward vertical edges of the superstructure and hangar face induce a flapping shear layer across the flight deck. However due to the increased angle of the flow, the main turbulent structures now extend over the port edge of the FSC designs and, to a lesser extent, the Type 23, as can be seen in the lateral turbulence intensities in Figs. 3.43 and 3.47. The effect of the different variants of the FSC on the flow across the deck and how they influence the flow structures passing across the deck at hangar height can be seen in Figs. 3.41 to 3.48. An overall assessment shows that FSC4 generates the least turbulent disturbances in the flow. At this wind angle there appears to be less influence on the airwake from the smooth sides of the FSC, for example in Fig. 3.38 the mean longitudinal velocity components no not suggest that the flow in the starboard face of the FSC is any less affected than for the Type 23. As the flow comes around more to the beam it can be expected that the smooth sides will have less influence on the airwake over the flight deck, so from the evidence of the three wind angles considered it appears that the smooth-sided geometry of the ship affects the airflow over the landing deck up to an angle of about 30° from the starboard.

The increased turbulence over the port edge of the deck as the wind angle has increased from 30° to 45° is also reflected in the VAD unsteady loads where it can be seen in Fig. 3.15 that the RMS loads are mostly higher when the aircraft is off the port side in the Green 45° wind than in the Green 30°. It can also be seen in the Green 45° wind that the unsteady loads are again higher for the FSC than for the Type 23, because of the larger superstructure. Consistent with the observation that FSC4 generates overall less turbulence than the other FSC variants, so the RMS data in Fig. 3.15 shows that FSC4 generally imposes lower unsteady loads on the helicopter than the other variants.

From the perspective of potential pilot workload, when landing to the different variants of the FSC, for the two oblique winds tested, FSC4 is noticeably better than the other versions. Once again the unsteady loads are greater for the FSC than for the Type 23, but how the increased unsteady loads manifest themselves in pilot workload ratings is not clear as the FSC has a larger deck on which to land the helicopter. If time and resources had allowed, the VAD analysis, which produces measures of RMS loads to represent pilot workload, could have been extended to simulated deck landings in the HELIFLIGHT-R motion base simulator to give an indication of how the ship design impacts on pilot workload ratings and helicopter operational envelope.

3.5 Chapter Summary

Aerodynamic data and predicted helicopter loads have been presented for three wind angles, for a Type 23 frigate and four versions of the Future Surface Combatant. It is the unsteady helicopter loads that translate into pilot workload and reduced SHOL envelopes, and these in turn are as a result largely of the turbulence in the flow.

The purpose of the study reported in this Chapter was to determine if there were any indications that any of the geometries would have a disproportionate adverse effect on the helicopter. Overall the FSC generates turbulent structures that are bigger and slower than the smaller Type 23. This is to be expected, and it can also be expected to lead to increased pilot control activity. However, the Type 26 has a bigger landing deck and so the increased activity will not necessarily lead to significantly restricted SHOLs.

The relative merits of the different designs of the FSC have been evaluated using the AirDyn, informed by reference to the airwake CFD. The main indicator for this analysis are the unsteady forces and moments shown in Figs. 3.11, 3.13 and 3.15, which can be considered in the context of the turbulence data in the CFD. From reviewing these data it can be seen that some designs do better than others in some circumstances, and less well in others. It has not been possible therefore to draw up a complete table of merit. However, FSC4 performs best in the oblique winds, and even in the headwind where all the geometries gave rise to similar unsteady loads, FSC4 imposes lower unsteady loads on the helicopter when it is in the hover over the spot.

What is clear from the analysis conducted in this chapter is that the larger FSC generates greater unsteady loads on the helicopter than does the smaller Type 23 frigate. This is consistent with the findings of Forrest et al when they conducted simulated deck landings to a Type 23 frigate and a Wave class tanker [5]. However, there is still a question mark over whether the more aggressive airwake of the larger ship is compensated for by the larger deck available for the pilot to land on. This question is addressed in the following chapter.

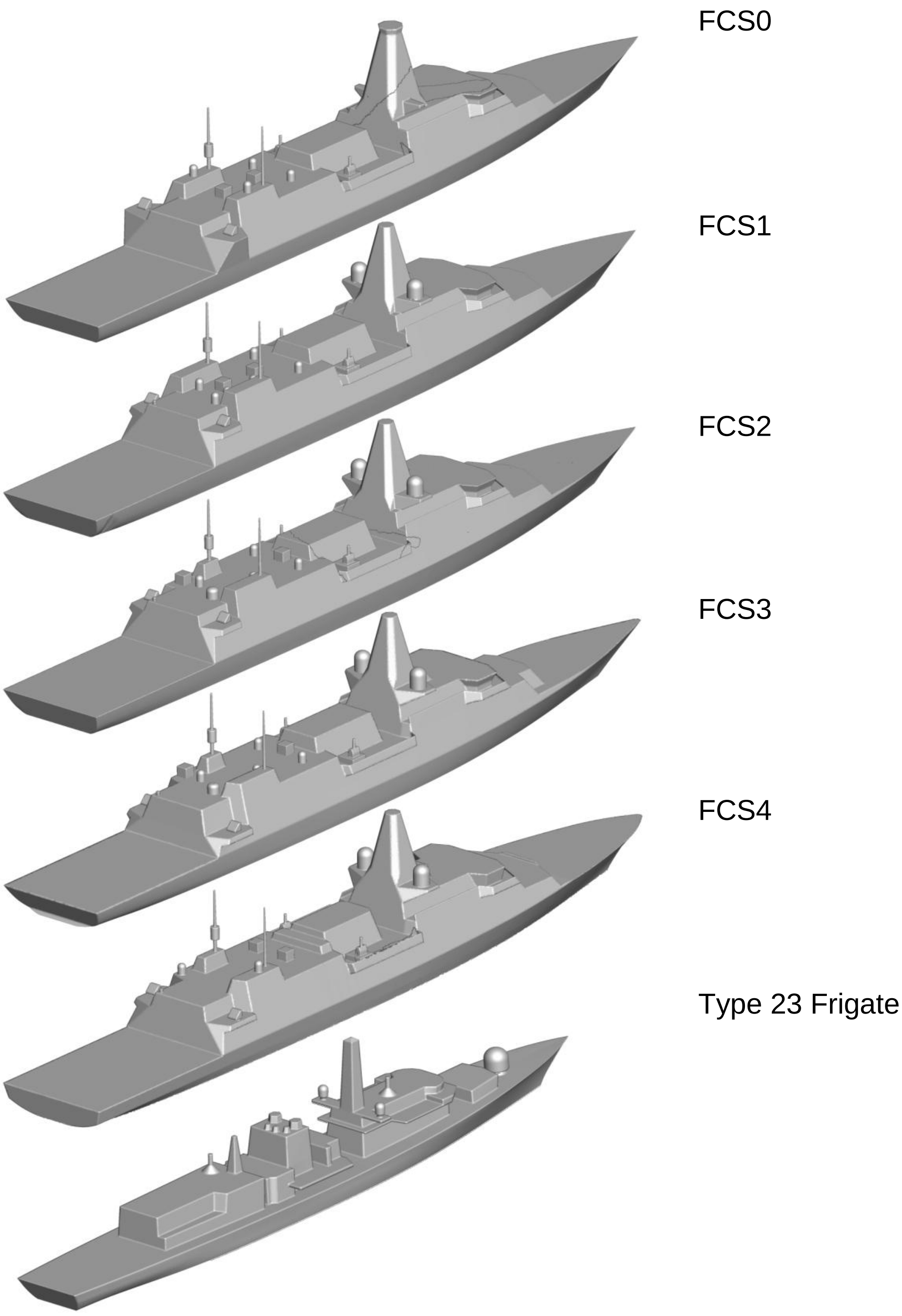

Figure 3.1 CAD geometries of different ship designs, and the Type 23 frigate

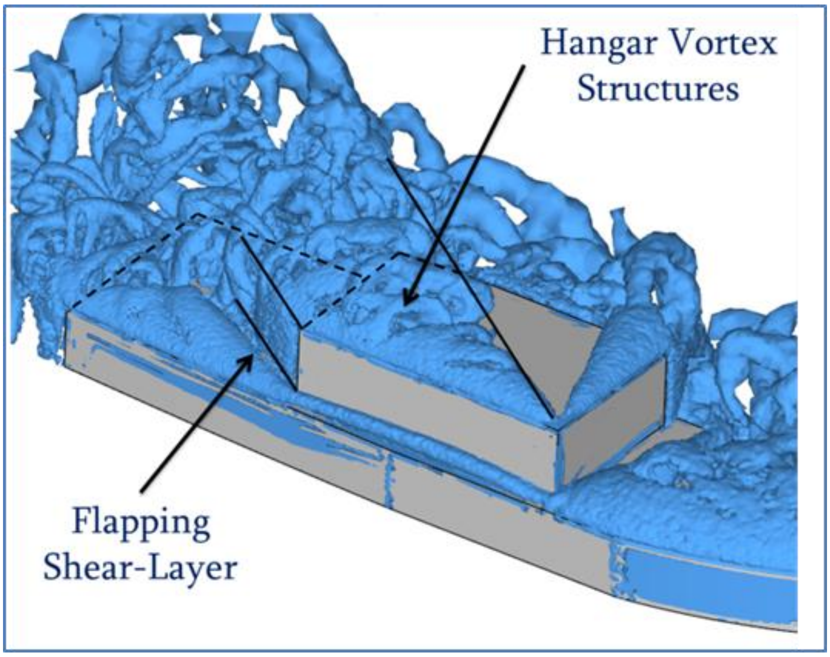

Figure 3.2 Visualisation of air flow over a simplified ship in oblique 45°winds by surfaces of iso-vorticity

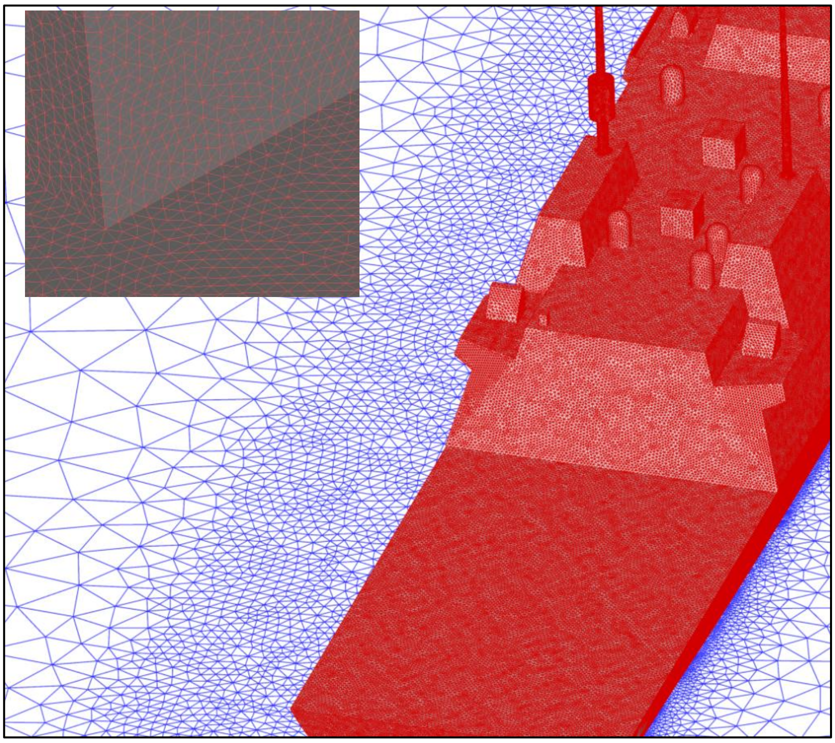

Figure 3.3 Surface mesh on FSC1, with inset figure showing close up of the mesh on the hangar face.

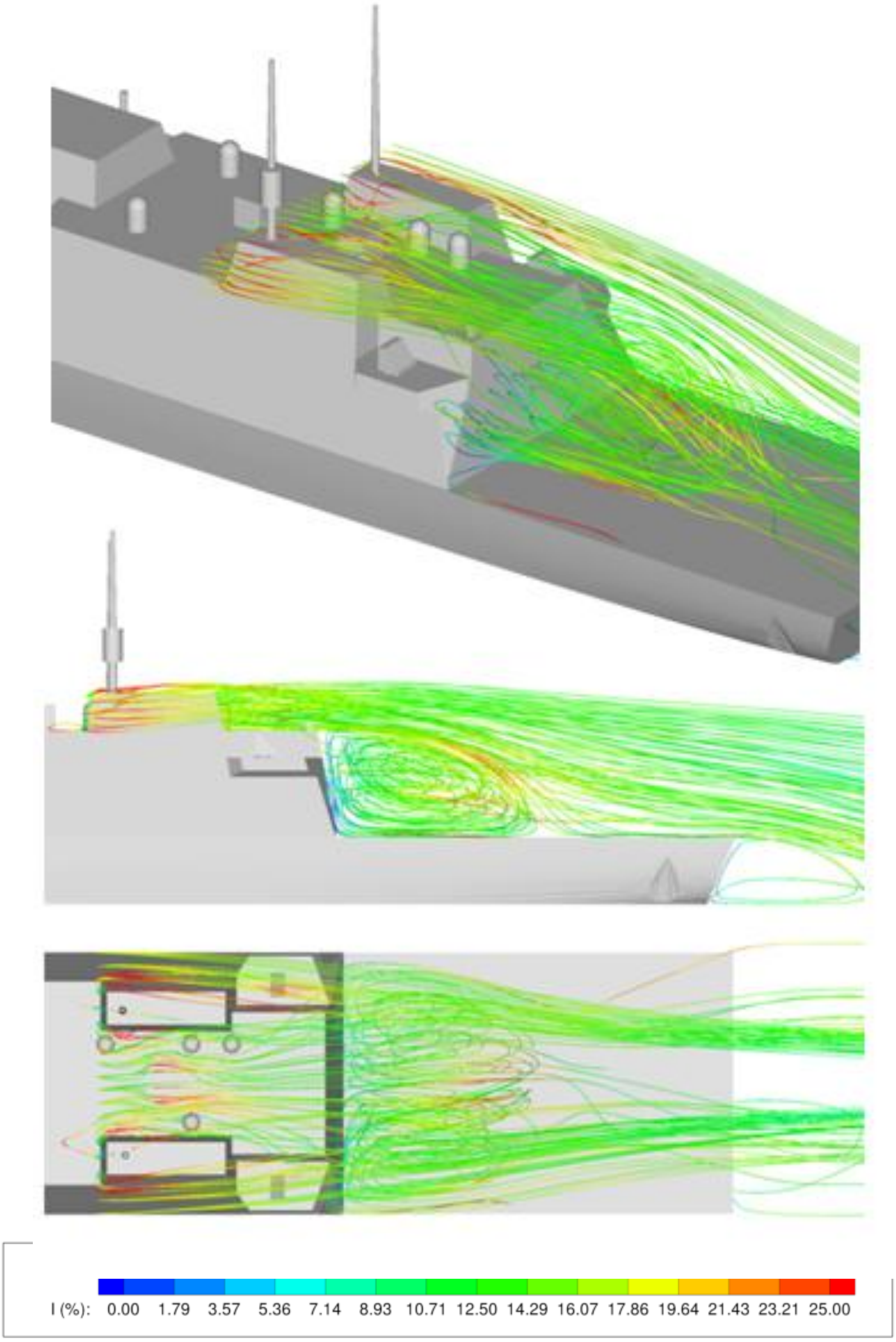

Figure 3.4 Streamlines showing flow around the hangar superstructure of FSC1 for the Headwind WOD, coloured by general Turbulence Intensity

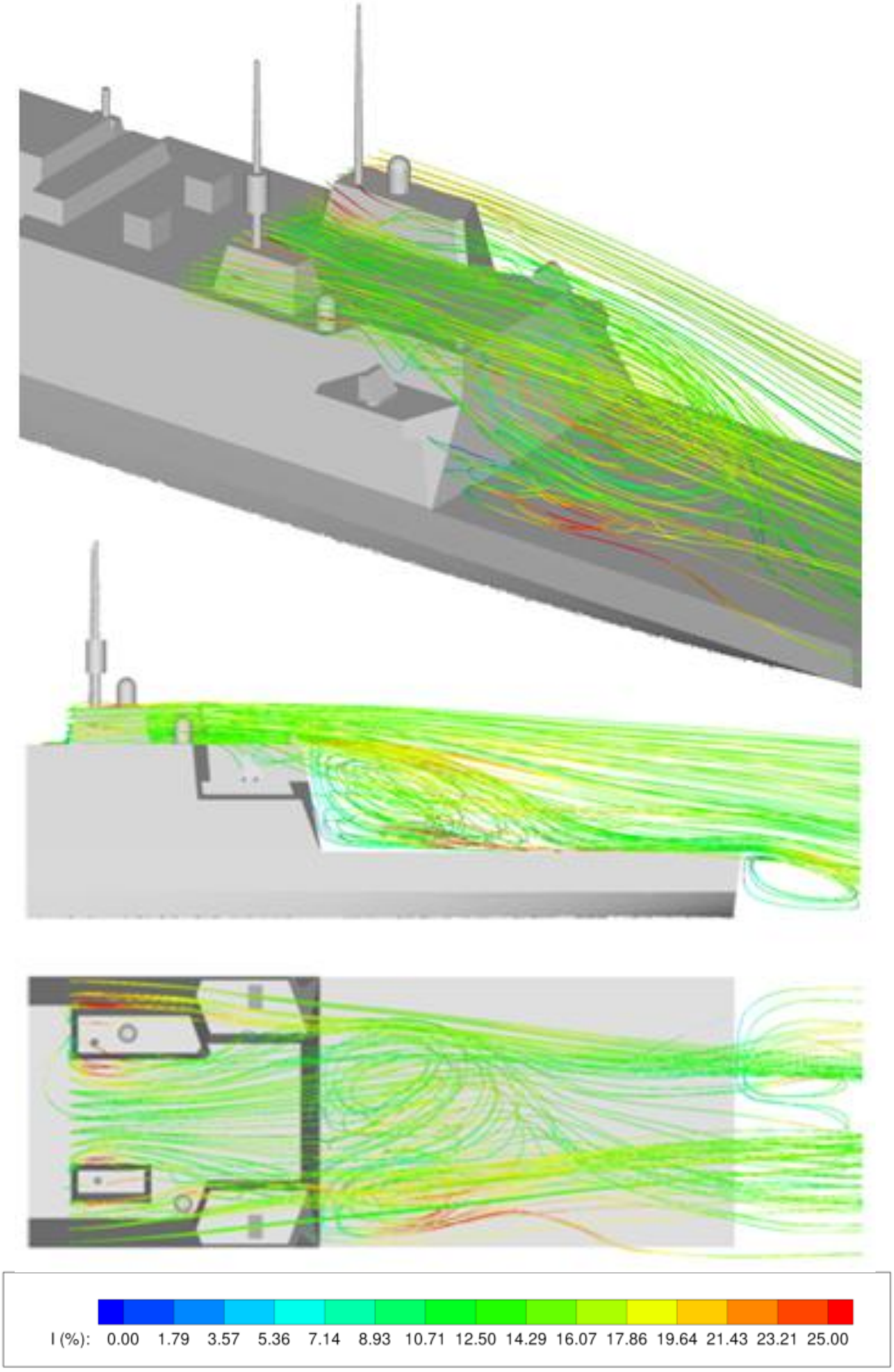

Figure 3.5 Streamlines showing flow around the hangar superstructure of the FSC4 for the Headwind WOD, coloured by general Turbulence Intensity

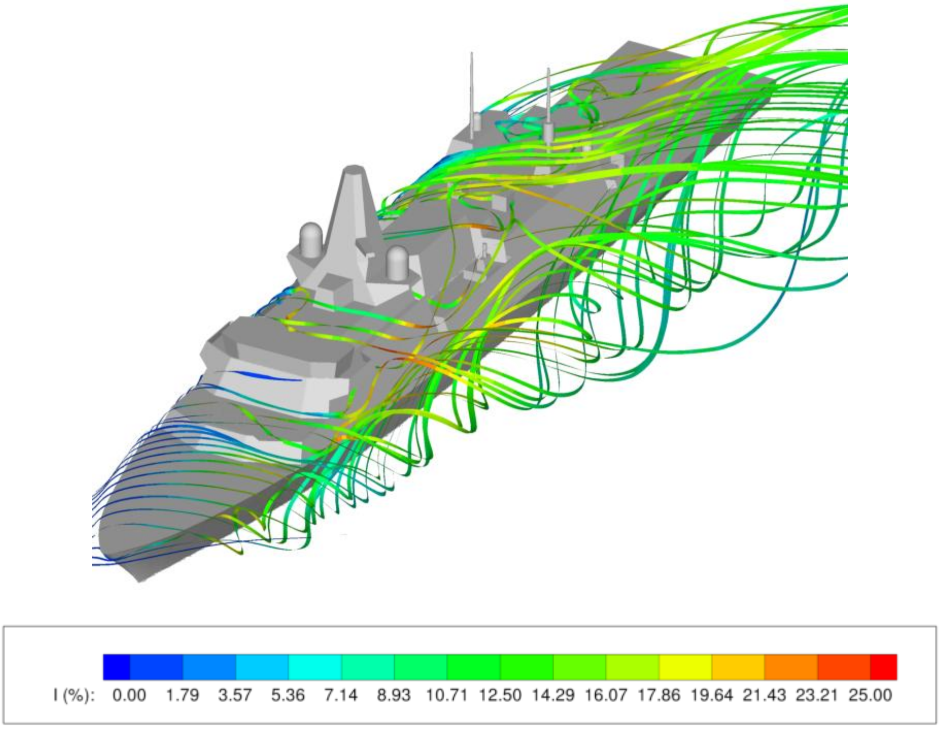

Figure 3.6 Streamlines showing flow over the superstructure of the FSC4 for Green 45 WOD, coloured by general Turbulence Intensity

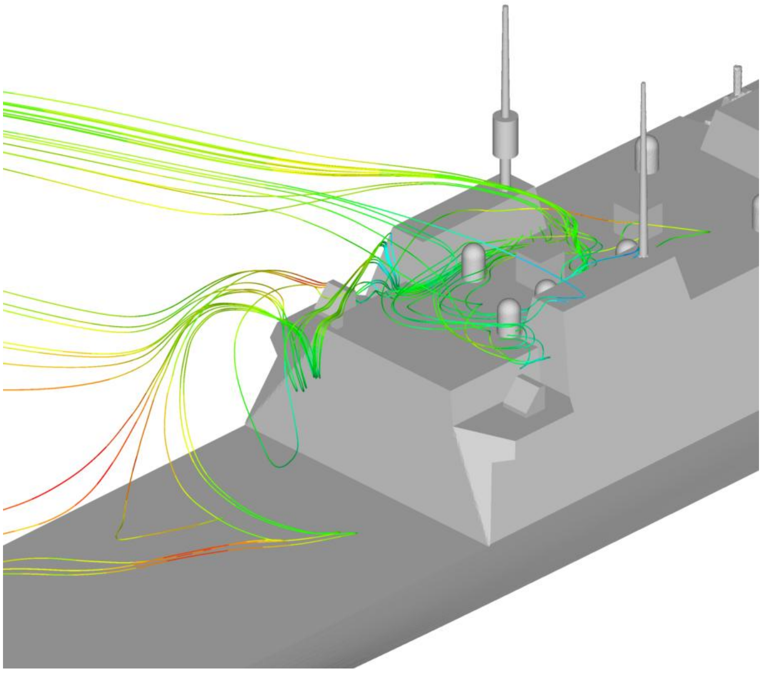

Figure 3.7 Streamlines showing flow over the funnel superstructure of the FSC1 for Green 45 WOD, coloured by general Turbulence Intensity

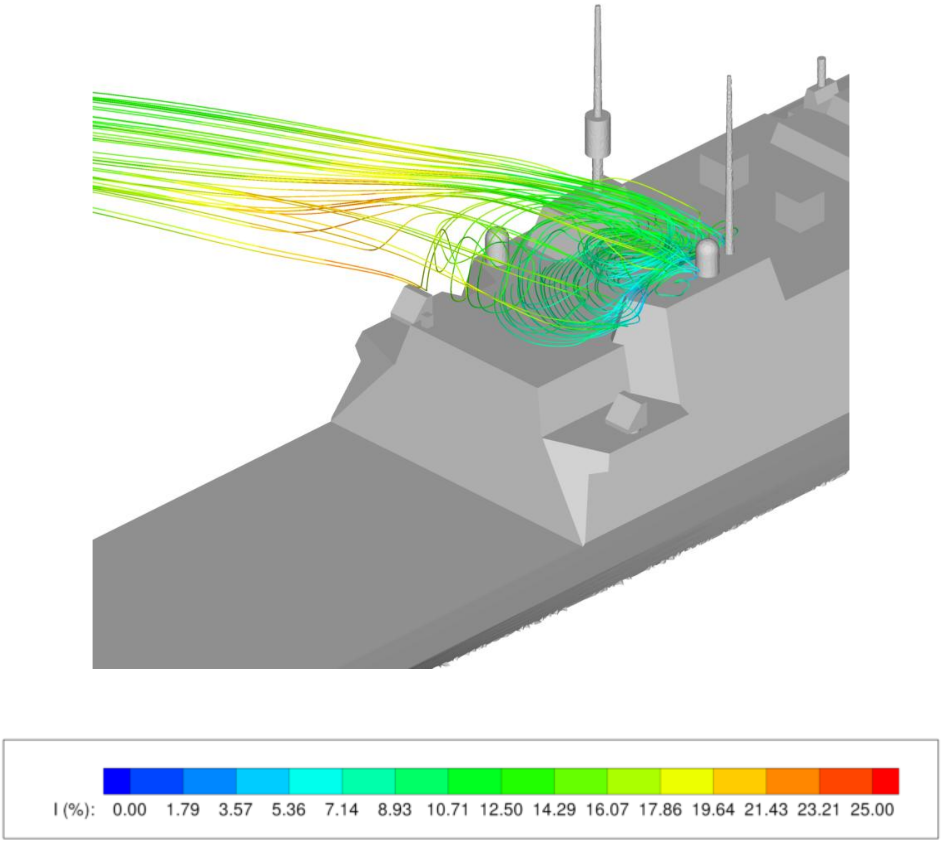

Figure 3.8 Streamlines showing flow over the funnel superstructure of the FSC4 for Green 45 WOD, coloured by general Turbulence Intensity

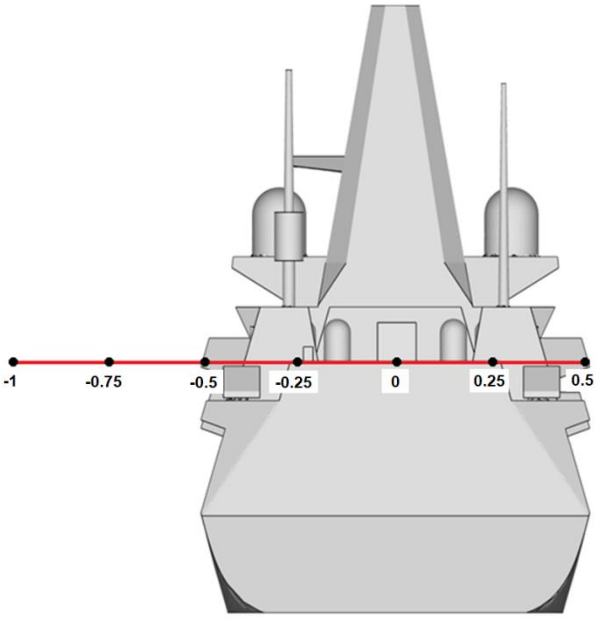

Figure 3.9 View from astern of FSC showing rotor hub positions of VAD in terms of lateral position (y/b)

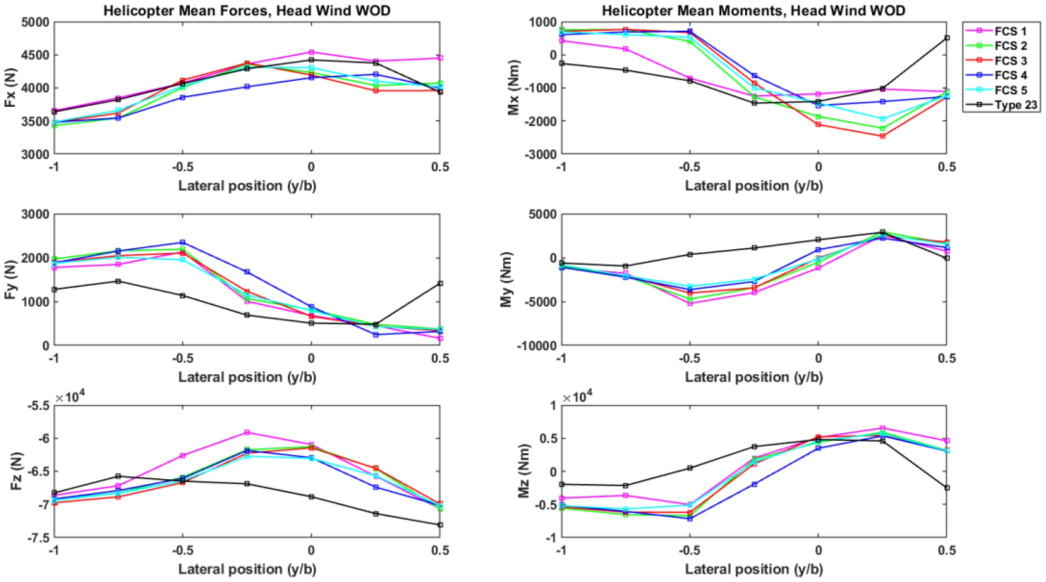

Figure 3.10 Mean VAD results for the headwind WOD case

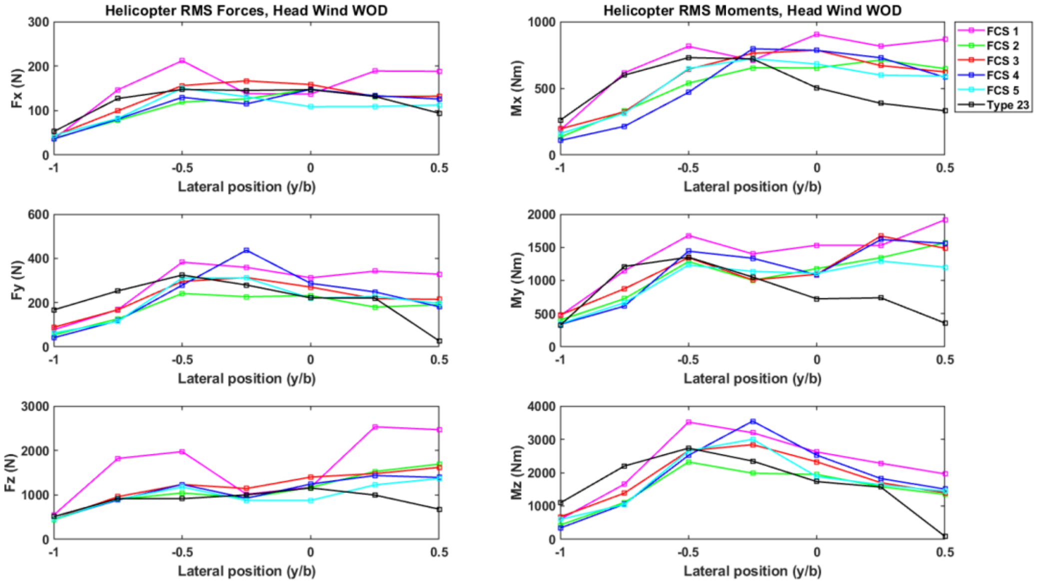

Figure 3.11 RMS VAD results for the headwind WOD case

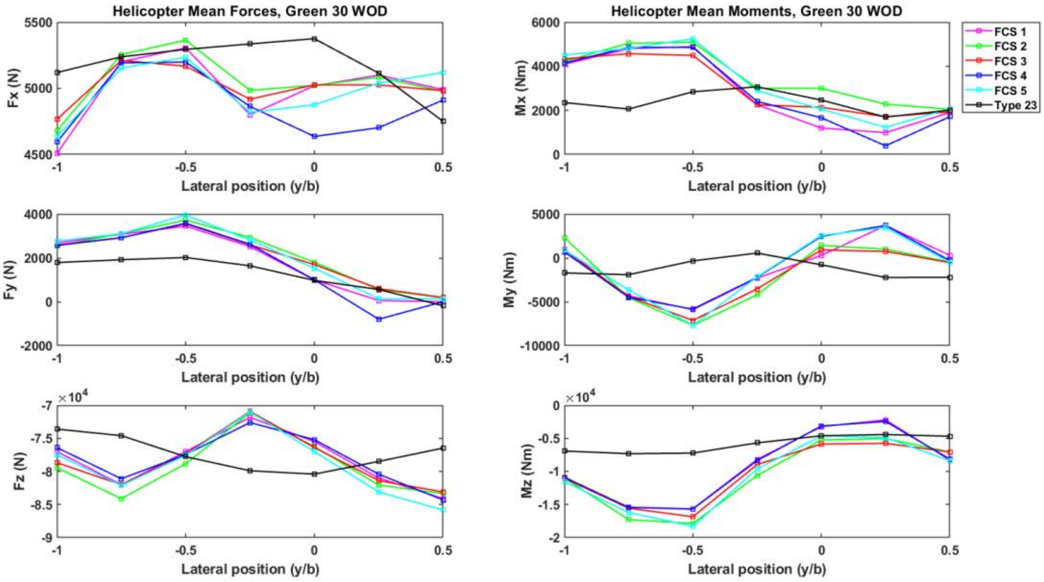

Figure 3.12 Mean VAD results for the Green 30 WOD case

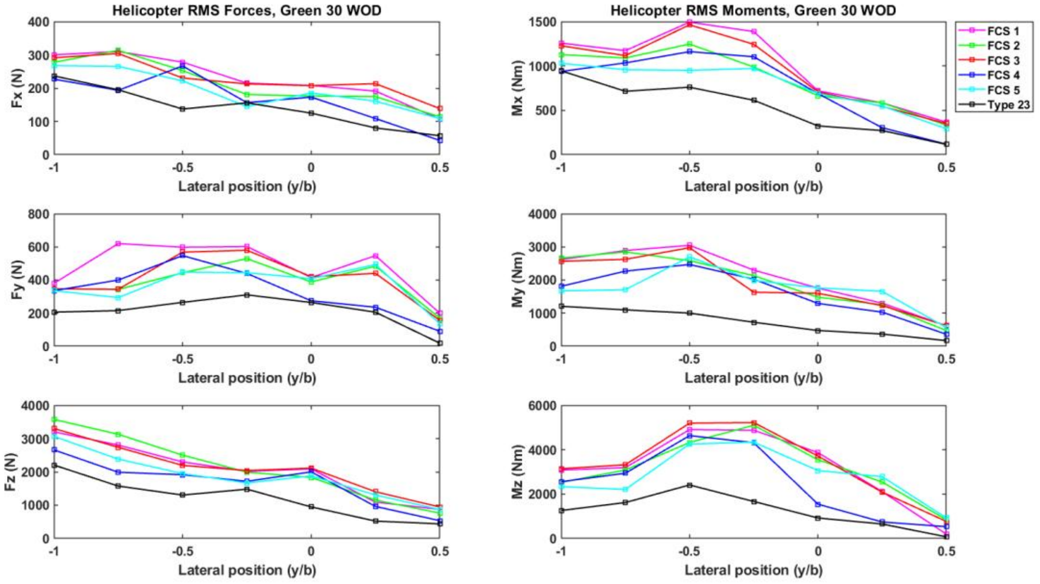

Figure 3.13 RMS VAD results for the Green 30 WOD case

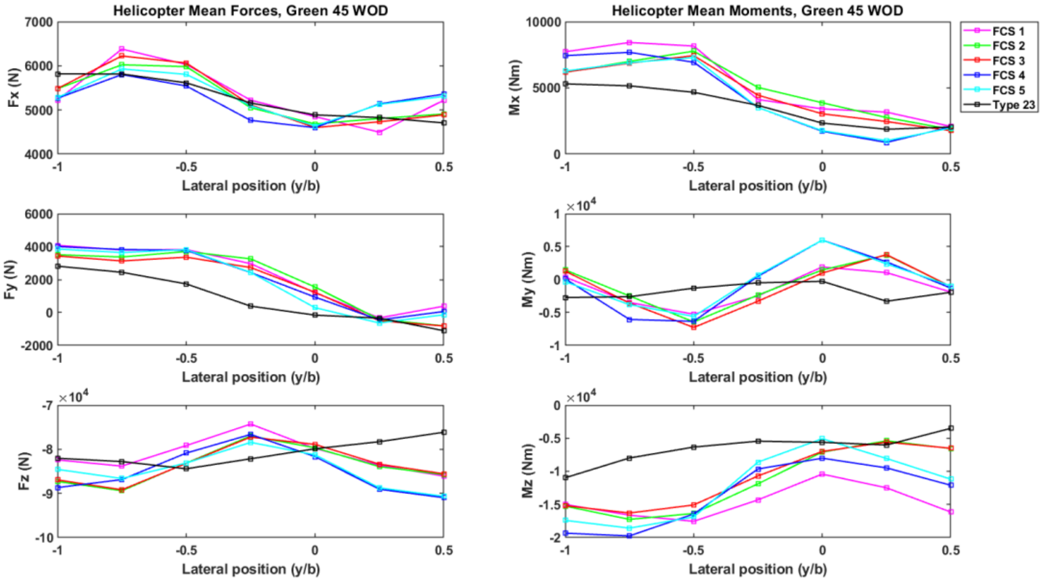

Figure 3.14 Mean VAD results for the Green 45 WOD case

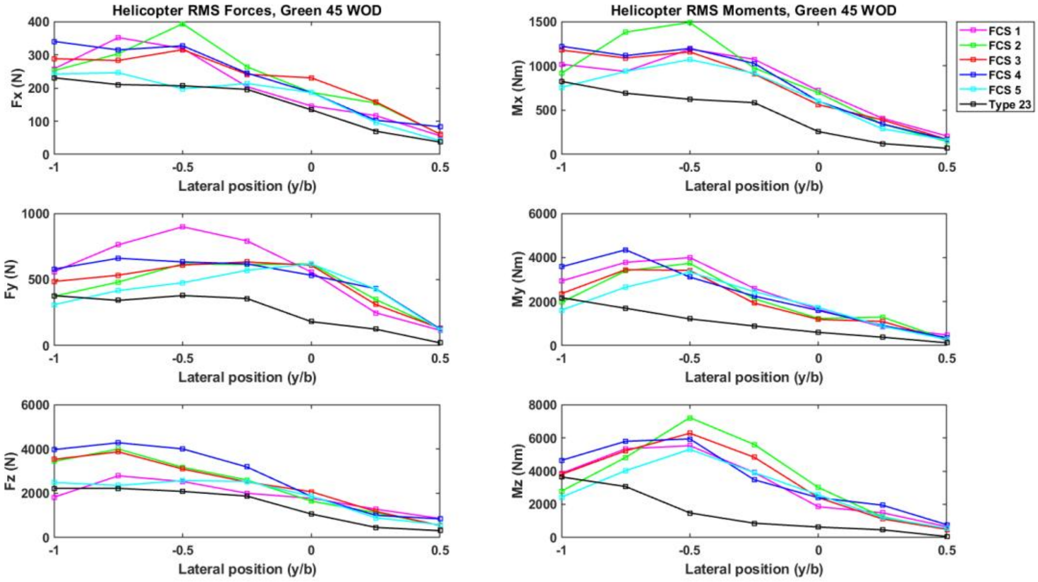

Figure 3.15 RMS VAD results for the Green 45 WOD case

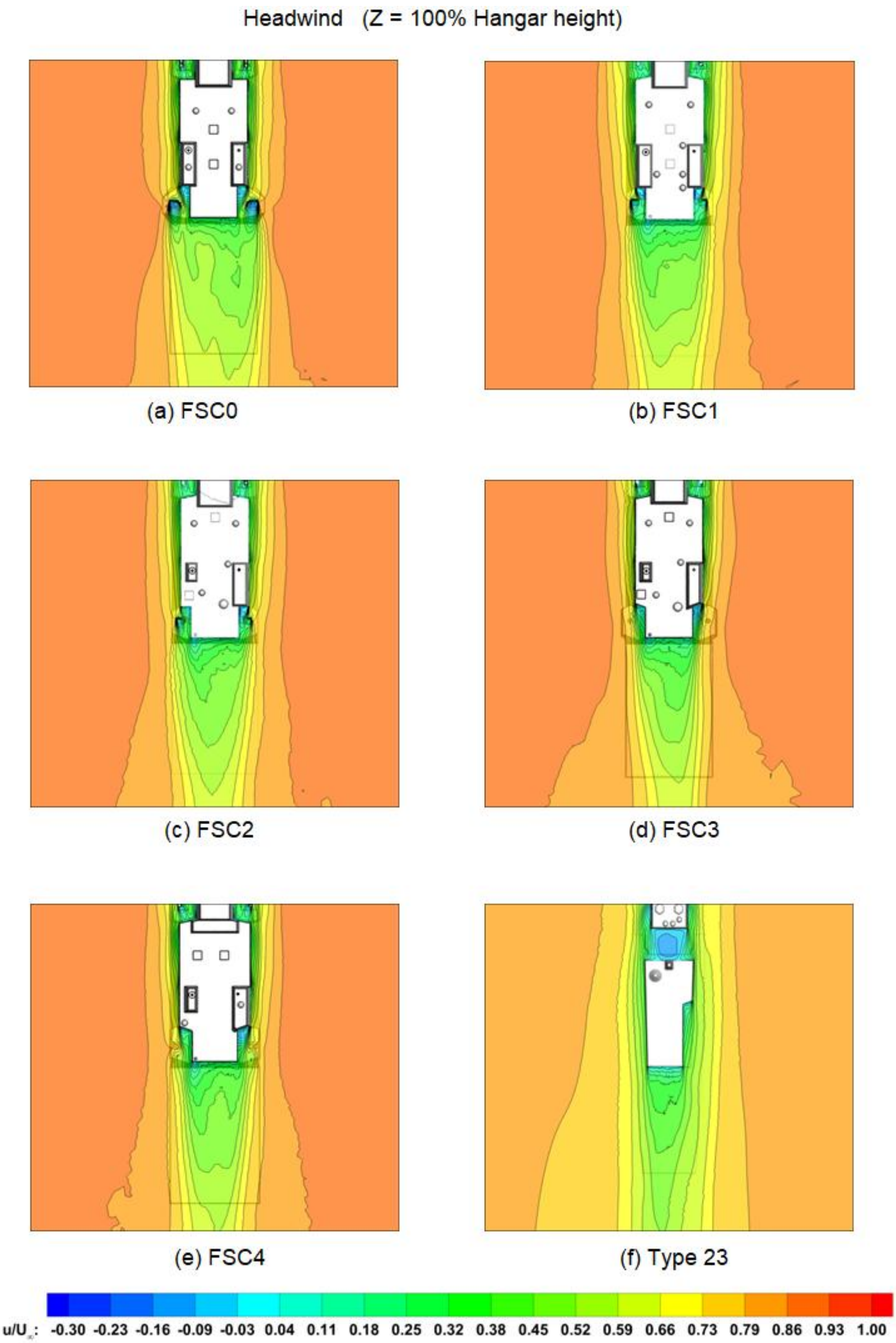

Figure 3.16 Mean longitudinal velocity contours at 100% hangar

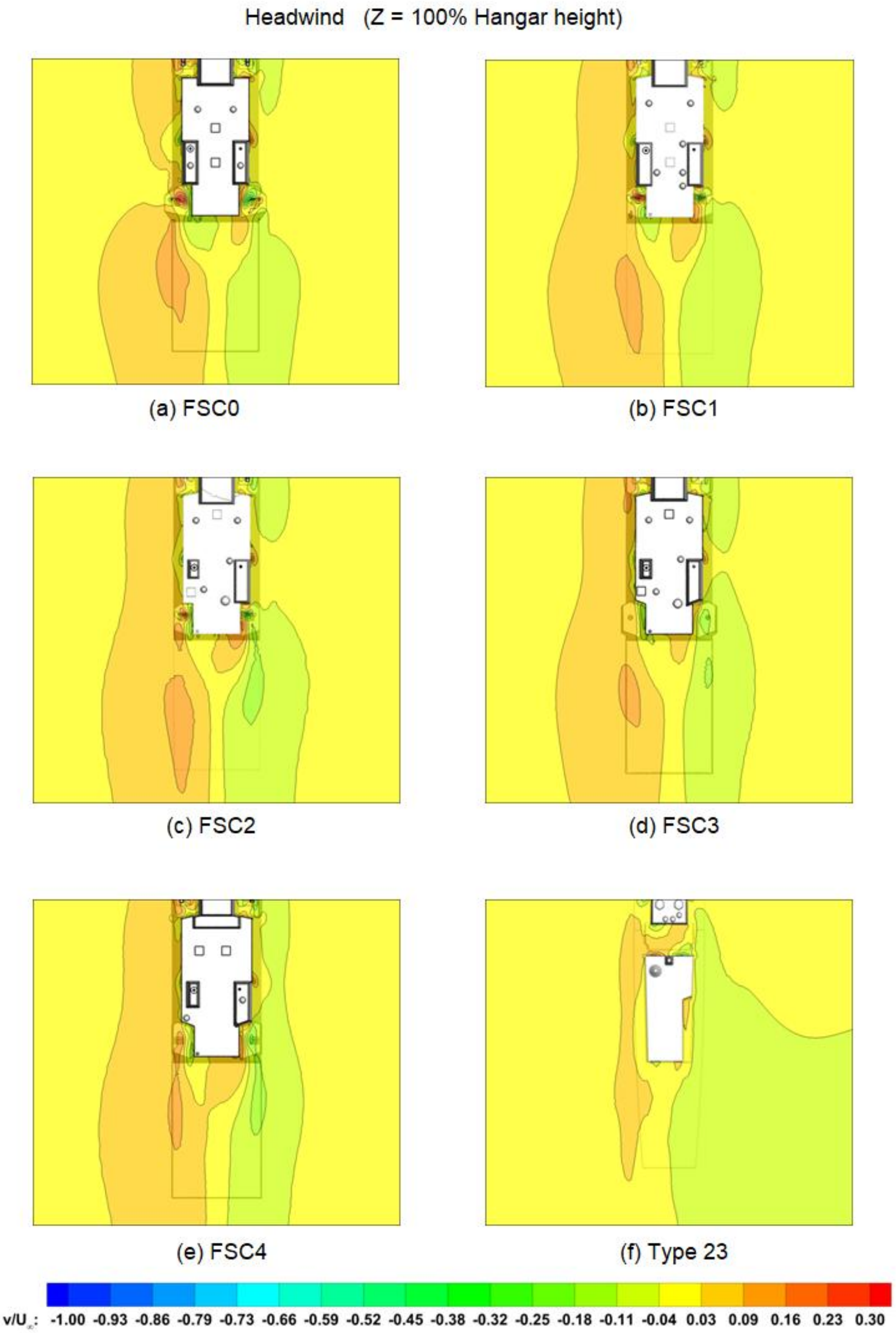

(a) FSC0

(b) FSC1

(c) FSC2

(d) FSC3

(e) FSC4

(f) Type 23

Figure 3.17 Mean lateral velocity contours at 100% hangar height

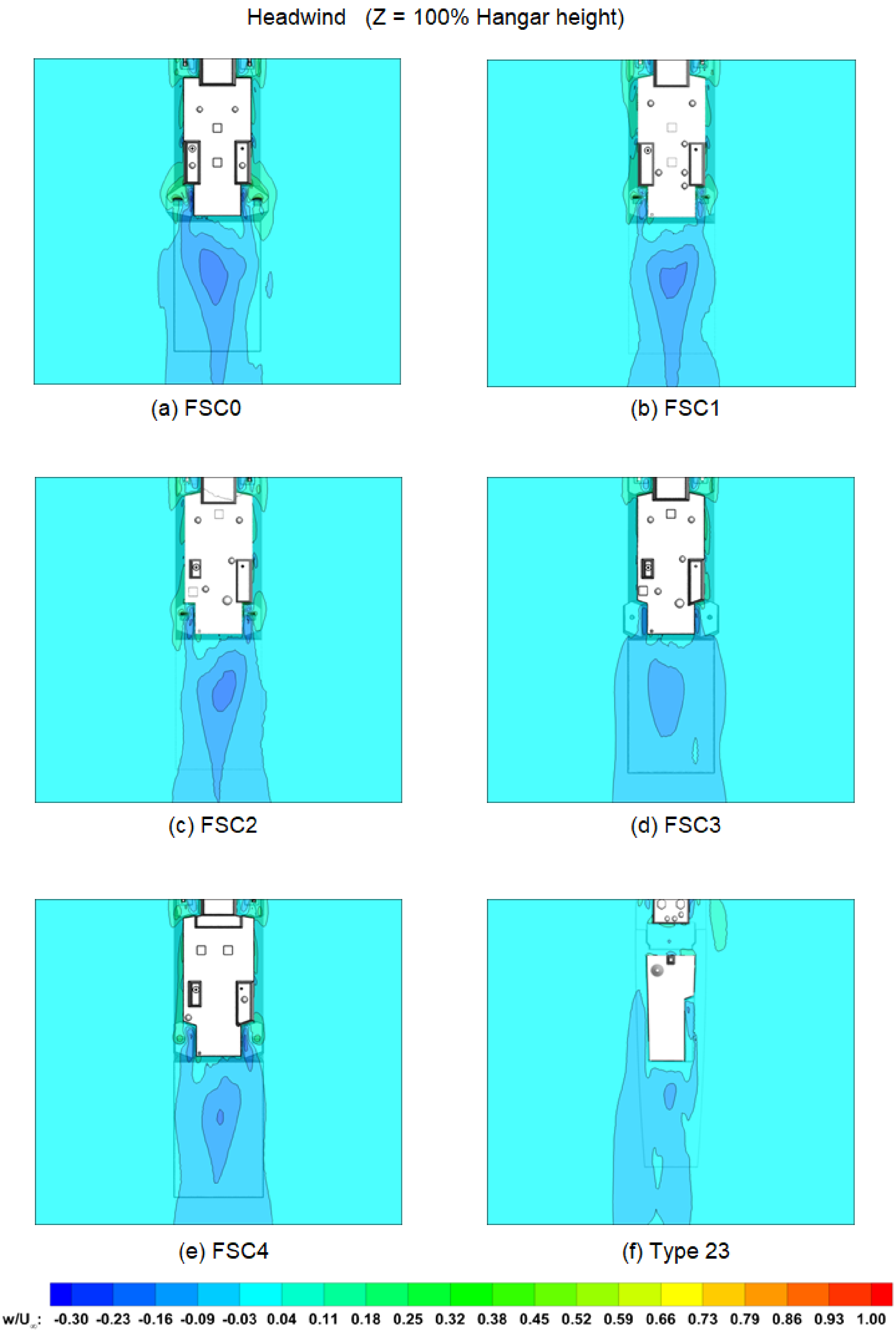

(a) FSC0

(b) FSC1

(c) FSC2

(d) FSC3

(e) FSC4

(f) Type 23

Figure 3.18 Mean vertical velocity contours at 100% hangar height

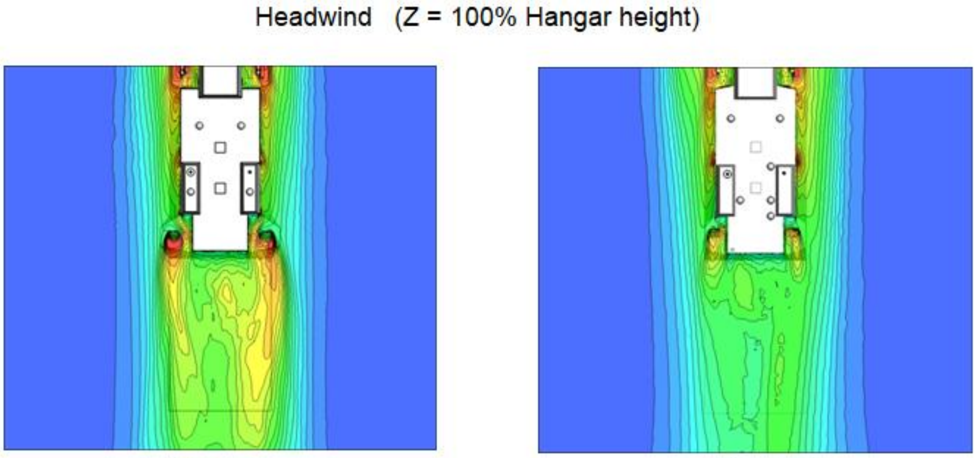

(a) FSC0 (b) FSC1

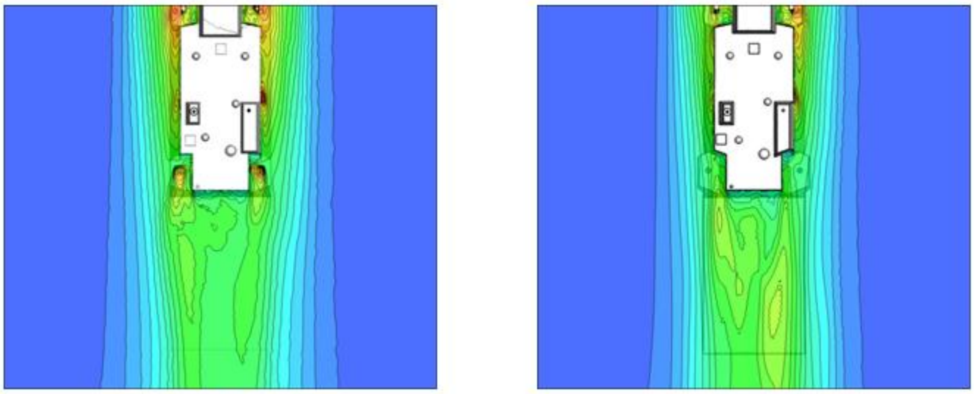

(c) FSC2 (d) FSC3

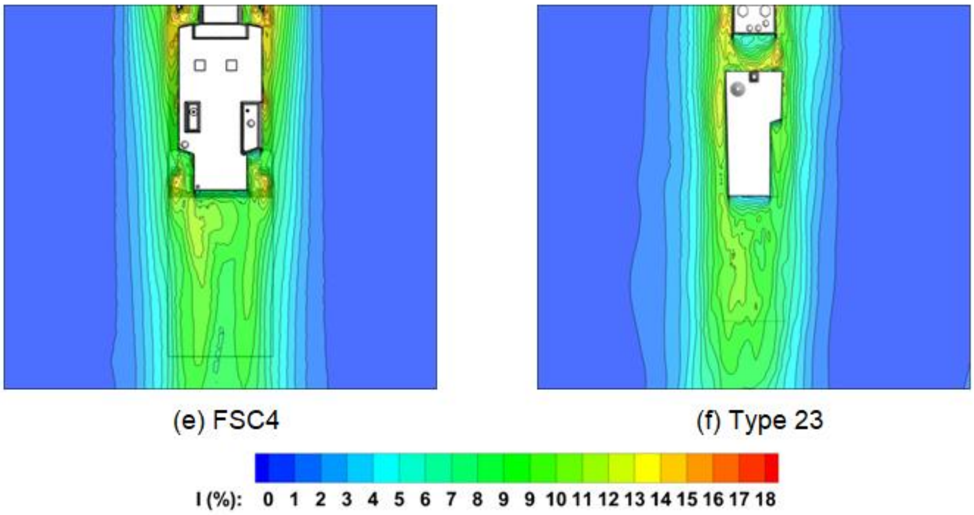

(e) FSC4 (f) Type 23

Figure 3.19 General turbulence intensity contours at 100% hangar height

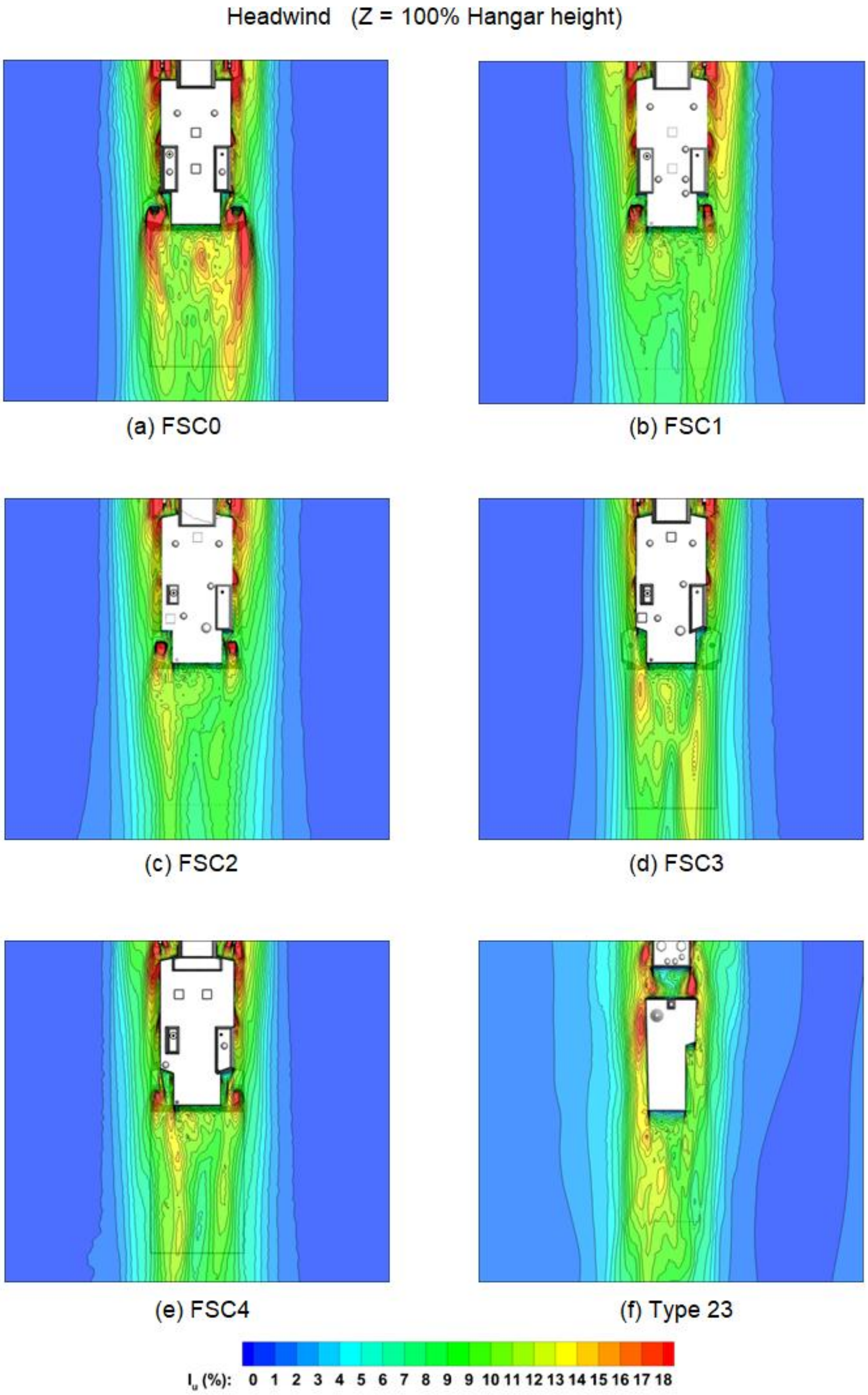

(a) FSC0 (b) FSC1

(c) FSC2 (d) FSC3

(e) FSC4 (f) Type 23

Figure 3.20 Longitudinal turbulence intensity contours at 100% hangar height

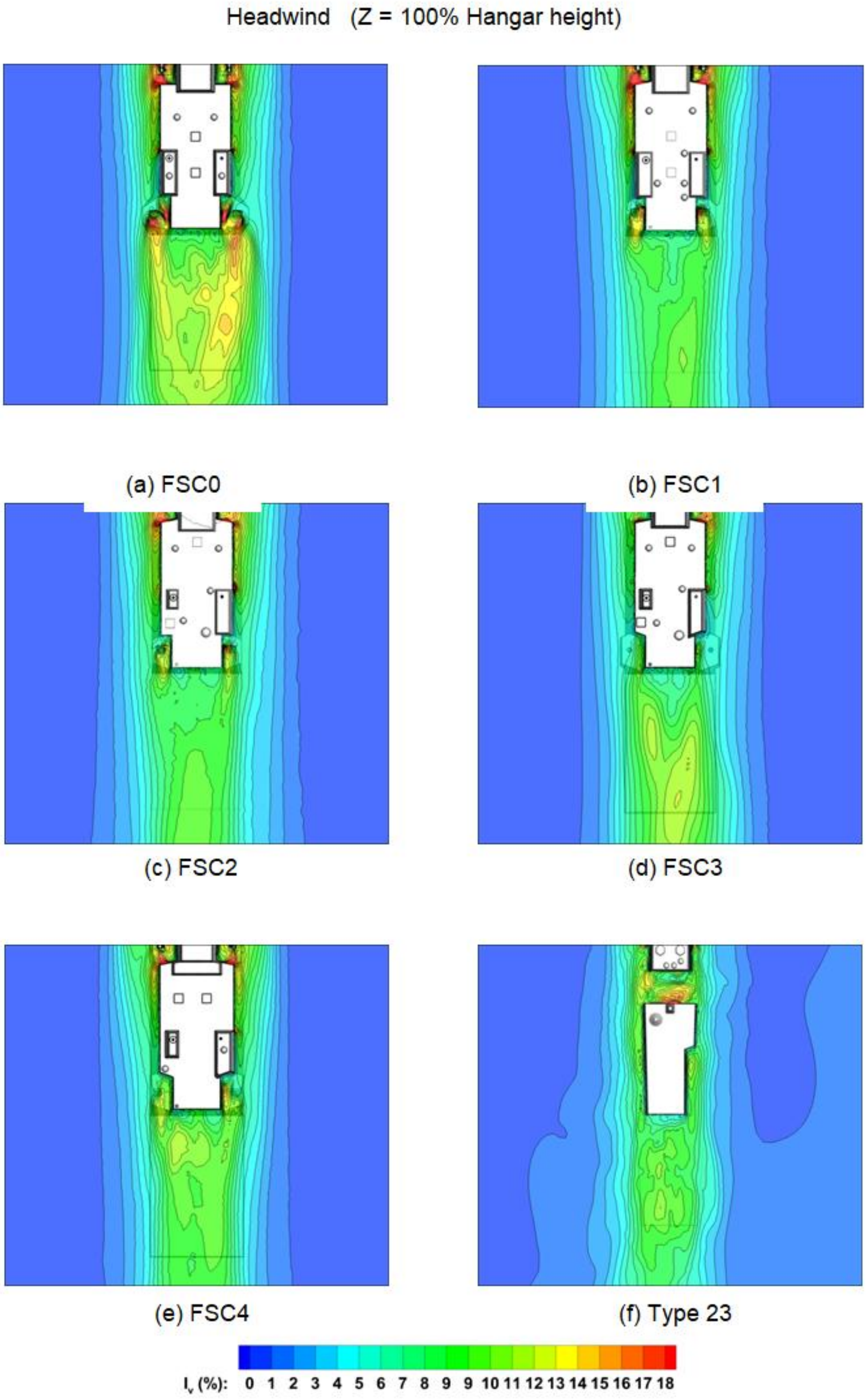

(a) FSC0

(b) FSC1

(c) FSC2

(d) FSC3

(e) FSC4

(f) Type 23

Figure 3.21 Lateral turbulence intensity contours at 100% hangar height

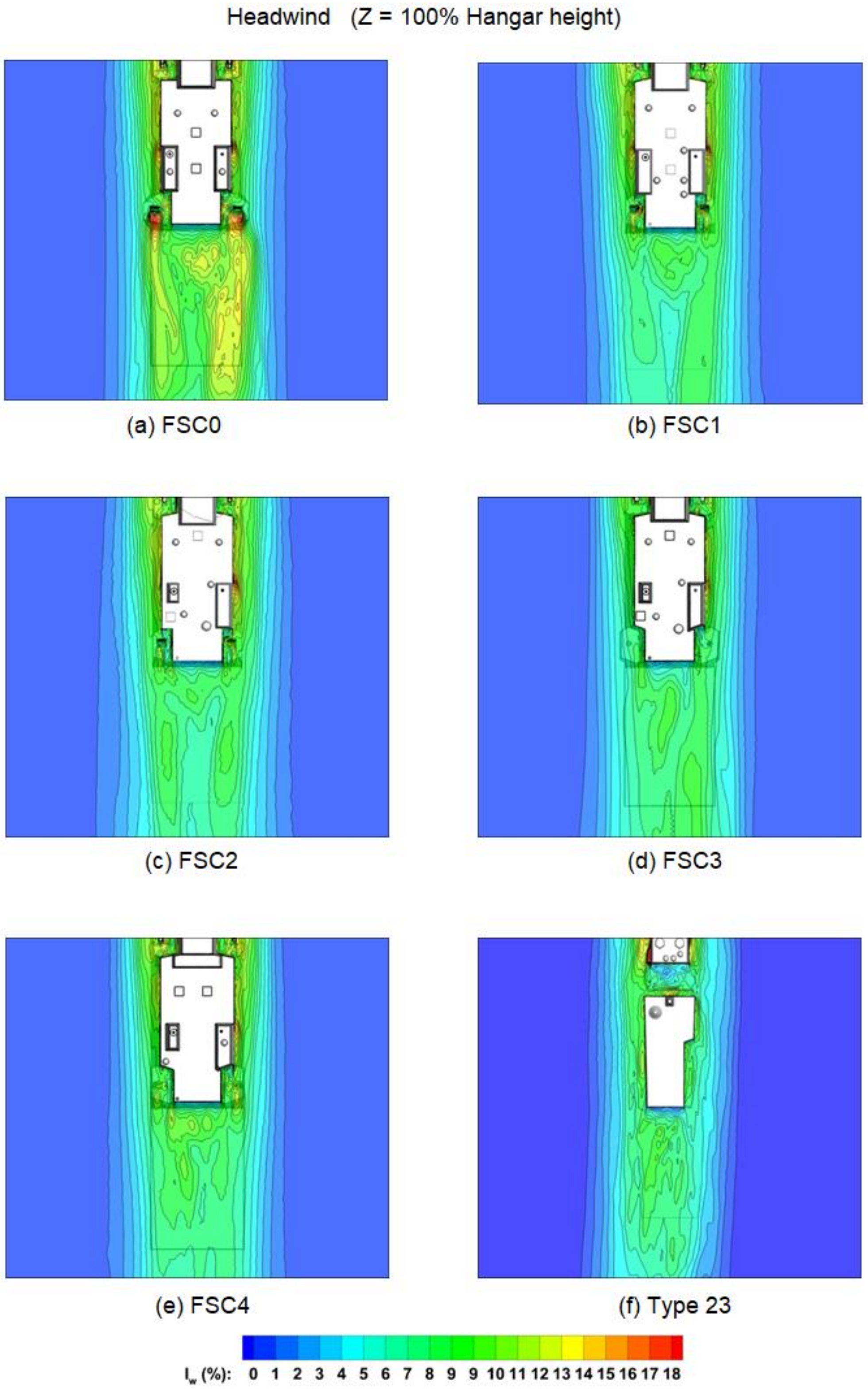

(a) FSC0

(b) FSC1

(c) FSC2

(d) FSC3

(e) FSC4

(f) Type 23

Figure 3.22 Vertical turbulence intensity contours at 100% hangar height

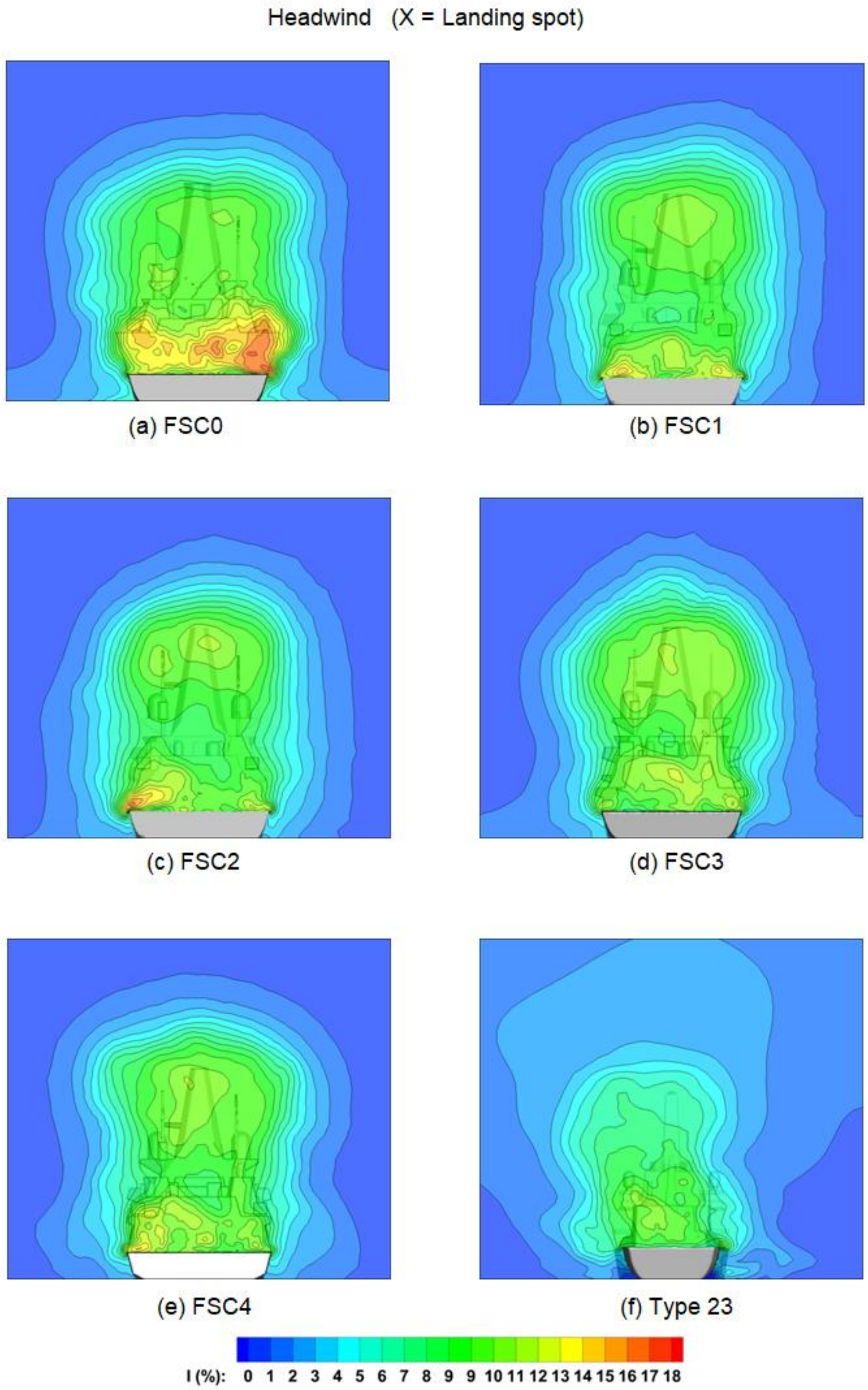

(a) FSC0

(b) FSC1

(c) FSC2

(d) FSC3

(e) FSC4

(f) Type 23

Figure 3.23 General turbulence intensity contours across landing spot

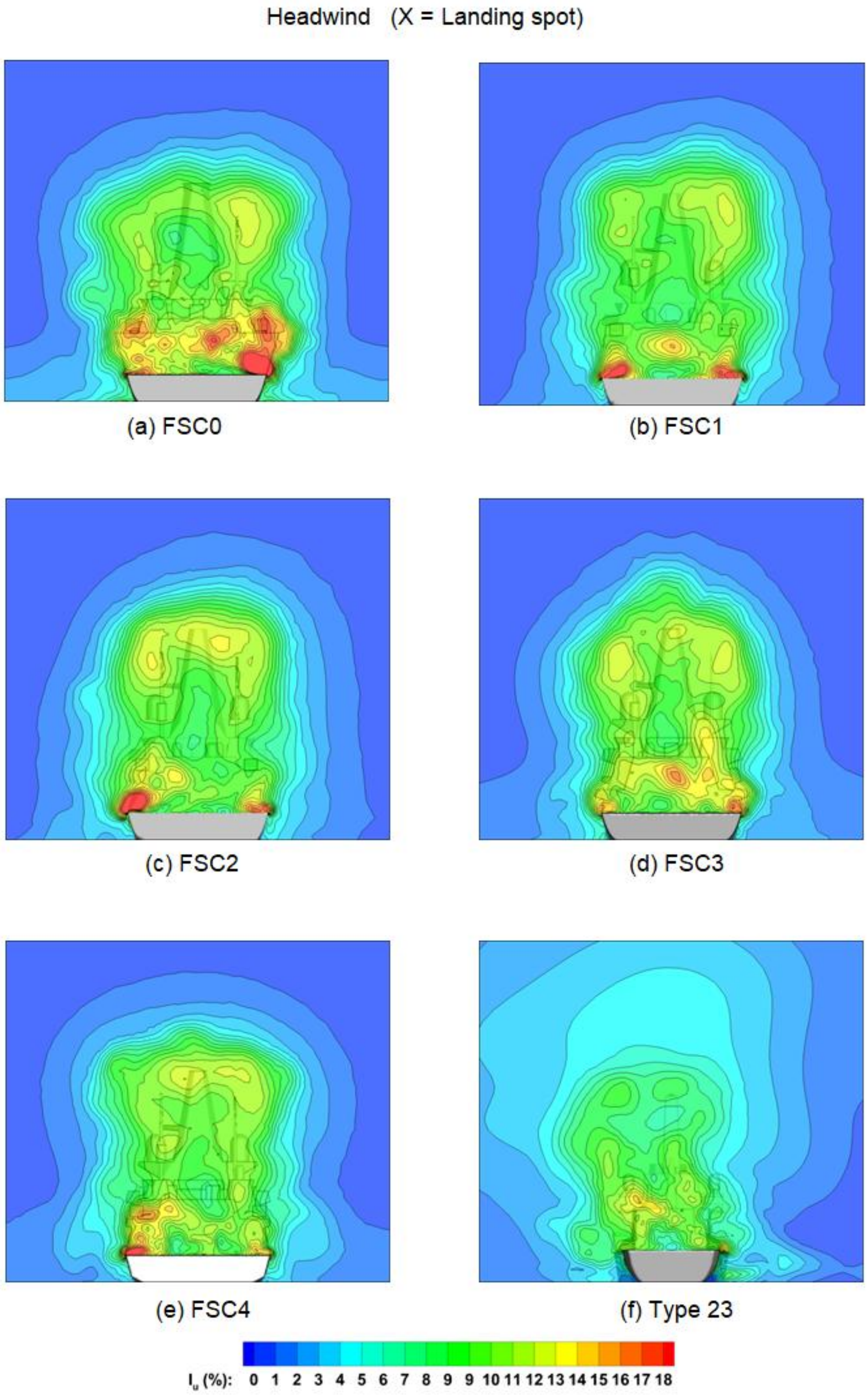
Headwind (X = Landing spot)

(a) FSC0

(b) FSC1

(c) FSC2

(d) FSC3

(e) FSC4

(f) Type 23

Figure 3.24 Longitudinal turbulence intensity contours across landing spot

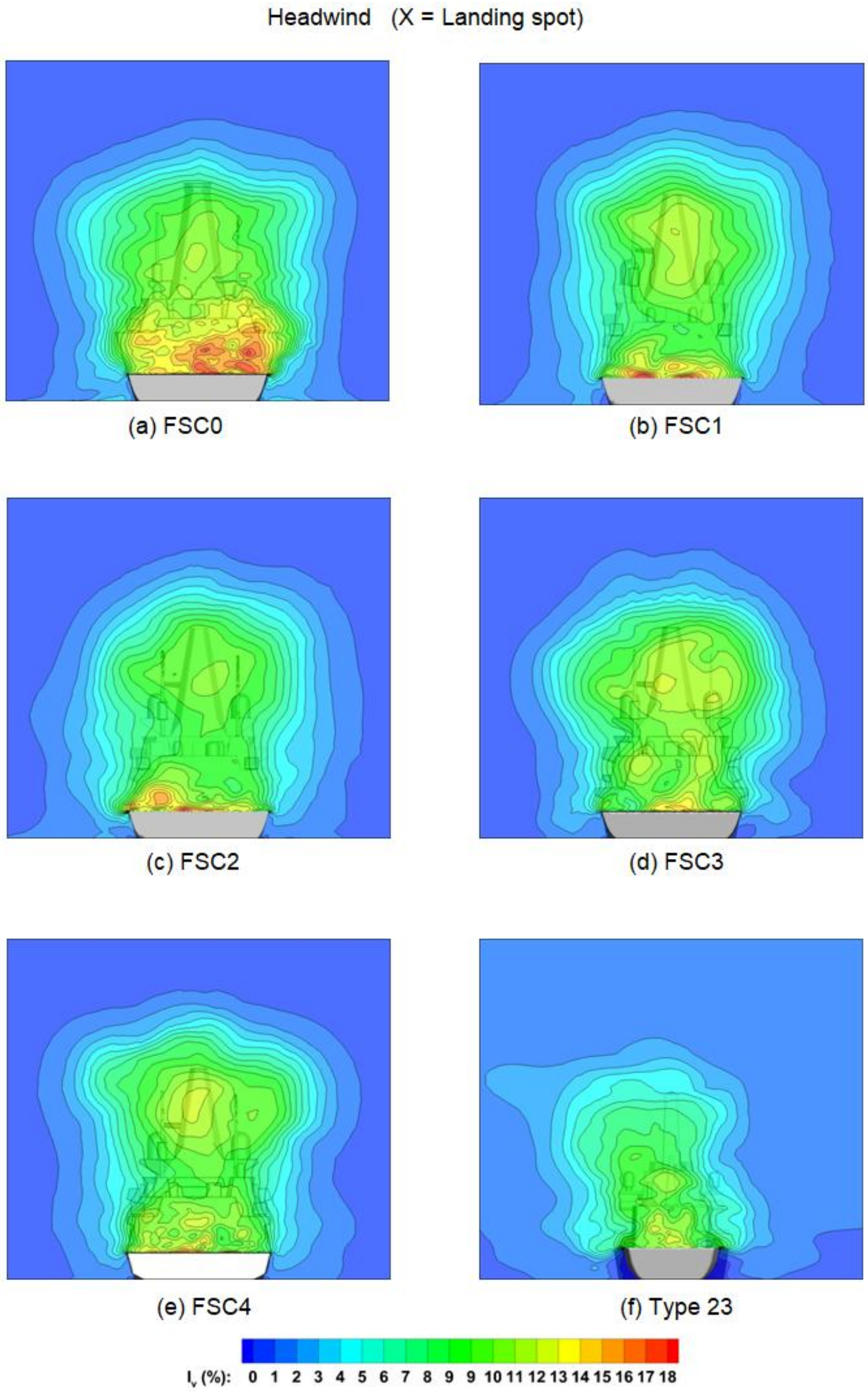

Figure 3.25 Lateral turbulence intensity contours across landing spot

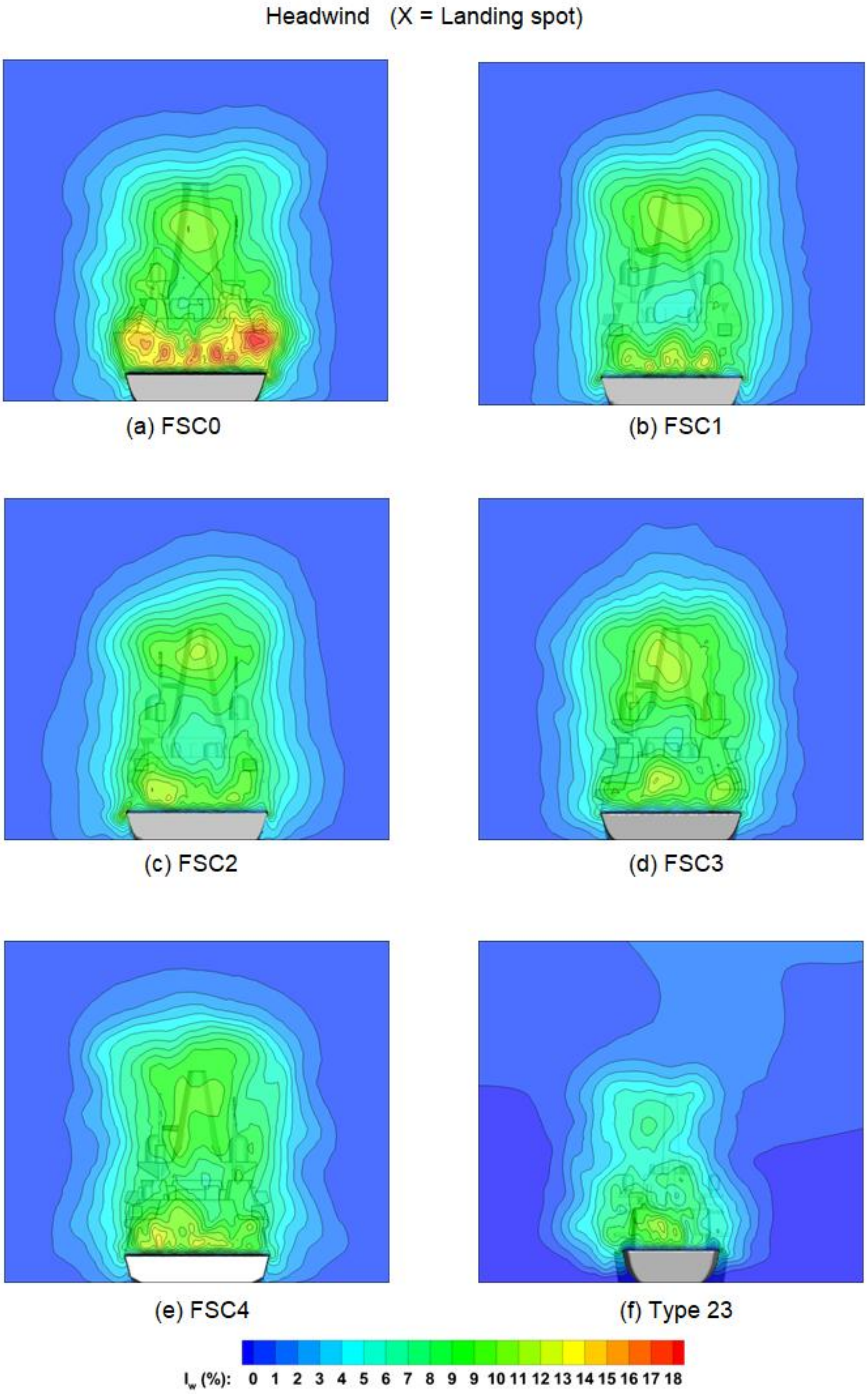

Figure 3.26 Vertical turbulence intensity contours across landing spot

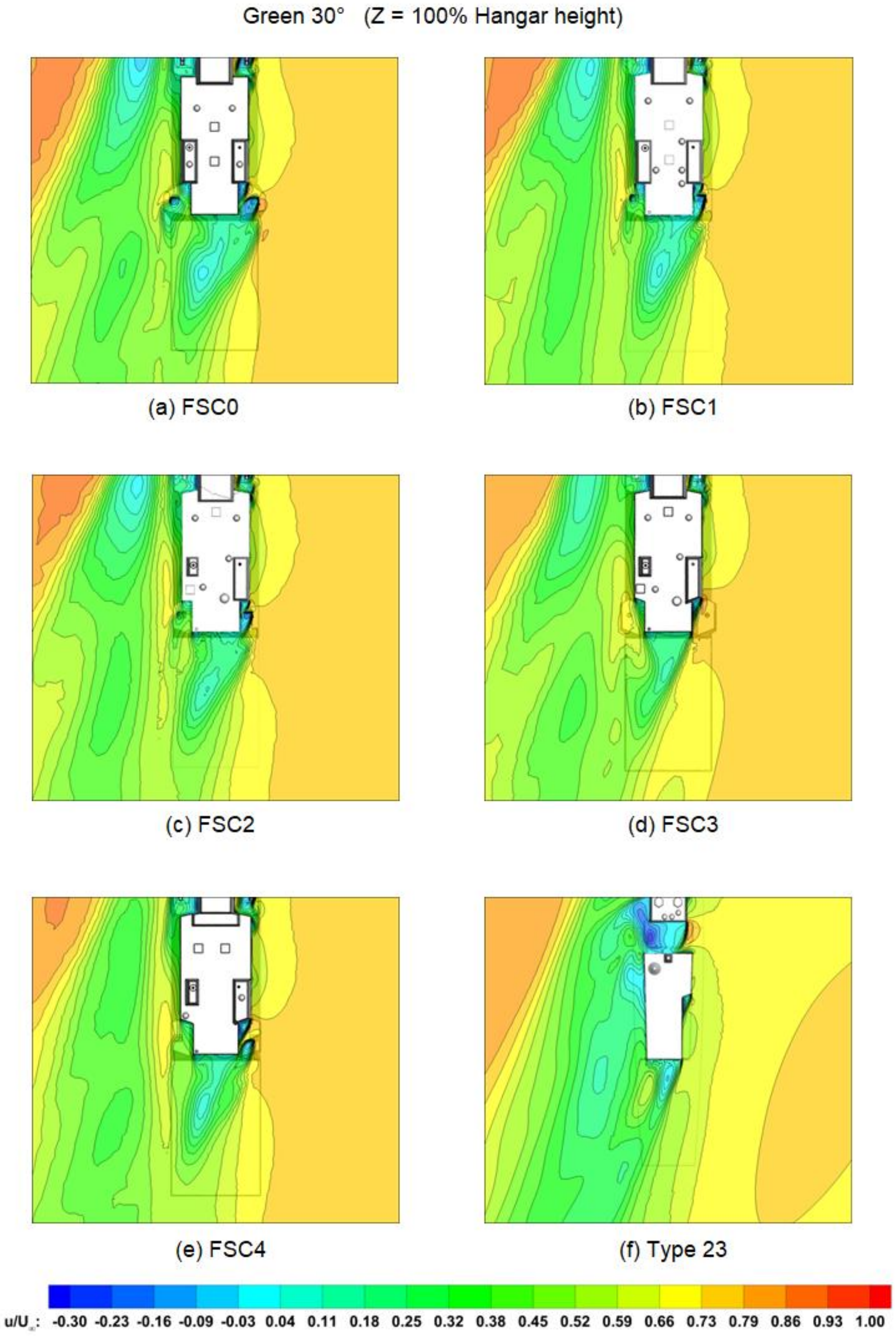

(a) FSC0

(b) FSC1

(c) FSC2

(d) FSC3

(e) FSC4

(f) Type 23

Figure 3.27 Mean longitudinal velocity contours at 100% hangar height

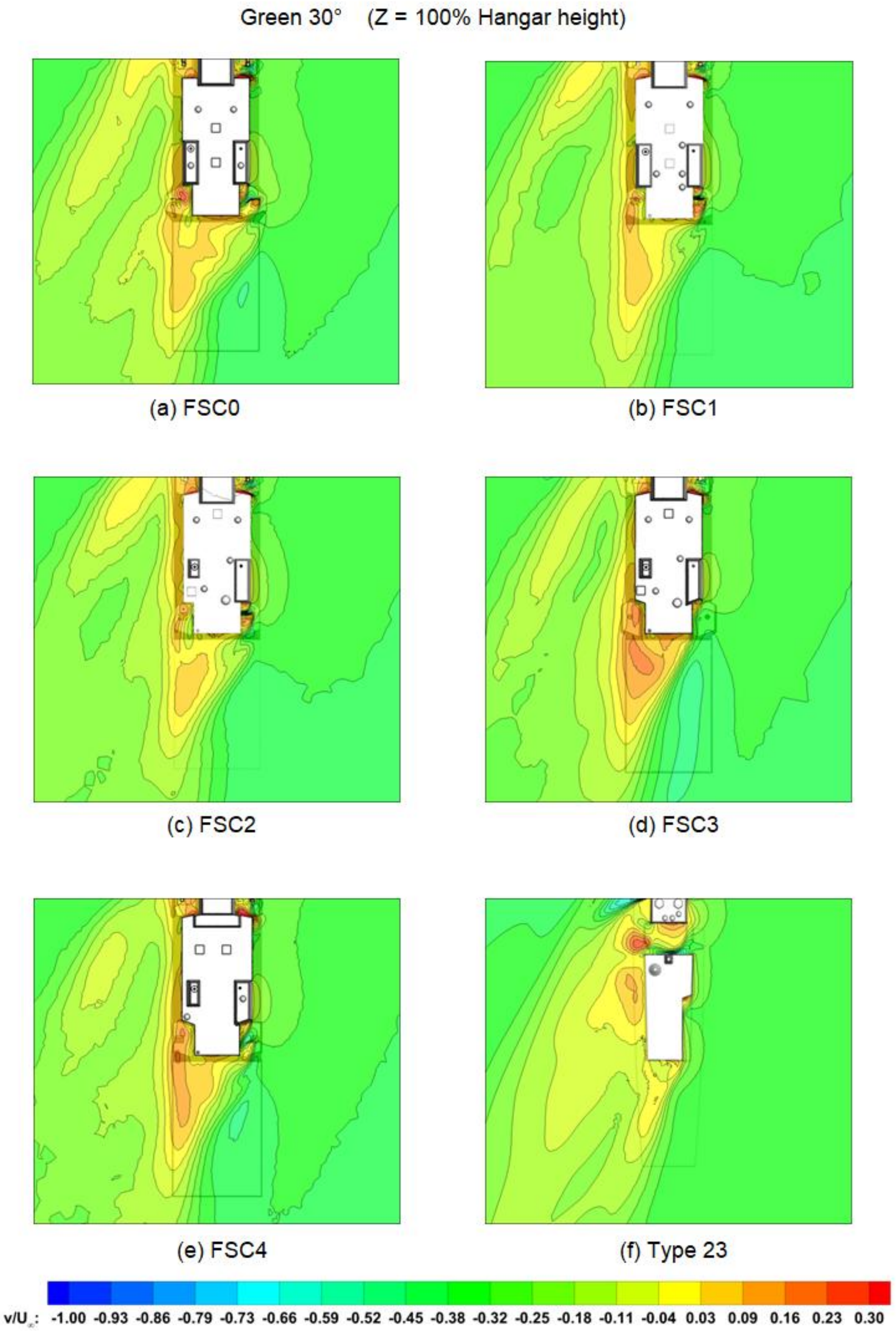

(a) FSC0

(b) FSC1

(c) FSC2

(d) FSC3

(e) FSC4

(f) Type 23

Figure 3.28 Mean lateral velocity contours at 100% hangar height

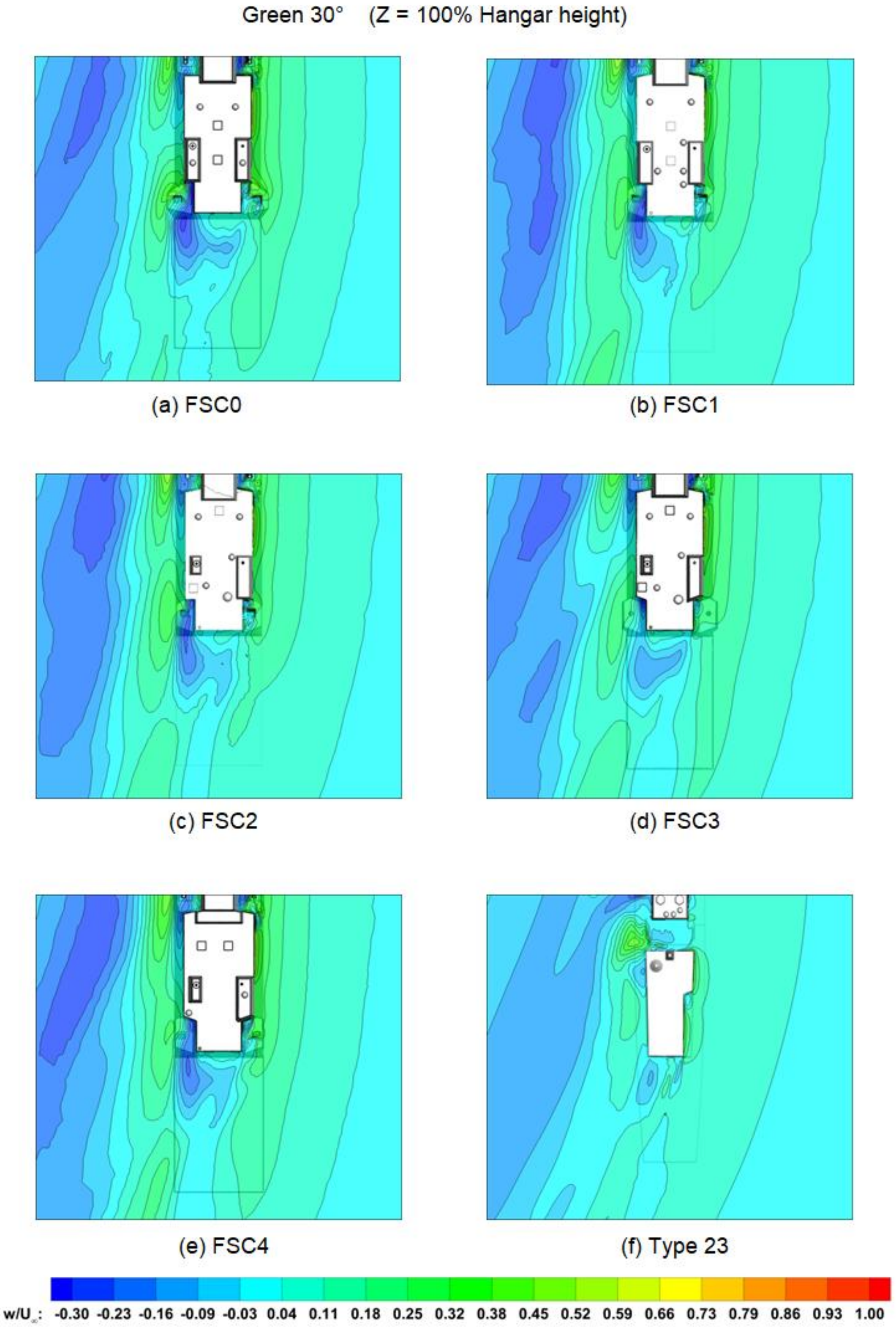

(a) FSC0

(b) FSC1

(c) FSC2

(d) FSC3

(e) FSC4

(f) Type 23

Figure 3.29 Mean vertical velocity contours at 100% hangar height

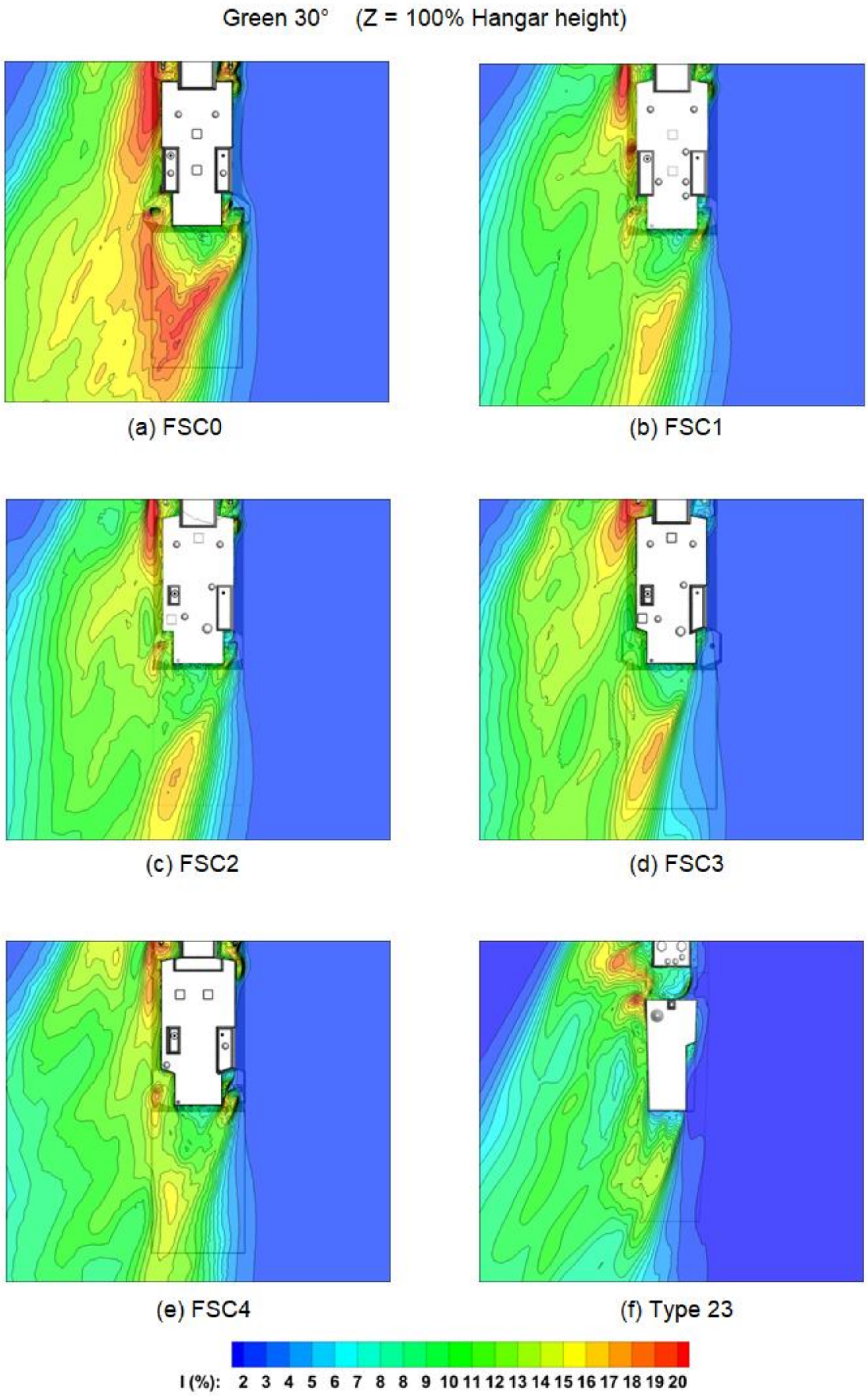

(a) FSC0 (b) FSC1

(c) FSC2 (d) FSC3

(e) FSC4 (f) Type 23

Figure 3.30 General turbulence intensity contours at 100% hangar height

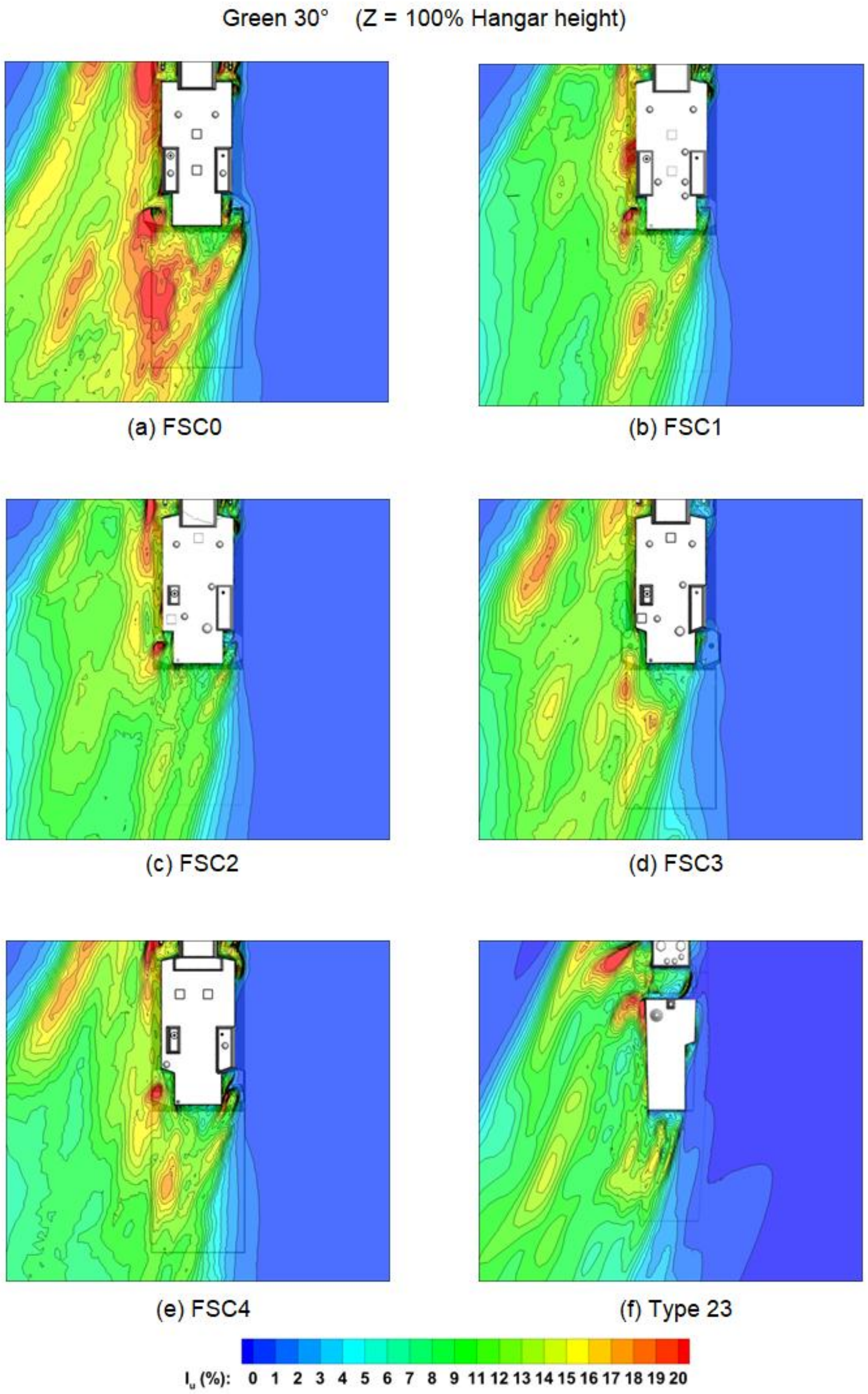

(a) FSC0

(b) FSC1

(c) FSC2

(d) FSC3

(e) FSC4

(f) Type 23

Figure 3.31 Longitudinal turbulence intensity contours at 100% hangar height

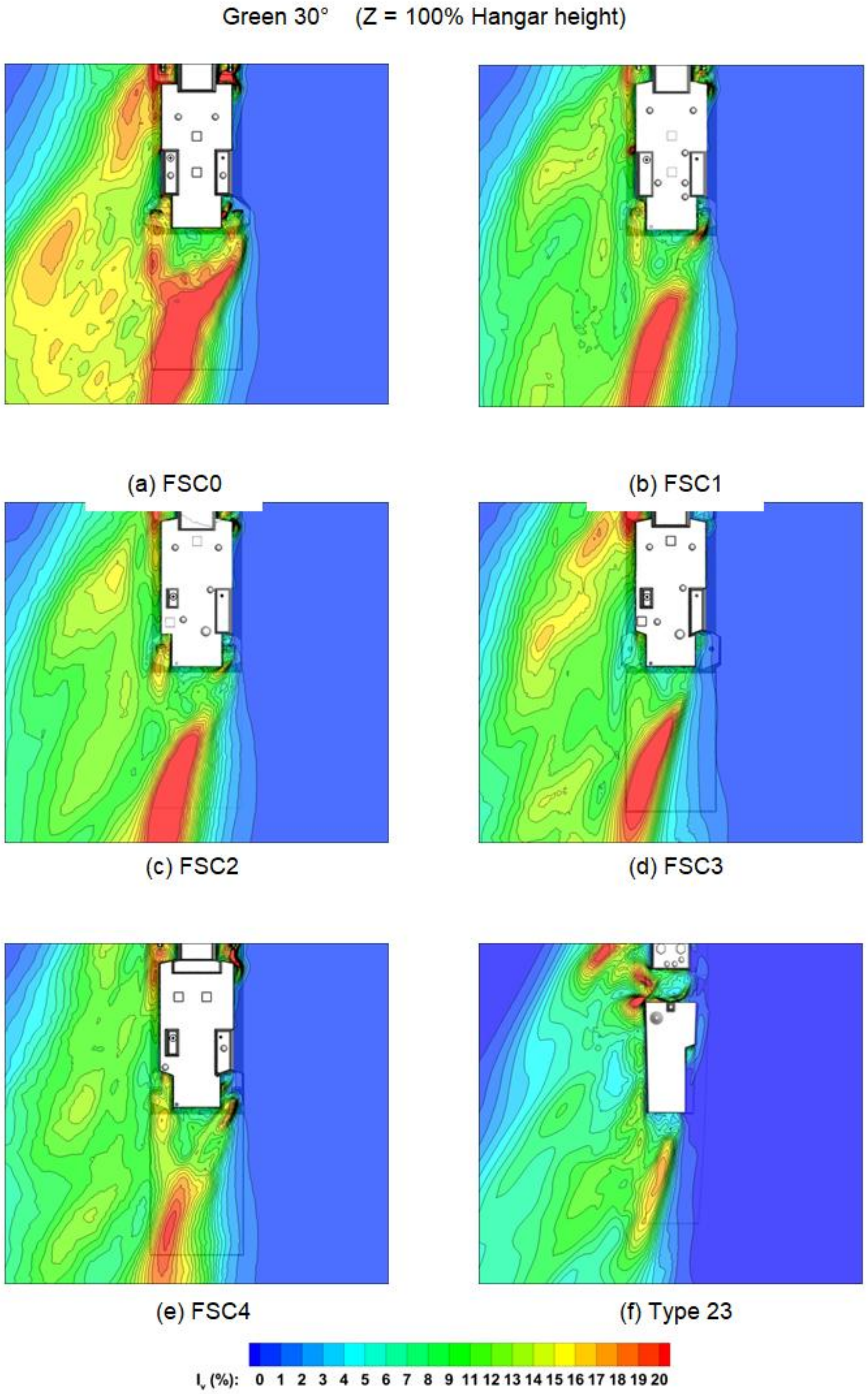

Green 30° (Z = 100% Hangar height)

(a) FSC0

(b) FSC1

(c) FSC2

(d) FSC3

(e) FSC4

(f) Type 23

Figure 3.32 Lateral turbulence intensity contours at 100% hangar height

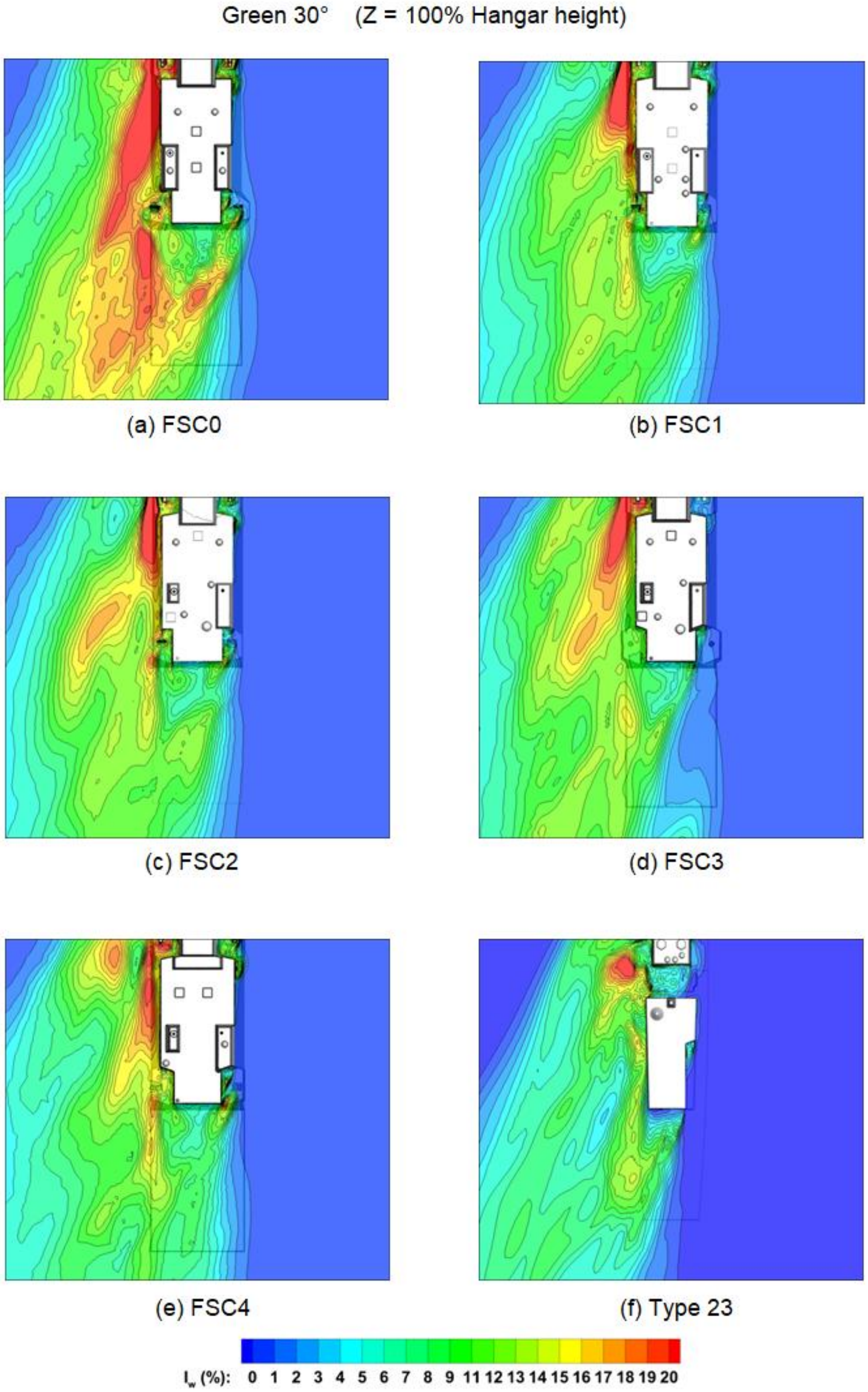

(a) FSC0

(b) FSC1

(c) FSC2

(d) FSC3

(e) FSC4

(f) Type 23

Figure 3.33 Vertical turbulence intensity contours at 100% hangar height

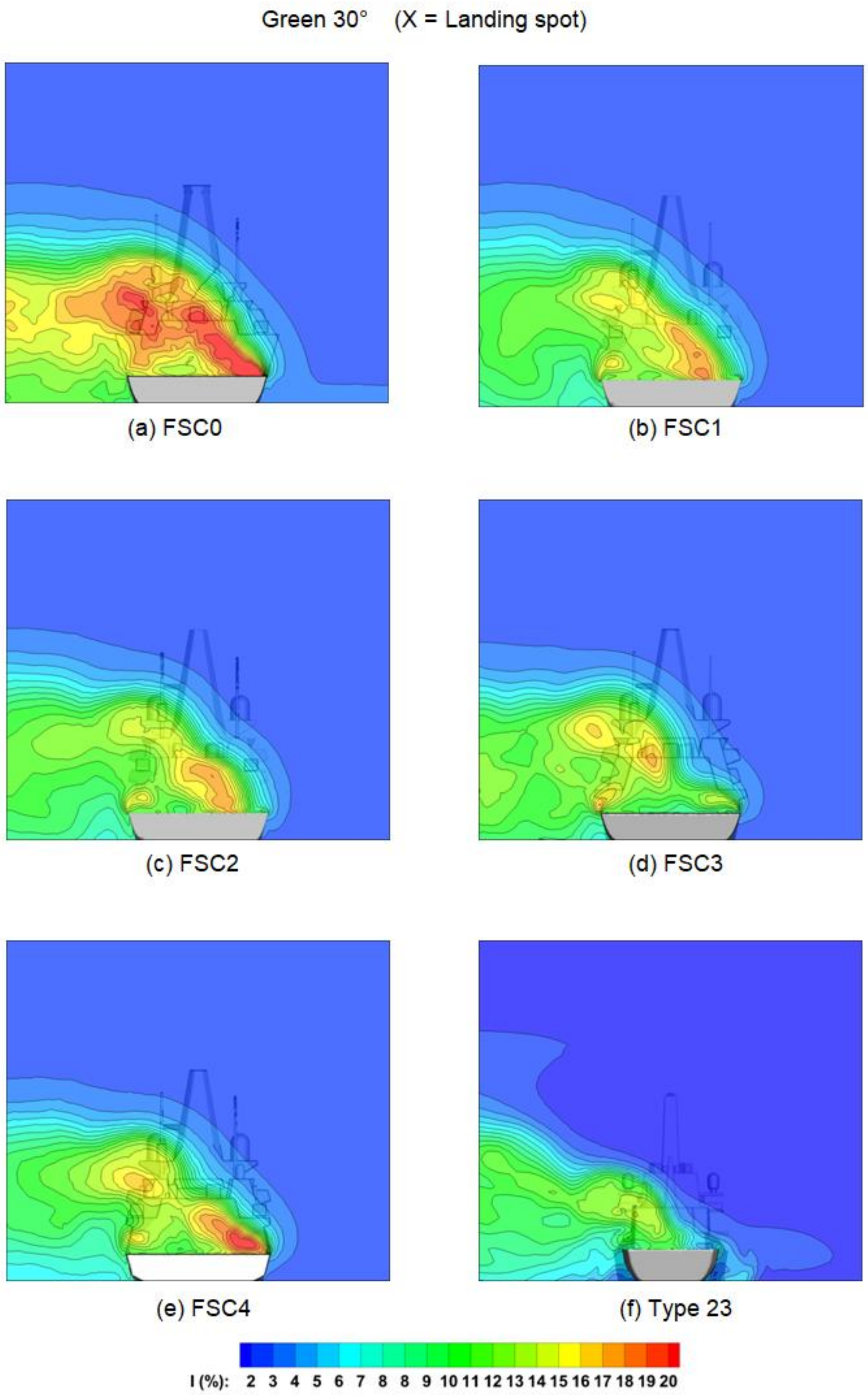

Figure 3.34 General turbulence intensity contours across landing spot

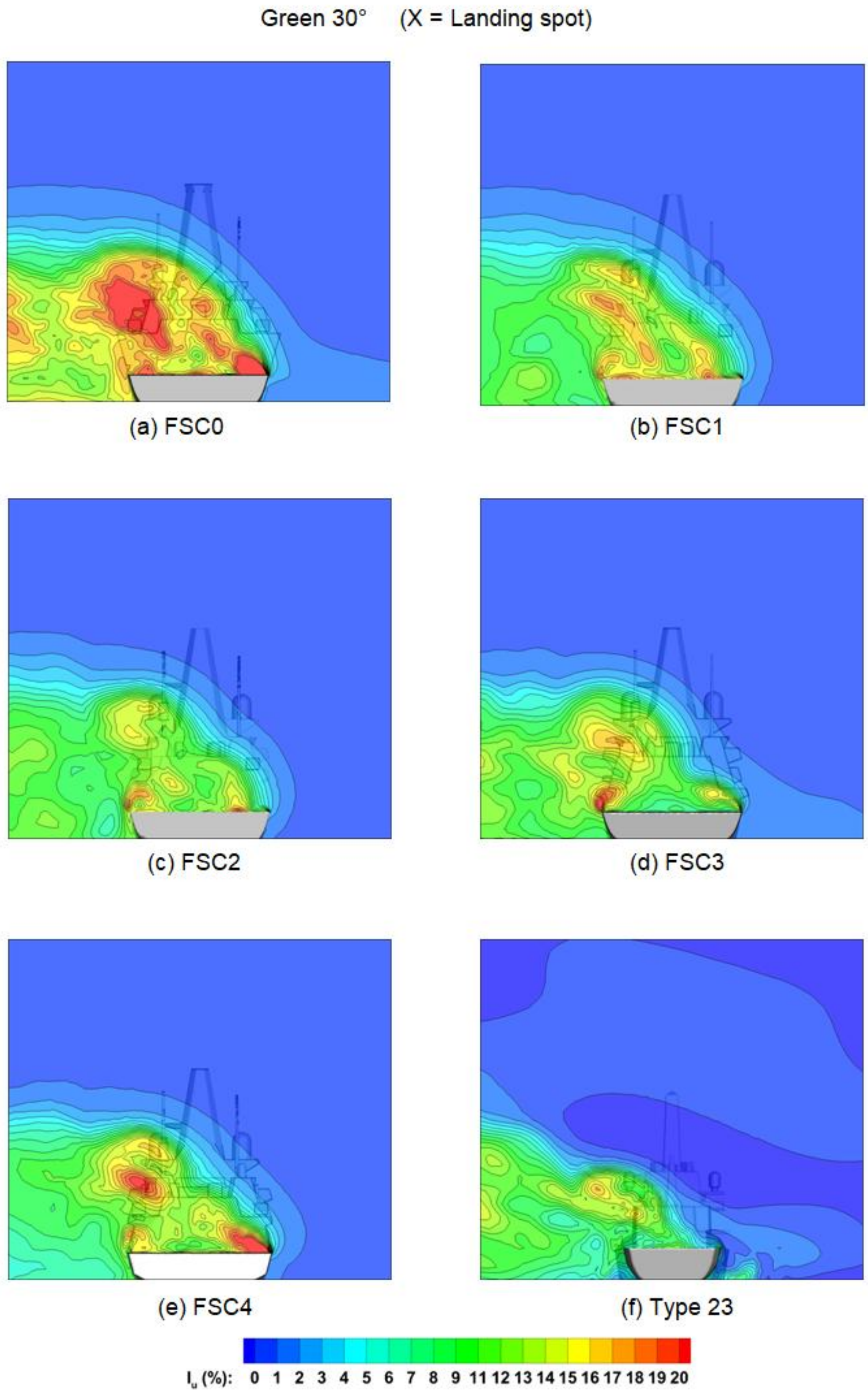

(a) FSC0 (b) FSC1

(c) FSC2 (d) FSC3

(e) FSC4 (f) Type 23

Figure 3.35 Longitudinal turbulence intensity contours across landing spot

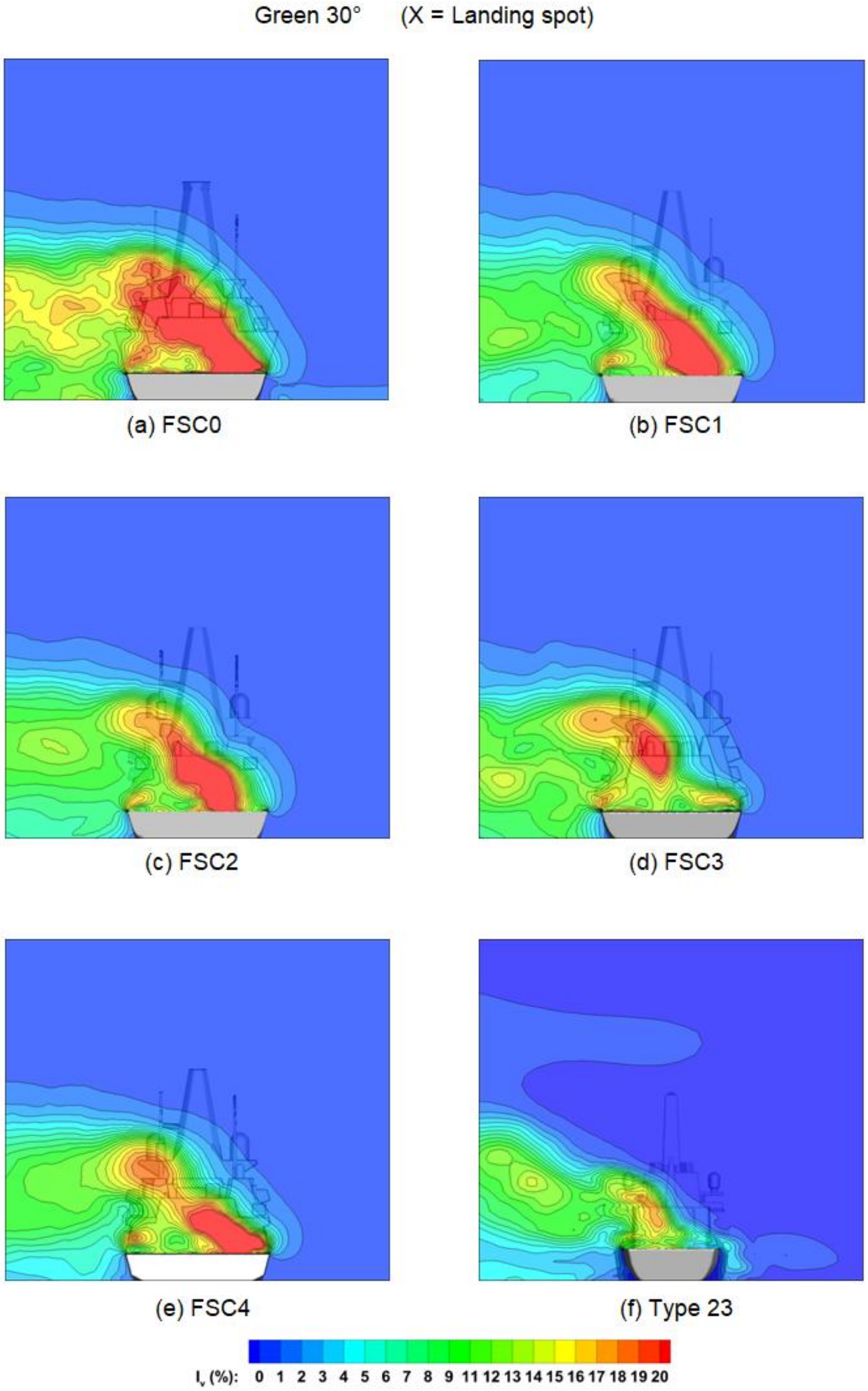

Figure 3.36 Lateral turbulence intensity contours across landing spot

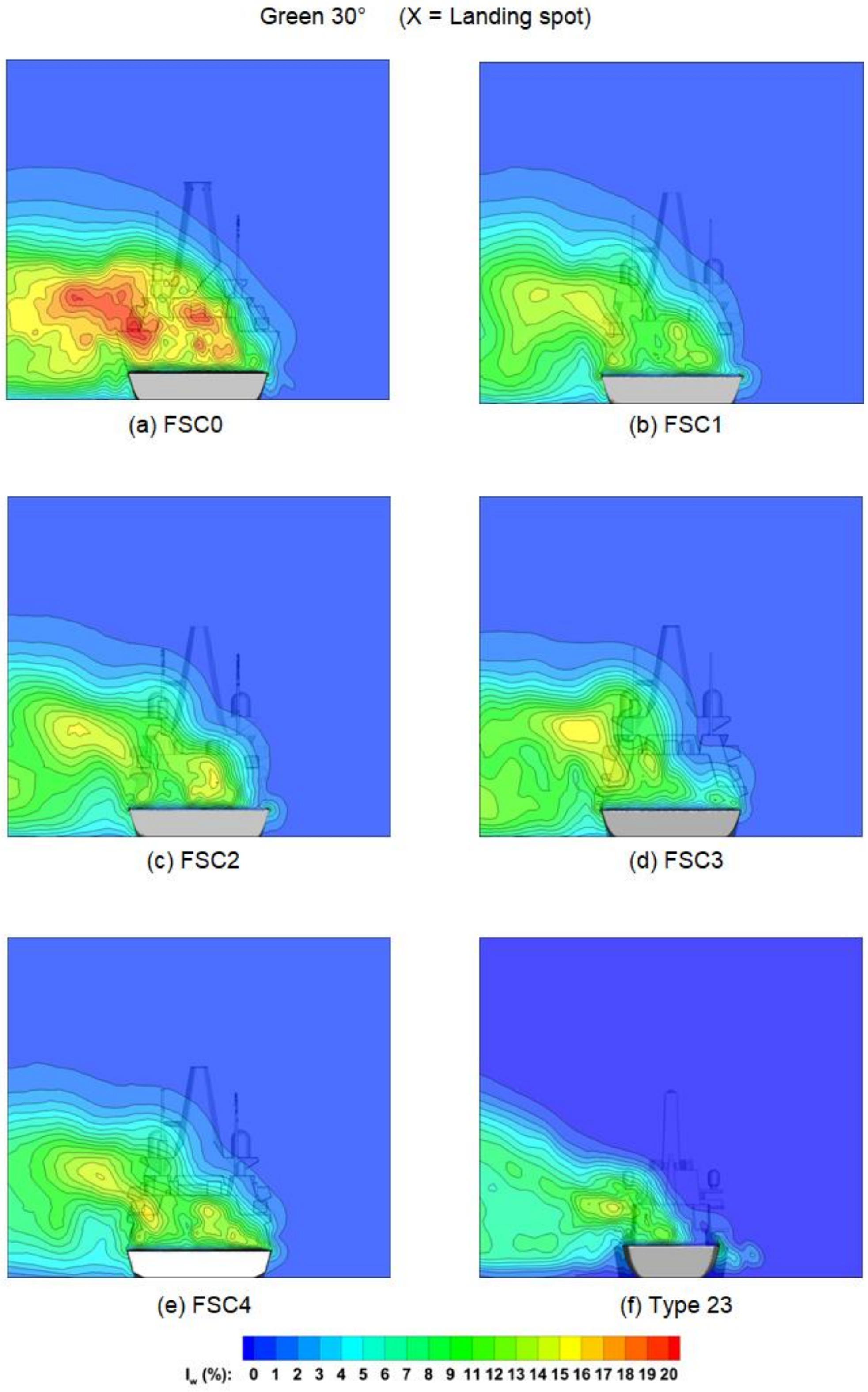

(a) FSC0

(b) FSC1

(c) FSC2

(d) FSC3

(e) FSC4

(f) Type 23

Figure 3.37 Vertical turbulence intensity contours across landing spot

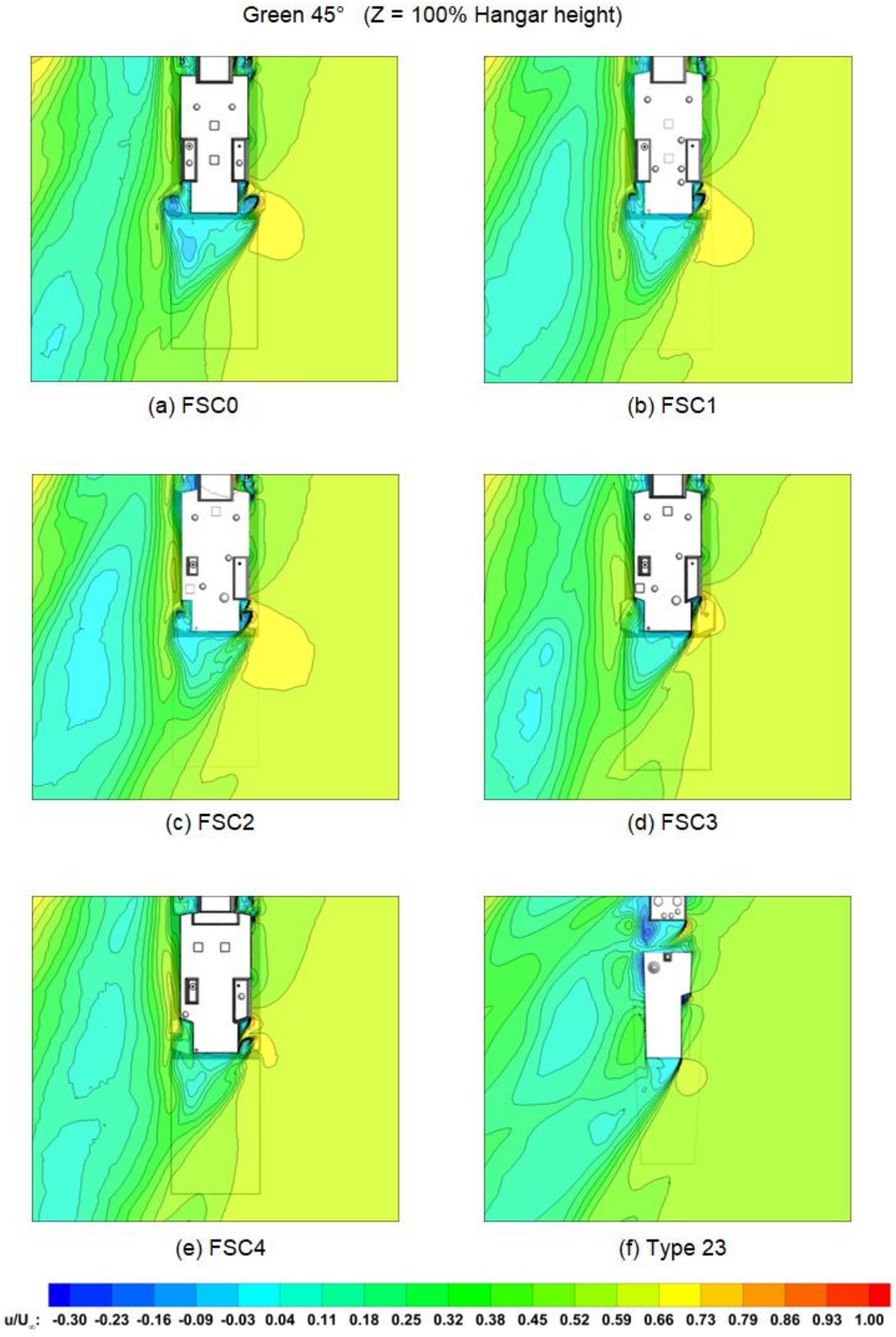

(a) FSC0

(b) FSC1

(c) FSC2

(d) FSC3

(e) FSC4

(f) Type 23

Figure 3.38 Mean longitudinal velocity contours at 100% hangar height

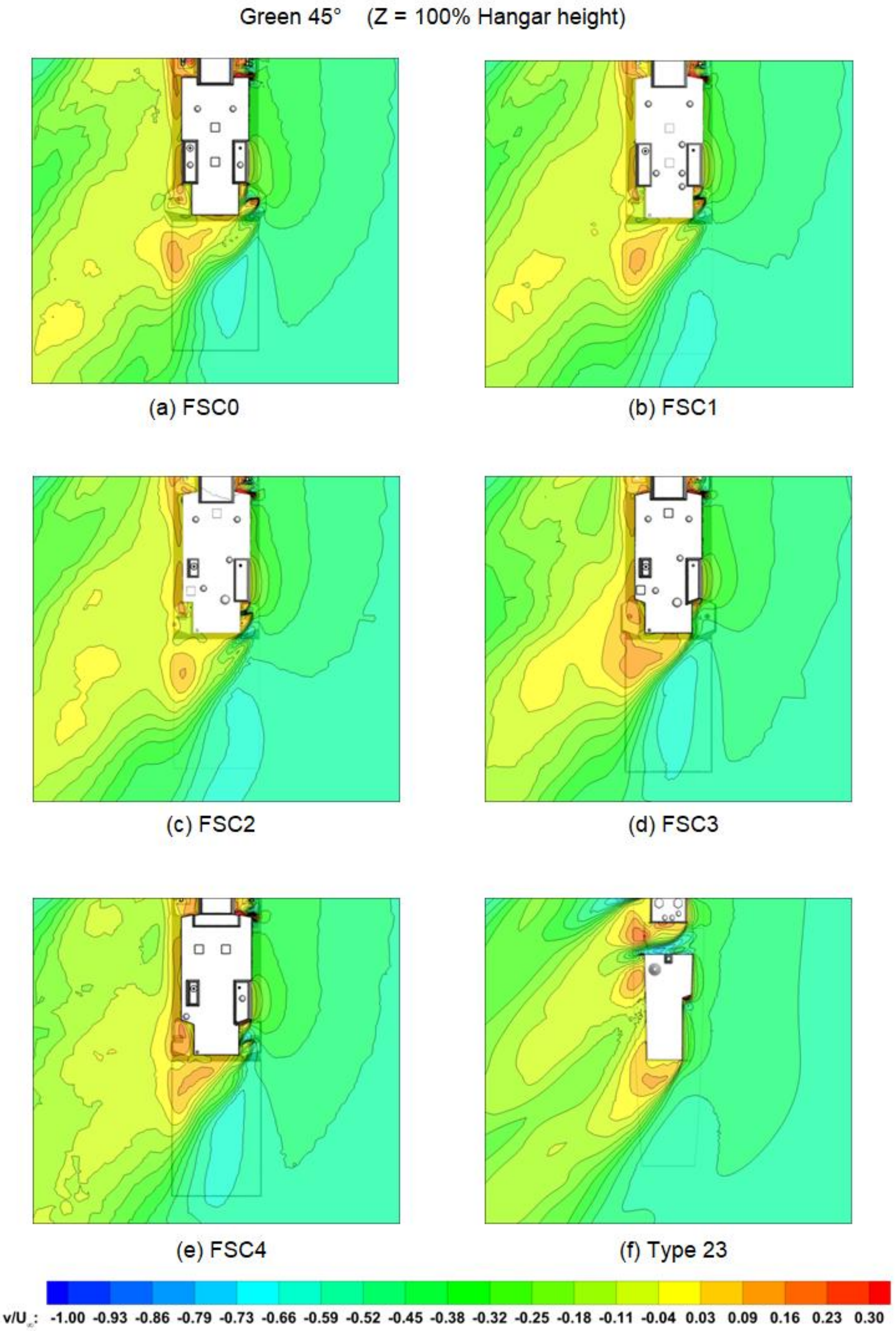

(a) FSC0

(b) FSC1

(c) FSC2

(d) FSC3

(e) FSC4

(f) Type 23

Figure 3.39 Mean lateral velocity contours at 100% hangar height

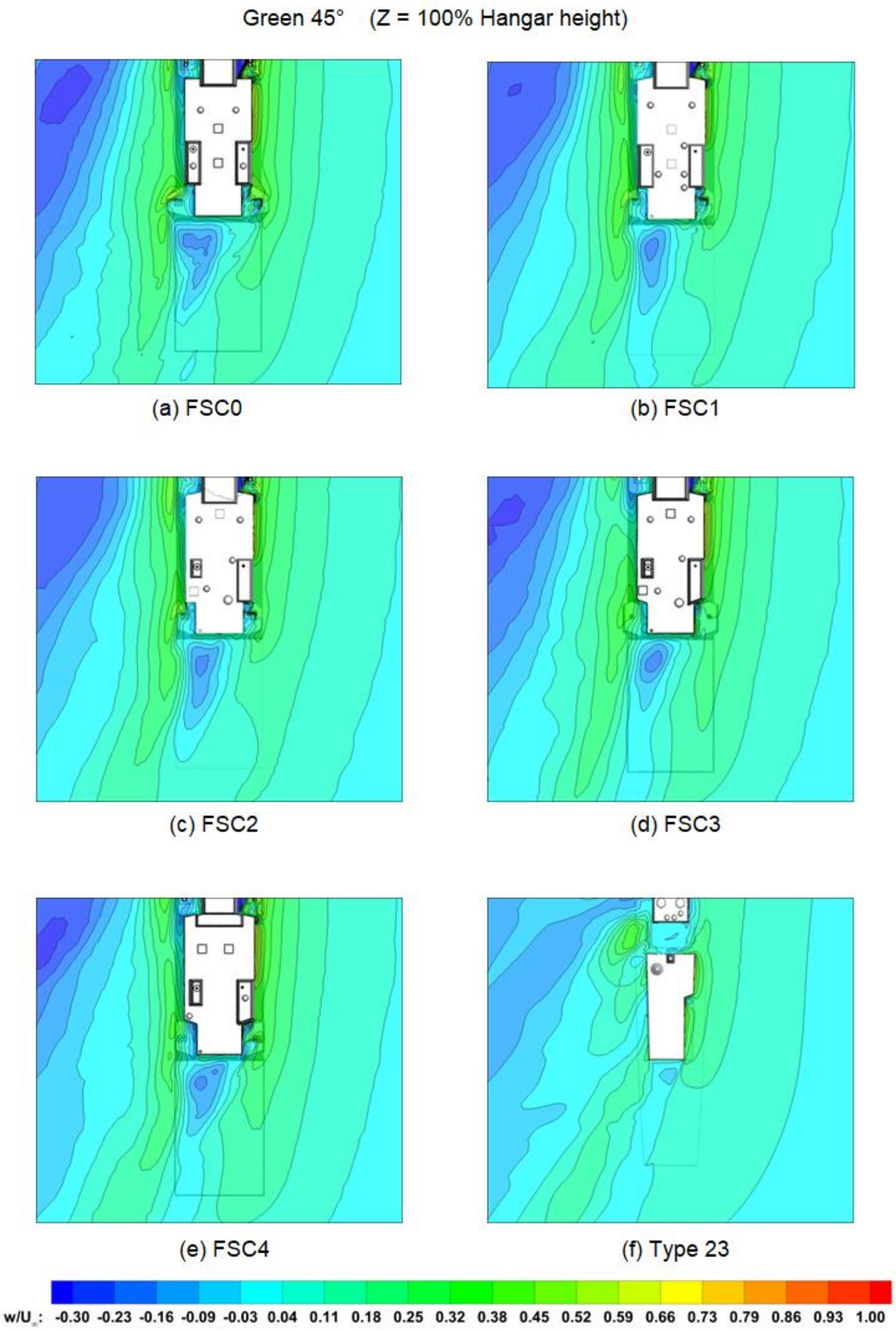

(a) FSC0

(b) FSC1

(c) FSC2

(d) FSC3

(e) FSC4

(f) Type 23

Figure 3.40 Mean vertical velocity contours at 100% hangar height

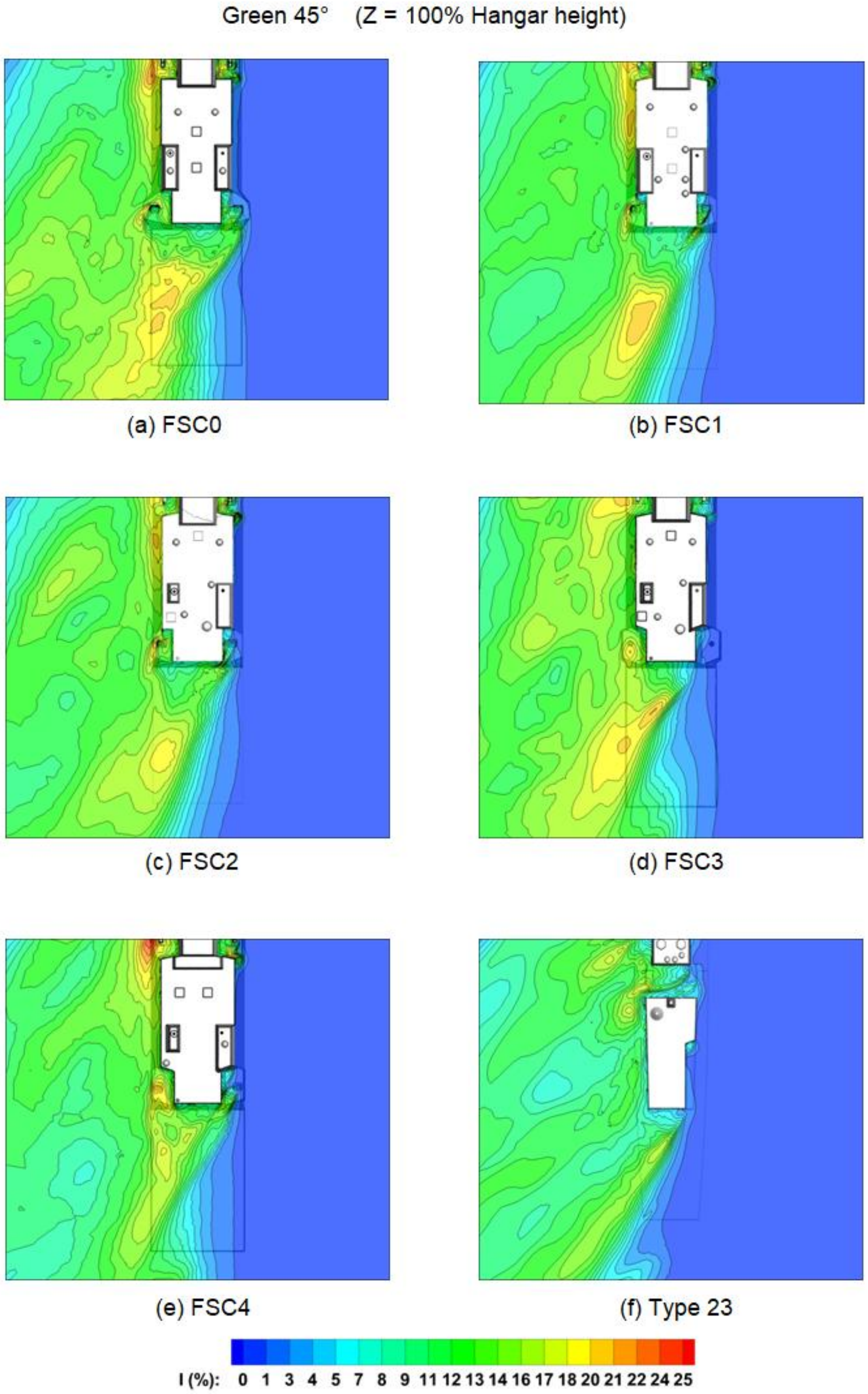

Figure 3.41 General turbulence intensity contours at 100% hangar height

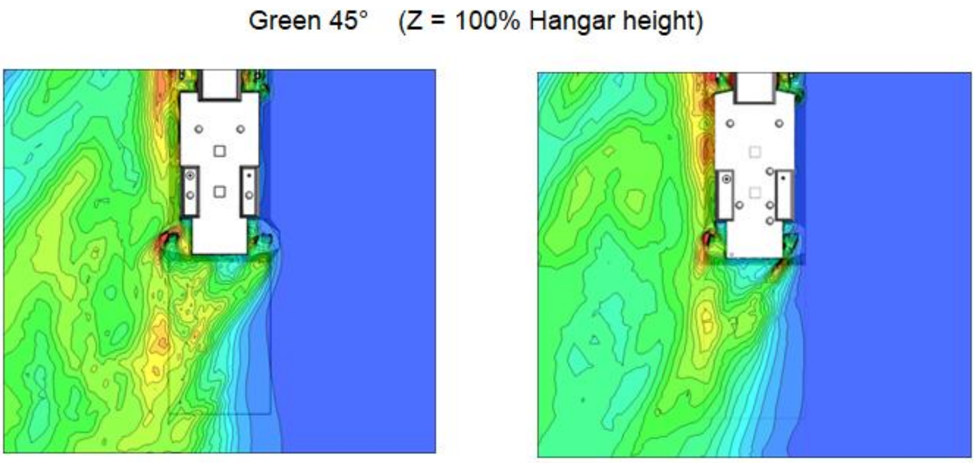

(a) FSC0

(b) FSC1

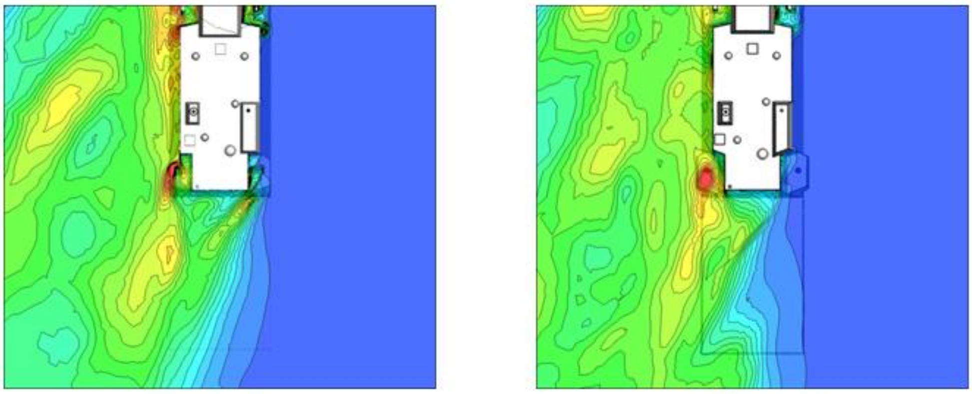

(c) FSC2

(d) FSC3

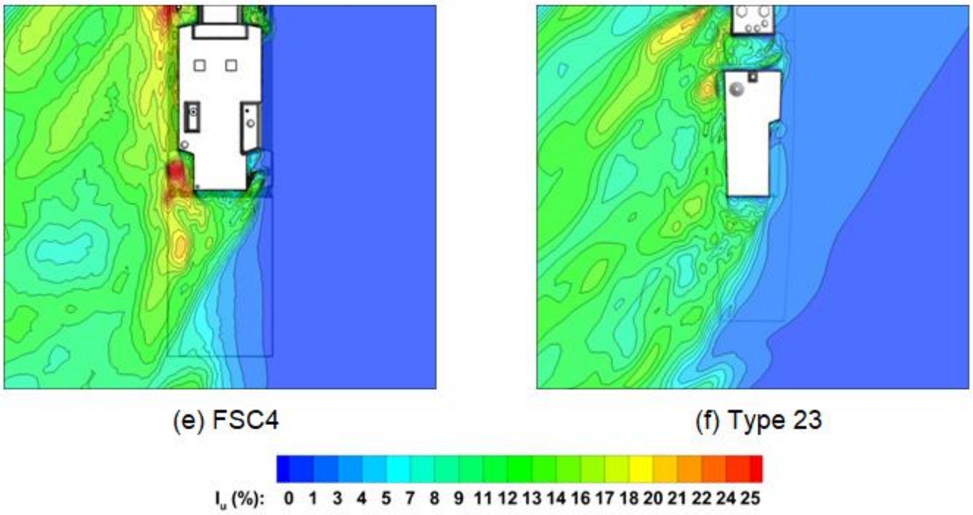

(e) FSC4

(f) Type 23

Figure 3.42 Longitudinal turbulence intensity contours at 100% hangar height

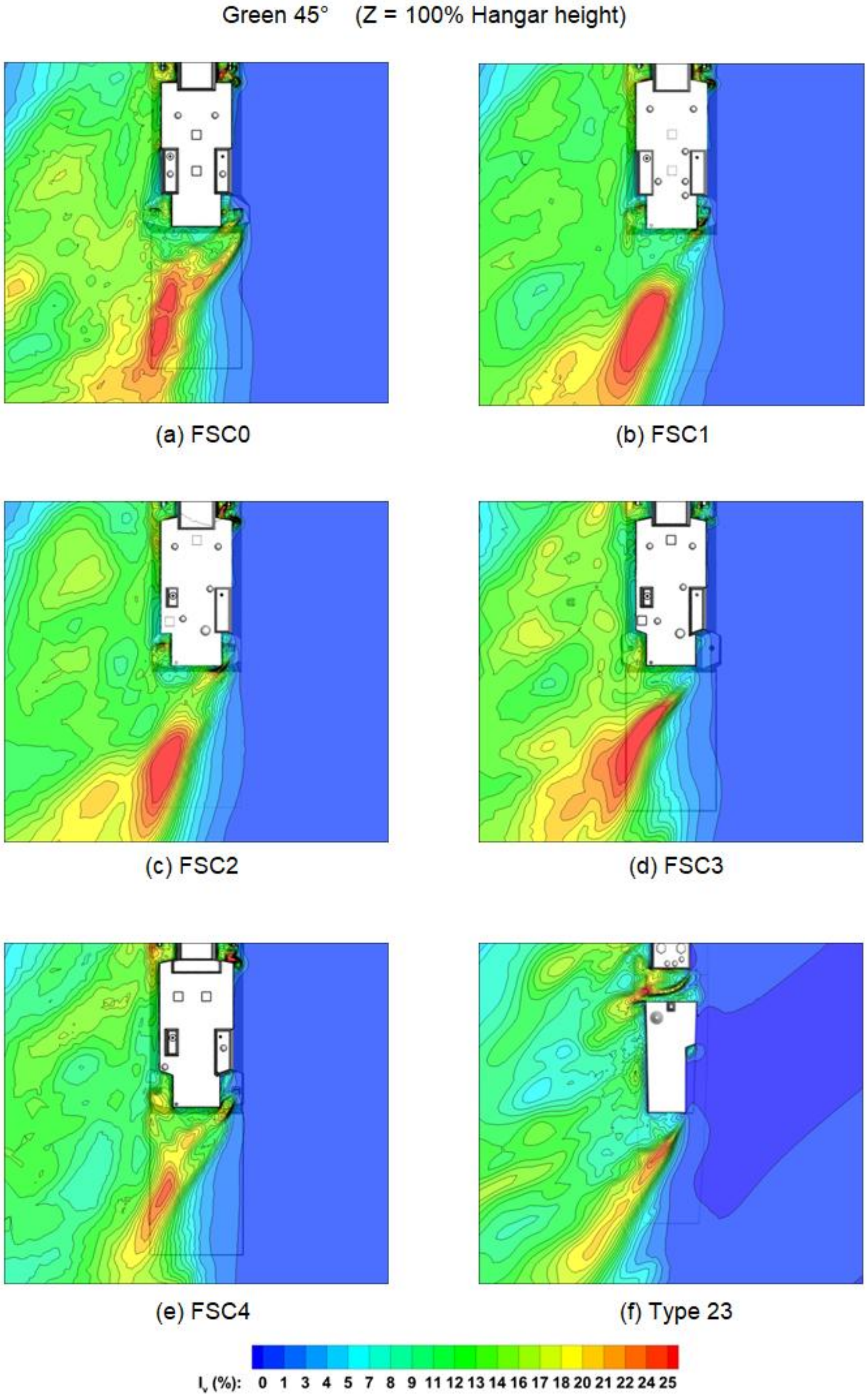

Figure 3.43 Lateral turbulence intensity contours at 100% hangar height

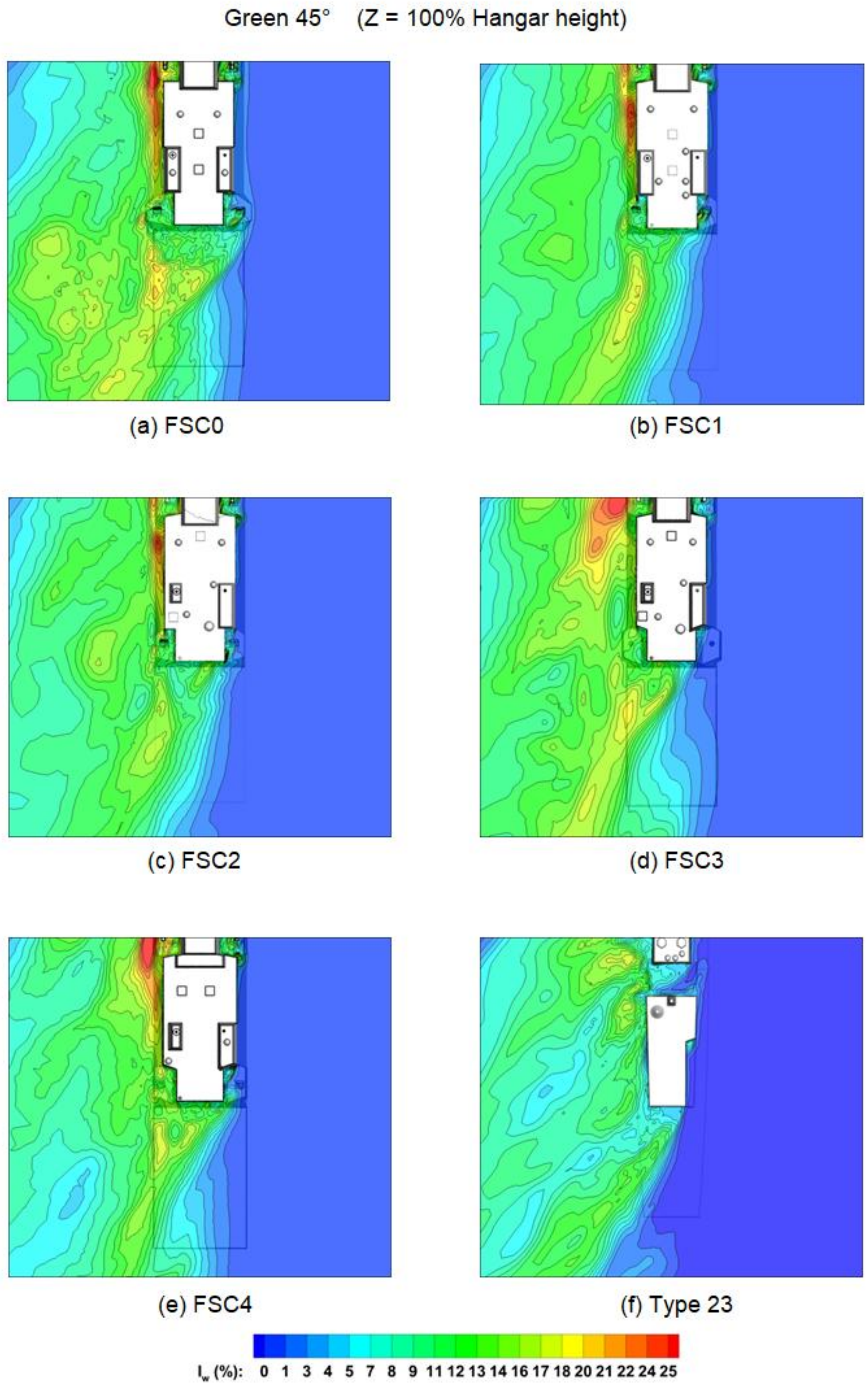

(a) FSC0 (b) FSC1

(c) FSC2 (d) FSC3

(e) FSC4 (f) Type 23

Figure 3.44 Vertical turbulence intensity contours at 100% hangar height

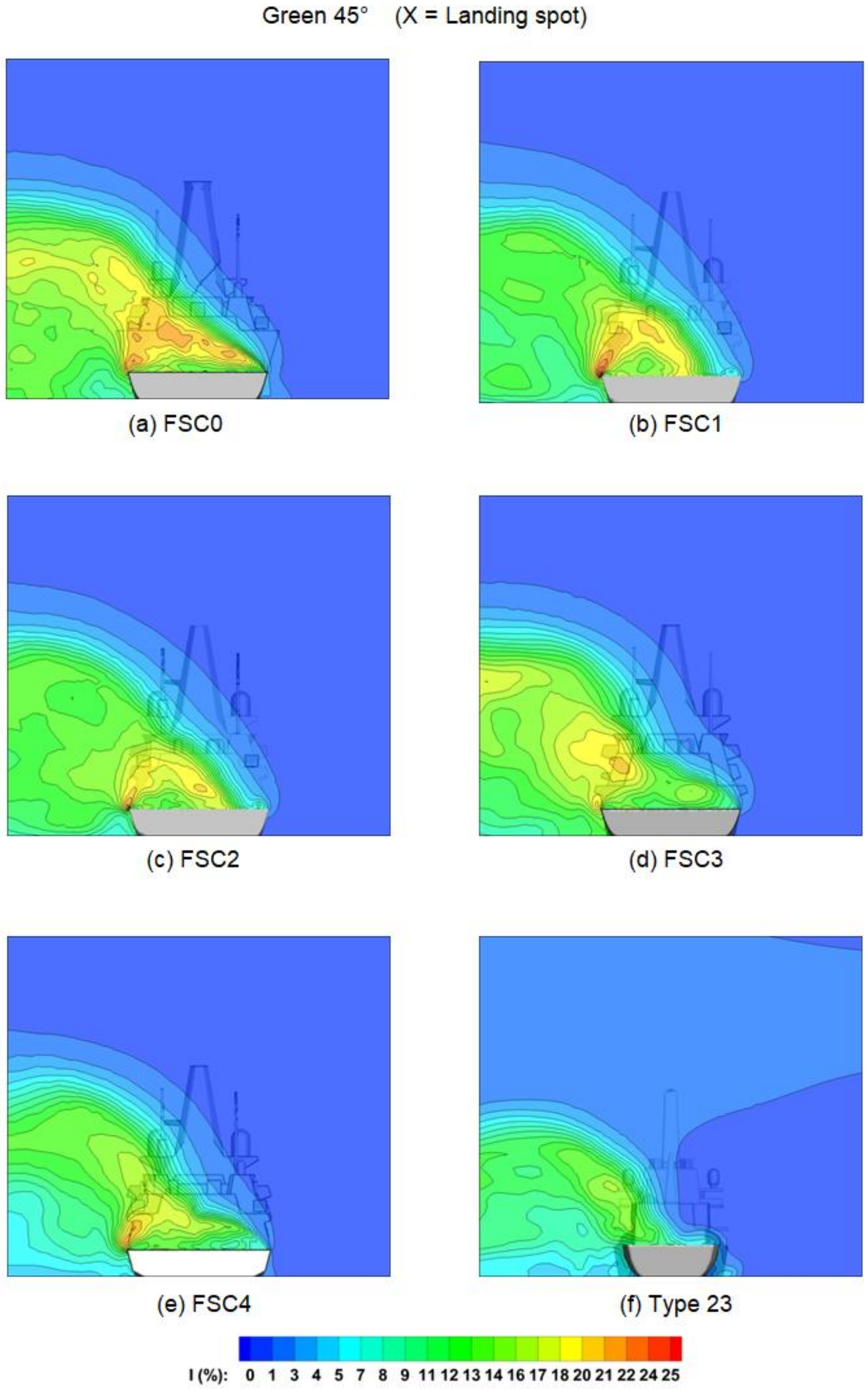

(a) FSC0 (b) FSC1

(c) FSC2 (d) FSC3

(e) FSC4 (f) Type 23

Figure 3.45 General turbulence intensity contours across landing spot

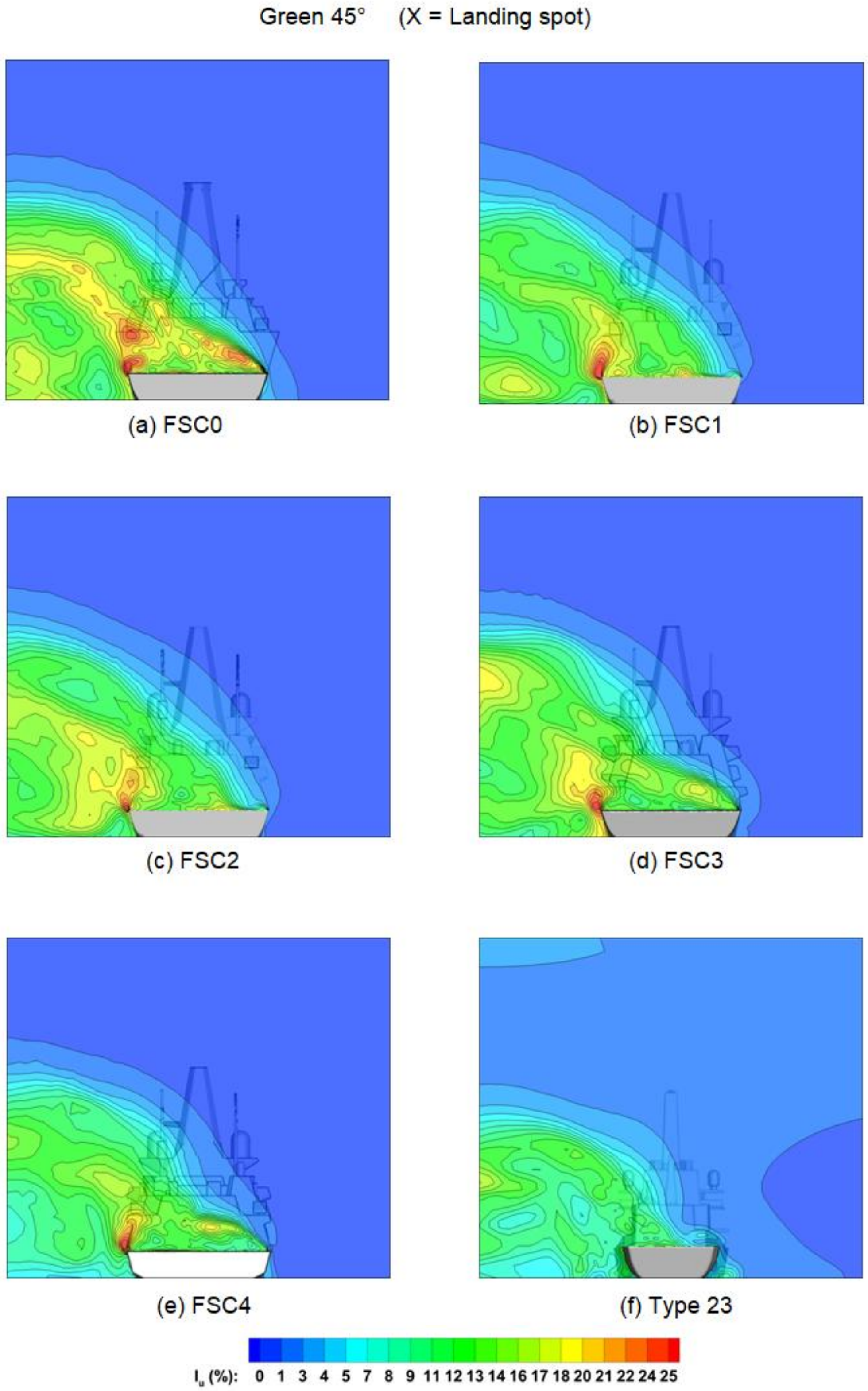

Figure 3.46 Longitudinal turbulence intensity contours across landing spot

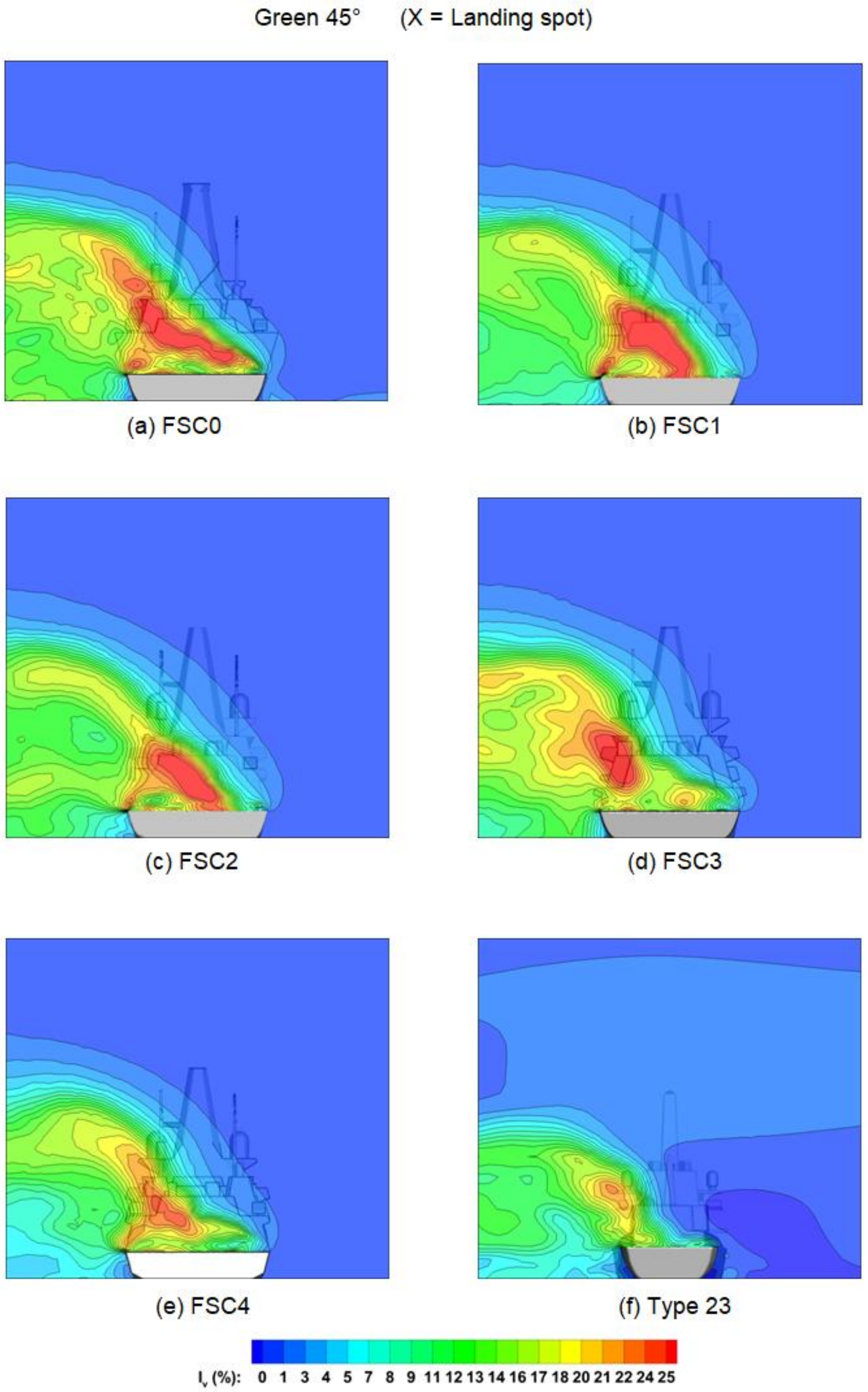

(a) FSC0

(b) FSC1

(c) FSC2

(d) FSC3

(e) FSC4

(f) Type 23

Figure 3.47 Lateral turbulence intensity contours across landing spot

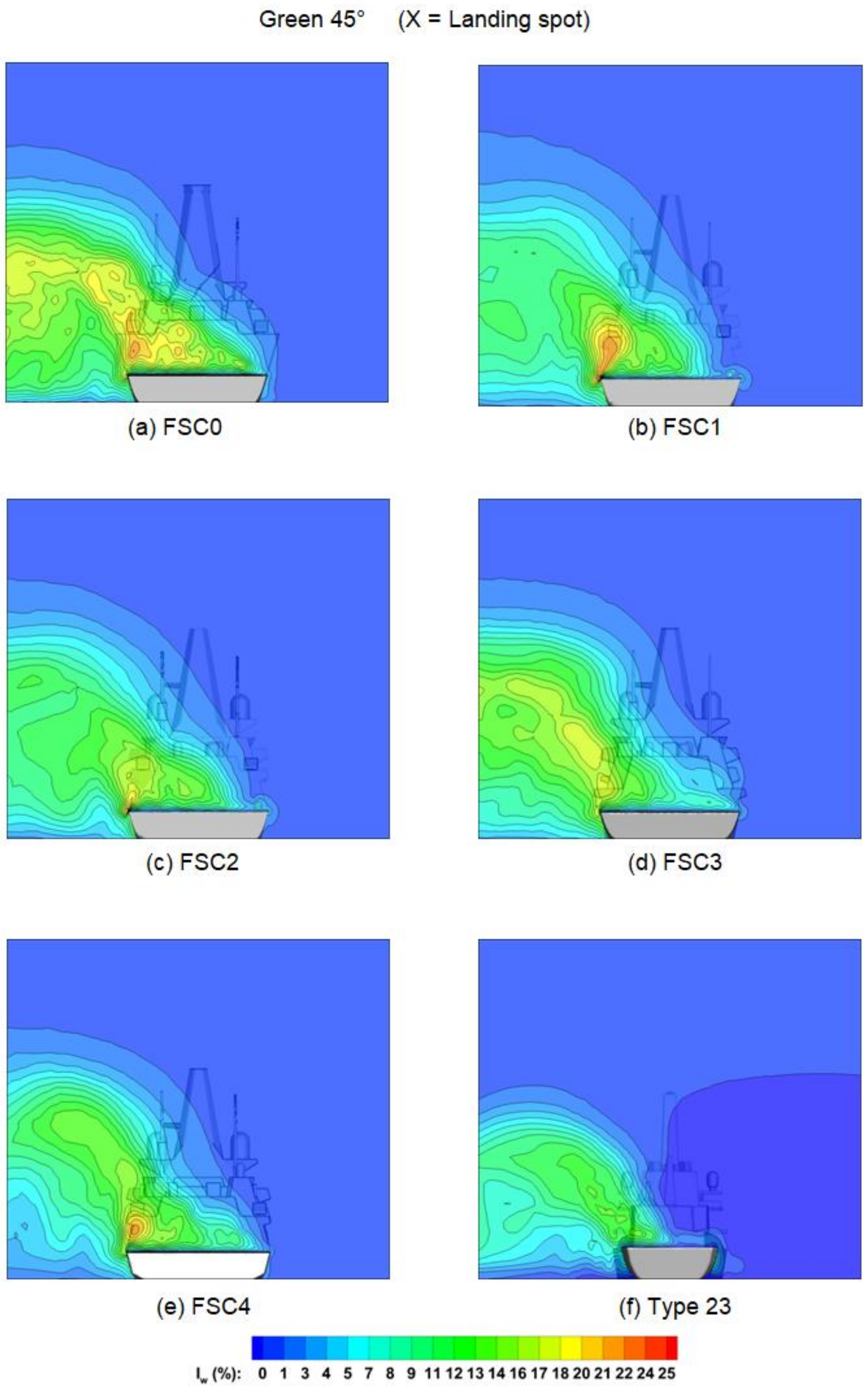

(a) FSC0

(b) FSC1

(c) FSC2

(d) FSC3

(e) FSC4

(f) Type 23

Figure 3.48 Vertical turbulence intensity contours across landing spot

CHAPTER 4

IMPACT OF SHIP SIZE ON MARITIME HELICOPTER OPERATIONS

In Chapter 2 it was described how airwakes for a given ship and a given wind angle can be computed at one wind speed and then scaled to different wind speeds through geometric and dynamic similarity, thereby reducing the effort required to generate the airwakes. In this chapter this concept is explored more fully and extended to consider airwake scaling for different size ships. The chapter will demonstrate how different size ships affect not only the airwakes, but also the loads imparted to the helicopter and the workload ratings awarded by the pilot for precision hover tasks and for the overall landing mission. Finally, different ship sizes will also have different motion for a given sea state, so a series of simulated deck landings were conducted in which the ship motion was realistic for the ship size, and the pilot had to contend with both the deck motion and the airwake characteristics of the different size ships.

4.1 Introduction

Using piloted flight simulation, Forrest et al [5] compared the simulated SHOLs of the UK's Type 23 naval frigate and the Wave class tanker. It was found that although the tanker has a much larger deck area, it had a more restricted SHOL than the Type 23 frigate due to the larger turbulent flow structures shed by the larger superstructure. The increased energy contained within the turbulent flow of the tanker in turn increased the level of pilot workload. Although the two ships were substantially different in shape, the conclusion was that larger ships created more problematic airwakes. The relative sizes of the two ships, and the heights of their landing decks above the water, can be seen in Fig. 4.1.

Building on this conclusion, the study reported in this chapter has investigated the effect of ship size on the airwake over the deck, and its impact on the helicopter and on pilot workload during a landing task; three geometrically similar ships of different sizes have been used. As indicated above, the airwake from the larger ship can be expected to provide greater disturbances to the aircraft, but the larger deck may be easier to land to. While a destroyer or frigate may have a typical length of 150m, the length of a helicopter-enabled patrol vessel may only be half of that. For example, HMS Clyde, a British River-class patrol vessel is 82m long, and its helicopter deck, which is just 24m in length and 13m wide, is designed to accommodate a 23m long AW 101 Merlin helicopter. A graphic of HMS Clyde with a Merlin Helicopter on the flight deck is shown in Fig. 4.2 [56].The small size introduces further challenges to pilots in that they are often required to operate much closer to the superstructure of the ship during launch and recovery than would be expected on a larger ship.

As described previously, producing unsteady full-scale CFD simulations of the ship airwake is extremely computationally expensive and time consuming, taking several days to compute the unsteady data required for implementation within flight modelling software. The following sections therefore explore the effectiveness of scaling airwakes for given wind directions and ship geometry for both wind speed and ship size. If the methodology is demonstrated to be valid then this significantly reduces the number of airwakes that need to be computed by CFD. Following this, the airwakes will then be used to investigate the effect of ship size on helicopter aerodynamic loads using the Virtual AirDyn described earlier in Chapter 3. Pilot workload when landing or hovering over the deck has also been explored using the HELIFLIGHT-R simulator; first with the same ship motion applied to the three ships, to isolate the effect of the different airwakes, and then including ship-specific motion to include the effect of ship size on both airwake and deck motion.

4.2 Ship Airwake Scaling

To investigate the aerodynamic effect of ship size, a generic ship model was created to be representative of a modern, single-spot naval frigate of 150m length and 20m beam. This ship model was then scaled up and down to create two further ship models that were 200m and 100m in length, Fig. 4.3. The airwakes for each of these three ship sizes were used to provide comparative data to (i) demonstrate the feasibility of Strouhal-scaling the airwake, and (ii) to investigate the consequences of a change in size on helicopter loads and pilot workload during a hover task and a complete deck landing. The ship model is different to the FSC used in Chapter 3, and is similar to the Daring class Type 45 destroyer (shown in the next chapter in Fig. 5.1).

The scaling of airwake data involves the use of the Strouhal number, shown below in Equation 4.1. The vortices shed from bluff bodies within a flow are created at distinct frequencies which can be described by the Strouhal Number (Reynolds number dependence is acknowledged, but is known to be less important at high values and for sharp-edged bodies). Strouhal number relates the characteristic length of a bluff body, l, the flow speed, v, and the frequency, f, of the vortices shed from the body. This simple relationship shows that for an increase in free stream speed there will be a proportional increase in shedding frequency, and for an increase in length scale there will be a proportional decrease in frequency. While this may be obvious for vortex shedding at a single frequency from a bluff body with a single characteristic length, the principle can also be extended to more complex shedding from the multiple bluff bodies that make up a ship's superstructure. To find the frequencies of the eddies being shed from the hangar, a point located in the region over the flight deck, at approximately hangar height was sampled during the CFD simulation to provide unsteady velocity data. This data was then used to find the dominant frequencies of the shedding vortices through use of a Fast Fourier Transformation, as illustrated in Fig. 4.4.

$$\mathrm{St} = \frac{\mathrm{f\,l}}{\mathrm{v}} \tag{4.1}$$

The scaling of airwakes in terms of velocity magnitude has been previously carried out by Polsky [57] who showed that the linear scaling of the airwake magnitude was possible. Further observations by Zan [58] noted that the airwake should be shifted in frequency content as well as the velocity magnitude due to the large scale turbulent structures within the ship airwake which are the result of flow separation, which in turn are dependent on the flow speed and ship size. In order to use Strouhal scaling to modify the airwake data, for example to change the airwake in terms of velocity magnitude from a free stream of 40 knots to 20 knots, the velocity components and frequency spectra are simply halved. Using this approach, Hodge et al [4] showed that the Strouhal scaling of CFD airwake data from 40 to 30 knots, in both frequency and velocity magnitude, gave good results when compared to a computed 30 knot airwake.

There is, however, an additional consideration when scaling for ship size. Adding an Atmospheric Boundary Layer (ABL) has been shown to be important for creating the correct airwake, but to obtain complete dynamic similarity between the flows over the three ship sizes, the inlet velocity profile should also be scaled. However, scaling the ABL is not realistic as it does not change with ship size. Therefore, to explore the effect of applying the same ABL to the three ship sizes, airwakes were also computed for a uniform inflow (i.e. no ABL) so achieving the correct conditions for dynamic similarity between the three cases.

The method of computing the airwakes was that which has been described earlier in Chapter 2. For this part of the study airwakes were computed for a Headwind and Green 45° WOD conditions. These airwakes were first scaled for different wind speeds, to confirm previous work, and then for different ship sizes. The airwakes were also implemented in the Virtual AirDyn (VAD) to evaluate the unsteady loads on the helicopter, and in the HELIFLIGHT-R simulator to evaluate pilot workload. Table 4.1 presents the WOD conditions for which CFD data was generated for the analyses discussed below.

Table 4.1 Matrix of CFD simulation conditions

Azimuth	Speed	Boundary Condition
Green 45°	30 Knots	ABL
Green 45°	40 Knots	ABL
Green 45°	40 Knots	UBL
Headwind	30 Knots	ABL
Headwind	40 Knots	ABL
Headwind	40 Knots	UBL

4.2.1 Airwake Scaling by Velocity Magnitude

Whilst previous studies have shown that velocity scaling was viable for a Simple Frigate Shape (SFS) [4], the geometry for the ship model used in this study, Fig. 4.3, has an increased level of complexity over that of the SFS. Therefore, the validation of the Strouhal scaling method was first carried out using the mid-scale ship geometry of Fig. 4.3 at anemometer wind speeds of 40 knots and 30 knots in a Headwind WOD. The computed 40 knot data was then scaled down to 30 knots in both velocity magnitude and frequency.

An example of the resulting unsteady velocity fluctuations above the landing spot at hangar height can be seen in Fig. 4.5. The scaled 30 knot case shows similar overall magnitudes to the computed 30 knot data with similar peak values. However, the resulting unsteady data in this form makes it difficult to draw any meaningful comparisons, thus the power spectral densities for each of the three cases for the

Headwind WOD are shown in Fig. 4.6 to allow a more comprehensive comparison between the airwake data sets.

As expected, the 40 knot data shows an increase in turbulent energy over the computed and scaled 30 knot cases, as indicated by the increased RMS value of 11.42 m/s for the 40 knot case, in comparison to the very similar values of 8.80 m.s^{-1} and 8.79 m.s^{-1} for the 30 knot and scaled 30 knot cases respectively. The RMS values were calculated in the normal way for determining the turbulence at a point in a flow. Overall the scaled 30 knot data shows good agreement with the computed 30 knot CFD data, showing that for complex ship geometries Strouhal scaling on velocity still holds.

4.2.2 Airwake Scaling on Characteristic Length (Ship Size)

Having confirmed the velocity spectra scaling based on a characteristic velocity, the next step was to demonstrate the scaling of velocity spectra based on characteristic length, or ship size. As before, the velocity PSD was extracted from the CFD at a point above the landing spot at hangar height, in both a Headwind and a Green 45° WOD. The airwakes were computed for the large and small ship, and then the velocity PSD for the large ship was scaled to represent the small ship; the computed and scaled PSDs were then compared to judge the effectiveness of the scaling.

Figure 4.7 shows the velocity data and scaling comparison for the case when the ABL was applied for a Headwind; the free stream velocity was 40 knots at the anemometer height. Despite the lack of dynamic similarity due to the ABL not being scaled, the scaling of the velocities from the large ship to the size of the small one does produce a reasonably representative velocity PSD.

In Fig. 4.8, the same comparison is made but this time with a uniform inlet velocity profile (UBL) of 40 knots, so that it matches the previous inlet velocity at anemometer height. By comparing Figs. 4.7 and 4.8 it can be seen that there are differences in the comparisons for the uniform and atmospheric profiles, but the magnitudes of the differences between the computed and scaled PSDs are similar. At this stage in the research it is not absolutely certain that airwakes including the ABL can be simply scaled between similar ships of different sizes to be used in flight simulation, but it looks promising.

Fig. 4.9 provides further evidence of the effectiveness of scaling the airwake for different sized ships when the ABL is included. In this case the airwake is in a Green 45 wind and the data is sampled over the port edge of the landing deck at hangar height, with the scaled spectra compare well with the computed spectra.

Overall this data suggests that Strouhal scaling is a feasible method to scale airwakes to account for changes in both ship size and velocity magnitude. The use of an ABL profile during the CFD simulation does not appear to preclude the use of airwake scaling.

4.3 VAD Analysis of Helicopter Loads for Different Ship Sizes

Using the methodology described earlier in Chapter 2, thirty seconds of unsteady airwake data was computed and interpolated onto a structured grid over the landing deck of the different sized ships. The helicopter was then held stationary at several positions along the translational approach from the port edge of the ship over the midpoint along the flight deck, with its hub at 100% hangar height, as shown earlier in Fig. 2.22.

The positions at which the helicopter is placed over the deck of the ship are normalised with the ship's beam width so that each sampling point is at the same position relative to the beam for each ship size tested. Point 3 lies directly over the centre of the deck with Points 1 and 5 over the deck edges, while Points 2 and 4 are equal to 0.25 of the beam width. Point 7 is located 1 beam width away from the centre of the ship, and Point 6 lies halfway between Point 7 and the port deck edge.

As described earlier, the FLIGHTLAB Generic Rotorcraft model used for this research was configured to be representative of the Sikorsky SH-60B Seahawk. The helicopter was initially trimmed under the freestream wind conditions away from any influence of the ship airwake. At each of the sampling locations over the ship, the helicopter was held stationary and the time histories of the unsteady moments and forces at the helicopter's centre of gravity were recorded over the full thirty seconds of airwake data. As the trimmed helicopter now experiences out-of-trim conditions, the forces acting on it are no longer in balance. The unsteady data was then time-averaged to provide the mean forces and moments acting on the helicopter at each of the seven test points.

The unsteady RMS forces and moments are produced using the method outlined by Wang et al [19], whereby the Power Spectral Densities of the signals are generated from the time histories given by the VAD, and the square root of the integral between the limits 0.2 to 2Hz is used to represent the Root Mean Square (RMS) loadings on the helicopter, as illustrated earlier in Fig. 2.24.. The frequency range of 0.2 to 2 Hz is used because this has the greatest influence on pilot workload [53].

The airwake that forms over the flight deck for the Headwind case is dominated by the separation that occurs from the hangar edges with a subsequent reattachment point approximately halfway along the deck. This occurs for all three ship scales due to the insensitivity of the flow over sharp-edged bluff bodies to the change in Reynolds Number. Figure 4.10 shows cross sectional contours of the mean, streamwise velocity over the flight deck for both the small-scale and large scale ships, showing the similarity of the flow between the two ship scales; the reverse flow in the recirculation zone can be seen in the two planes nearest to the hangar. The vertical velocity profile of the incoming ABL does not seem to have noticeably affected the velocity field between the small and large ships.

As the helicopter size is fixed and the aircraft follows the same translational path for each ship in terms of hangar height and distance from the hangar, the helicopter will be progressively shielded from the increasing freestream velocity away from the ship as its size increases. Figure 4.11 shows the relative size of the helicopter rotor as the ship size increases. Due to the helicopter being initially trimmed in a 40 knot freestream wind in ‘clean’ air outside of the ship’s airwake, the rotor disc, empennage and tail rotor will be providing the necessary thrust forces to remain stationary. However once the helicopter comes within the influence of the airwake, those thrust forces are no longer in balance due to changes in the inflow angle of the rotor, the change in the fuselage drag and the flow through the tail rotor, for example. These changes can in turn affect the torque required to hold the helicopter in position and the thrust required to maintain altitude, giving rise to changes in body forces and moments about the aircraft’s centre of gravity. It can also be seen in Fig. 4.11 that the lateral turbulence levels at hangar height increase slightly with ship size, possible showing some effect of the ABL.

Figures 4.12 and 4.13 show the results from the VAD; the general form of the plots was described earlier in Chapter 3. Figure 4.13 shows a comparison of the mean forces generated by the VAD analysis for the Headwind WOD case. While all three ship scales show broadly similar trends as the helicopter passes through the airwake, there are notable differences in the loads imposed by the larger ship airwakes. For example the unbalanced longitudinal force (F_x) on the helicopter can be seen to rise with a decrease in ship scale. This is due to more of the aircraft being exposed to the influence of the airwake as the helicopter gets proportionally larger and is less sheltered by the hangar. Also when off the port side at Point 7, some of the helicopter's rotor disc will be passing over the flight deck of the smaller ship as can be seen in Fig. 4.11.

Over the landing spot, at Point 3, the mean forces generated along the vertical axis (F_z) shown in Figure 4.12 suggest that as the ship scale increases, the thrust deficit increases due to the stronger downdraught from the large ship's hangar affecting a larger portion of the rotor disc.

The lateral turbulence intensity contours at 100% hangar height for all three ship scales, Figure 4.11, show that although the areas of turbulence are not greatly dissimilar, because of the increasing relative size of the helicopter, the total turbulence seen at the rotor disc will vary greatly, as will that experienced by the fuselage and tail rotor. Looking at Figure 4.13, showing the comparison of RMS forces and moments generated by the turbulent flow, each ship size shows similar trends in the longitudinal and lateral components up until Point 5, which lies over the Port edge of the ship. At this point, half of the rotor disc lies directly within the lee of the hangar where the difference in the magnitude of the vortices created by the change in ship size gives rise to the change in RMS forces. As expected, the larger vortical structures of the larger ship contain more energy and are shed at a reduced frequency, so generating greater unsteady aerodynamic loads on the aircraft than does the small-scale ship.

4.4 Piloted Flight Simulation for Different Size Ships with Equal Ship Motion

While the VAD analysis can show how the airwakes of the larger ships affect the mean and unsteady loads on the helicopter, and it can be deduced that higher RMS values equate with greater pilot workload, there may not be a direct correlation. Therefore the investigation progressed to using full-motion piloted flight simulation with a point of interest being whether the more benign airwake of the small ship would be negated by the smaller deck and reduced space for manoeuvre. It was decided that, rather than include both scale-representative airwakes and ship motion in one step, the airwake effects would be investigated first with the different ships having the same displacements applied to their centres of gravity. This means that the vertical displacements at the decks of the large and small ships would be 1/3 greater and smaller than the 150m ship respectively; angular displacements in roll and pitch would be the same for the three ships. The motion was equivalent to sea state 3 for the medium size ship.

To re-emphasise the space restriction in the horizontal plane the rotor disc diameter is superimposed on CFD data in Fig. 4.14. As can be seen, the shear layer that is formed across the deck in a Green 45° WOD is larger and more turbulent for the larger ship, which can be expected to affect the unsteady loading on the helicopter. It is likely that as the wind approaches the starboard vertical edge of the hangar, the velocity at the top of the larger ship's hangar will be higher due to the ABL as the incoming velocity profile will not have been mixed as it will be by the ship's superstructure in the headwind; this will explain the higher turbulence intensity levels for the larger ship.

As part of the scaling investigation described in the previous sections, the Headwind and Green 45° airwakes were computed separately for each size of ship, and they were then scaled up and down from the computed velocity of 40 knots at the anemometer height to produce airwakes for a range of wind speeds.

The unsteady airwakes for each of the three ship sizes were therefore formatted and integrated into the FLIGHTLAB software, as described in Chapter 2. An experienced test pilot was tasked with conducting approaches to each of the ships using the HELIFLIGHT-R motion base flight simulator. The piloted flight testing consisted of a series of approaches to each of the three ships for the Headwind and Green 45° WOD conditions while subjected to a range of wind speeds. The pilot was asked to give an assessment of the difficulty of maintaining a hover position using the Bedford Workload Rating Scale, which was described earlier in Chapter 2, Fig. 2.21. The pilot was also asked to award DIPES ratings for the overall landing task as described earlier, Fig. 2.20.

The landing approach was based on the standard approach to a ship as used by the Royal Navy, also shown earlier in Fig. 1.2 in Chapter 1. This technique involves an approach to a hover, approximately one beam width off the port side of the ship, followed by a lateral translation to a hover over the deck spot before descending to land on the flight deck. During the manoeuvre, the pilot was asked to hold a hover position over the port edge of the flight deck at approximately hangar height for thirty seconds and provide a Bedford workload rating, followed by a thirty second hover

over the flight deck, again providing a workload rating, and finally asked to award a DIPES rating for the whole landing task.

The ratings awarded by a pilot may be subject to change as different pilots may feel a particular test point is subjectively different than a rating awarded by another pilot. This subjectivity may also occur when using the same pilot on repeated test conditions and when there has been a period of time elapsed between testing. However, due to the limited availability of experienced test pilots during this study, repeated flight tests have not been carried out. Nonetheless, the time test pilots have accrued during their service in the Royal Navy and within flight simulators, gives a high degree of confidence in their reported ratings.

4.4.1 Flight Tests in Headwind with Limited Ship Motion

Figure 4.15 shows the Bedford workload ratings given by the pilot for the Headwind WOD when asked to maintain a hover position over the flight deck landing spot for each of the three ships. As is usually the case, the workload in a Headwind case is less than that in a Green wind so for that reason the maximum wind speed in the Headwind was 60 knots, while it was 40 knots in the Green 45 wind.

Pilot assessment of their workload is a subjective process and, although guided by the methodology of the rating scale, each workload rating will have an uncertainty attached to it. Also, the rating scale is not linear, i.e. a rating of 4 does not reflect twice as much work as a rating of 2. To add further complexity, the reasons for the workload will also vary between test points; for example the effort being expended could be in the cyclic controls, or in a combination of collective and pedal controls.

Bearing in mind the previous comments, the workload ratings in Fig. 4.15 show that the effort required by the pilot to hold position over the landing spot, while in a Headwind, was low for wind speeds up to 30 knots, and the ship size did not seem to matter. However, as the wind speed increases the workload also increases, as the airwake becomes more aggressive, and also the increase in workload is greater for the larger ship. The pilot comments also revealed that the reason for the workload ratings changed between ships from being due to difficulty in holding position due to the severity of the fluctuating airwake loads over the large ship, to difficulty in holding position while so close to the superstructure of the small ship.

Figure 4.16 shows the trace history of the cyclic control inceptor for the hover task over the flight deck of both the large and small ships for a 40 knot wind speed. The control activity for the large ship shows larger inputs were required to maintain position than was seen for the small scale ship.

The time histories of the lateral cyclic activity for both the large and small ships for a 40 knot Headwind, shown in Fig. 4.17, also demonstrate the larger displacements applied by the pilot to the cyclic when holding position over the landing spot for the larger ship, and also the lower frequency, reflecting the loads imparted by the stronger and slower airwakes of the larger ship.

The pilot was also required to provide a rating from the Deck Interface Pilot Effort Scale (DIPES), which requires the test pilot to give a rating of 1-5 for any given launch/recovery task. A rating of 1-3 is considered to be acceptable, with the task considered to be within the abilities of an average fleet pilot. Conversely, a rating of 4 is deemed to be unacceptable on the basis that an average fleet pilot would not be able to complete the task in a consistently safe manner, while a rating of 5 indicates that the task cannot be safely completed by the test pilot even under controlled test conditions. Additionally, the test pilot can apply one or more letter suffixes to a DIPES rating which describe the cause(s) of the increased workload e.g. T for turbulence.

The DIPES ratings awarded by the pilot for the overall landing task are shown in Fig. 4.18. It can be seen that for the headwind up to 40 knots the ratings are 1, i.e. “slight to moderate effort”. As the headwind increases to 50 knots the 150m and 200m ships have a DIPES rating of 2 (concentrated effort), while in the 60 knot wind the large ship has a rating of 3 (highest tolerable). Therefore, consistent with the Bedford ratings for the hover tasks, the larger ship has a more aggressive airwake and the landing task is harder, even though the deck is larger.

4.4.2 Flight Tests in Green 45 WOD with Limited Ship Motion

Considering the Green 45 WOD condition, the workload ratings for the station-keeping task above the port edge of each ship are given in Fig. 4.19. In this case the hover is over the deck edge because in the oblique wind this position provided more energetic airwake disturbances. Despite the scatter in the data, the trend is the same, i.e. workload increases with wind speed and is greater for the larger ship. The pilot comments about the reasons for the workload ratings, i.e. aerodynamic perturbations versus superstructure proximity were consistent with those for the Headwind tests. Wind speeds were limited to 40 knots and at this speed the port edge hover tasks for the mid and large scale ships were awarded a Bedford rating of 5, compared with 3 over the landing spot in the headwind. Over the landing spot in the Green wind, Fig. 4.20, the ratings were lower than those given when station keeping over the port edge of the ships but higher than in the headwind (Fig. 4.15). Comments made by the pilot during the tasks indicated that the aerodynamic perturbations and subsequent upset on the aircraft were reduced as the helicopter translated across the deck.

Figure 4.21 shows the path followed by the helicopter's rotor hub while the pilot translates the aircraft from off the port side to over the landing spot, including holding the positions over the port deck edge and the landing spot for 30 seconds each; the WOD is a 40 knot Green 45. At the beginning of the flight test the control of the aircraft is handed over to the pilot while the aircraft is hovering off the port side of the ship. Therefore at the start of each trace an initial vertical displacement is seen where the pilot takes control and adjusts to the task in hand. Despite the size of the ship, and the different airwake characteristics, the trajectory followed by the pilot is relatively consistent for the two ship sizes. The 30 second station-keeping task over the port edge shows greater vertical displacement for the smaller ship, although the pilot did not report greater workload for the smaller ship at that position and wind strength. The similarity of the flightpaths for the different size ships does not contradict the observation that the workload was higher for the bigger ship, but indicates that the pilot had to work hard to maintain position and flightpath in the more aggressive airwake.

The contours of turbulence intensity, shown previously in Fig. 4.14, highlight that for this WOD the proportion of the helicopter‘s rotor disc operating in turbulent flow is greater for the larger ship, which is reflected in the greater excursion in the cyclic activity recorded in Fig. 4.22.

Another interesting observation from Fig. 4.22 is that for the smaller ship the cyclic activity has moved forward. An explanation for this can be found in Fig. 4.23 which shows contours of mean vertical wind velocity at the rotor during the hover task. For the smaller ship, the rotor is placed into a region of flow where there is an updraft of 2.5 - 3 m/s passing through the starboard segment of the rotor, as the flow passes over the starboard edge of the ship and flight deck. This updraft results in a change in the aerodynamic loading of the rotor and, due to the 90° phase delay that occurs between a change in load being applied to the rotor and the rotor reacting [47], the rotor disc will pitch backwards requiring the pilot to maintain a constant correction with forward cyclic to maintain position over the deck. This behaviour was also observed by Forrest et al [59] when conducting simulated deck landings to a Type 23 frigate and shows that a pilot's control strategy must account for both the mean and unsteady velocity components of the flow.

Finally, for the limited ship motion tests, Fig. 4.24 shows the DIPES ratings awarded by the pilot for the overall landing task in the Green winds. Comparing Fig. 4.24 with Fig. 4.18 (up to 40 knots) it can be seen that while the ratings in the 45° winds are slightly higher, this only occurs for the higher wind speeds and over the larger ships.

4.5 Piloted Flight Simulation for Different Size Ships with Realistic Ship Motion

As in the previous section, flight tests were conducted in winds from ahead and Green 45. Sea states increase with wind speed over the ocean and so as the winds in the simulation are increased it can be expected that the sea would become rougher. It was therefore decided that the ship forward speed would be 12 knots and the remainder of the WOD would be due to the wind speed. This assumption enabled the sea state to be roughly correlated with the WOD. The ship motion calculations were carried out by a colleague, Michael Kelly, and so only minimal information is supplied in this thesis; however, more detail can be found in [38,60].

Three random seaways were generated representing sea states 4, 5, and 6, using the Bretschneider spectrum [61], which is widely used to model point wave spectra in the open ocean. Significant wave heights ($H_{1/3}$) and peak wave periods (T_p) used for each sea state are given in Table 4.2. For a 12 knot ahead ship speed, sea states 4, 5, and 6 were taken as representative of conditions encountered in the North Atlantic for the WOD headwinds tested.

Table 4.2 Conditions for sea states 4-6

WOD (kts)	Sea State	T_p (s)	$H_{1/3}$ (m)
15, 25	4	8.8	1.9
35, 40	5	9.7	3.3
45, 50	6	12.4	5.0

The motions of the three ships at sea were simulated using ShipMo3D, a well-validated ship motion potential-flow code developed at Defence Research and Development Canada (DRDC) – Atlantic, and made available to the UoL. Validation has shown ShipMo3D can predict RMS motions to typically be within 10 to 30 percent of observed values, with heave predictions being the most accurate and roll predictions being the least accurate [62].

Geometry representative of the hull of the 150 m long ship was input into ShipMo3D as a set of hull surface coordinates. Ship appendages were also included, with the hull featuring a bulbous bow, two rudders, two propellers, two bilge keels, two roll stabilisers, and a skeg. The hulls and their appendages were linearly scaled in size to match the 100m and 200m ships, and while it is acknowledged that hull appendages will not necessarily be linearly scaled with ship length, appendages were scaled in this manner to maintain a consistent comparison between the three ships. The ship hull geometries are shown in Fig. 4.25. The wet and dry hull panels are shown as yellow and green, respectively, with the hydrostatic waterline located at the interface between these surfaces.

While a unidirectional Bretschneider spectrum can be used to approximate long-crested oceanic waves, lateral motion (roll, sway, and yaw) will be absent due to the symmetry of the ship geometry travelling directly into two-dimensional waves, and so a cosine-squared spreading function was implemented with a 90° spreading angle and 15° heading interval, as supported by trials evidence for typically occurring conditions in the open ocean [63]. In this way a more representative short-crested wave spectrum was generated, represented by eleven reduced Bretschneider spectra distributed around the dominant ahead wave direction; this has the advantage of imposing realistic lateral forces upon the symmetrical ships in the ahead case that cause the ships to roll, which they would not do in a unidirectional wave spectrum.

The ship motions were calculated as roll, pitch and heave at the ships' centres of gravity. These were then imported into the FLIGHTLAB simulation environment, which creates a deck contact area for launch and recovery operations with deck motion calculated from the modelled displacements at the ship's centre of gravity. Figure 4.26 shows an example of the deck motion (roll, pitch and heave) at the landing spot for the three ships travelling at 12 knots through sea state 5, with the waves coming from ahead. Looking at the small ship data, maximum roll and pitch are about ±3˚, and maximum heave is about ±2m, compared with less than ±1˚ pitch and roll, and about ±1m for the large ship. It can also be seen in Fig. 4.26 that there are periods in the ship motion that have smaller displacements than others and it is these naturally occurring quiescent periods that the pilot waits for to execute a landing.

There are generic guidelines for deck roll and pitch limits for a helicopter launch: 2.5° for roll and 1.5° for pitch [64]; these values are RMS of amplitude. From Fig. 4.26 the maximum pitch and roll for the small ship, at about ±3°, exceeds these values, but not for the larger ships. It can also be deduced from Fig. 4.26 that the period of oscillation for the small ship is about 6.5 seconds, while it is about 10.5 seconds for the large ship; these compare with the wave period of 9.7 seconds in Table 4.2. The deck displacements, velocities and accelerations for the smaller ship are high and can be expected to challenge the pilot.

With the realistic ship motion the pilot was again asked to conduct deck landings and to maintain precision hover tasks in the winds from Ahead and Green 45. During the testing, the pilot was given the flexibility to adjust altitude as deemed fit to accommodate the ships' deck motions.

4.5.1 Flight Tests in Headwind with Realistic Ship Motion

The Bedford workload ratings awarded by the pilot for each of the three ships for the thirty second deck spot hover task in the headwind case are given in Fig. 4.27. As the wind speed over the sea increases, so the sea state can be expected to increase. In this case the expected sea state for the wind speed is shown on the graph, and the motion of each ship was computed for that sea state and a ship forward speed of 12 knots.

It can be seen in Fig. 4.27 that, for all three ships, the workload required to maintain the hover over the moving deck increased as the wind strength increased. Also, as the wind speed increases so too does the sea state and the displacement of the ships' deck. It can also be seen that the workload required to hold the hover position over the small ship is higher than for the medium and large ship. This is despite the fact that the small ship's airwake is the least aggressive, and the higher workload must therefore be due to the large displacements of the small ship's deck with some additional workload arising from the airwake disturbances. It can also be seen in Fig. 4.27 that the large ship has generated workload ratings that are generally one rating less than those awarded for the hover task over the small ship and one rating higher than those awarded for the medium size ship. In each case the minimum workload rating is awarded for the medium size ship. The pilot is having to contend with both the deck motion and the airwake and it appears that the 150m ship (which is typical of a single-spot frigate) has the ‘best’ combination of moderate deck motion and airwake. The small ship has the least aggressive airwake, but the greatest deck motion, and the large ship has the most aggressive airwake and least deck motion.

The results in Fig. 4.27 can be compared those in Fig. 4.15 where the ship motion is at sea state 3 and consistent between the different size ships. Without the realistic ship motion the workload ratings awarded for the hover task can be seen to increase with wind speed, but with much lower values than in Fig. 4.27. It is already clear from comparing Figs. 4.15 and 4.27 that realistic ship motion is essential for simulated landings of a helicopter to a ship.

Further insight into the difficulty of holding the helicopter in a stable hover over the landing spot can be gained by looking at the control activity of the pilot during the hover task. Figure 4.28 shows the pilot’s cyclic control inputs, which are used for lateral and longitudinal positional control during the 30 second hover over the landing spot. The largest excursions are for the large ship and will be due to the larger, slower moving vortices being shed from the ship superstructure. The smaller ship shows the smallest excursions while the control activity for the medium ship lies between the two. Comparing Fig. 4.28 with Fig. 4.16, it can be seen that the cyclic displacement applied by the pilot is much greater with realistic ship motion, although in both cases the larger cyclic displacements are for the larger ship suggesting that the cyclic activity is due mainly to the ship airwake.

The data in Fig. 4.28 does not explain why the pilot awarded the greatest workload ratings to the hover task over the smallest ship. However, Fig.4.29 shows the pilot’s control inputs to the collective, which provides power and thrust to main rotor (and which then also interacts with the pedal control as the aircraft changes attitude in yaw). It can be seen in Fig. 4.29 that the greatest activity in the collective control is for the hover task over the small ship, while the lowest is for the large ship. As the small ship’s airwake is the least disruptive the pilot is therefore having to work hard to hold vertical position over the landing spot as the ship moves about violently, as seen earlier in Fig. 4.26. The same situation is seen in the pedal control activity in Fig. 4.30 where the largest excursions are over the small ship. The workload ratings awarded in Fig. 4.27 are a combination of the total control activity, as well as the visual and motion cues the pilot will receive while conducting the hover task.

The DIPES ratings awarded for the overall landing task for headwind speeds from 15 to 50 knots and for the three ship sizes with appropriate sea-state motion are shown in Fig. 4.31. Again, it can be seen that in general the pilot's workload increase as the wind speed increases, and the greatest effort is required for the landing to the smaller ship. It should also be noted that the safe limit for the landing task is 3 so that for a headwind of 45 knots it is unsafe to land to the small ship, and for a headwind of 50 knots it is unsafe to land to the small and medium ships.

Comparing Fig. 4.31 with Fig. 4.18 it can be seen that the realistic ship motion has significantly increased the pilot's workload. The highest workload is for the small ship and the pilot deemed the landing unsafe for winds of 45 and 50 knots. As well as awarding the DIPES ratings in Fig. 4.31, at higher workload the pilot also identified the causes. For the large ship the pilot indicated that fore-aft positioning and turbulence were the limiting factors. For the smaller ship the limiting factors were difficulty of ship tracking and positional accuracy as well as torque limit while trying to track the deck vertically; i.e. ship motion was the determining factor. For the medium ship the pilot reported that a combination of turbulence and ship motion made it difficult to hold position.

4.5.2 Flight Tests in Green 45 WOD with Realistic Ship Motion

Figure 4.32 shows the computed ship motion in roll, pitch and heave at the landing spot for the ship travelling at 12 knots and the waves coming from 45° off the starboard bow, i.e. Green 45, in sea state 5. As can be seen, the small ship is now predicted to roll at about ±5° with excursions up to ±10°, while the larger ship is typically rolling at ±5°. In pitch the smaller ship is predicted to have a displacement up to ±3.5° but more typically the three ships have a pitch of about ±2°. The heave at the landing spot for the three ships is reaching ±2m on a number of cycles. The Green 45 waves cause a period of oscillation of about 10 seconds for the large ship and about 7.5 seconds for the small ship. Overall the displacements are significantly greater than for waves from Ahead and can be expected to present major challenges to the pilot.

Figure 4.33 shows the Bedford workload ratings awarded by the pilot for the hover task over the landing spot. The wind speeds were only up to 40 knots, unlike the 50 knots in the headwind, and it can be seen that there is now a consistent order where the small ship is presenting a greater challenge to the pilot. Given the relative strengths of the airwakes, it is clear that deck motion is the major factor. Unlike the headwind case in Fig. 4.28, the cyclic activity is now more consistent for the three ships, as seen in Fig. 4.34. The collective activity in Fig. 4.34 shows there is greater displacement in this inceptor for the small ship, although the deck heave presented in Fig.4.32 shows the small and large ship have similar vertical displacements, but the frequency of displacement is higher for the small ship and the visual cues will be showing the small ship's superstructure to be closer and more threatening to the pilot. The pedal activity in Fig. 4.36 shows more reversals for the small ship, and noticeably fewer for the larger ship. This is reflected in the plots of power spectral density for the thirty second deck spot station keeping task, for a 40 knot, Green 45 WOD, with limited and realistic ship motion, Figs 4.37 and 4.38. The plots show that greater control activity was needed by the pilot to maintain position for the large scale ship when ship motion was not a factor, however when the tasks were repeated with realistic ship motion, the control activity increases for both, with the small scale ship showing higher workloads throughout the frequency range. Overall the activity in all three controls during the hover task is consistent with the workload reported by the pilot.

The DIPES rating for the overall landing task, Fig. 4.39, also shows the small ship to be the hardest to land to and the largest ship the 'easiest', although it should be borne in mind that a rating of 3 is the highest for a safe landing so in a 40 knot wind, with a corresponding sea state of 6 the small- and mid-sized ships are unsafe to land to. In the headwind with realistic ship motion, Fig. 4.31, it was considered safe to land on all three ships for a 40 knot wind, but unsafe for the small- and mid-sized ships at 50 knots.

4.5 Chapter Summary

Whether assessing ship superstructure modifications or developing simulated SHOLs, at the beginning of the process is the production of unsteady airwakes for different ships, wind strengths and wind direction. This is a lengthy and expensive process that, in relevant circumstances, can be reduced using the scaling techniques described in this chapter, even if an ABL is used.

For the three geometrically similar ships of length 100m, 150m and 200m that have been considered, the Virtual AirDyn showed that the airwakes shed from the larger ship produced the higher RMS forces and moments on the helicopter, thereby supporting earlier studies which had suggested that bigger ships were more problematic for the pilot to land to. This observation is also consistent with the pilot's experiences in the simulated flight trials reported in this chapter when the ship motion was limited and the same for the three ships.

However, when the realistic ship motion is included, flight simulation showed that in a headwind the pilot workload was highest when landing to the smaller ship and lowest when landing to the medium size ship. In the 45° waves and wind the deck displacements became more aggressive, particularly for the small ship. This, together with the reduced deck size made the small ship the most difficult to land to, with the large ship being the least demanding.

It cannot simply be said therefore that as the ship gets larger the airwake becomes more aggressive and the landing gets more difficult. When ship motion is significant the moving deck provides a greater challenge to the pilot than does the airwake. With larger ships, the deck motion presents less of a challenge, while the unsteady loads from the airwake dominate the pilot's workload. Small, helicopter-enabled ships such as the River class patrol vessel shown in Fig. 4.2 will have limited SHOLS in rough seas.

Figure 4.1 Wave Class tanker and Type 23 Frigate

Figure 4.2 Graphic of HMS Clyde, a River-class Patrol vessel with a Merlin helicopter on the flight deck

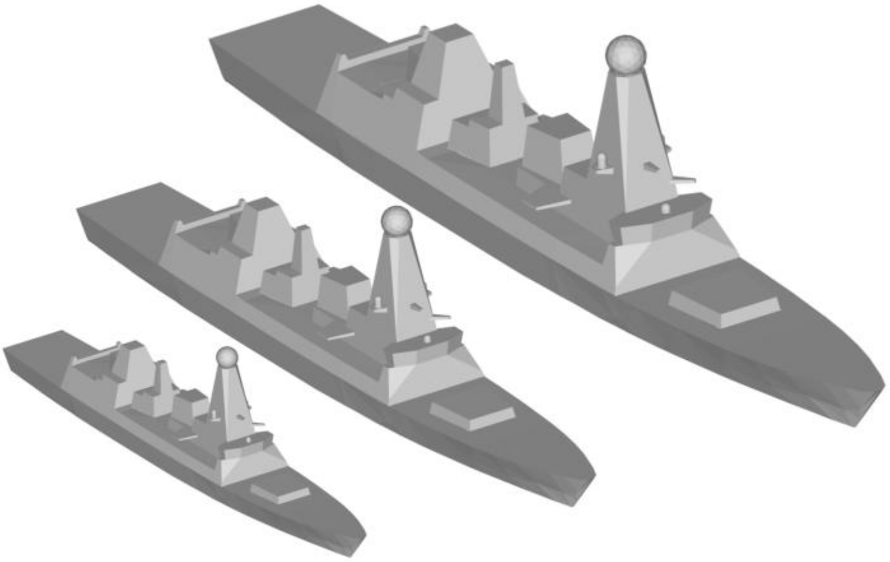

Figure 4.3 The generic naval frigate geometry and the range of ship sizes (lengths 100, 150 & 200 m)

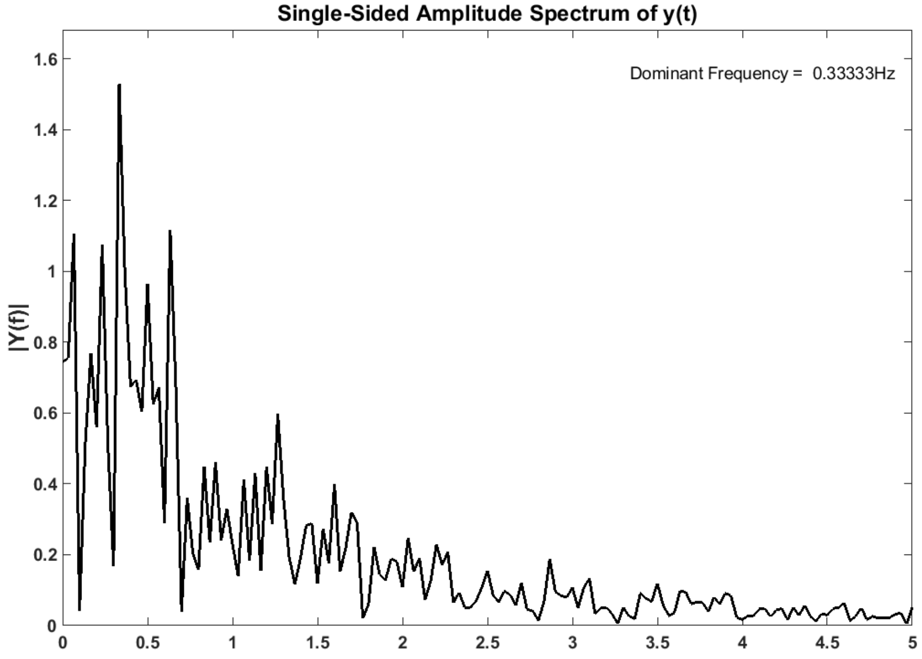

Figure 4.4 Dominant eddy frequency aft of the hangar face, above the flight deck, for the 150m ship in a Headwind WOD condition

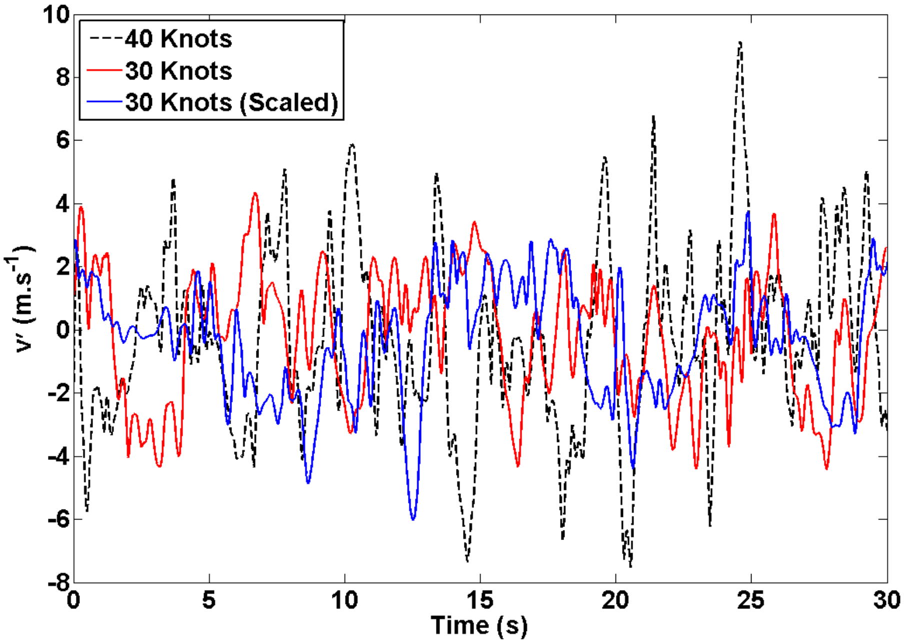

Figure 4.5 Normalised unsteady total velocity data above landing spot for the computed 40 and 30 knot data and the scaled 30 knot case

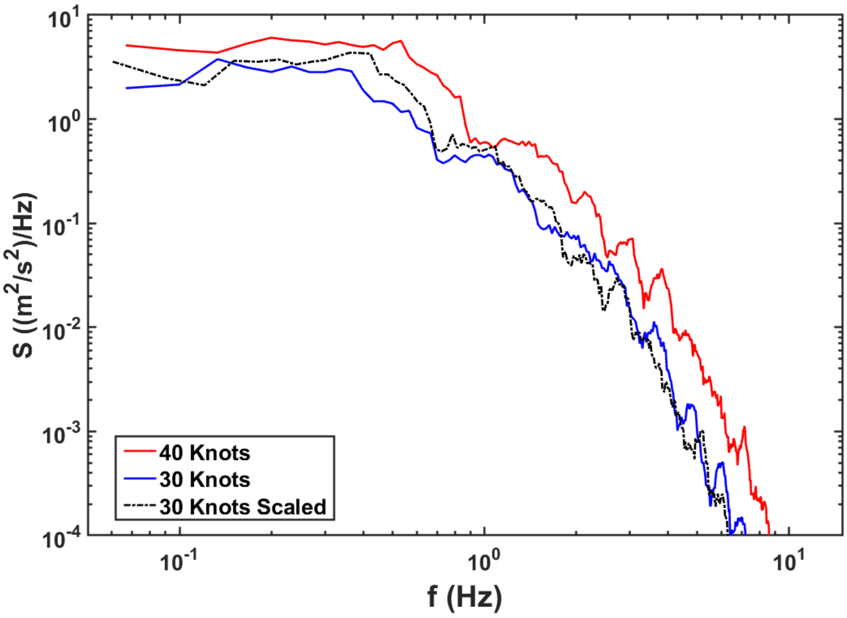

Figure 4.6 Power spectral densities of the total velocity above landing spot for the computed 40 and 30 knot data and the scaled 30 knot case

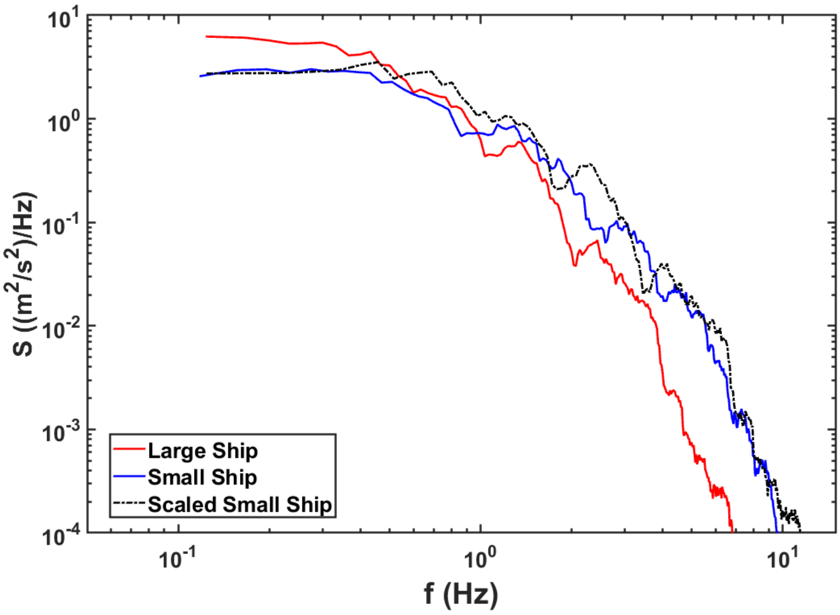

Figure 4.7 Power spectral densities of the total velocity above landing spot for a Headwind WOD using an ABL, showing computed data for the small ship compared with the data scaled from the large ship

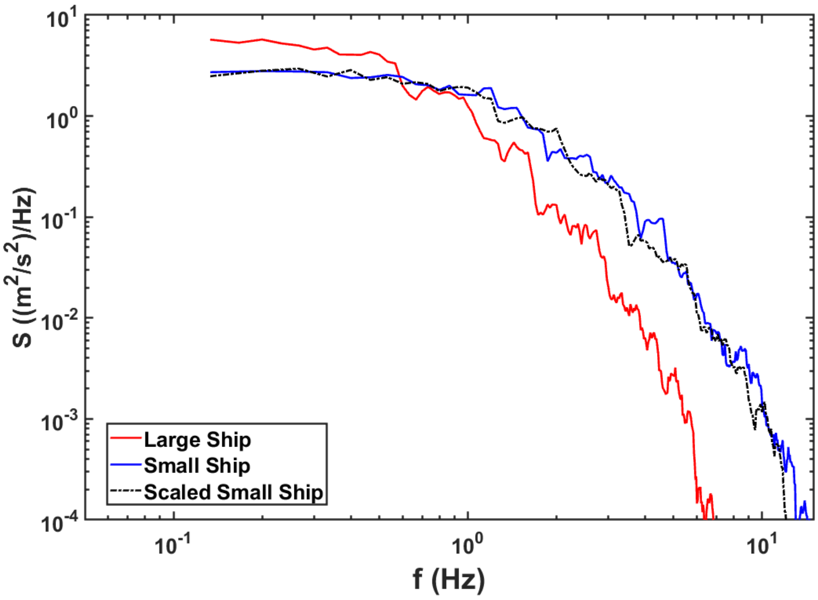

Figure 4.8 Power spectral densities of the total velocity above landing spot for a Headwind WOD using a UBL, showing computed data for the small ship compared with the data scaled from the large ship

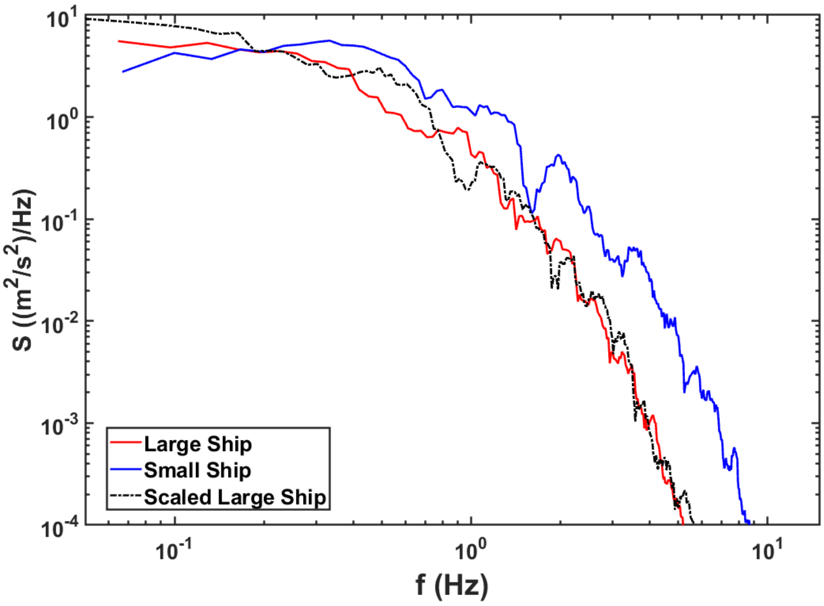

Figure 4.9 Power spectral density of the total velocity for a Green 45° WOD showing computed small-scale and un-scaled data and the scaled down data over port edge at hangar height, using an ABL.

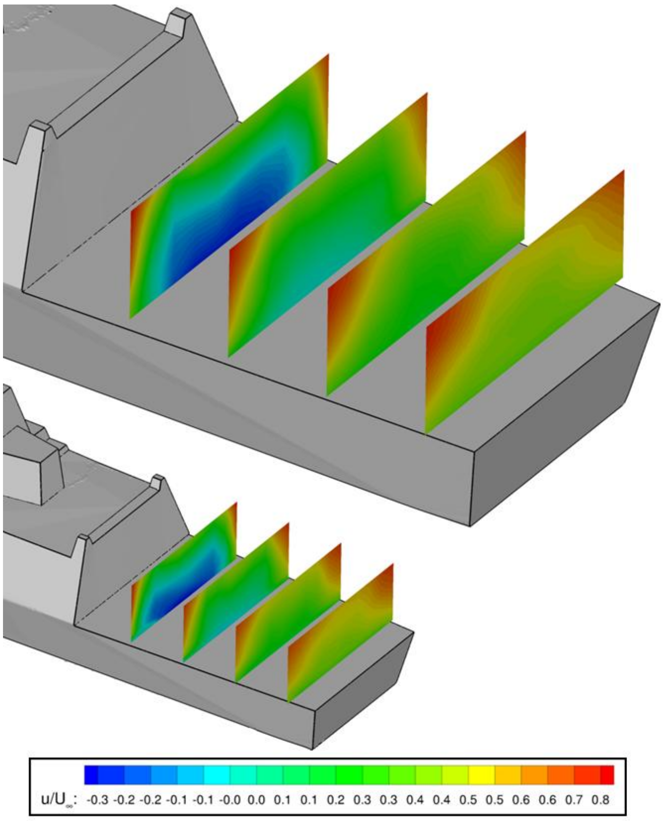

Figure 4.10 Normalised longitudinal velocity contours over the flight decks of the small and large scale ships for the Headwind case.

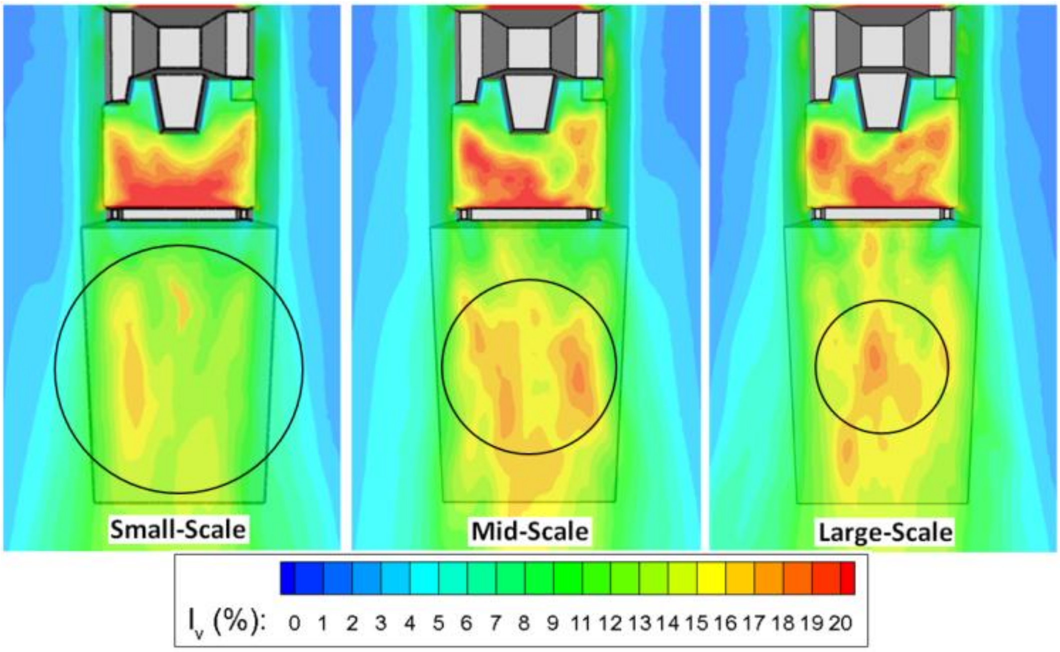

Figure 4.11 Comparisons of lateral turbulence intensity at 100 % hangar height showing the change in scale of the helicopter rotor disc over the deck

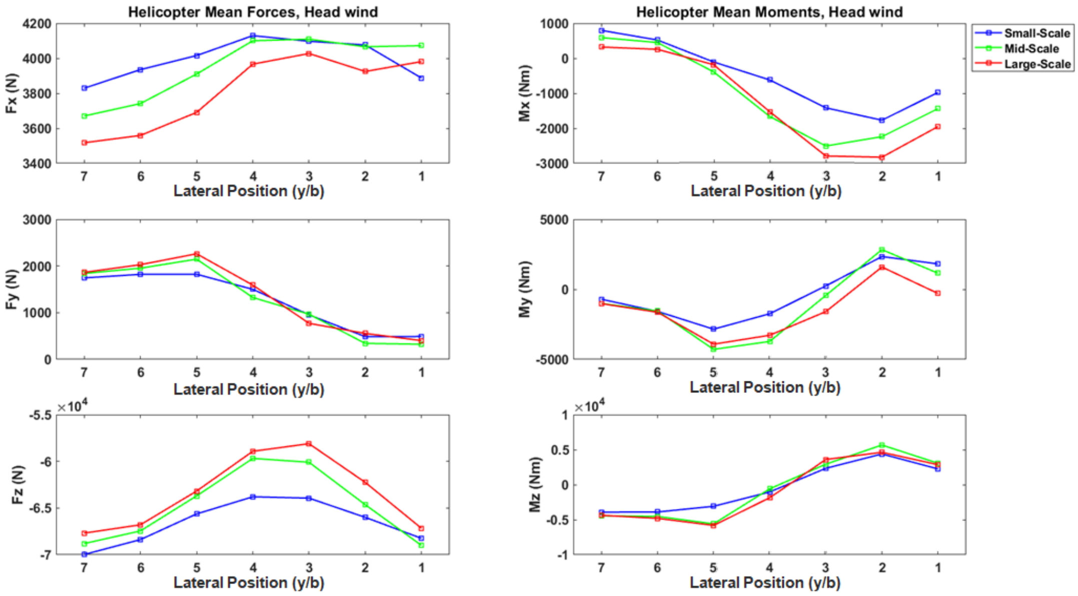

Figure 4.121 VAD comparison of mean forces

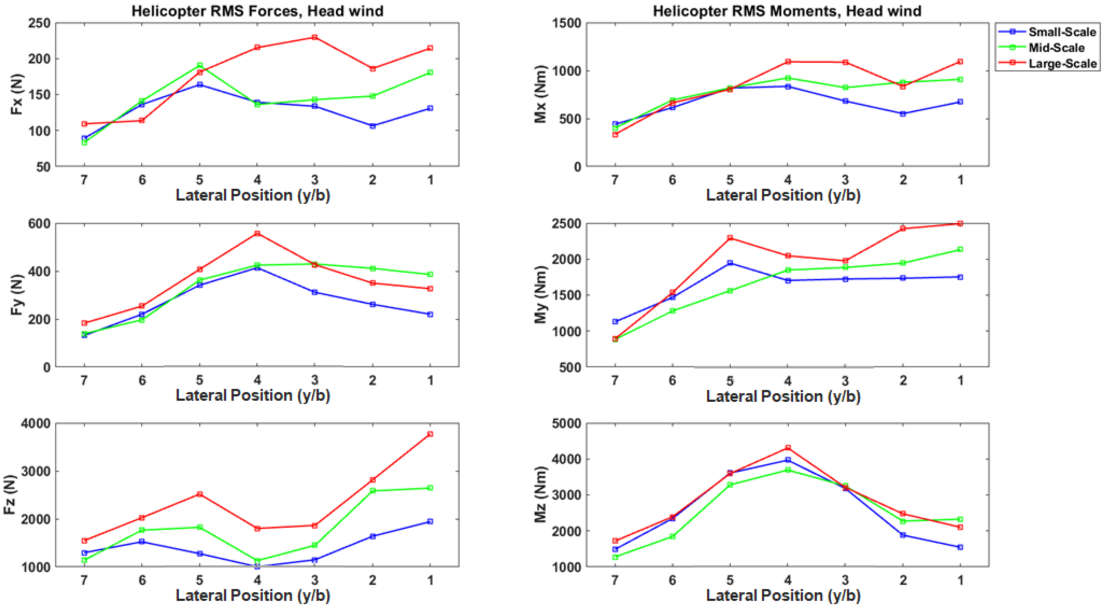

Figure 4.13 VAD comparison of RMS forces

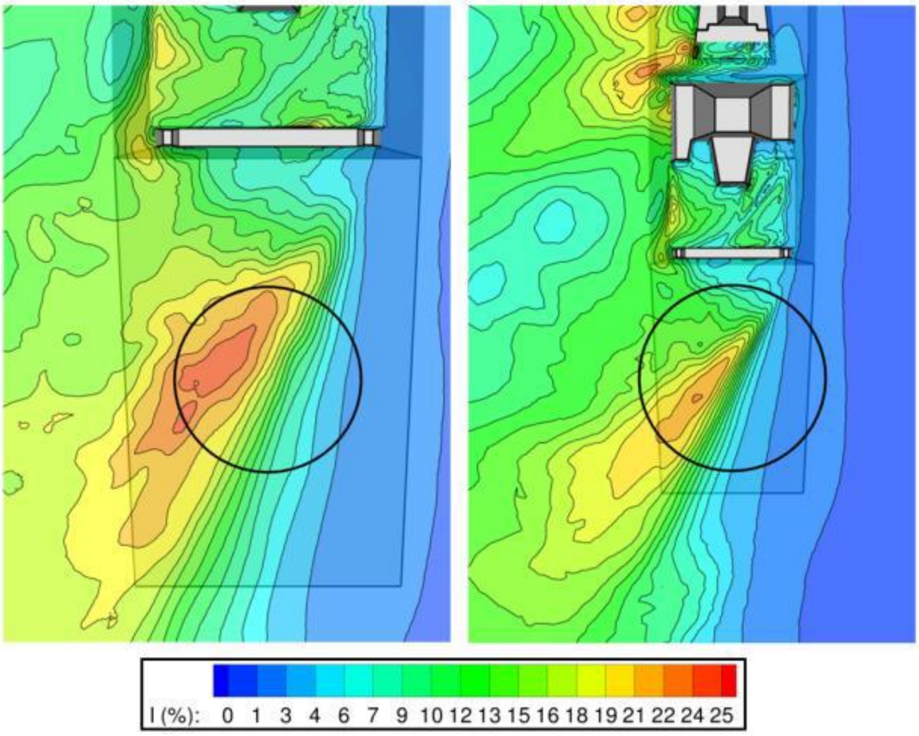

Figure 4.14 Comparisons of turbulence intensity contours at 100 % hangar height showing the relative size of the helicopter rotor disc over the large and small flight decks in a Green 45° WOD

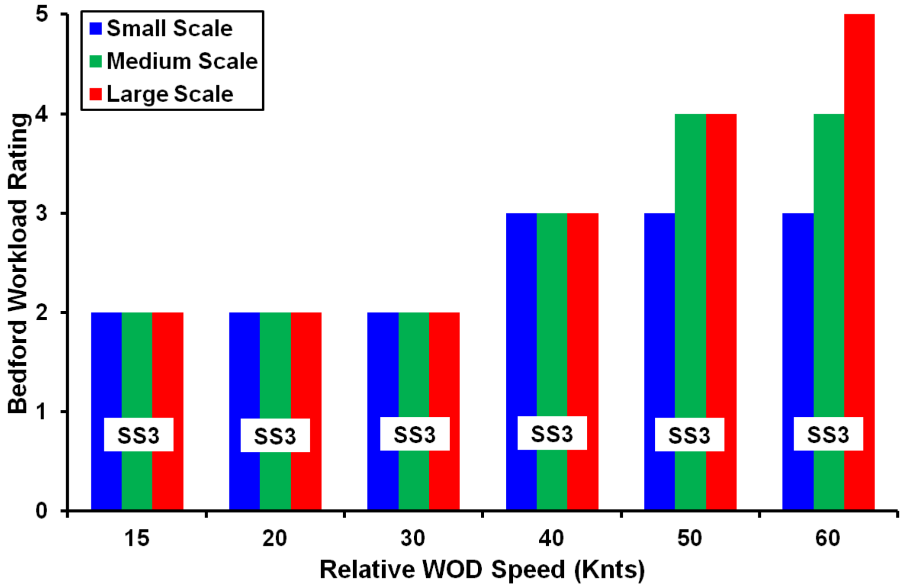

Figure 4.15 Bedford Workload Ratings for the hover position over the flight deck for the Headwind case with equal and limited ship motion

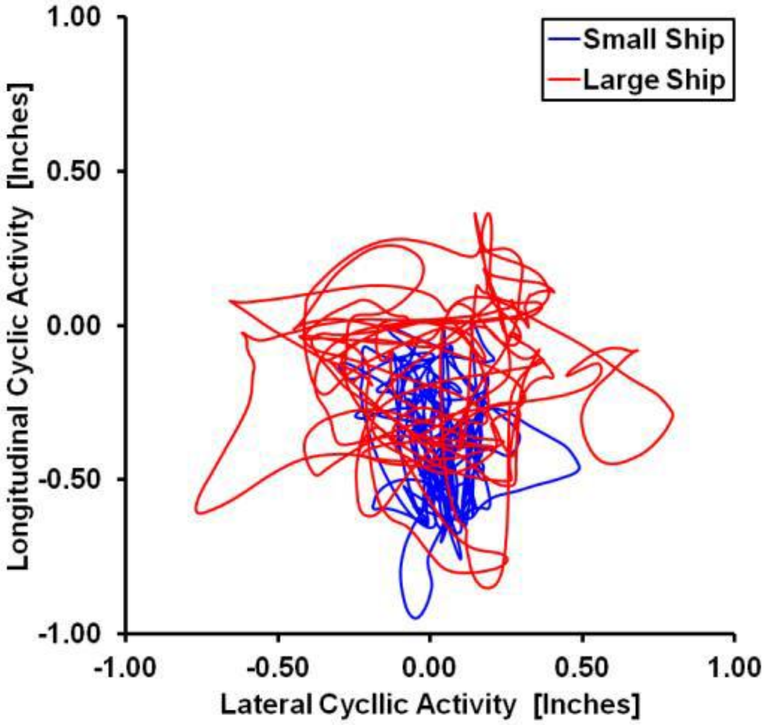

Figure 4.16 Cyclic control activity during station keeping task over landing spot for a 40 knot Headwind WOD case with equal and limited ship motion

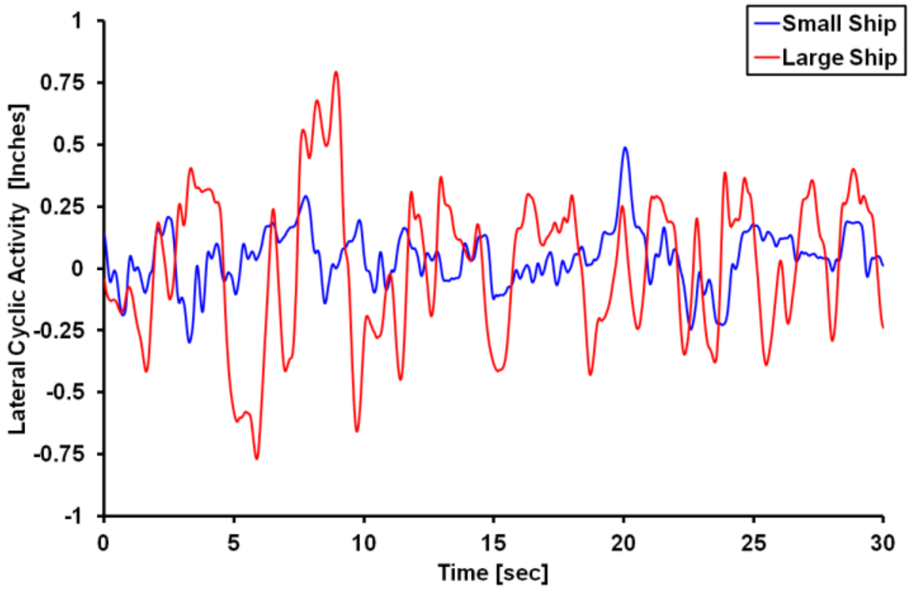

Figure 4.17 Time histories of lateral cyclic activity during station keeping task over landing spot for a 40 knot Headwind WOD case with equal and limited ship motion

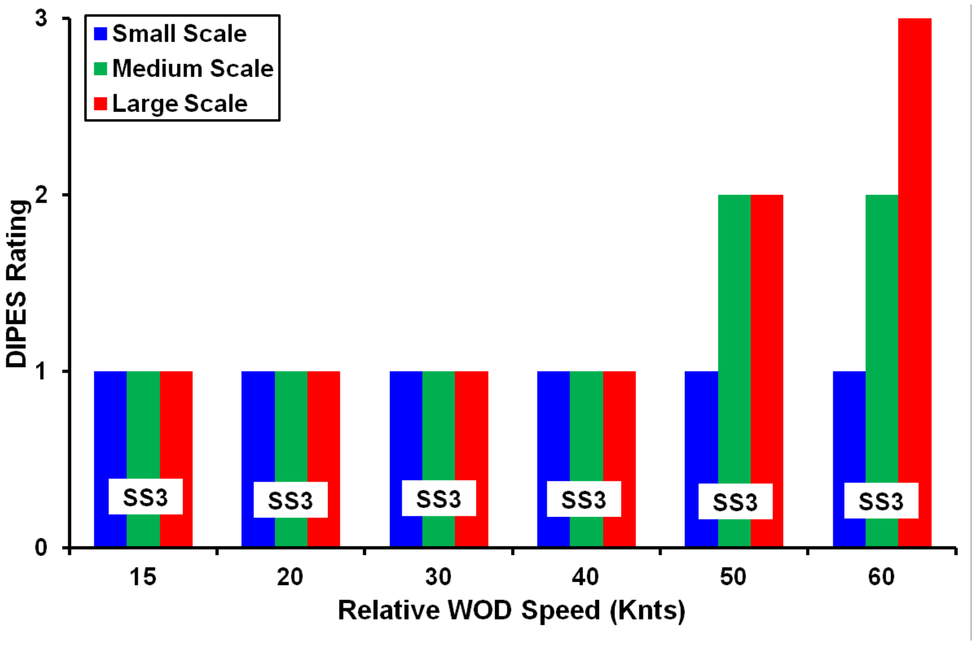

Figure 4.18 DIPES ratings awarded by pilot for the landing task. Headwind, with equal and limited ship motion

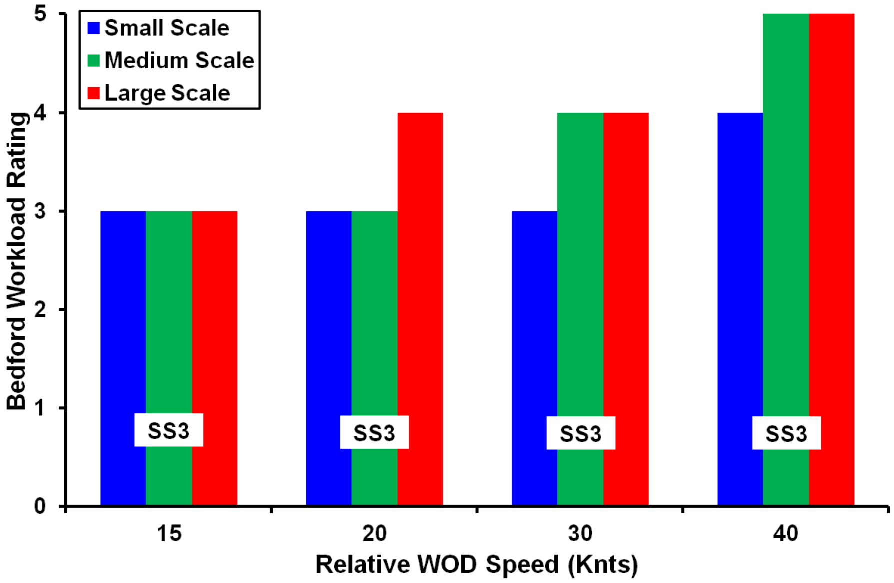

Figure 4.19 Bedford Workload Ratings for the hover position over the port edge for the Green 45° case, with equal and limited ship motion

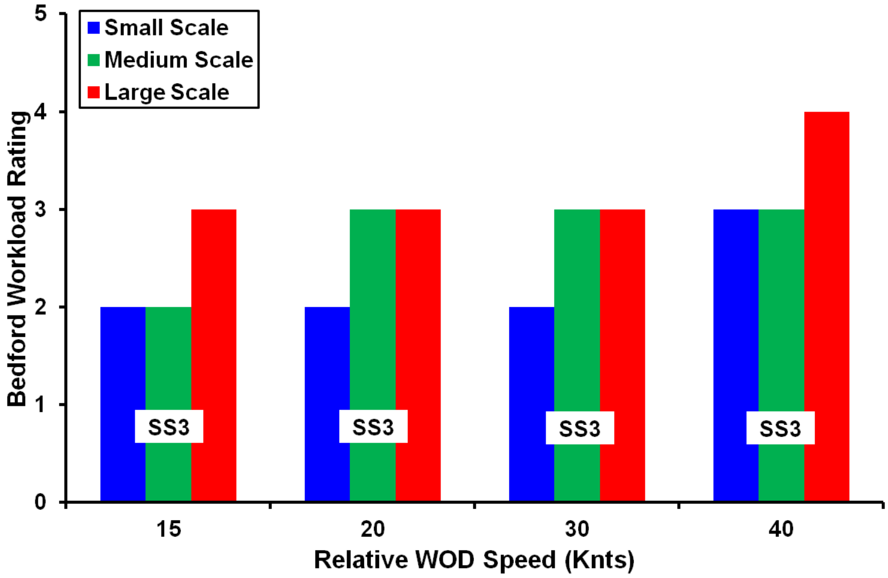

Figure 4.20 Bedford Workload Ratings for the hover position over the flight deck for the Green 45° case, with equal and limited ship motion

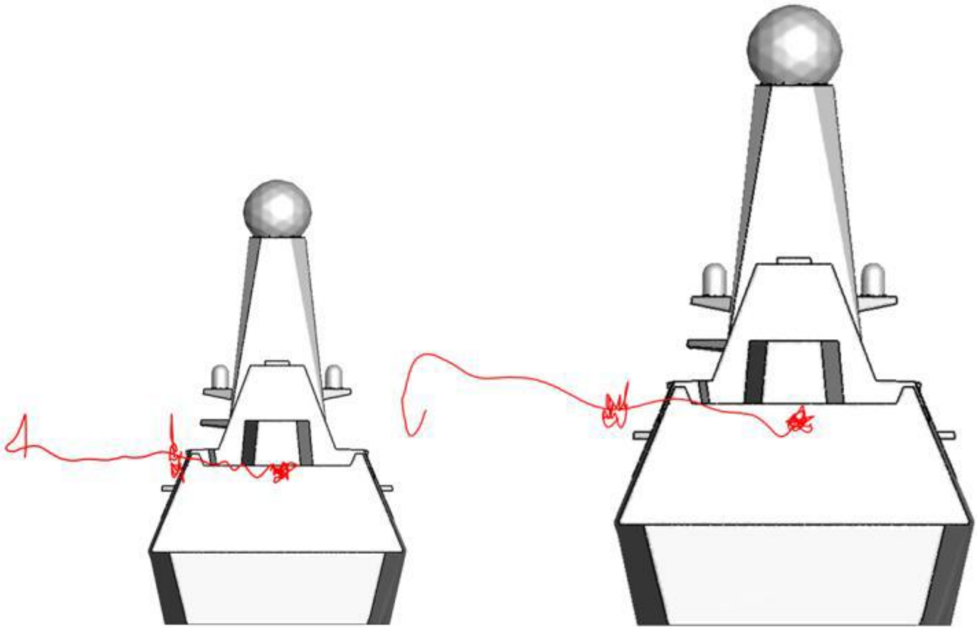

Figure 4.21 Trajectory of the path taken by the helicopter during the approach and station keeping to both the large and small scale ships for a 40 knot wind, Green 45 WOD case, with equal and limited ship motion

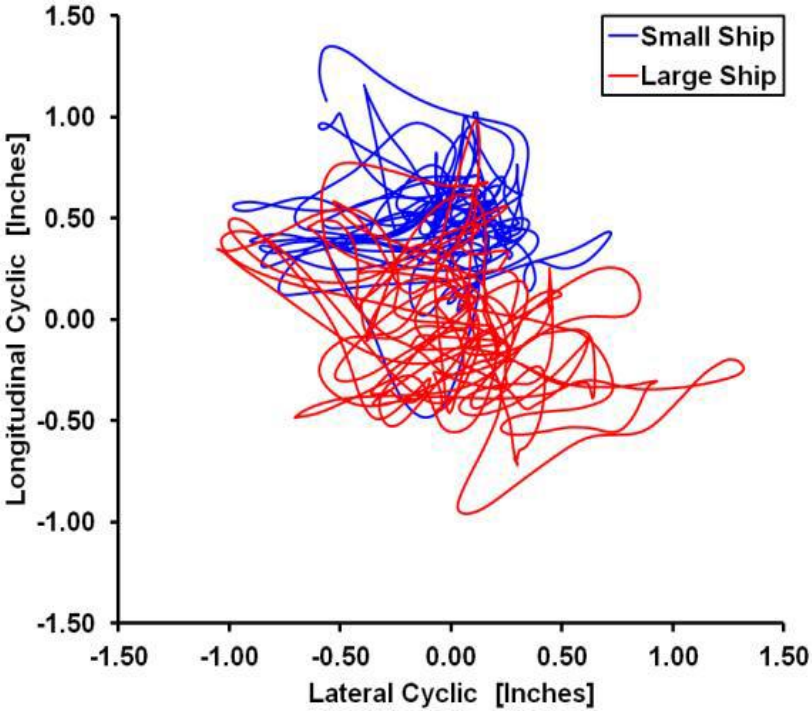

Figure 4.22 Cyclic control activity during station keeping task over landing spot for a 40 knot, Green 45° WOD case, with equal and limited ship motion

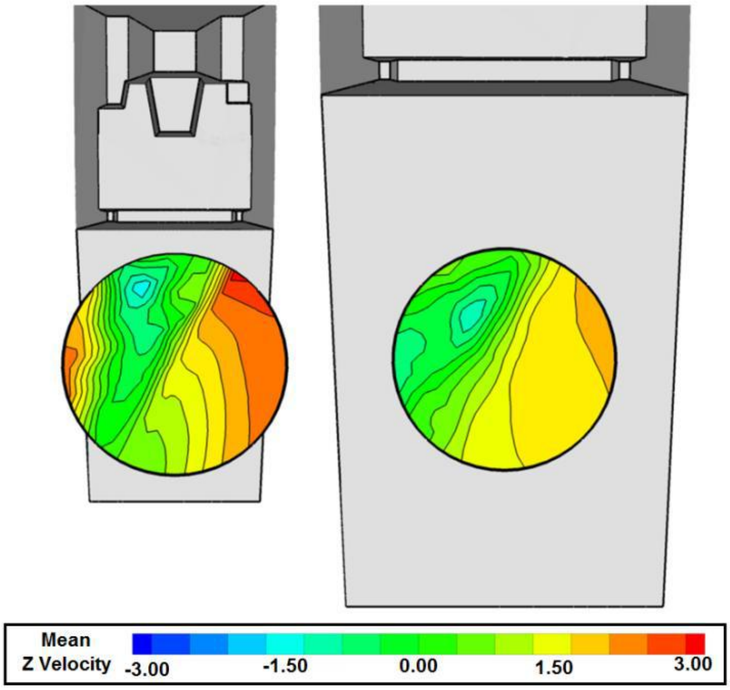

Figure 4.23 Contours of mean, vertical wind velocities shown at the rotor disc during the hover task.

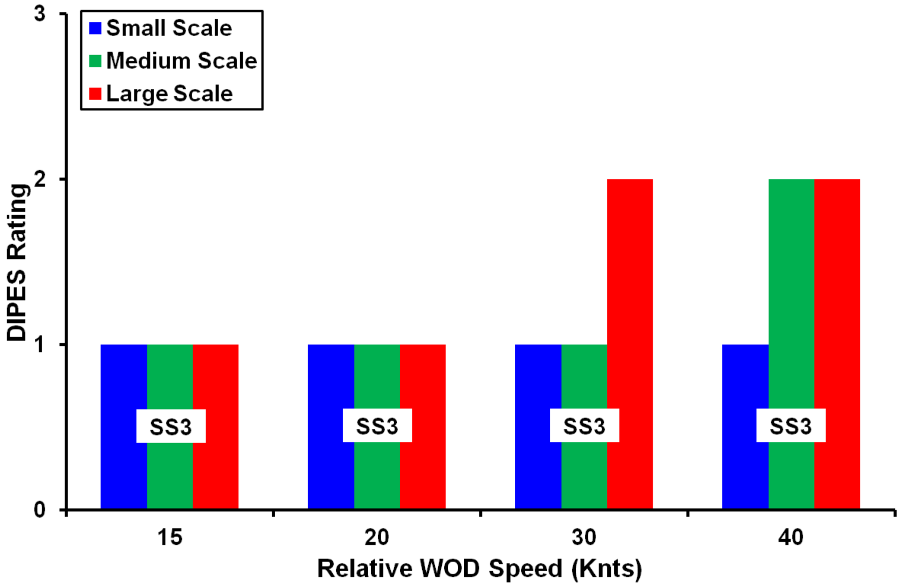

Figure 4.24 DIPES ratings awarded by pilot for the landing task. Green 45, with equal and limited ship motion

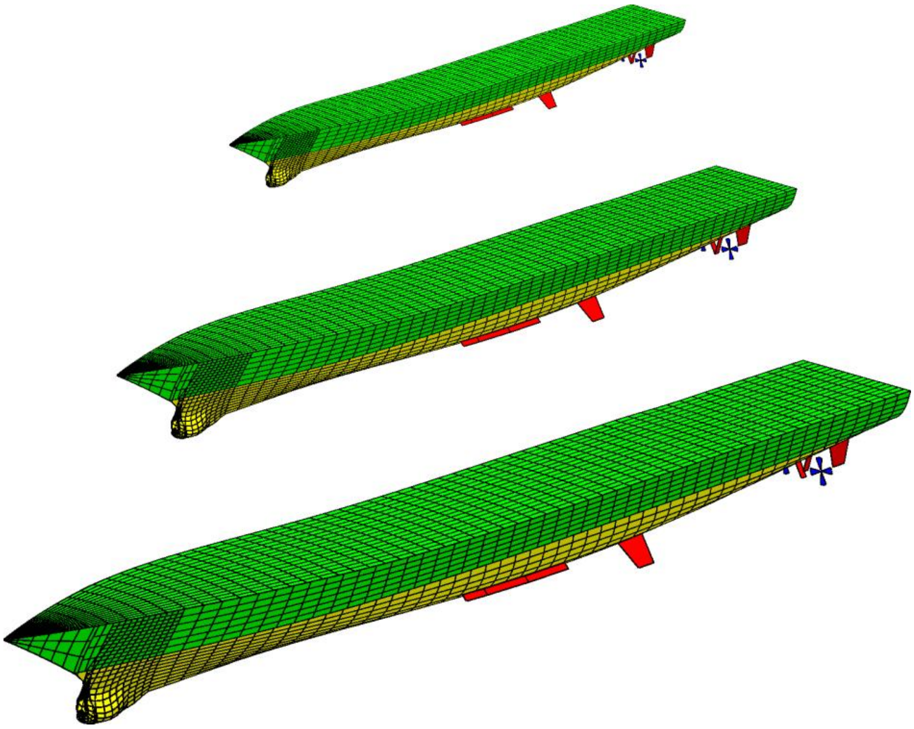

Figure 4.25 Ship hulls with appendages

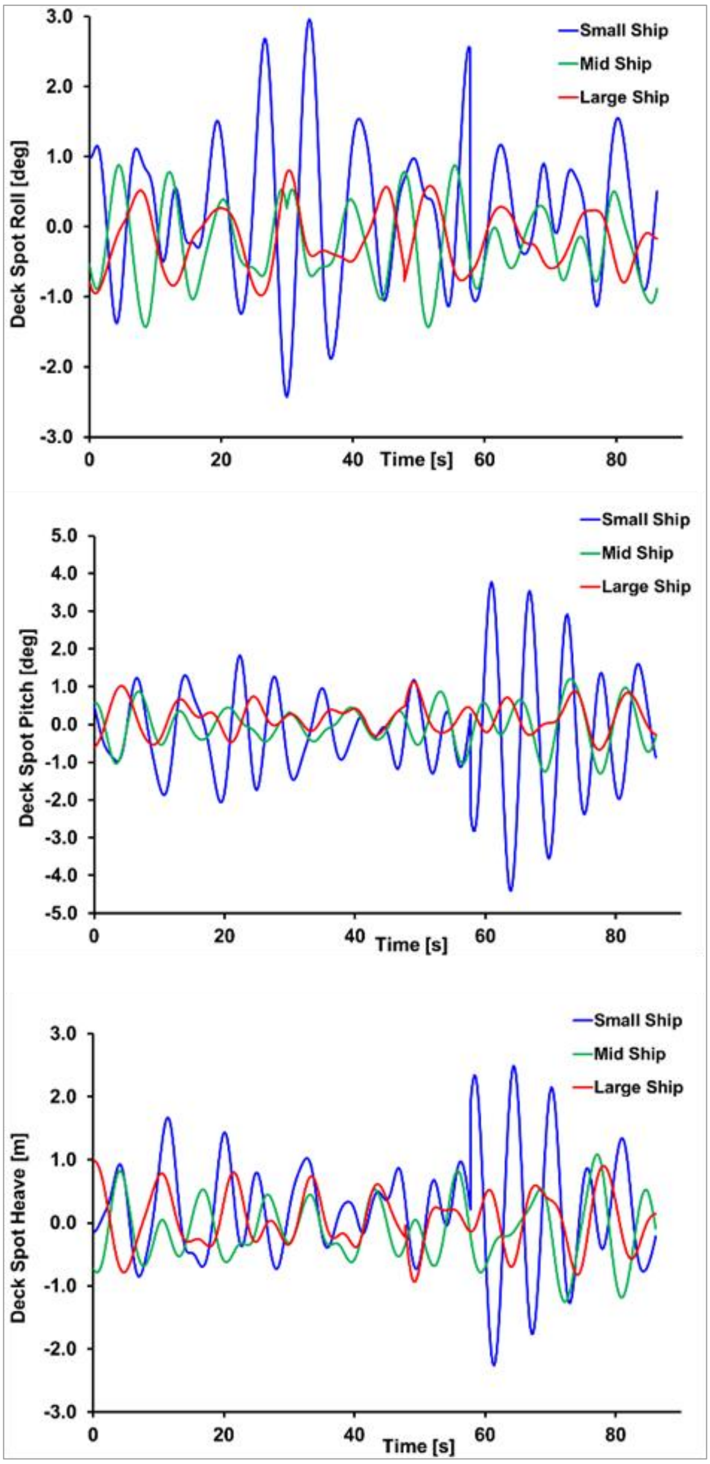

Figure 4.26 Computed displacements of the landing spot for the three ships travelling at 12 knots through sea state 5 with waves coming from ahead

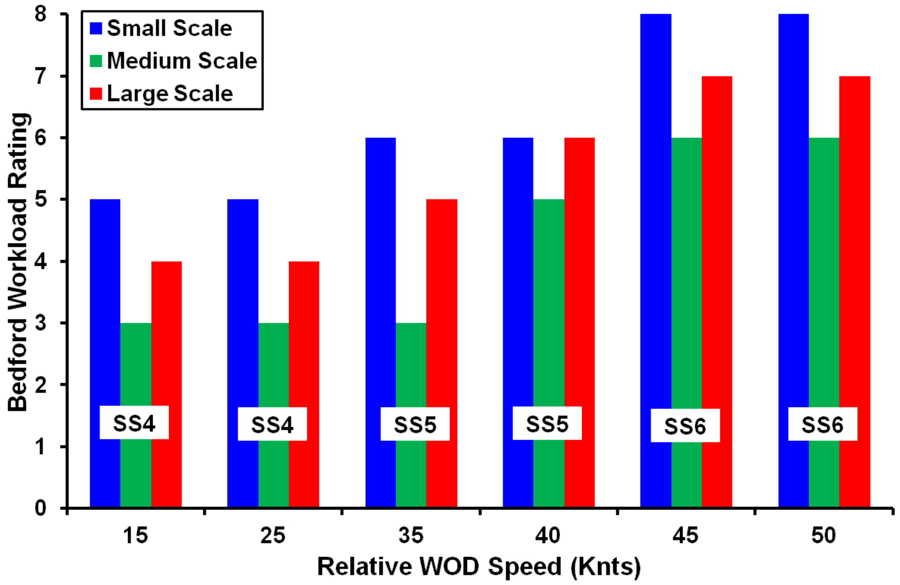

Figure 4.27 Bedford workload ratings awarded by pilot for the hover task above the deck spot, headwind, realistic ship motion, 12 knots ship speed.

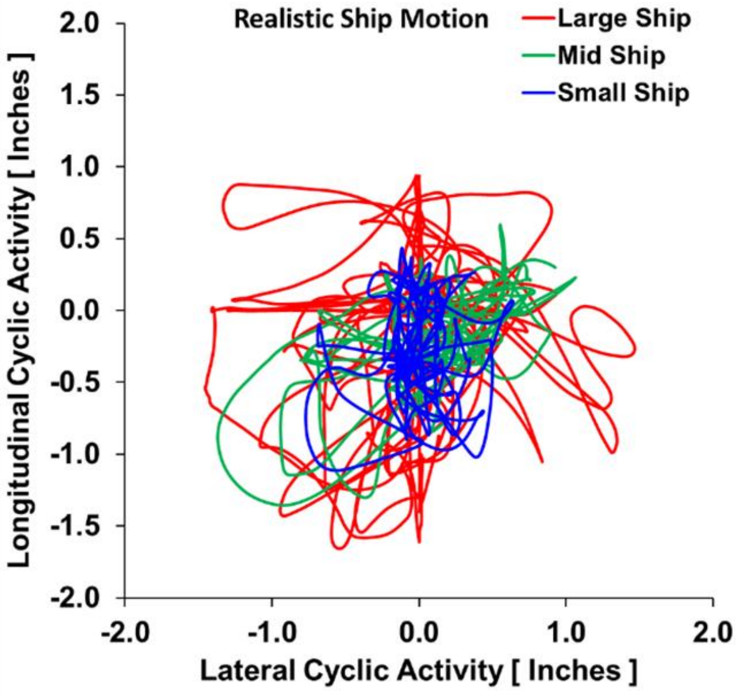

Figure 4.28 Cyclic control activity during hover task over landing spot for a 40 knot headwind, sea state 5, realistic ship motion

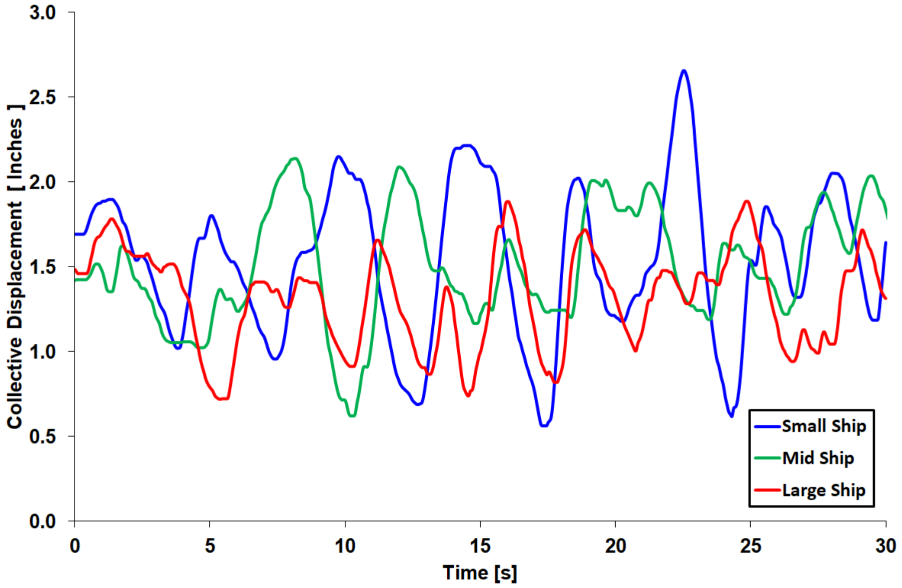

Figure 4.29 Collective control activity during hover task over landing spot for a 40 knot headwind, sea state 5, realistic ship motion

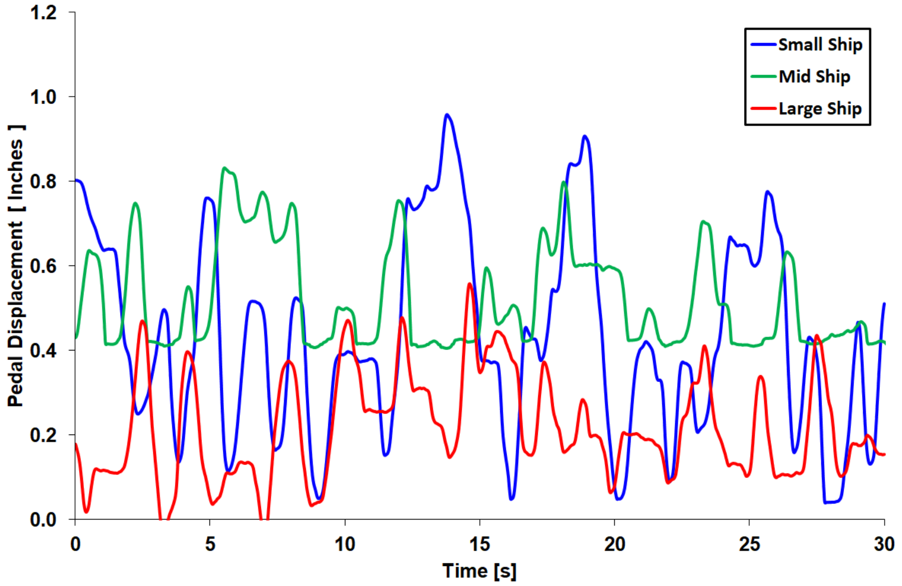

Figure 4.30 Pedal control activity during hover task over landing spot for a 40 knot headwind, sea state 5, realistic ship motion

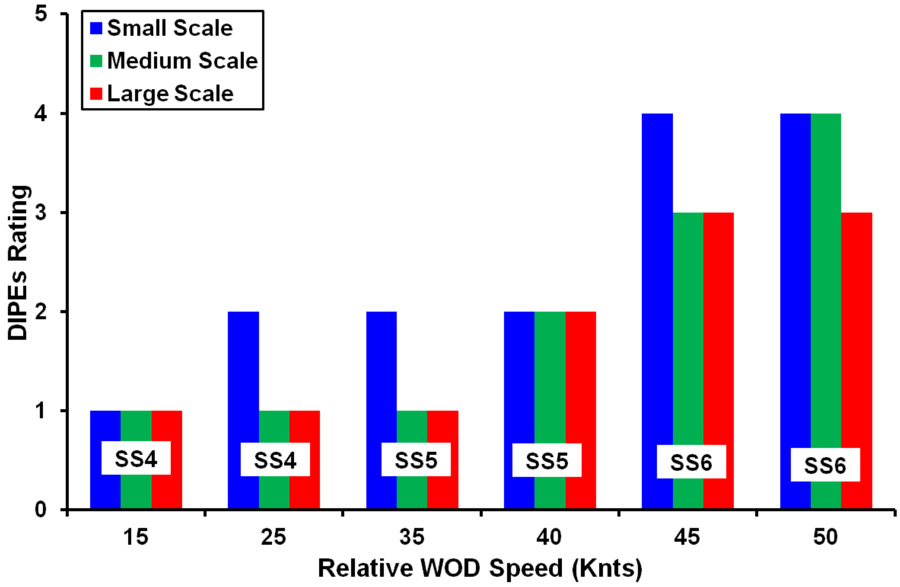

Figure 4.31 DIPES ratings awarded by pilot for the landing task. Headwind, with realistic ship motion.

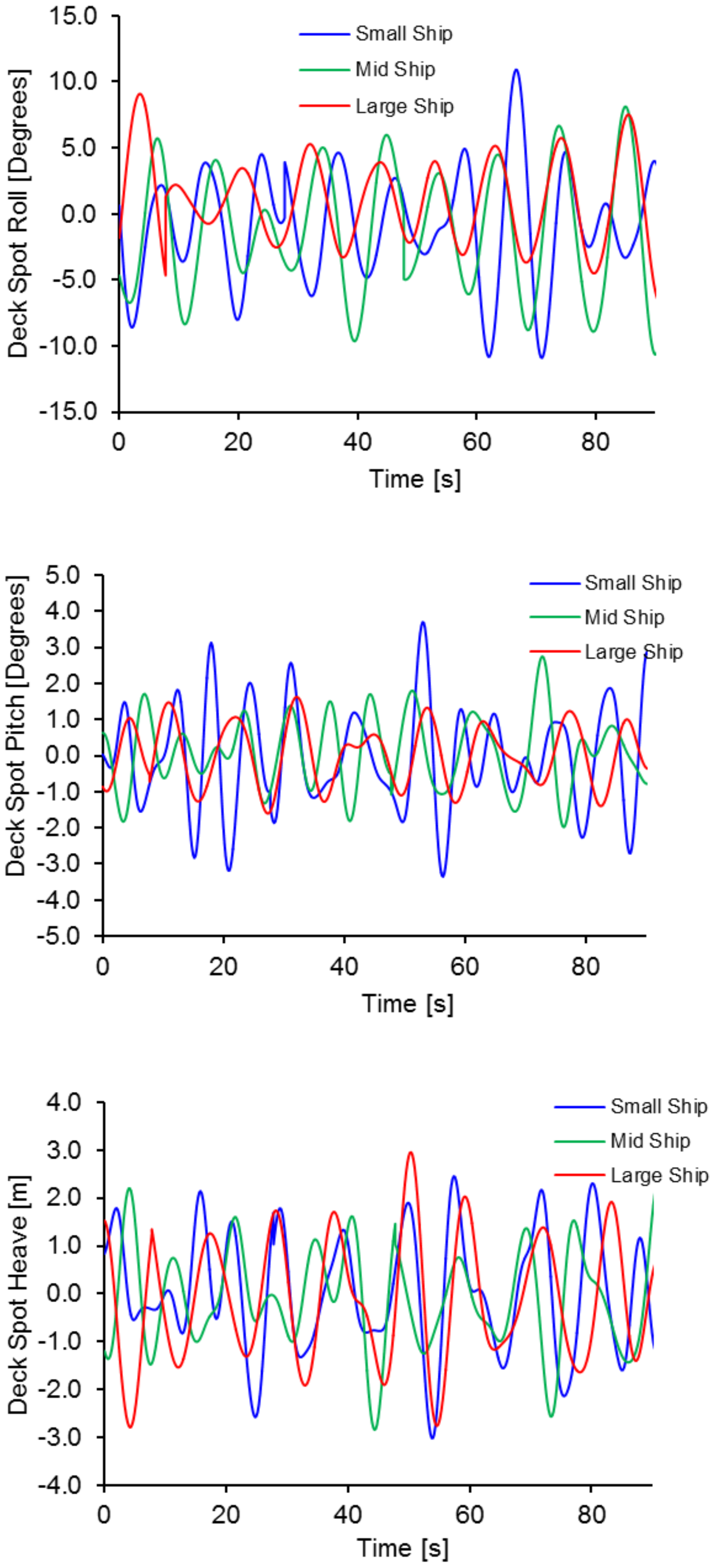

Figure 4.32 Computed displacements of the landing spot for the three ships travelling at 12 knots through sea state 5 with waves coming from Green 45

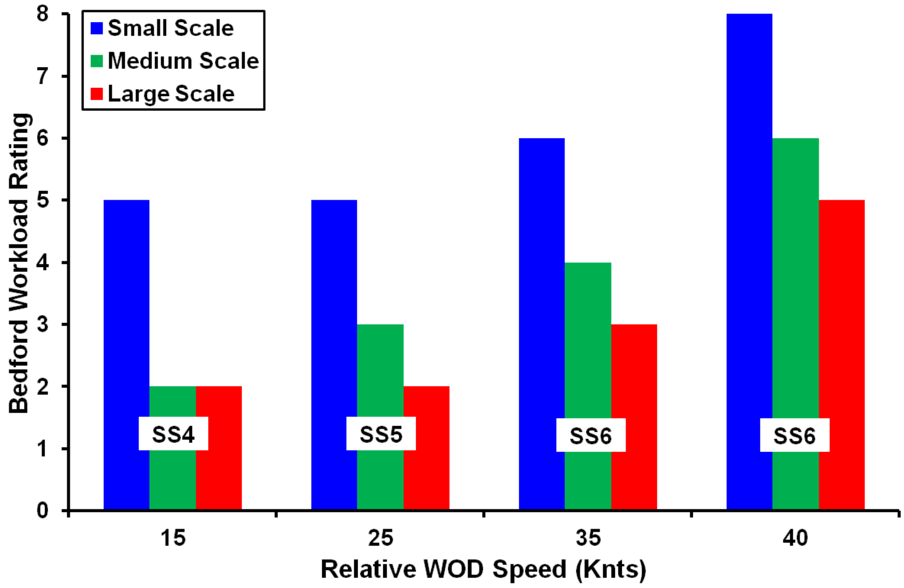

Figure 4.33 Bedford workload ratings awarded by pilot for the hover task above the deck spot, Green 45 WOD, realistic ship motion, 12 knots ship speed.

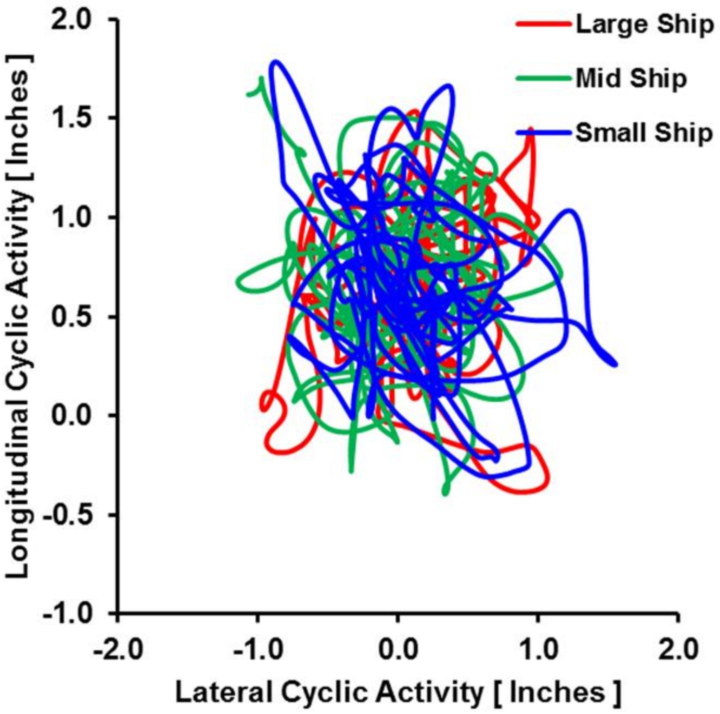

Figure 4.34 Cyclic control activity during hover task over landing spot for a 40 knot Green 45 WOD, sea state 5, realistic ship motion

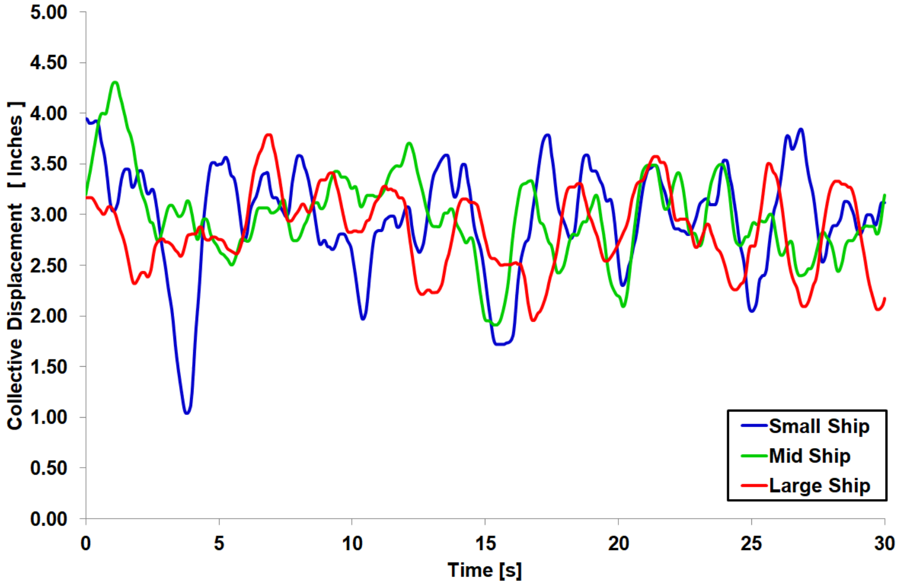

Figure 4.35 Collective control activity during hover task over landing spot for a 40 knot Green 45 WOD, sea state 5, realistic ship motion

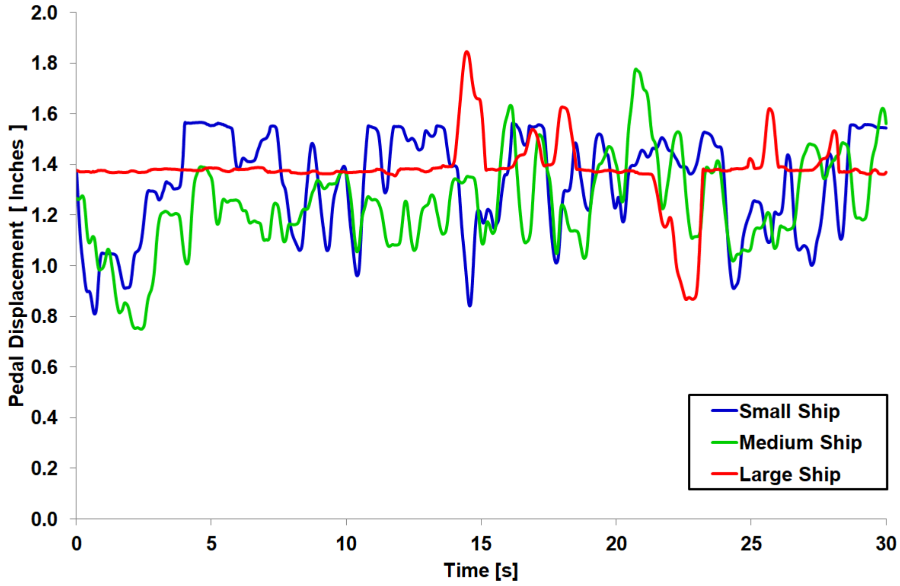

Figure 4.36 Pedal control activity during hover task over landing spot for a 40 knot Green 45 WOD, sea state 5, realistic ship motion

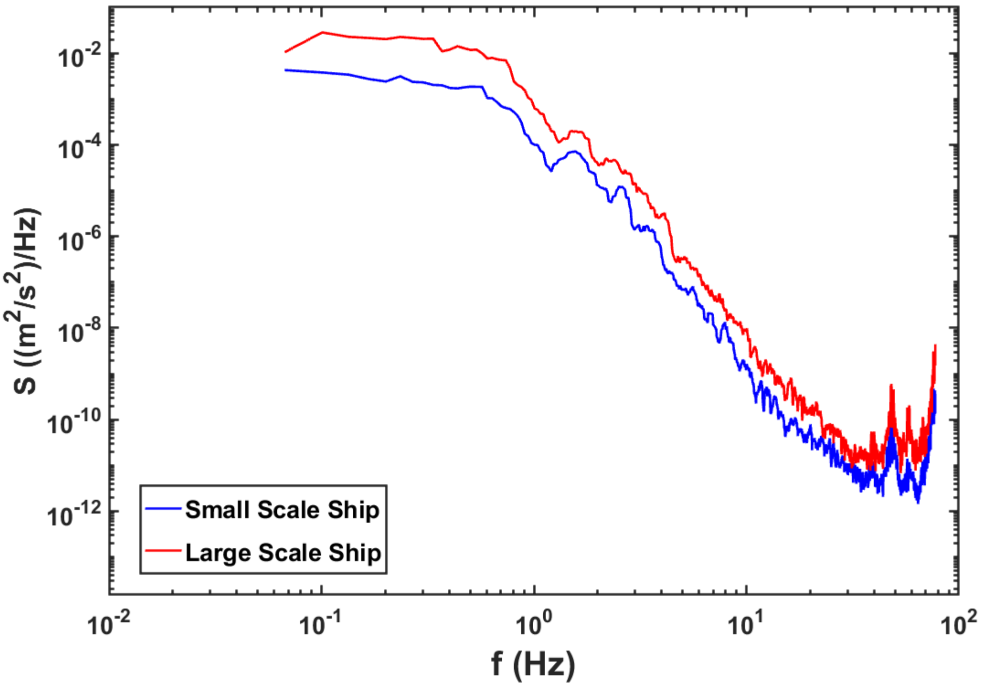

Figure 4.37 Power spectral density plots for the pedal activity, during a thirty second hover above the deck spot, for a 40 knot, Green 45 WOD and limited ship motion.

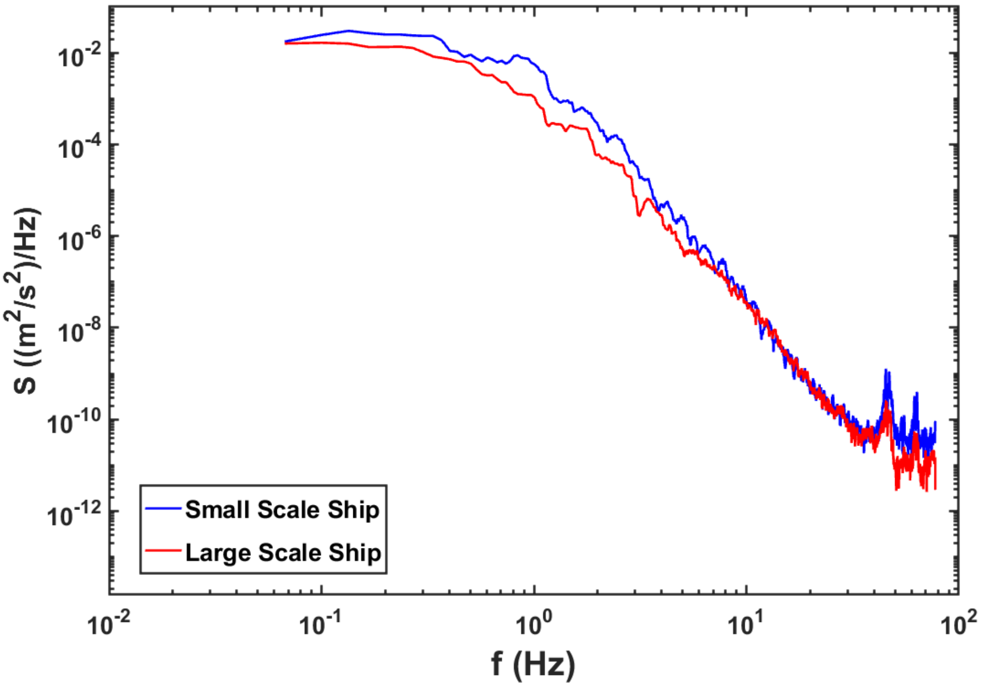

Figure 4.38 Power spectral density plots for the pedal activity, during a thirty second hover above the deck spot, for a 40 knot, Green 45 WOD with realistic ship motion.

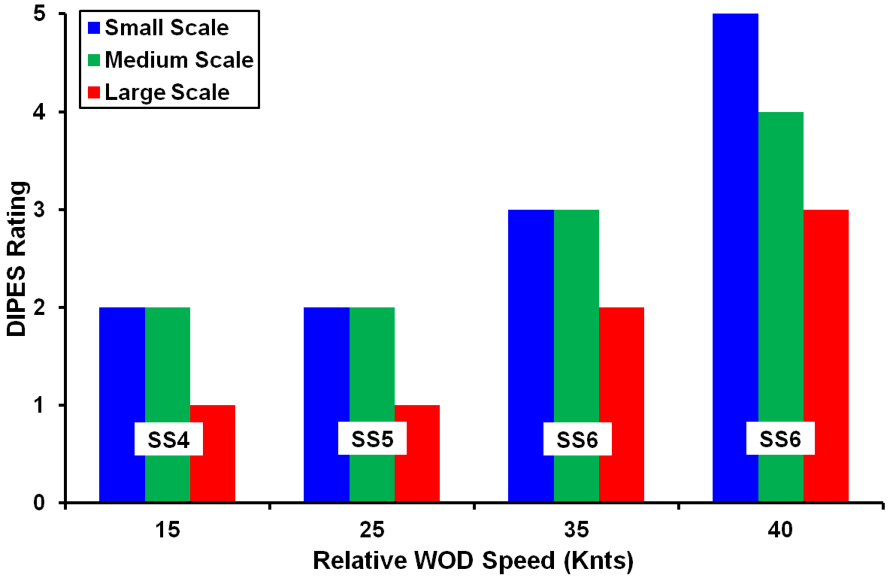

Figure 4.39 DIPES ratings awarded by pilot for the landing task. Green 45 WOD, with realistic ship motion.

CHAPTER 5

SHIP ENGINE EXHAUST MODELLING

This chapter presents the results of a study into the hot gas flows from the ship’s engine exhausts. CFD simulations have been carried out in which the hot exhaust gases mix with the ship’s airwake and flow through the areas that affect helicopter operations where elevated air temperatures are a concern. Parallels are drawn with helicopter operations in the offshore oil and gas industry.

5.1 Introduction

The designs of ship exhaust uptakes and funnels have changed markedly over the years. In the age of steam propulsion the funnel exhaust was often dirty, containing large amounts of particulates, causing problems for the crew above and below decks, as well as making the ship visible at sea. In the years following World War II, a number of studies were carried out to investigate the effects of funnel designs on exhaust gas dispersion using wind tunnels and smoke flow visualization to highlight issues with entrainment of the ship's exhaust [65]. These studies produced design guidance for naval architects, giving suitable dimensions and geometric ratios for features commonly found on a ship's superstructure, including the funnel [66].

In 1976, Baham and McCullum [67], produced a report which updated the guidance on ship funnel designs, along with estimations of exhaust plume temperatures and plume trajectories. It was around this period that ship superstructures were starting to become populated with sensitive electrical equipment, and heating and contamination by exhaust gases was becoming an issue for the ship's instrumentation. As steam propulsion gave way to Diesel and gas turbine engines, the problem of dirty exhaust gas from the use of heavy oils diminished; however, attention became more focused on ship visibility through radar, and the curved surfaces often used on exhaust stacks were removed in an effort to reduce the radar reflections. An example of changes in funnel design can be seen in Fig. 5.1, where the Type 42 Destroyer, which first came into service with the Royal Navy in 1975, is compared with the modern Type 45 Destroyer which entered service in 2009. The Type 42 can be seen to have a funnel which is housed in an aerodynamic fairing with the uptakes protruding through the fairing; this allows the exhaust flow to be carried away by the airwake, above the superstructure. The Type 45 uptakes are flush with the funnel, which is now housed within a sharp edged, rectangular structure which encourages the efflux to become entrained within the turbulent wake in the lee of the funnel and the ship's main mast. The modern design of the Type 45 reflects the advances in management of the radar signature and is less concerned with the behaviour of the exhaust plumes, a common trend amongst current ship designs.

Another factor which is found in more modern ships is the use of combined engine systems to provide propulsive power. The prime movers used by the Type 42 were solely gas turbine engines; however, modern naval vessels often have an integrated electrical propulsion system (IEP), which makes use of Diesel engines to generate electrical power to drive the ship, with gas turbines used to provide power during peak loads. There can therefore be multiple sources of exhaust efflux along the superstructure rather than a single exhaust stack.

While concerns over the dispersion of the exhaust gases and smoke were originally brought forth due to crew health and comfort, visibility of the plume, and the interaction of hot gases and particulates with sensitive instrumentation, modern ship building now also incorporates composite materials which can be degraded when in prolonged contact with hot gas.

Given the various issues that arise from the trajectory and temperature of the exhaust plume, accurately modelling its trajectory and dispersion is an important part of the ship design assessment. Normally, wind tunnel testing is carried out and studies that are published in the public domain often involve simple ship models [68,69,70] although some work has been carried out on modern generic frigate models [71]. Some wind tunnel studies have made use of iso-thermal jets to model the exhaust flows [68], while others have used heaters to produce hot plumes to create buoyancy; in both approaches smoke has been injected to visually track the trajectory of the plumes [72].

More recent work has made use of CFD simulation to allow an increase in both fidelity and complexity of the investigations of ship plume modelling. The majority of the work carried out so far has only been concerned with steady-state calculations of the plume dynamics, although Huang et al [73] used a simplified ship model and RANS simulations to model plume behaviour while the ship was undergoing computed ship motion in heavy seas.

Kulkarni et al [74] produced a comprehensive set of results through use of both steady-state CFD and wind tunnel modelling of a simplified superstructure model. Using a similar topside geometry to the work carried out in the previous references [67,68,69], Vijayakumar et al [75], produced a steady-state CFD study using a heated exhaust jet and found good agreement with the wind tunnel test data. Steady-state CFD modeling of a ship's exhaust was also undertaken by Ergin et al [37], who used a heated jet to show that while some buoyancy effects were noticeable within the plume, these are negligible in comparison with the momentum of the heated jet.

Park et al [76] undertook a steady-state CFD analysis of the exhaust efflux of a large cargo ship to assess possible locations for electronic equipment to minimise potential heat damage from the hot exhaust. Camelli et al [77,78] made use of Large Eddy Simulation (LES) to model the unsteady temperature flow field and emissions around the superstructure of a realistic cargo ship geometry. Although unsteady temperatures were sampled during the CFD simulation, the purpose of the study was to inform on potential issues with personnel operating in noxious conditions and to track the trajectory of the plume.

5.2 Potential Implications for Helicopter Operations

Although, as reported in this thesis, there has been considerable research into understanding the unsteady airwake produced by a ship and its interaction with a maritime helicopter, there has been no comparable study of the effects of entrained hot gases from the ship's exhaust. As previously discussed, modern, single-spot naval vessels often rely on combinations of both Diesel and gas turbine engines to provide power for propulsion, and in doing so emit large volumes of hot exhaust gases which will mix with the ship's airwake and can be carried over the flight deck. The air flow over and around the landing deck will therefore have elevated temperatures that may affect the helicopter's performance; surprisingly, the effect of air temperatures over and around the flight deck on naval helicopter operations has previously received little attention.

Ship exhaust gases potentially impact on helicopter operations when they are drawn into and through the rotor, creating changes in lift due to the localised reductions in air density; furthermore, the helicopter engine intakes are often situated directly beneath the main rotor, so any hot gas passing through the rotor is likely to be ingested by the engines, potentially leading to a loss of power, compressor surging or even flame-out [79,80]. While there is also a potential problem for the helicopter engine if it ingests oxygen-depleted air, this is not a problem for the ship's gas turbine exhausts which operate with considerable excess air, and neither is there believed to be a problem with marine diesel exhausts due to the low volume of diesel exhaust gases emitted in comparison to gas turbine exhaust plumes.

Despite these potential performance and safety issues, there appears to be little evidence from naval helicopter pilots that ship exhaust gases give rise to problems, except for complaints that fumes in the cockpit can be unpleasant. Figure 5.2 shows a Chinook over the landing deck of a RN Fleet Auxiliary vessel, directly in line with an exhaust vent. It could be that the transient disturbances caused by the unsteady air temperatures due to the exhaust plume are indistinguishable from the more general transient disturbances due to the ship's airwake.

In contrast to naval operations, there has been significant concern, research and guidance in relation to gas turbine exhausts on offshore oil rigs and their effect on the helideck environment and helicopter operations. In 2000 the UK Civil Aviation Authority (CAA) and the Health and Safety Executive (HSE) published a report into research on offshore helideck environmental issues [79]. The research was in response to concerns in the UK offshore industry about the threat to helicopter safety from structure-induced turbulence, down-draughting and hot gas plumes generated by gas turbine exhausts and flarestacks. Setting the scene for the research, the report includes the results of a survey of offshore helicopter pilots; one question was *“does turbulence around the platforms cause you a high workload or a safety hazard?”* Of the 145 respondents the answer was an overwhelming *‘yes’* with many of the comments referring to turbine exhausts on the platform.

Also included in [79] are summaries of eighteen incident reports published between 1976 and 1998; eight of these reports cited gas turbine or flarestack plumes as primary or secondary causes of the incident. A particular incident that caused concern occurred in 1995 on the Claymore accommodation platform, 94nm northeast of Aberdeen, where a Sea King helicopter suffered an uncontrolled rapid descent to the helideck. During the approach to the platform, the crew reported that they were aware, from the smell, of the helicopter becoming engulfed in the plume. The hard landing caused the main rotor to deflect downwards so that it impacted the tail boom and severed the tail rotor drive shaft. In 1998, on the Ravenspurn North platform in the southern North Sea, a Eurocopter AS365 suffered compressor surge when applying take-off power from the hover position 10ft above the deck, during which the crew reported audible 'popping' noises. The platform at the time was operating two gas turbine generators rather than the usual single engine and both exhausts were positioned in close proximity to the deck. In 2002 a civil Jet Ranger helicopter was operating close to the chimneys of a power station in Ireland, as the helicopter passed through the plume of the chimney the helicopter engine lost power and ran down. The pilot reported that the entire windscreen had misted over and that no plume was visible at the time of the incident [80]. The reports for these incidents highlighted that high temperature exhaust plumes were significant contributing factors in each case.

5.3 Civilian Aviation Standards for Offshore Oil Platforms

Gas turbines are used on offshore platforms for power generation. The exhaust gases are usually, although not always, discharged vertically upwards and temperatures in excess of 400°C are common. The scenario is similar to that on a ship, except the rig exhausts are generally higher above the deck, and the wind over deck is that due to the prevailing wind alone. The environmental research described in [79] is reflected in CAP 437 “Standards for Offshore Helicopter Landing Areas” [81] which sets limits for the air temperatures over platform helidecks. As far back as 1981, when little research had been carried out and helicopter operator experience was limited, CAP 437 was advocating a temperature rise limit of 2°C or 3°C. The origin of this criterion is not clear but it is believed to relate to the loss of lift equivalent to one passenger; it may also relate to the resolution of the Weight Altitude and Temperature (WAT) charts used by pilots to determine the payload for a given set of environmental factors. CAP 437 has had numerous revisions and the 2013 version still contains the temperature criterion, but it has now been sharpened so that the limit is 2°C above ambient, averaged over three seconds. The three second period is representative of the response time of a helicopter engine to a sudden temperature change. The volume of airspace to which the criterion applies is up to a height above the deck of 30ft plus wheels-to-rotor height plus one rotor diameter; overall, typically around 30m for a medium-weight helicopter.

The statement of the temperature criterion in CAP 437 includes: “*when the results of wind tunnel or CFD modelling indicate a temperature rise of more than 2°C, averaged over a three second period, the helicopter operator should be consulted at the earliest opportunity so that appropriate operational restrictions may be applied*”. This statement recognises that there will be occasions when the criterion cannot be met, so pilots may be required to take measures such as avoiding the exhaust plume when close to the rig, adjusting the payload accordingly, and generally exercising care.

The NORSTOCK Standard [82], developed by the Norwegian petroleum industry for the offshore helicopter industry, is aligned with the UK standard CAP 437, although it discusses air temperatures in terms of mean values and does not mention the three second time interval. At the rig design stage the Standard makes recommendation for stack exhaust height and distance from the landing deck. The Standard also outlines a CFD method for determining acceptable risk for helicopter operations in relation to air temperature rises over the landing deck. The methodology uses CFD to evaluate mean temperatures in the exhaust plumes from gas turbines. The Standard discusses RANS analysis, and requires that the CFD be carried out for a wind direction which takes the plume over the centre of the landing deck, and for different wind speeds. The computed average air temperatures at different heights above the deck are then compared with the Temperature Gradient Matrix shown in Fig. 5.3. Depending on where the temperature/height data point falls, the Matrix then recommends: normal operations, caution, or no operation, corresponding to the green, amber and red sections of the Matrix. It can be seen that caution is triggered by a 2°C temperature rise, and no operation by a 30°C rise. The cautionary measures will be similar to those in CAP 437, i.e. avoid the exhaust plume when close to the rig, adjust payload accordingly, and exercise care.

Within reference [79] there is some simple analysis of the adverse effects of temperature gradients due to hot plumes on a helicopter. If the air temperature passing through the rotor increases, then lift is reduced. Therefore, to support the weight of the helicopter, the power to the main rotor needs to be increased, which means that the margin of thrust control left to the pilot is reduced. The 2°C threshold in CAP 437 requires an increase in power of 0.24% which equates to a loss of thrust margin of 0.17%. The corresponding figures for a 10°C rise in air temperature are 1.22% and 0.86%.

Reference [79] also discusses the effect of temperature change on helicopter engine performance and shows that a 10°C rise in temperature is estimated to result in a transient loss of power of 1.65%, and a loss of control margin of 1.1%. Graphs of simulated engine response are shown in Fig. 5.4. The upper graph shows a step increase in the engine inlet temperature of 10°C, which is held for 3 seconds before a step reduction of 10°C back to ambient. The increase in air temperature means a lower air mass flow into the engine, so in response the rotational speed of the engine increases as shown in the middle graph. The theoretical result of these transient changes on the power output is seen in the lower graph where there are momentary spikes in the power output.

Although these percentages may not seem significant, a 10°C temperature rise will lead to a combined loss of control margin due to the rotor and the engine of about 2%; a pilot is required to maintain a spare 10% of control margin for safety, so 1/5th of that can be lost due to a 10°C rise in ambient temperature.

Another concern of rapid rise in air temperature highlighted in [79] is that of engine surge, which is a concern if the intake air temperature increases at a rate approaching 1000°C per second. The situation can be further complicated if the air temperature is different across the face of the engine, which it could well be due to the discrete turbulent structures that form within the airwake carrying the exhaust plume over the flight deck.

From the discussion above it is clear that the ship exhaust gases could have a negative effect on the helicopter, particularly while it is immersed in the unsteady airwake and flying in close proximity to the moving deck and superstructure of the ship. However there appears to be no previously published research on the effect of ship exhaust gases on helicopter operations. Previous CFD research has been solely used for the investigation of the plume trajectory and its interaction with the airwake produced by the superstructure. In this study the CFD analysis of the plume/airwake interaction is specifically investigated in terms of its relevance to helicopter operations.

5.4 CFD Methodology

As described earlier in this thesis, CFD has been used extensively as a modelling tool to predict the turbulent flow of the ship’s airwake. However, the modelling of hot plumes together with the turbulent airwake involves some extra considerations not required when performing iso-thermal simulations. It was found through experience that the regions occupied by the plume in the immediate vicinity above the superstructure needs careful consideration during the meshing process in order to prevent divergence of the solution. The growth of the cells above the superstructure should be constrained to prevent excessive growth to at least two beam widths above the ship with cells not exceeding 50% of the surface mesh size. An example of the refined mesh can be seen in Fig. 5.5.

To model the transport of the hot exhaust gases from the ship into the airwake, the energy equation was activated within the ANSYS Fluent solver, along with the solution of additional transport equations to account for the buoyancy of the plume. Although the efflux has both momentum and buoyancy, in the near field, where the exhaust is injected into highly disturbed air, the plume is momentum-dominated rather than buoyancy-dominated as observed by Ergin et al [37], amongst others.

ANSYS Fluent solves the energy equation in the following form, shown in equation 5.1 [25]:

$$\frac{\partial}{\partial t}(\rho E) + \nabla \cdot \left(v(\rho E + p)\right) = \nabla \cdot \left(k_{eff} \nabla T - \sum_j h_j J_j + (\tau_{eff} \cdot v)\right) \qquad (5.1)$$

Where k_{eff} is the effective conductivity ($k + k_t$), with k_t defined as the turbulent thermal conductivity, dependent on the turbulent model used. The term J_j describes the diffusion flux of the species j, (in this study the exhaust has been modelled as hot air). The first three terms on the right hand side of the equation represent the transfer of energy due to conduction, species diffusion and viscous dissipation respectively.

To model the exhaust flows for this study, the boundary conditions of both the Diesel and gas turbine exhausts, whose locations are highlighted in Fig. 5.6, were designated as 'mass flow inlets'. However, to give a representation of the velocity profile of the exhaust flow, the exhaust ducting was also included within the model so that the injected mass flow was allowed to develop from a uniform velocity profile for five duct diameters. The gas turbine boundary was specified with a mass flow rate of 131kg.s^{-1} and a temperature of 565°C, while the Diesel exhaust boundaries were both given a mass flow rate of 5.5 kg.s^{-1} at a temperature of 400°C. These figures are typical for ship engines used in frigates that do not utilise waste heat recovery systems. The individual exhaust gas species were not specified and the exhaust was simply defined as air. The ambient temperature was set to ISA standard day conditions of 15°C. For the purposes of this study, the Diesel and gas turbine engines were considered to be operating simultaneously.

The CFD simulations of the exhaust flows around the ship were carried out for a headwind, Green 30° and Green 45° WOD conditions at 40 knots wind speed at anemometer height using an atmospheric boundary layer. The simulations were otherwise carried out as previously described in Chapter 2. The ship geometry is that of the FSC4, seen earlier in Chapter 3.

5.5 Analysis of CFD Flow Fields

This section presents the results from CFD cases for the headwind, Green 30° and 45° WOD conditions simulated with the ship exhaust present, as described above.

5.5.1 Headwind Case

The structure of the plume for the headwind WOD case can be seen in Fig. 5.7, highlighted by iso-surfaces of three constant, mean temperature values above ambient. It is important to note that although the plots of iso-surfaces indicate the topography of the plume dispersal, it does not give an indication of the temperature distribution within the plume.

It is possible in Fig. 5.7 to distinguish between the Diesel and gas turbine plumes, with the greater momentum of the gas turbine exhaust enabling the plume to reach a greater height above the superstructure than the Diesel efflux. The region immediately aft of the main mast shows that some of the hot gases from the turbine have been captured within its wake, while the Diesel exhaust gases is being entrained into the recirculation zone behind the hangar face.

It should also be noted that while the gas temperatures at the turbine and Diesel uptakes are 565°C and 400°C respectively, the gases over the flight deck region have cooled considerably due to their being mixed with the ship's airwake. The mean temperatures above ambient in a vertical plane drawn through the centre of the turbine exhaust can be seen in Fig. 5.8. The high-speed exhaust flow rises to the height of the main mast before being deflected, and by the time it passes over the landing deck the temperatures can be seen to have reduced significantly to about 15°C above ambient.

Figure 5.9 shows the mean temperature contours above the flight deck, but this time in the vertical plane across the landing spot for the headwind WOD case; consistent with Fig. 5.8, the plume shows a central core of hot gas, cooling radially away from the centre. In the immediate vicinity of the flight deck, there is a small temperature rise due to the Diesel exhaust being entrained into the hangar wake.

Although the plots of the mean temperature field in Fig. 5.7 suggest there is little mixing of the gas turbine and Diesel plumes and with few vortical structures present, viewing the instantaneous data for a single time step in Fig. 5.10 shows the presence of chaotic turbulent structures mixing and convecting the hot exhaust over the flight deck. In particular the flow aft of the main mast shows a large region of elevated temperatures due to entrainment of hot efflux, potentially leading to an increase in the ship's thermal signature. Although the exhaust gas itself is at a high temperature, the thermal emissivity of the gases is low and any detectable thermal signature will be due to particulates contained within the exhaust gases; however, the hot efflux could lead to hotspots on the ship superstructure giving a detectable thermal signature.

Careful inspection of the unsteady iso-surface plot in Fig. 5.10 shows that although the bulk of the temperature rise immediately over the flight deck for this WOD condition is due largely to the Diesel exhausts, there is some disruption within the gas turbine plume as it encounters the ship's airwake, carrying exhaust gases towards the flight deck which, due to the unsteady nature of the plume, was not shown in the time-averaged data. It is this mechanism by which temperature fluctuations occur over the flight deck in what appear to be benign regions of the flow, with little temperature variations.

The magnitude of the unsteady temperature fluctuations over the flight deck obtained from the CFD simulation can be seen in Fig. 5.11. The unsteady temperatures were sampled from the CFD at a position above the landing spot at three fractional hangar heights and can be seen to peak at 10°C above ambient, consistent with Figs. 5.8 and 5.9 at those heights (again it should be remembered that the original exhaust temperatures were 565°C and 400°C). To assess the unsteady temperature variations in accordance with the limits set out by CAP 437, the data shown in Fig. 5.11 were then modified to give the three-second moving average temperatures shown in Fig. 5.12. The moving average temperatures show that the 2°C limit is exceeded for significant periods of time at each of the heights sampled with the largest excursions at 100% and 150% hangar heights.

The addition of a bounding box to Fig. 5.10, as shown in Fig. 5.13, highlight the physical limits set out in CAP 437 for which the 2°C limit applies (30 ft plus wheels-to-rotor height plus one rotor diameter). The two helicopter images show the approximate hover positions during a normal translation over the flight deck and at a high hover position used for at-sea replenishment. During a normal translation the main rotor and the engine intake will typically be at about hangar height and will be exposed to the air temperatures shown in Figs. 5.11 and 5.12. Although the effects of the rotor disc are not accounted for within the CFD simulation, it is possible to postulate that the rotor will be drawing in some of the higher temperature flow contained within the core of the gas turbine plume, which are predicted to be about 15°C above ambient. The rotor will experience reduced lift and the helicopter engines will see a reduction in shaft power, potentially impacting on the aircraft, particularly when heavily loaded as could be the case during slung load operations. This condition relates directly to the engine data described in section 5.2 and the associated discussion.

The unsteady temperatures over the starboard edges of the flight deck, Fig. 5.14, show that the temperature rise is negligible at the three hangar heights as neither the Diesel nor the gas turbine plumes extend over the full beam of the ship. Also, despite the asymmetry in the ship's superstructure, with the Diesel funnels present on the port side of the ship, the temperatures over the port edge of the flight deck were seen to be similar to the starboard results.

5.5.2 Green 30° Case

As can be seen in the three views of mean temperature iso-surfaces in Fig. 5.15, unlike the headwind case there now appears to be little interaction between the gas turbine and Diesel exhaust plumes for this WOD case. The Diesel exhaust gases are entrained within the wake of the hangar, while the gas turbine plume is angled away from the flight deck, off the port side of the ship. It is here that the ship’s airwake exhibits a significant downwash in the lee of the ship’s superstructure, putting the gas turbine plume into the flight path for approaching helicopters during the UK RN port-side landing approach. As the gas turbine plume no longer passes over the flight deck there is only a limited temperature rise in that area.

Figure 5.16 shows the mean temperature contours in an oblique vertical plane drawn through the centre of the gas turbine exhaust plume for the 30° WOD. Compared with Fig. 5.8, it can be seen that although the high exhaust gas temperatures are quickly cooled, the rate of cooling is less than in the headwind case where the wake of the main mast enhances the mixing between the exhaust gases and the ship’s airwake.

Figures 5.17 and 5.18 show the three-second average temperatures sampled above the landing spot and over the port edge of the flight deck respectively. Above the landing spot, the temperature is higher closer to the flight deck due to the entrainment of the Diesel efflux into the hangar wake and it can be seen that the 2°C limit as specified in CAP 437 is not exceeded. However over the port edge of the flight deck the core of the Diesel plumes are found in the region of 100% and 150% hangar heights and the 2°C limit is marginally exceeded at the higher sampling point. In the vicinity of the landing deck the hot exhaust gases have significantly cooled through mixing with the ship's turbulent airwake.

Further away from the flight deck, the mean temperature contours in Fig. 5.19 show that the gas turbine plume is now much lower than in the headwind case. The plume can be seen to create a region of elevated temperatures approximately one beam width off the port edge of the flight deck, at an elevation of approximately two hangar heights.

5.5.3 Green 45° Case

With the increase in wind angle to 45°, the efflux from both the gas turbine and Diesel uptakes do not appear to encroach the flight-critical regions over the deck, as shown in Fig. 5.20. As such, the temperature changes over the deck are not significant for helicopter operations, however the plume has now moved significantly off to the port side of the ship, with the core of the plume approximately three beam-widths from the flight deck.

Figure 5.21 shows the contours of mean temperature in an oblique vertical plane through the centre of the gas turbine plume. Taken together with Fig. 5.22, which shows the contours of mean temperature in the transverse vertical orthogonal plane through the landing spot, it can be seen that the trajectory of the exhaust plume is away from the landing deck. The gas turbine exhaust has been entrained into the airwake and into the downwash in the lee of the ship so that one beam width off the port edge of the ship, average temperatures are seen to be approximately 2°C above ambient. Nevertheless, at this distance the gas turbine exhaust has been diluted to the extent that the temperature rise is not excessive and there is no temperature rise above the landing deck.

5.6 Surface Heating

The entrainment of ship exhaust gases can also present problems with regards to localised heating of surfaces bordering the exhaust uptakes, increasing the infra-red signature of the vessel and possibly impacting upon the operation of sensitive electronic equipment and personnel.

As well as the attention applied by ship designers to the reduction of the radar signature, the thermal (infra red) signature of the ship is also important. Although solar heating may raise temperatures significantly above those generated by encounters with exhaust gases, the operation of ships during the night or in cold weather may expose a ship prone to surface heating. One of the advantages of the use of CFD simulation is that the temperatures of the flow immediately adjacent to the surface can be interrogated to give an indication of where potential issues may occur.

As previously shown in Fig. 5.6, the Diesel exhaust funnel is located in close proximity to the hangar and weapon platform. This configuration presents an unfavourable situation as the Diesel efflux, unlike that from the gas turbine uptake, has relatively low momentum with the plumes unable to break through the shear layer arising from the funnel structure. Furthermore, there is a large degree of entrainment of hot gases that occurs above the weapon platform which can give rise to an increase in surface temperature, as seen in Fig. 5.23. Using streamlines coloured by mean temperature to provide flow visualisation of the mean velocity flow field in this area reveals the presence of a strong vortex core which captures the hot gas and could lead to a surface heating of up to 9°C above ambient. Once free of the weapon platform, the exhaust gases are then further entrained within the hangar wake, slightly increasing the surface temperature of the flight deck and hangar face. The temperatures that the metal surfaces of the ship will be heated to will depend not just on the temperature of the gases adjacent to the surface, which is what is shown in Fig. 5.23, but also the local heat transfer coefficient and the rate of heat conduction into the superstructure. Hence the temperatures shown are the maximum the surface could reach.

5.7 Modification of Airwake Due to Presence of Exhaust Plumes

The flow over the flight deck has previously been shown in Chapter 3 to be affected by changes to the ship's superstructure; likewise when a large exhaust plume is ejected from the ship, the airwake may be modified. The plume of a gas turbine can be a significant structure in itself, being many metres in height and width along with mass flow rates up to 140 $Kg.s^{-1}$ resulting in high efflux speeds. Figure 5.24 shows the ship's airwake in a vertical plane along the centerline of the ship as contours of normalised longitudinal mean velocity for the Headwind WOD case, with and without the presence of the exhaust plumes.

The mean flow field in the presence of the exhaust plume can be seen to be identical to the iso-thermal case forward of the main mast, however aft of this the airwake has been significantly changed with a reduction in the flow speeds occurring high above the flight deck due to the turbine plume presenting itself as a blockage to the air flow over the ship.

A comparison of the turbulence intensities over the flight deck, presented in Fig. 5.25, is further evidence of the flow being modified over the flight deck because of the turbine plume, with a 50% reduction in the magnitude of the turbulence in the region above the hangar. Below the hangar, close to the flight deck, there is a similar, albeit less significant reduction in the turbulence between the cases with and without the exhaust plume.

It should be noted that although this modification to the flow over the flight deck implies that aircraft operations may benefit as a result of a reduction in the turbulent wake, the large volume of heated air passing through this region will create fluctuations in air density, resulting in changes the aerodynamic loading of the rotor system potentially negating any gains from the modified wake.

5.8 Chapter Summary

The study described in this study has shown that, for the headwind conditions considered, the 2°C limit as defined in CAP 437 can be exceeded for locations over the central area of the flight deck, with the recirculation behind the hangar creating a turbulent environment to transport the hot exhaust gases down towards the deck surface. The magnitude of the temperature rise increases with height above the deck as the gas turbine plume becomes more influential. It is assumed that the presence of a helicopter, hovering at hangar height will draw in some of the gas turbine plume, exacerbating the temperatures experienced by the aircraft, particularly in high hover positions as shown in Fig. 5.13. However, practical experience shows that when the gas turbine is operating, the ship will be at high speed, (typically around 25 knots), and at these speeds the helicopter will not normally perform high hover maneuvers.

Closer to the deck, the turbulence generated by the superstructure leads to greater fluctuations in temperature which could impact on the helicopter's engine performance and rotor thrust, particularly as the turbulent structures will be carrying discrete masses of hot gas, therefore presenting the face of the engine intake and the main rotor with temperatures that vary both temporally and spatially.

For the Green 30° and Green 45° WOD cases the magnitude of the unsteady temperatures measured over the flight deck are reduced in comparison to the headwind case. However the exhaust efflux in the lee of the ship exhibits a significant downwash, bringing the Diesel and gas turbine plumes to levels approaching hangar height, which may impact on helicopters operating off the port side of the ship.

The CFD simulations were carried out for an ambient temperature of 15°C, however maritime operations are also carried out in parts of the world where the ambient temperature can approach 50°C. Although air properties will change with temperature, the temperature field resulting from the mixing of the heated and ambient gases is due to momentum-dominated mixing and the temperature increases above ambient will be much the same for different ambient temperatures. Therefore temperature fluctuations of 10°C above a 50°C ambient may have an even greater impact on the flight performance of a helicopter already operating with reduced engine power

Although care is taken by naval architects to reduce the radar cross sectional area as much as possible, the use of exhaust uptakes that are flush with the superstructure can result in localised heating of the ship's topside surfaces, increasing its infra-red signature. Furthermore the placement of exhaust stacks close to areas used by aircraft, personnel and equipment is detrimental as the exhaust constituents of Diesel engines can be more hazardous than gas turbine exhaust, giving rise to adverse environmental considerations especially as the efflux velocity of the Diesel engines’ exhaust may not be sufficient to allow it to break away from the ship's airwake.

Figure 5.1 Funnel designs of the Type 42 (top) and the Type 45 (bottom)

Figure 5.2 Ship exhaust discharging over helicopter deck.
Photo by Courtesy of Lt Cdr RN L S Evans

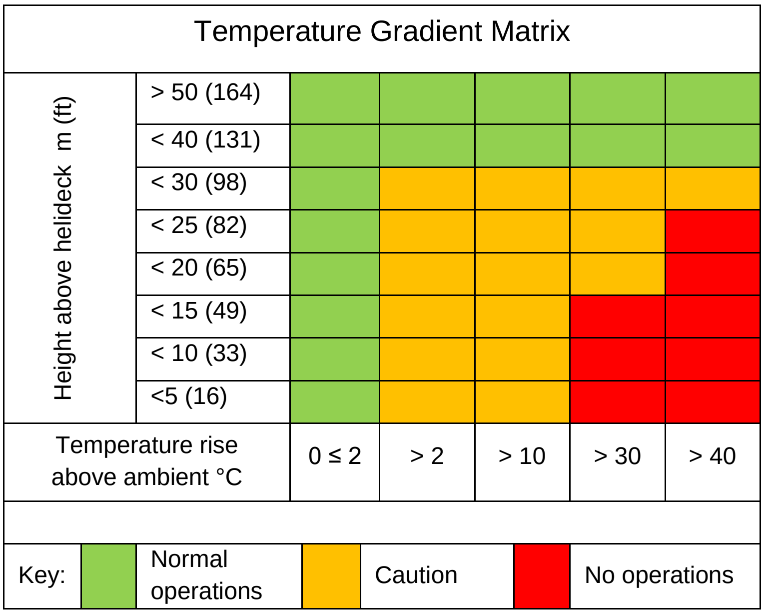

Temperature Gradient Matrix						
Height above helideck m (ft)	> 50 (164)	🟩	🟩	🟩	🟩	🟩
	< 40 (131)	🟩	🟩	🟩	🟩	🟩
	< 30 (98)	🟩	🟧	🟧	🟧	🟧
	< 25 (82)	🟩	🟧	🟧	🟧	🟥
	< 20 (65)	🟩	🟧	🟧	🟧	🟥
	< 15 (49)	🟩	🟧	🟧	🟥	🟥
	< 10 (33)	🟩	🟧	🟧	🟥	🟥
	<5 (16)	🟩	🟧	🟧	🟥	🟥
Temperature rise above ambient °C		0 ≤ 2	> 2	> 10	> 30	> 40
Key:	🟩	Normal operations	🟧	Caution	🟥	No operations

Figure 5.3 A sample NORSOK chart showing acceptable levels of temperature rise over the flight deck [82]

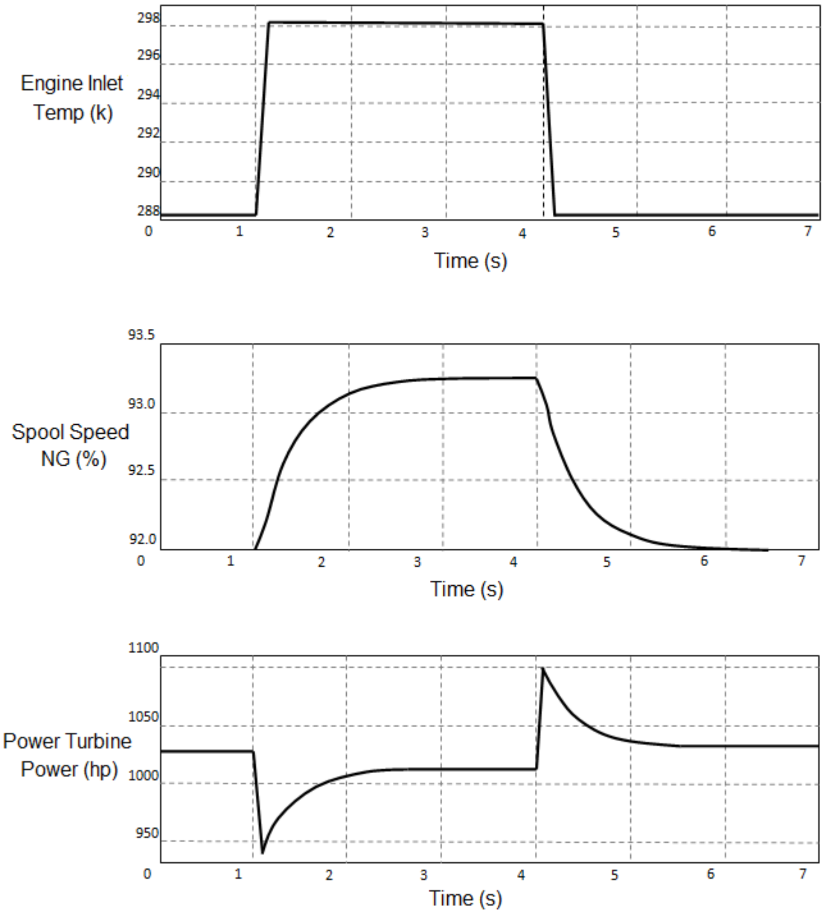

Figure 5.4 Simulated response of a typical helicopter engine to a 10°C change in bulk inlet temperature over a three second period [79]

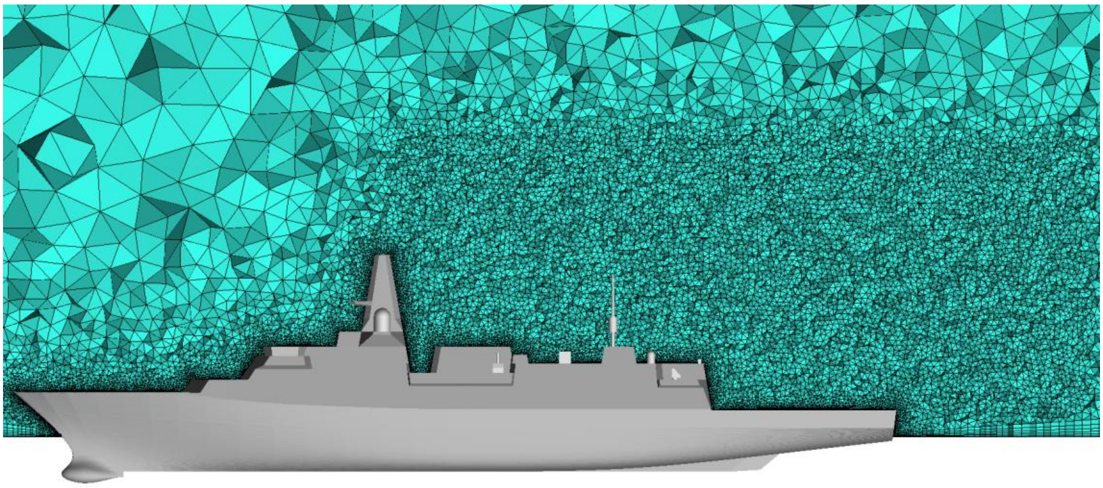

Figure 5.5 Detail of meshing refined for exhaust simulations

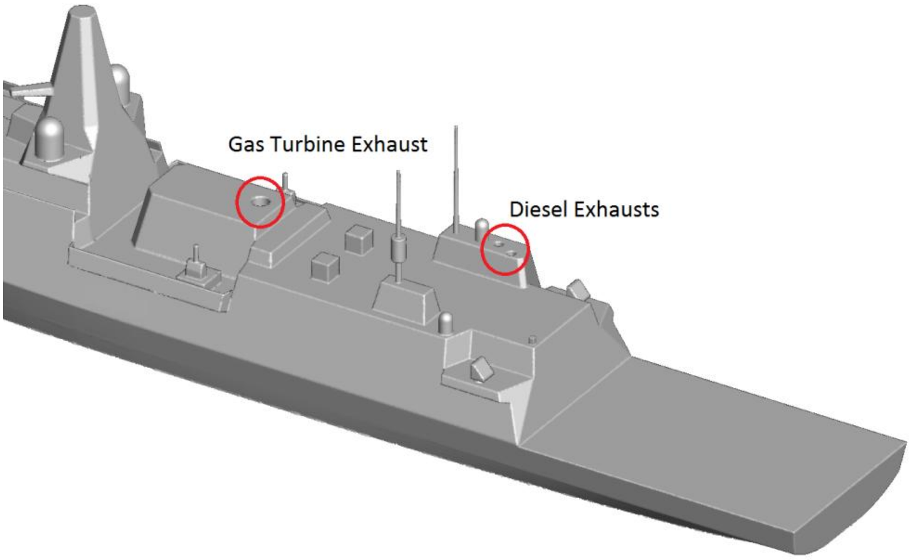

Figure 5.6 Location of exhaust uptakes used for the CFD simulations

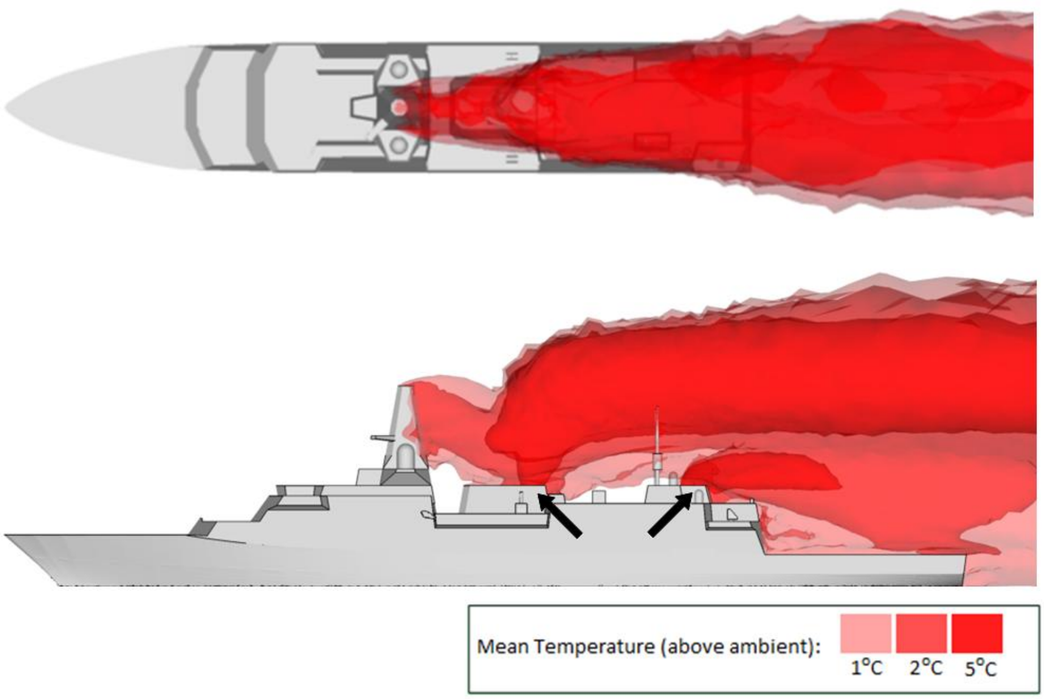

Figure 5.7 Iso-surfaces of mean temperature for a Headwind WOD

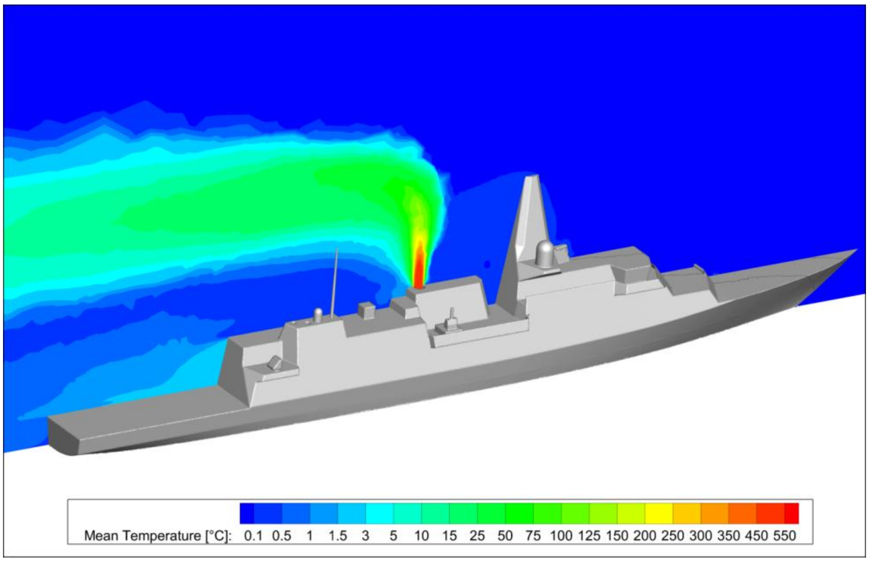

Figure 5.8 Contours of mean temperature in the vertical plane through the centre of the gas turbine exhaust plume for the headwind WOD

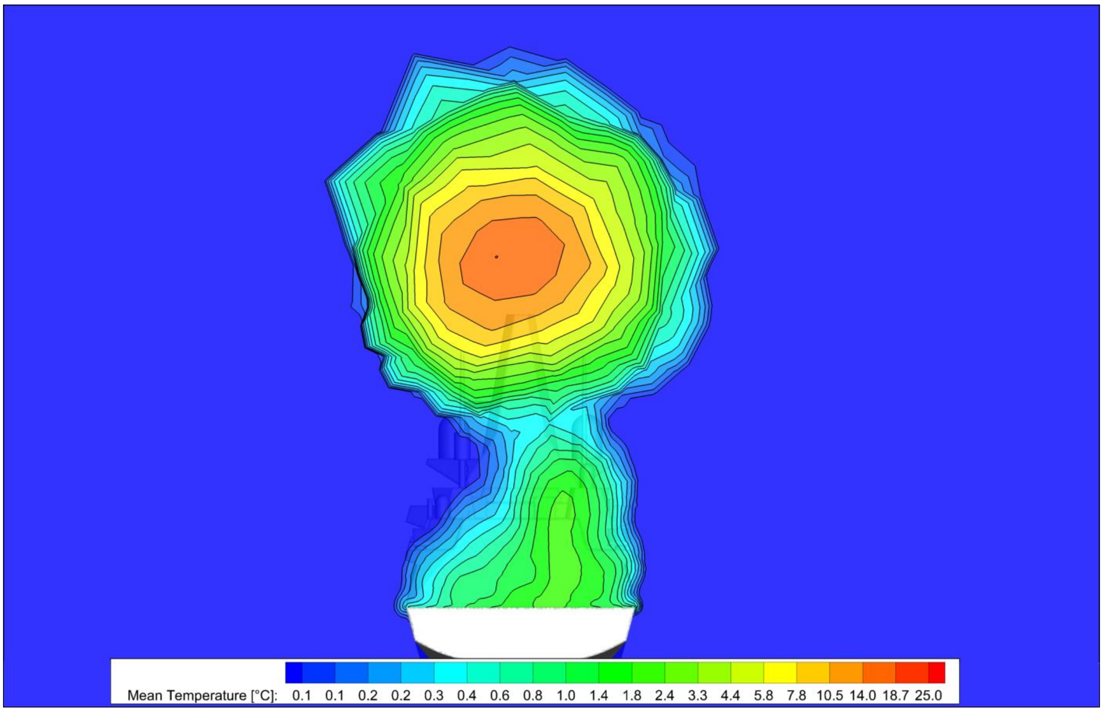

Figure 5.9 Mean temperature contours above ambient in a vertical plane through the landing spot for the Headwind WOD case

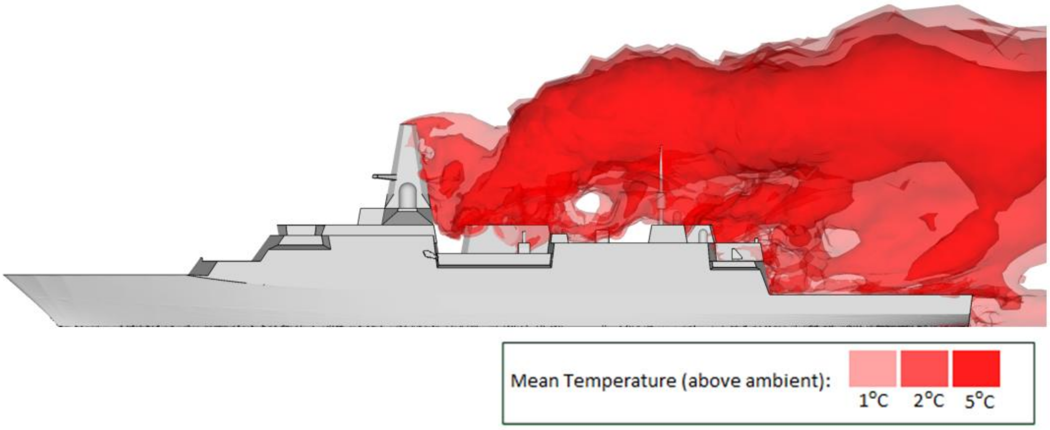

Figure 5.10 Unsteady iso-surfaces of temperature for the Headwind WOD case

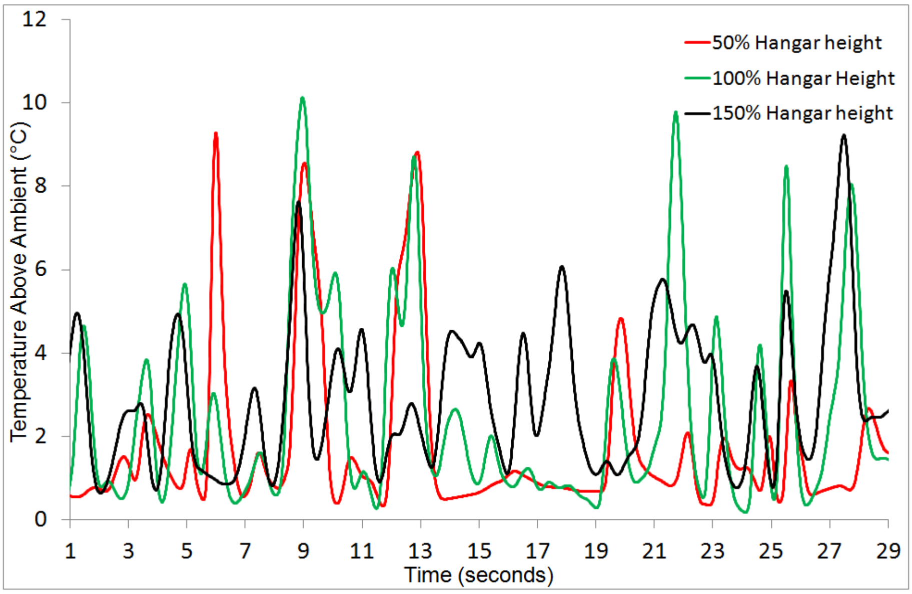

Figure 5.11 Unsteady temperature variation over the landing spot for the Headwind WOD

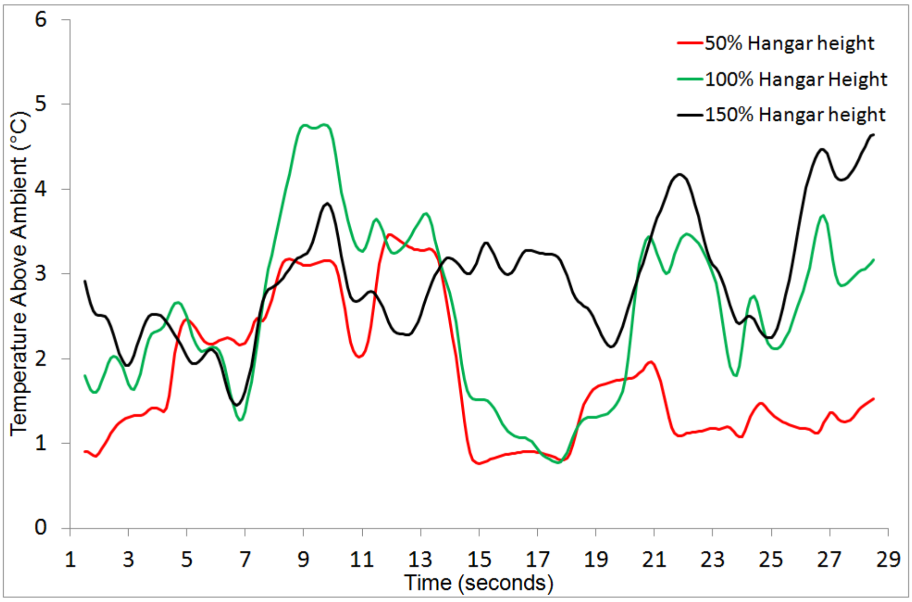

Figure 5.12 Three-second moving average temperatures over the landing spot derived from the data shown in Figure 5.11

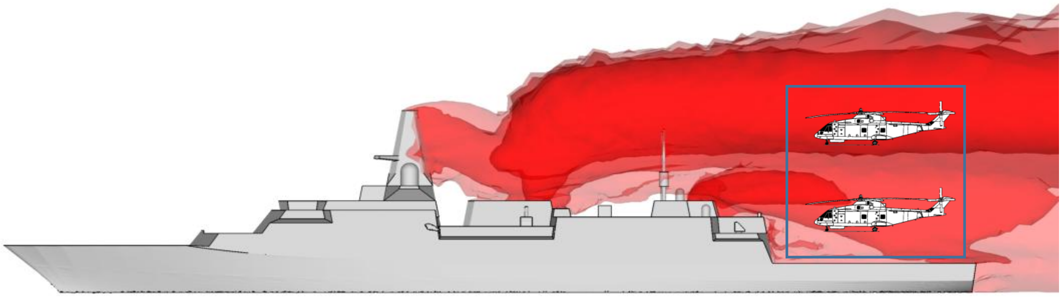

Figure 5.13 Definition of the boundaries as set out in CAP437, also showing a helicopter operating at hover positions during both standard approaches and slung load operations

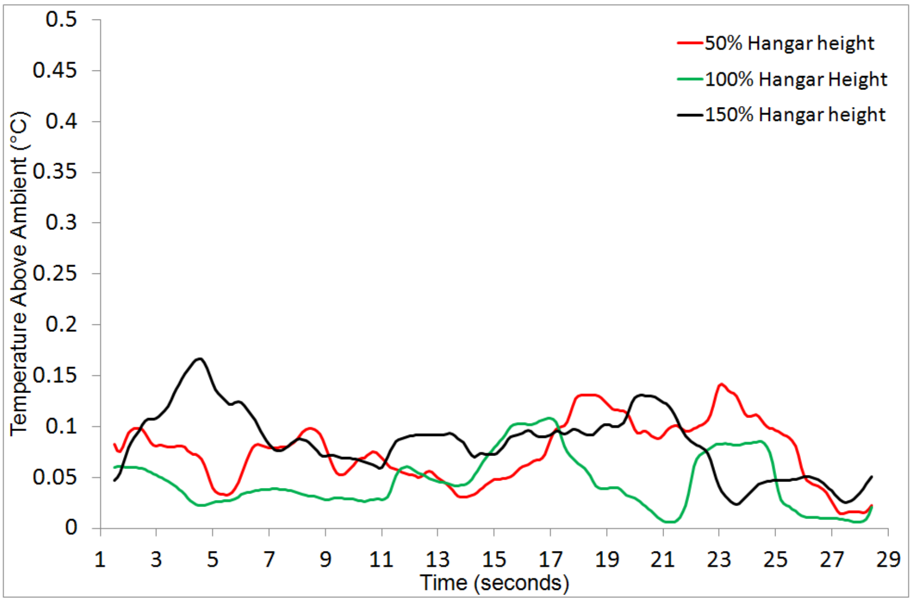

Figure 5.14 Three-second moving average temperatures over the starboard edge

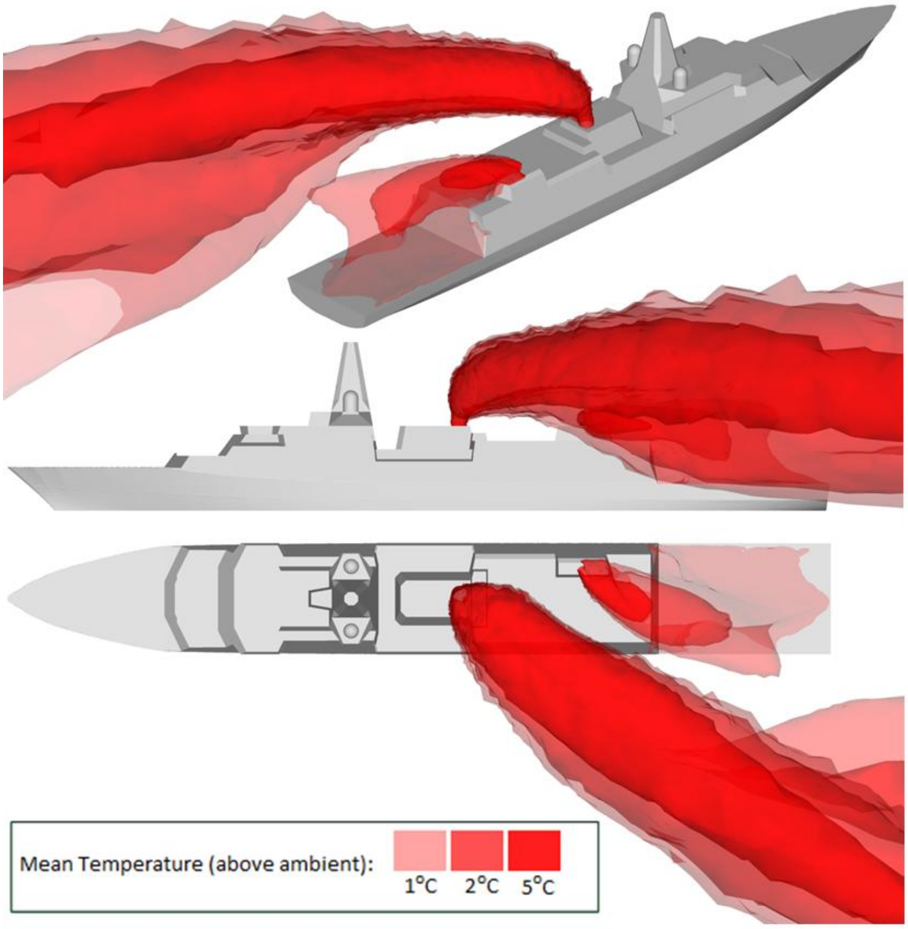

Figure 5.15 Iso-surfaces of mean temperature for the Green 30° WOD case

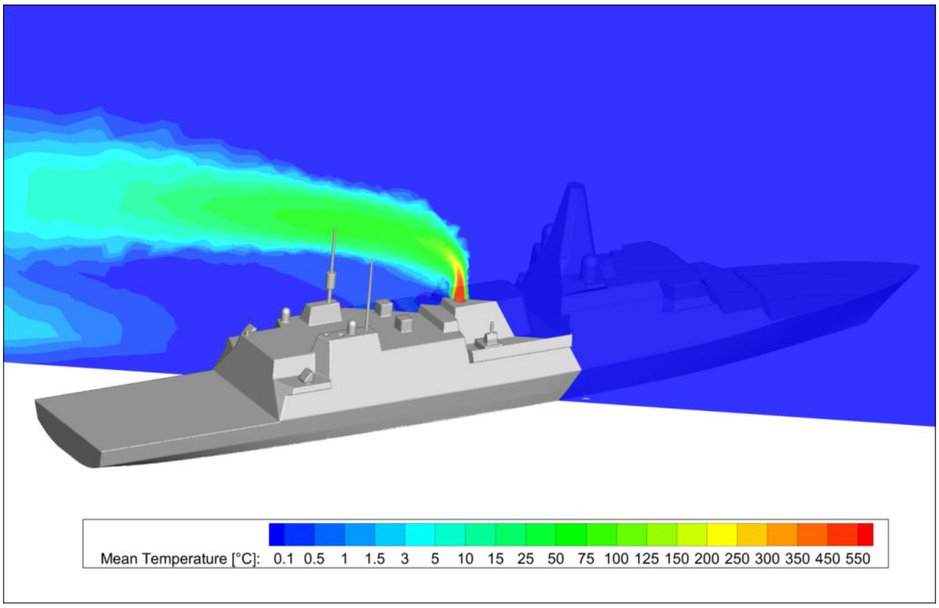

Figure 5.16 Contours of mean temperature in the vertical plane through the centre of the turbine exhaust plume in a 30° WOD

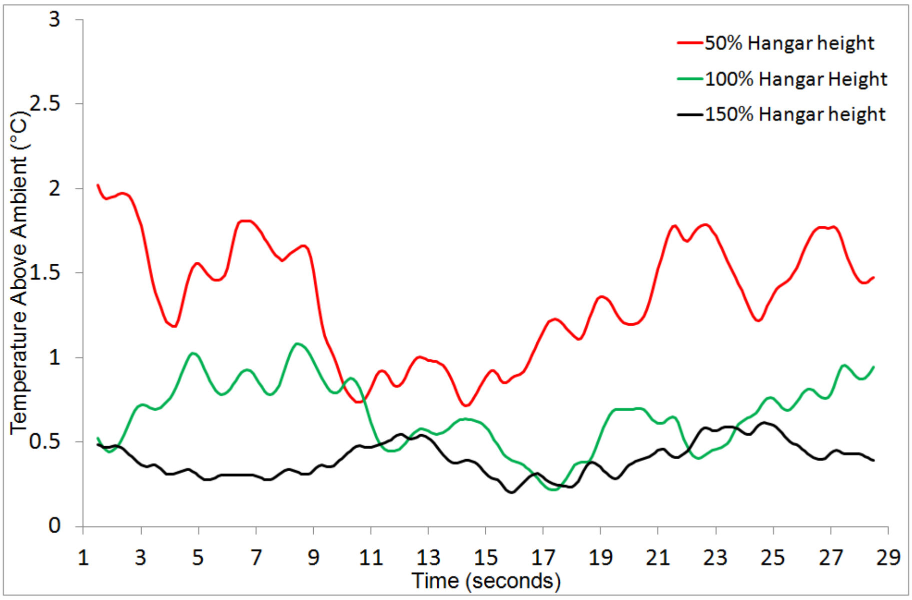

Figure 5.17 Three-second moving average of the temperatures over the landing spot

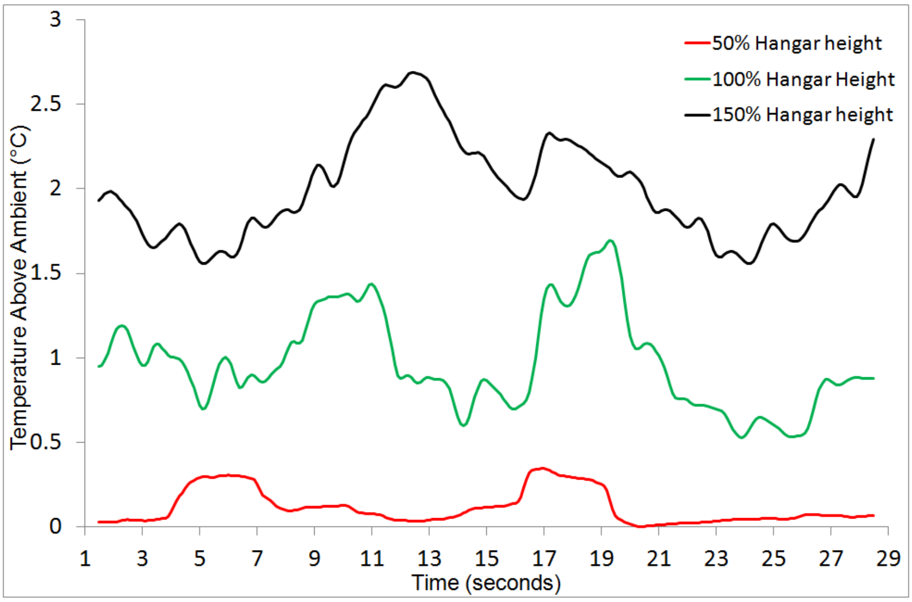

Figure 5.18 Three-second moving average of the temperatures over the port deck edge

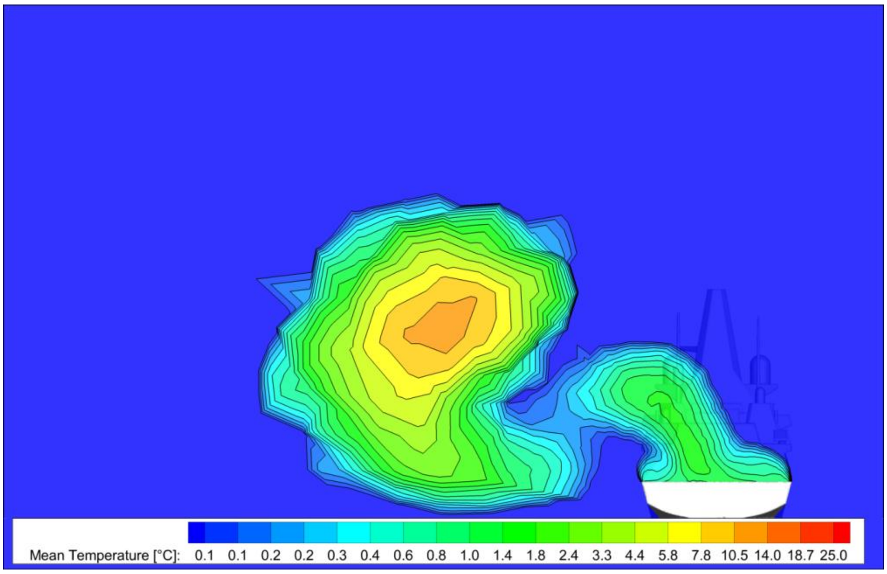

Figure 5.19 Contours of mean temperature, in a vertical plane across the landing spot for the Green 30° WOD case

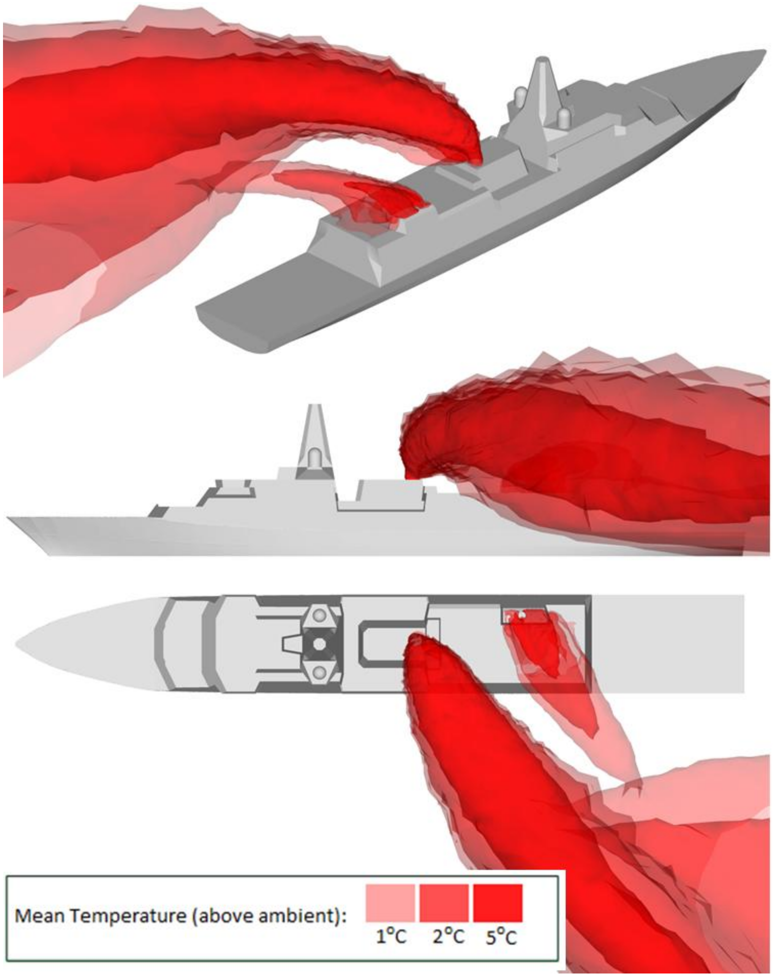

Figure 5.20 Iso-surfaces of mean temperature of the mean flow field for the Green 45° WOD case

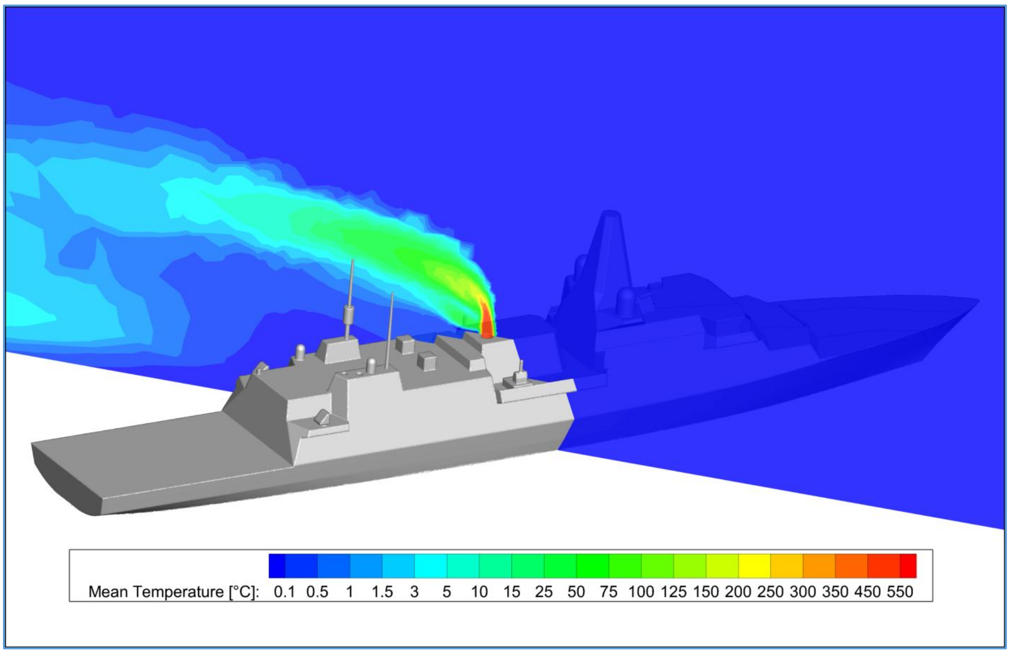

Figure 5.21 Contours of mean temperature in the vertical plane through the centre of the turbine exhaust plume in a 45° WOD

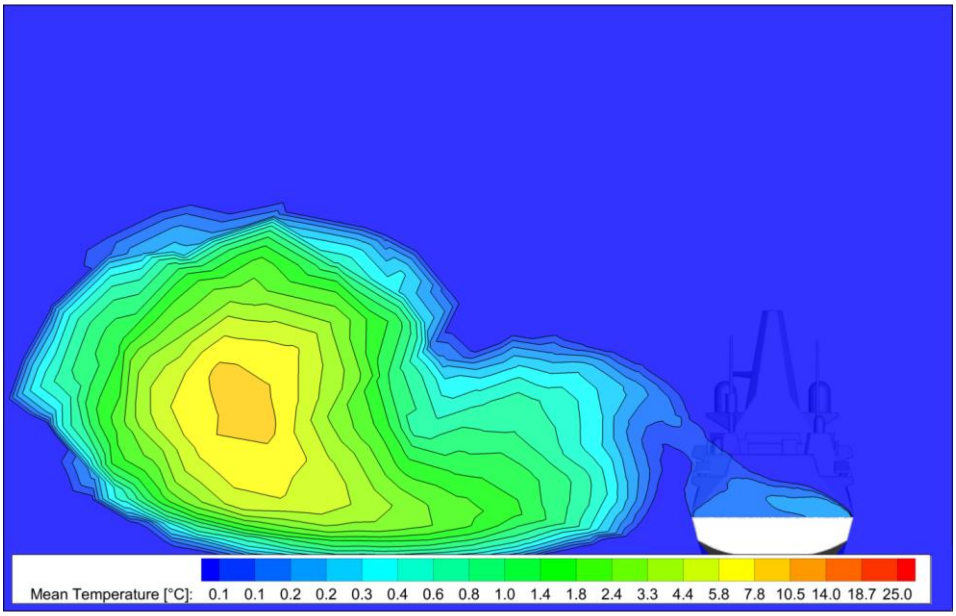

Figure 5.22 Contours of mean temperature, in a vertical plane across the landing spot for the Green 45° WOD case

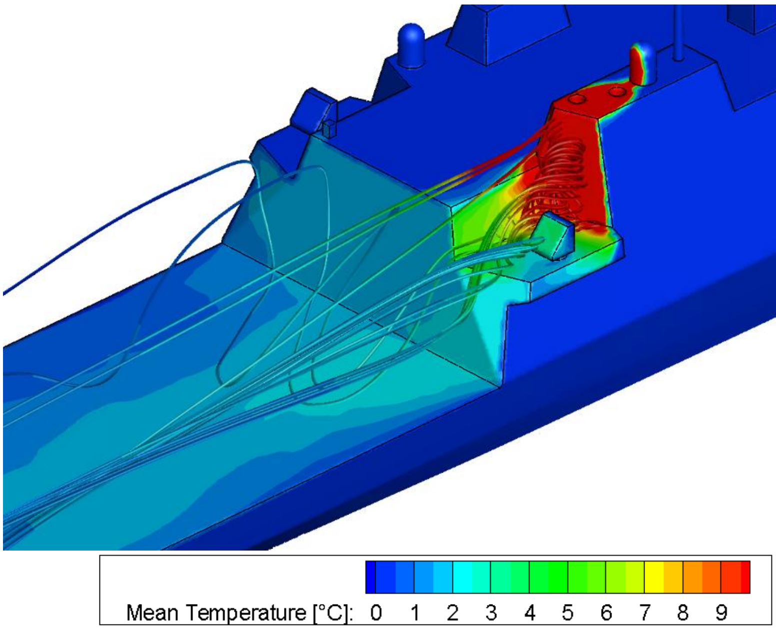

Figure 5.23 Contours of mean surface temperature above ambient and streamlines indicting recirculating flow, coloured by mean temperature

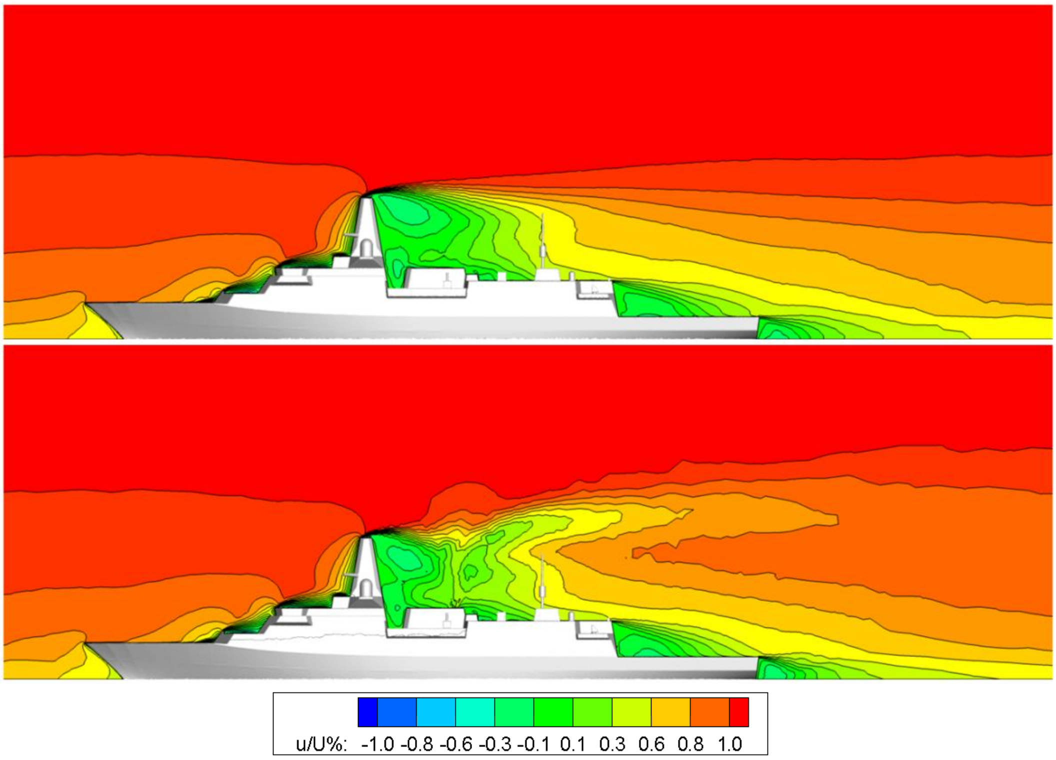

Figure 5.24 Contours of normalised longitudinal velocity for an iso-thermal case (top) and in the presence of ship exhaust (bottom) for the Headwind WOD case

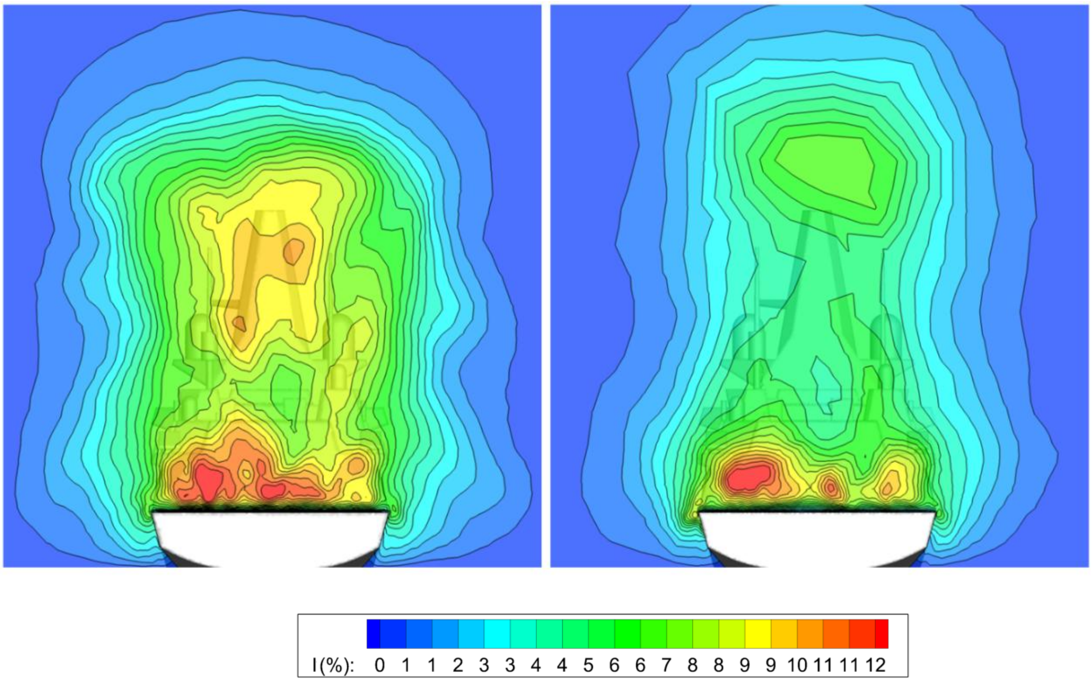

Figure 5.25 Contours of turbulence intensity for an iso-thermal case (left) and in the presence of ship exhaust (right) for the Headwind WOD case

CHAPTER 6

CONCLUSIONS AND RECOMMENDATIONS

This final chapter will draw out the main conclusions from the research that has been reported in the thesis. A number of recommendation are also made on how the application of modelling and simulation can be developed further, for both ship design and SHOL testing.

A very positive aspect of the research that has been carried out is that it was conducted in parallel with the design development of a real ship, working closely with colleagues at BAE Naval Ships. The interaction has been alluded to within the thesis, but is not explicitly stated because of confidentiality restrictions.

There are many conflicting requirements that have to be considered during the design of a ship, not least the layout of the many complex systems which, once placed on the ship, constrain any later proposed design modifications. From the aerodynamic perspective, the drive to reduce the radar cross section of the ship takes precedence over the operability of the ship's helicopter. Despite these practical considerations a number of design changes have been made to a future ship and this is the first time that a British warship will have been designed taking into account the operational envelope of the helicopter. Having introduced to the design process the concept of modelling and simulation in support of helicopter operations, it is important that work to improve and refine the simulation processes continues. Simulation is the imitation of the real world and as such it will never be perfect; the question that is always pursued is: when is the simulation good enough? The simulation of the ship-helicopter dynamic interface is still not good enough and the quest to improve it will continue.

6.2 Conclusions

The contributions that the research described in this thesis have made to current knowledge and understanding have been discussed in the relevant chapters. The main conclusions are as follows:

1. Computational fluid dynamics is an effective tool for modelling the time-accurate airwake of a full-scale warship. CFD is also an effective tool for modelling the

dispersion of hot gases from the ship's engines. Overall, CFD is a suitable and more flexible method for modelling the ship aerodynamics than is wind tunnel testing. The use of density boxes has been shown to be beneficial for sustaining turbulent fluctuations in the flow and for providing finer details of the flow when required.

2. The Virtual AirDyn has been shown to be an effective tool for distinguishing how different design configurations of a ship's superstructure will affect the unsteady loads on a helicopter.
3. Of the four ship design options examined in this thesis, FSC4 was identified as creating an airwake that would impose the lowest combined unsteady loads on a helicopter.
4. The airwake of the smaller Type 23 frigate created lower unsteady loads than any of the larger FSC variants, consistent with the observation of earlier studies that larger ships shed larger vortices at a lower frequency and may lead to an increase in pilot workload when flying in the airwake.
5. The smooth sides of a modern warship that has been designed to reduce radar cross-section will affect the airwake over the landing deck, particularly in winds from ahead and up to 30°. The wind will flow unimpeded along the side of the ship and the air will have a higher velocity when it separates from the hangar edges, so creating stronger wakes and shear layers with steeper velocity gradients than for ships with irregular, modular superstructures.
6. When using time-accurate CFD to create unsteady airwakes for a particular ship geometry, a new airwake has to be created for every wind angle. However, the airwake that has been computed for one wind speed can be effectively scaled on Strouhal number to different wind speeds.
7. It has also been demonstrated that a CFD-generated airwake for a given flow direction can be scaled for ships that are geometrically similar but of different size. Even though the inclusion of an atmospheric boundary layer does not comply with the scaling criteria, the scaling is still effective if the ABL is included in the CFD.
8. Piloted simulation of helicopter landings to ships of different sizes has confirmed that when the ship motion is limited, the airwakes of larger ships create higher pilot workload when flying to the larger ships, even though the deck of the smaller ship is more confined and the superstructure is closer to the aircraft.
9. When realistic ship motion that is consistent with the ship size and is based upon sea states that increase with wind speed is used in the piloted simulation, the previous observation that larger ships create higher pilot workload is no

longer necessarily true. A smaller ship will have greater roll and pitch than a larger one and the resultant deck motion will be more dynamic, as well as being more confined. Simulated deck landings must include realistic ship motion.

10. Notwithstanding the previous conclusion, when simulation and modelling is being used to compare the effect of ship geometry changes on the helicopter's aerodynamic loads, this can still be done with no motion because a ship superstructure that has poor aerodynamics will do so whether it is moving or not.
11. It is known that higher air temperatures adversely affect both helicopter rotor lift and engine power. For the operation of maritime helicopters in the offshore oil and gas industry there are recommendations for the safe limits of localised air temperature rises. There are no such recommendations for shipborne helicopters where ship engine exhaust gases can also increase the local air temperatures.
12. Ship engine exhaust gases can be entrained into the wakes of elements of the ship's superstructure and can lead to surface heating and hence increased infra-red emissions. Surface heating should be included in the aerodynamic analysis of a warship.
13. For the conditions and ship configuration considered in this thesis, the exhaust gases from the main gas turbine, which had an initial temperature of 565°C were significantly cooled through mixing with the turbulent cross-flow of the ship's airwake. Nevertheless, air temperatures of up to 20°C or more were predicted at the core of the plume above the flight deck. The temperature of the ship's engine exhaust gases should be assessed more carefully at the design stage and additional cooling or waste heat recovery should be considered.

6.2 Recommendations for Future Work

During the course of the research, a number of observations have been made that would continue the improvement of the modelling and simulation techniques that have been described in this thesis.

1. The creation of ship airwakes has evolved and become more comprehensive as CFD techniques and computing power have developed. To produce a single airwake for a 150m long ship can take about 3 days on 128 processors (recent work on the Queen Elizabeth aircraft carrier took 30 days to create a comparable airwake). The simulation techniques would be more useful if the

airwakes could be created more quickly so that superstructure assessment could be made within the design cycle, preferably on a desktop computer.

- It is therefore recommended that a simpler technique, such as an unsteady inviscid solution on a less refined grid be assessed to see if it is still effective as a means to evaluate the effect of ship superstructure modifications on helicopter loads.

2. While the AirDyn has been demonstrated to be a useful tool for assessing the effect of ship superstructure modifications on unsteady helicopter loads, the appraisal of twelve parameters (mean and RMS loads in six axes) is subjective. To enhance this simulation tool a pilot model or autopilot could be included and, instead of holding the helicopter fixed at locations, it could be flown through a prescribed landing flightpath and the necessary control inputs could be assessed as a measure of pilot workload.
    - It is therefore recommended that an existing pilot model be adopted and integrated with the AirDyn to produce an enhanced tool for assessing the effect of ship airwakes on a helicopter.

3. If recommendations 1 and 2 are successfully carried out, then a desktop design tool is feasible.
    - It is therefore recommended that recommendations 1 and 2 be built upon to develop a desktop design tool that can be used within the design cycle of a helicopter-enabled ship.

4. Including ship motion in the simulation raises questions about the CFD-generated airwake which is currently produced for a stationary ship and moves with the ship motion in the simulation. This has long been recognised as an area for investigation and the current mitigation is that while it is accepted that the ship motion will affect the airwake, the frequency of the additional perturbation is outside of the frequency range that adds to the pilot workload. Notwithstanding the previous recommendation about simplifying ship airwakes,
    - It is recommended that ship airwakes be created with and without ship motion and implemented in both the Virtual AirDyn and in piloted flight simulation to assess the effect on simulation fidelity.

5. CFD-generated airwakes have been successfully compared with wind tunnel and at-sea measurements and there is confidence in their fidelity. However, in this thesis it has been reported how CFD has also been used to study the mixing of the ship's hot engine exhaust gases with the airwake and there are no reliable unsteady measurements available in the literature with which to compare.
    - It is therefore recommended that an experimental wind tunnel study be carried out to model the discharge of hot air from an exhaust uptake on a simple bluff body superstructure to provide unsteady air temperatures over a range of conditions, and to compare these with a time-accurate CFD analysis of the experiment.

6. As noted in the Conclusions above, there are currently no recommendations for temperature limits arising from ship engine exhaust gases in relation to helicopter performance.
    - It is therefore recommended that the effect of unsteady air temperatures on helicopter performance should be established and recommendations for safe limits for naval operations should be developed.

REFERENCES

1. Lumsden, B. and Padfield, G.D. “Challenges at the Helicopter-Ship Dynamic Interface”, Military Aerospace Technologies – Fitec ‘98, IMechE Conference Transactions, Institution of Mechanical Engineers, Wiley, UK, 1998.
2. Roper, D., Owen, I., Padfield, G.D. & Hodge, S. J., “Integrating CFD and piloted simulation to quantify ship-helicopter operating limits”, Aeronautical J, 2006, 110 (1109), 419-428.
3. Forrest, J. S. & Owen, I., “An Investigation of Ship Airwakes Using Detached-Eddy Simulation,” Computers & Fluids, 2010, 39 (4), 656–673.
4. Hodge, S.J., Forrest, J.S., Padfield, G.D. & Owen I., “Simulating the Environment at the Helicopter-Ship Dynamic Interface: Research, development and Application”, Aeronautical J., 2012, 116 (1185), 2012, 1155-1184.
5. Forrest, S.J., Owen, I., Padfield, G.D. & Hodge, S.J., “Ship-helicopter operating limits prediction using piloted flight simulation and time-accurate airwakes”, J. Aircraft, 2012, 49 (4), 1020-1031.
6. Hoenkamp, A., Lee, D., Pavel, M.D. & Stapersma, D., “Lessons learned from NH90 NFH helicopter-ship ineterface: testing across the complete Dutch fleet”, 40th European Rotorcraft Forum, Southampton, 2-4 September 2014.
7. Tai, T. & Carico, D., "Simulation of DD-963 ship airwake by Navier-Stokes method", 23rd Fluid Dynamics, Plasmadynamics, and Lasers Conference, Orlando, FL, 6-9 July 1993.
8. Advani, S.K. and Wilkinson, C.H. “Dynamic interface modelling and simulation – a unique challenge”, RAeS Flight Simulation Group Conference on The Challenge in Achieving Realistic Training in Advanced Rotorcraft Simulators, London, UK, November 2001.
9. Roscoe, M. & Wilkinson, C.H., “DIMSS – JSHIP’s modelling and simulation process for ship/helicopter testing & training”, Proc. AIAA Modelling & Simulation Technologies Conference, Monterey, CA, AIAA 2002-4597.
10. Cox, I., Turner, G., Finlay, B. & Duncan, J., “The ship/air interface framework (SAIF) project: dynamic challenges”, Maritime Operations of Rotorcraft, RAeS Conference, London, UK 11-12 June 2008.
11. Turner, G., Clark, W., Cox, I., Finlay, B. & Duncan, J., “ Project SAIF – assessment of ship helicopter operating limits using the Merlin helicopter simulator”, AHS 62nd Annual Forum, Phoenix, AZ, 9-11 May 2006.
12. Padfield, G.D. & White, M.D., “Flight simulation in academia: HELIFLIGHT in its first year of operation at the University of Liverpool”, Aeronautical J., 2003, 107 (1075), 529-538.
13. White, M.D., Perfect, P., Padfield, G.D., Gubbels, A.W. & Berryman, A.C., “Acceptance testing and commissioning of a flight simulator for rotorcraft simulation fidelity research”, Proc. IMechE Part G: J Aerospace Engineering, 2012, 226(4), 638-686.

14. Roper, D. M., Integrating Computational Fluid Dynamics and Piloted Simulation to Quantify Ship-Helicopter Operating Limits, Ph.D. thesis, Department of Engineering, University of Liverpool, 2006.
15. Wilkinson, C., Zan, S., Gilbert, N., Funk, J., 1998. Modelling and simulation of ship airwakes for helicopter operations – a collaborative venture. In: Proceedings of the RTO AVT Symposium of Fluid Dynamics Problems of Vehicles Operating Near or in the Air–Sea Interface, RTO-MP-15, Amsterdam, pp. 8.1–8.12.
16. Forrest, J. F., Predicting Ship-Helicopter Operating Limits using Time-Accurate CFD Ship Airwakes and Piloted Flight Simulation, Ph.D. thesis, Department of Engineering, University of Liverpool, 2009.
17. Hodge, S. J., Dynamic Interface Modelling and Simulation Fidelity Criteria, Ph.D. thesis, Department of Engineering, University of Liverpool, 2010.
18. Spalart PR, Squires KD. The status of detached-eddy simulation for bluff bodies. In: Direct and large eddy simulation V. Springer; 2004.
19. Wang, Y., Curran, J., Padfield, G. D., Owen, I., AirDyn: an instrumented model-scale helicopter for measuring unsteady aerodynamic loading in airwakes, Measurement Science and Technology, 2011, 22, 045901.
20. Kaaria, C.H., Investigating the Impact of Ship Superstructure Aerodynamics on Maritime Helicopter Operations, Ph.D. thesis, Department of Engineering, University of Liverpool, 2012.
21. Kaaria, C.H., Wang, Y., White, M.D. and Owen, I. An experimental technique for evaluating the aerodynamic impact of ship superstructures on helicopter operations, Ocean Engineering, 2013, 61, pp 97-108.
22. Kaaria, C.H., Forrest, J.S. and Owen, I. The virtual AirDyn: A simulation technique for evaluating the aerodynamic impact of ship superstructures on helicopter operations, Aeronautical J., 2013, 117, (1198), pp 1233-1248.
23. Hodge, S.J., Zan, S.J., Roper, D.M., Padfield, G.D. and Owen, I. “Time-accurate ship airwake and unsteady aerodynamic loads modelling for maritime helicopter operations”. Journal American Helicopter Society, 2009, 54(2), 022005-1 – 022005-16.
24. Strelets M. Detached eddy simulation of massively separated flows. In: 39th AIAA aerospace sciences meeting and exhibit, Reno, NV; 2001.
25. ANSYS Fluent Theory Guide, Release 18, ANSYS Inc., 2017.
26. Spalart, P. R., “Young-Person’s Guide to Detached-Eddy Simulation Grids,” Tech. Rep. NASA/CR-2001-211032, NASA, 2001.
27. Polsky, S.A., Wilkinson, C.H., Nichols, J., Ayers, D., Mercado-Perez, J., Davis, T.S. “Development and application of the SAFEDI tool for virtual dynamic interface ship airwake analysis”, 54th AIAA Aerospace Sciences Meeting, AIAA SciTech Forum, (AIAA 2016-1771), San Diego, CA, 2016.

28. Forrest, J.S., Owen, I. and Padfield, G.D. "Detached-Eddy Simulation of Ship Airwakes for Piloted Helicopter Flight Simulation", Proc International Aerospace CFD Conference, Paris, June 2007
29. Yesilel H, Edis FO. Ship airwake analysis by CFD methods. Am Inst Phys Conf. Proc. 2007;936:674–7.
30. Smagorinsky, J., "General Circulation Experiments with the Primitive Equations," Monthly Weather Review, Vol. 91, No. 3, 1963, pp. 99–164.
31. Spalart, P. R., Jou, W. H., Strelets, M., and Allmaras, S. R., "Comments on the Feasibility of LES for Wings, and on a Hybrid RANS/LES Approach," Advances in DNS/LES, Greyden Press, 1997, pp. 137–147.
32. Thompson, N., "Characteristics of Atmospheric Turbulence near the Ground," Tech. Rep. 74030, ESDU, 1974.
33. Richards, P. J., Quinn, A. D., and Parker, S., "A 6 m Cube in an Atmospheric Boundary Layer Flow Part 2. Computational Solutions," International Journal of Wind and Structures, Vol. 5, No. 2-4, 2002, pp. 177–192.
34. Polsky, S., "CFD Prediction of airwake flowfields for ships experiencing beam winds", AIAA Applied Aerodynamics Conference, AIAA Paper 2003-3657, AIAA, Orlando, FL, USA, 2003.
35. Counihan, J., "Adiabatic Atmospheric Boundary Layers: A Review and Analysis of Data from the Period 1880-1972," Atmospheric Environment, Vol. 9, No. 10, 1975, pp. 871–905.
36. Riddle, A., Carruthers, D., Sharpe, A., McHugh, C., and Stocker, J., "Comparisons Between FLUENT and ADMS for Atmospheric Dispersion Modelling," Atmospheric Environment, Vol. 38, No. 7, 2004, pp. 1029–1038.
37. Ergin, S. and Dobrucali, E., "Numerical modelling of exhaust smoke dispersion for a generic frigate and comparison with experiments", J. Marine Sci. Appl., 2014, Vol. 13, 206-211.
38. Kelly, M.F., White, M.D., Owen, I., and Hodge, S.J., "Piloted flight simulation for helicopter operations to the Queen Elizabeth class aircraft carriers", Presented at 43rd European Rotorcraft Forum, Milan, 12th-15th Sept. 2017.
39. Morton, S. A., Forsythe, J. R., Squires, K. D., and Wurtzler, K. E., "Assessment of Unstructured Grids for Detached Eddy Simulation of High Reynolds Number Separated Flows," Proceedings of the 8th International Conference on Numerical Grid Generation for Compuational Field Simulations, Honolulu, HI, 2-6 June 2002, pp. 571–586.
40. Xia, H. and Qin, N., "DES Applied to an Isolated Synthetic Jet Flow," *Advances in Hybrid RANS-LES Modelling*, edited by S.-H. Peng and W. Haase, Vol. 97 of Notes on Numerical Fluid Mechanics and Multidisciplinary Design, Springer-Verlag, Berlin, Germany, 2008, pp. 252–260.
41. DuVal, R. W., "A Real-Time Multi-Body Dynamics Architecture for Rotorcraft Simulation", RAeS Rotorcraft Group conference on 'The Challenge in Achieving

Realistic Training in Advanced Rotorcraft Simulators', 7-9 November 2001, London, UK.

42. Howlett, J.J., "UH-60A Black Hawk Engineering Simulation Program: Volume I – Mathematical Model", NASA-CR-166309, December 1981.
43. Daintree, R. M., "Blade Element Theory Rotor Simulation", RAeS Rotorcraft Group conference on '*Progress in Helicopter and V/STOL Aircraft Simulation*', 1-2 May 1990, London, UK.
44. Peters, D. A., and He, C., "Finite State Induced Flow Models Part II; Three Dimensional Rotor Disk", Journal of Aircraft, Vol. 32, No. 2, March-April 1995, pp. 323-333.
45. Hilbert, K. B., "A Mathematical Model of the UH-60 Helicopter", NASA-TM-85890, April 1984.
46. Bailey, J. F., "A Simplified Theoretical Method of Determining the Characteristics of a Lifting Rotor in Forward Flight", NACA Report 716, 1941.
47. Padfield, G. D., Helicopter Flight Dynamics, Blackwell Science, Oxford, UK, 2nd ed., 2007.
48. Barnes, A. G., and Yager, T. J., "Enhancement of Aircraft Ground Handling Simulation Capability", AGARD-AG-333, August 1998.
49. McTaggart, K., "Validation of ShipMo3D Version 1.0 User Applications for Simulation of Ship Motion", Technical Memorandum, DRDC Atlantic TM 2007-173, August 2007.
50. Finlay, B.A. "Ship Helicopter Operating Limit Testing – Past, Present and Future", RAeS Rotorcraft Group Conference on 'Helicopter Operations in the Maritime Environment', London, UK, March 2001.
51. Roscoe, A. H., and Ellis, G. A., "A Subjective Ratings Scale for Assessing Pilot Workload in Flight: A Decade of Practical Use," RAE, TR TR90019, 1990.
52. Forrest, J.S., Kaaria, C.H. and Owen, I. "Evaluating ship superstructure aerodynamics for maritime helicopter operations through CFD and flight simulation", Aeronautical J, Oct 2016, 120 (1232), 1578-1602.
53. McRuer, D.T. Interdisciplinary interactions and dynamic systems integration, *Int J Control*, 1994, **59**, (1), pp 3-12.
54. Lee, R.G. and Zan, S.J. Unsteady aerodynamic loading on a helicopter fuselage in a ship airwake, *J American Helicopter Society*, April 2004, **49**, 2, pp 149-159.
55. Owen, I, White, M.D., Padfield, G.D. and Hodge, S.J. "A virtual engineering approach to the ship-helicopter dynamic interface – a decade of modelling and simulation research at the University of Liverpool", The Aeronautical Journal, doi:10.1017/aer.2017.102. Available on line, Oct 2017.
56. Royal Navy website, accessed July 2017, http://www.royalnavy.mod.uk/our-organisation/the-fighting-arms/surface-fleet/patrol/river-class/hms-clyde

57. Polsky, S.A. and Bruner, C.W.S. “Time-Accurate Computational Simulation of an LHA Ship Airwake”, AIAA Paper No. 2000-4126, 18th Applied Aerodynamics Conference, Denver, Colorado, USA, August 2000.
58. Zan, S.J., “On Aerodynamic Modeling and Simulation of the Dynamic Interface”, Proceedings of the Institute of Mechanical Engineers, Part G, Journal of Aerospace Engineering, Vol 219 (5), 2005.
59. Forrest, J.S., Hodge, S.J., Owen, I., and Padfield, G.D., "An investigation of ship airwake phenomena using time-accurate CFD and piloted helicopter flight simulation", 34th European Rotorcraft Forum, Liverpool, UK, September 16-19, 2008.
60. McTaggart, K.A. and Langlois, R.G., “Physics-Based Modelling of Ship Replenishment at Sea Using Distributed Simulation”, Society of Naval Architects and Marine Engineers Annual Meeting and Expo, Providence, Rhode Island, USA, 20-23 October 2009.
61. ITTC Seakeeping Committee Report. In 15th International Towing Tank Conference, Vol. 1, pp. 55–114. The Hague, 1978.
62. McTaggart, K., “Validation of ShipMo3D Version 1.0 User Applications for Simulation of Ship Motion”, Technical Memorandum, DRDC Atlantic TM 2007-173, August 2007.
63. Cummins, W.E. and Bales, S.L., “Extreme value and rare occurrence statistics for Northern Hemisphere shipping lanes”, 1980 SNAME Spring Meeting and STAR Symposium, California, USA, 3-7 June 1980.
64. Military Agency for Standardization (MAS). Common Procedures for Seakeeping in the Ship Design Process. North Atlantic Treaty Organization (NATO), 2000. Standardization Agreement. 3rd Edition. STANAG 4154 (NATO Unclassified).
65. Acker, H.C., “Stack design to avoid smoke nuisance”, SNAME Trans., Vol. 60, 1952, 566-594.
66. Ower, E. & Third, A.D., “Superstructure design in relation to the descent of funnel smoke”, Trans Institute of Marine Engineers (London), Vol. 1, 1959, 109-138.
67. Baham, G.J. & McCallum, D., “Stack design technology for naval and merchant ships”, SNAME Trans., Vol. 85, 1977, 324-349.
68. Kulkarni, P.R., Singh, S.N. & SEshadri, V., “Flow visualisation studies of exhaust smoke – superstructure interaction on naval ships”, Naval Eng. J., ASNE, Vol. 117(1), 2005, 41-56.
69. Seshadri, V., Siingh, S.N. & Kulkarni, P.R., “Study of problem of smoke ingress into GT intakes of a naval ship”, J. Ship Tehnology, Vol 2(1), Jan 2006, 22-35.
70. Vijayakumar, R., Seshadri, V., Singh, S.N. & Kulkarni, P.R., “A wind tunnel study on the interaction of hot exhaust from the funnel with the superstructure of a naval ship”, Oceans 2008, Kobe Japan, 18-21 April, 2008.

71. Kulkarni, P.R., Singh, S.N. & SEshadri, V., “Flow visualisation studies of exhaust smoke – superstructure interaction on naval ships”, Naval Eng. J., ASNE, Vol. 117(1), 2005, 41-56.
72. Vijayakumar, R., Seshadri, V., Singh, S.N. & Kulkarni, P.R., “A wind tunnel study on the interaction of hot exhaust from the funnel with the superstructure of a naval ship”, Oceans 2008, Kobe Japan, 18-21 April, 2008.
73. Huang, J., Carrica, P.M. & Stern, F., “A method to compute ship exhaust plumes with waves and wind”, Int. J. Numer. Meth. Fluids, Vol. 68, 2012, 160-180.
74. Kulkarni, P.R., Singh, S.N. & Seshadri, V., “Parametric studies of exhaust smoke – superstructure on a naval ship using CFD”, Computers & Fluids, Vol. 36, 2007, 794-816.
75. Vijayakumar, R., Singh, S.N. & Seshadri, V., “CFD prediction of the trajectory of hot exhaust from the funnel of a naval ship in the presence of ship superstructure”, Intl. J. Maritime Eng., Vol. 156, Part A1, 2014, A1-A23.
76. Park, S., Heo, J., YU, B.S. & Rhee S.H., “Computational analysis of ship’s exhaust-gas flow and its application for antenna location”, Applied Thermal Engineering, Vol. 31, 2011, 1689-1702.
77. Camelli, F., Soto, O, Lohner, R, Sandberg, W.C. & Ramamurti, R., “Topside LPD17 flow and temperature study with an implicit monolithic scheme”, 41st Aerospace Science Meeting and Exhibit, Reno, Nevada, 6-9 January 2003, AIAA 2003-969.
78. Camelli, F., Lohner, R, Sandberg, W.C. & Ramamurti, R., “VLES study of ship stack gas dynamics”, 42nd Aerospace Science Meeting and Exhibit, Reno, Nevada, 5-8 January 2004, AIAA 2004-72.
79. Civil Aviation Authority. 'Research On Offshore Helideck Environmental Issues'. London: Civil Aviation Authority. CAA Paper 99004, 2000.
80. Liddy, G. (2004). AAIU Synoptic Report No: 2004-001. Shannon: Irish Aviation Authority.
81. Civil Aviation Authority. “Standards for Offshore Helicopter Landing Areas”. CAP 437, London, 2013.
82. Norweigian Oil and Gas Association, “Helicopter Deck On Offshore Installation”. NORSOK Standard C-004, 2013.

APPENDIX

PUBLISHED PAPERS

1. Scott, P.M., Owen, I. and White, M.D. “The Effect of Ship Size on the Flying Qualities of Maritime Helicopters', Proceedings 70th Annual Forum of the American Helicopter Society, 2014, May 20-22, Montreal, Canada.
2. Scott, P., White, M.D. and Owen, I. “Unsteady CFD Modelling of Ship Engine Exhaust Gases On Over-Deck Air Temperatures and the Implications For Helicopter Operations” 71st Annual Forum of the American Helicopter Society, 5-7 May 2015, Virginia Beach
3. Scott, P, White, M.D. and Owen, I., “The effect of ship size on airwake aerodynamics and maritime helicopter operations”, Proc 41st European Rotorcraft Forum, September 1-4, 2015, Munich.
4. Owen, I., White, M.D., Scott, P., Mateer, R and Kelly, M.F. “Modelling and Simulation at The University of Liverpool in Support of UK Naval Aviation”, American Society of Naval Engineers Launch & Recovery Symposium, MITAGS, Linthicum Heights, MD USA, Nov 16-17 2016
5. Mateer, R., Scott, P., White, M.D. and Owen, I. “A CFD Study of the Aerodynamics of a Ship’s Bulky Enclosed Mast”, American Society of Naval Engineers Launch & Recovery Symposium, MITAGS, Linthicum Heights, MD USA, Nov 16-17 2016
6. Scott, P.M., Kelly, M.F., White, M.D. and Owen, I., “Using piloted simulation to measure pilot workload of landing a helicopter on a small ship”, 43rd European Rotorcraft Forum, Milan, 12th-15th Sept. 2017.

THE EFFECT OF SHIP SIZE ON THE FLYING QUALITIES OF MARITIME HELICOPTERS

Paul Scott
p.m.scott1@liv.ac.uk
University of Liverpool
Liverpool, UK

Ieuan Owen
iowen@lincoln.ac.uk
University of Lincoln
Lincoln, UK

Mark White
mdw@liv.ac.uk
University of Liverpool
Liverpool, UK

ABSTRACT

This paper describes the use of Computational Fluid Dynamics (CFD) to produce unsteady ship airwakes to investigate the effect of ship size on the pilot workload at the helicopter-ship dynamic interface. A ship model was created to represent modern naval vessels and geometrically scaled to represent smaller and larger scale ships that currently operate maritime helicopters. An unsteady airwake for each ship was computed at 40 knots for both the Headwind and Green 45° Wind Over Deck (WOD) conditions, while the mid-scale ship was also computed at 30 knots. Using Strouhal scaling, the mid-scale ship airwake was scaled both in terms of velocity and ship size. Comparisons of the resulting small and large scaled data were made with the computed CFD data and the use of Strouhal scaling was found to a feasible method for the modification of airwake data. An offline analysis using a SH60B Seahawk-like helicopter was used to determine the impact of the ship size on the pilot workload. As the ship size increased, so did the levels of predicted pilot workload due to the increasing energy contained within the turbulent wake as the ship size was increased.

NOTATION

ACP	Airload Computation Points
CFD	Computational Fluid Dynamics
HP	High Performance Computing
RMS	Root Mean Square
SFS	Simple Frigate Shape
VAD	Virtual AirDyn
WOD	Wind Over Deck
d	Depth (m)
f	Frequency (Hz)
l	Characteristic Length (m)
l_s	Ship Length (m)
r	Radius (m)
St	Strouhal Number
v	Flow Speed ($m.s^{-1}$)
v'	Normalised Flow Speed
v_{ref}	Reference Speed ($m.s^{-1}$)
z	Height (m)
z_{ref}	Reference Height (m)
α	Surface Terrain Constant

INTRODUCTION

The launch and recovery of maritime helicopters to single spot naval ships can prove to be a demanding task for the pilot [1,2]. The rolling, pitching and heaving of the deck, coupled with the turbulent wake produced by the air moving over the ship, can lead to situations in which even the most experienced pilots find it difficult to safely conduct operations. The turbulent air wake of the ship is a product of the ships forward speed and the local prevailing wind conditions interacting with the superstructure. Furthermore, the design of modern frigates has tended towards less cluttered 'slab' sided ships to reduce the radar cross section. The sharp edges of these frigates produce a highly complex airwake composed of a number of unsteady turbulent structures and steep velocity gradients in the shear layers, all of which can adversely affect the performance of the helicopter. The flow over and around the flight deck during a headwind is dominated by a strong shear layer that separates the comparatively undisturbed air flowing across the deck from the turbulent flow in the lee of the superstructure. As the relative angle of the wind over deck moves from a headwind towards more oblique angles, the flow becomes increasingly complex with larger vortical structures being produced with these fluctuations containing higher velocities and increased spatial scales.

As the helicopter passes through the turbulent wake there will be large changes in the aerodynamic loading and rotor response due to the unsteady velocity fluctuations, particularly in the closed-loop pilot response frequency range 0.2 to 2Hz [3]. Disturbances within this frequency range have been shown to have the greatest impact on the pilot's workload [4].

Presented at the AHS 70th Annual Forum, Montréal, Québec, Canada, May 20–22, 2014.

On encountering a disturbance the pilot may be required to react by implementing a control input to correct a change in altitude, attitude and heading. The aerodynamic characteristics of a ship design can therefore dominate the pilot's workload, especially during the landing phase as a helicopter translates across the deck through the airwake. While headwind conditions are usually relatively benign in respect to pilot workload, in certain Wind Over Deck (WOD) conditions, such as Green 45° conditions, the pilot workload may exceed the pilot's spare capacity such that a landing becomes dangerous.

Over the past twelve years the Flight Science and Technology Research Group at the University of Liverpool has developed rotorcraft flight simulation rotorcraft research facilities whose aim is the continued improvement in the fidelity of flight simulation and particular attention has been paid to the helicopter-ship dynamic interface. Recent work at the University of Liverpool has established that 'time-accurate' unsteady airwakes can be computed using CFD and implemented within a full motion flight simulator giving a high fidelity simulation environment [5-7]. The aircraft disturbances and pilot workload levels were shown to be representative of the helicopter-ship dynamic interface [8].

Figure 1. Knud-Rasmussen Class Patrol vessel [9]

The current study is concerned with the investigation of the size of the ship on which helicopter-deck operations take place and its effect on the pilot workload. As the ship size is increased, the superstructure will experience a higher freestream speed due to the increased height into the Atmospheric Boundary Layer (ABL) whilst also generating larger, slower turbulent structures. Smaller ships however will generate smaller eddies at higher frequencies. Naval ships routinely operating helicopters can be as small as half the size of a conventional frigate, such as the Knud-Rasmussen class patrol vessel operated by the Royal Danish Navy with a length of 71m, (Figure 1).

With a change in the WOD angle, the effects of ship size are believed to affect the levels of pilot workload experienced during deck operations, as the magnitude of the unsteady velocity fluctuations within the airwake will change with ship size, impacting the aerodynamic loading of the helicopter.

AIRWAKE SCALING

To investigate the effect of ship size on the change in pilot workload, a generic ship model was geometrically scaled such that the upper and lower ends of helicopter operating ship sizes were encompassed, the ship models used in this study are shown in Figure 2. The unscaled model has a length of 150m which typifies the average naval single spot frigates; this model was then increased and decreased in size by 30% to produce ship models with lengths of approximately 100m and 200m. The airwakes for each of these three ship sizes were used to provide comparative data to demonstrate the feasibility of Strouhal scaling and to investigate the consequences of a change in size on helicopter operations.

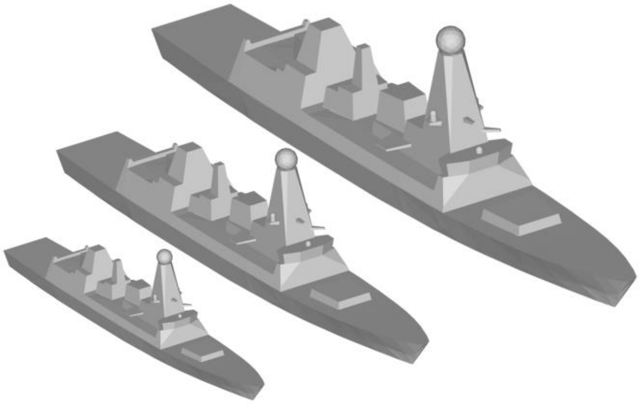

Figure 2. The three ship model scales considered.

The scaling of airwake data involves the use of the Strouhal number, shown in Equation 1. Objects within a flow that shed consistent vortices at distinct frequencies can be described by the Strouhal Number. It relates the characteristic length of an object, *l*, within a flow of speed *v*, and the frequency of the vortices shed from the object *f*. This simple relationship shows that for an increase in freestream speed there will be a corresponding increase in shedding frequency, likewise doubling the characteristic length scale halves the frequency.

$$St = \frac{fl}{v} \tag{1}$$

The scaling of airwakes in terms of velocity magnitude has been previously carried out by Polsky [10] who showed that the linear scaling of the airwake magnitude was possible. Further observations by Zan [11] noted that the airwake should be shifted in frequency as well as the velocity magnitude due to the large scale turbulent structures within the ship airwake which are the result of flow separation which in turn is dependent on the flow speed and ship size. Using this approach, Forrest went on to show that the Strouhal scaling of CFD airwake data from 40 to 30 knots, in both frequency and velocity magnitude, gave good results when compared to a computed 30 knot airwake [5].

In order to use Strouhal scaling to modify the airwake data, for example to change the airwake in terms of velocity magnitude from a freestream of 40 knots to 20 knots, the velocity components and frequency are simply halved.

The computational time required to generate an unsteady airwake typically may take several days to produce the thirty seconds of unsteady data needed for use within a flight simulation environment. It is therefore impractical to compute every possible wind speed likely to be experienced by a ship and so the airwake is computed at a single freestream speed and the freestream speed is scaled as mentioned previously. Consequently the ability to scale CFD airwake data to account for various ship sizes rather than the generation of multiple simulations would prove to be a efficient use of resources. However, changes in WOD angle can have significant differences within the flow field thus airwakes still need to be computed for different wind azimuths. For the purposes of this study, the airwake was computed at both a Headwind and Green 45° WOD conditions to determine if airwake scaling holds for more complex flow fields.

CFD METHODOLOGY

Geometry and Meshing

A ship model was imported into the Ansys ICEM mesh generation software, so that it could be 'cleaned' to repair any erroneous surfaces and to remove small features to create geometry suitable for meshing. Features such as small antennas, railings and other small deck clutter would have little effect on the airwake but if not removed would increase the cell count and hence the run time of the CFD. Generally objects that are less than 0.3m in diameter are negated.

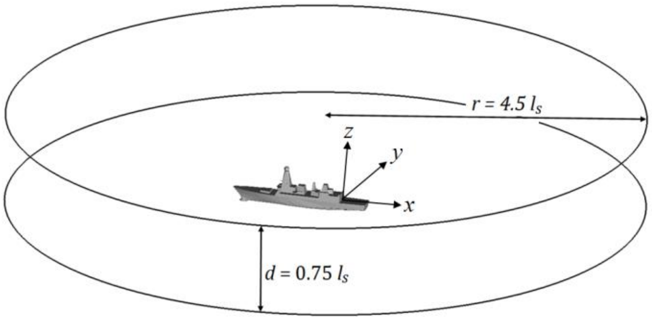

Figure 3. the computational CFD domain

The final ‘clean’ ship model was then placed within a cylindrical domain, (shown in Figure 3); this style of flow domain allows the relative WOD angle to be varied by changing the magnitudes of the *x* and *y* freestream velocity components of the flow, without having to change the computational domain. The orientation of the domain is such that the x-direction is in line with the longitudinal axis of the the ship, while the y-direction runs through the lateral plane of the ship. The size of the cylindrical domain [12] is sized so that the boundaries are sufficiently far away from the ship to prevent inaccuracies in the predicted flow from blockage effects.

An unstructured meshing approach was used as this suits the Detached Eddy Simulation turbulence model (DES) well due to the near isotropic nature of the tetrahedra away from the walls [12]. The mesh was generated by creating a surface mesh from which a Delauney volume mesh was then grown. The surface mesh size was set to 0.05 times the hangar height and the growth of the volume mesh was controlled using an expansion ratio of 1.2 so that a smooth transition occurred away from the ship surfaces.

Areas of particular interest within the mesh, such as the region immediately above the flight deck, were refined using regions of dense mesh within the volume to provide better resolution of the turbulent structures within the wake. Several layers of prisms were grown from both the ground plane and the ships surface into the volume mesh to resolve the boundary layers. These techniques allowed better resolution of the vortical features shed from the ship and ensure the velocity shear within the atmospheric boundary layer profile was modelled correctly. The surface mesh can be seen in Figure 4. The typical number of cells for each mesh was typically 15 million.

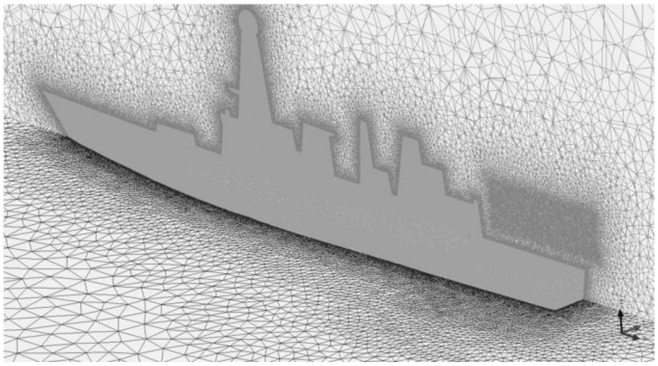

Figure 4. Cross sectional view of the meshed domain, (note region of dense mesh over the flight deck)

Boundary Conditions

The Ansys Fluent CFD solver used for this study which requires that all the surfaces within the mesh are defined with a specified boundary type, along with any data or conditions that govern the behaviour of the flow at the boundary. The surface of the ship is modelled as a series of walls with a zero-slip condition, setting the velocity at the surface as zero allowing for the formation of a boundary layer. The sea surface was also set as a wall but with zero shear stress, as this allows Fluent to apply a specified atmospheric velocity profile to propagate unchanged through the domain. The top of the computational domain was set to a symmetry condition, which assumes there is zero flux across the boundary while specifying a zero shear condition.

The outer circumference of the domain is set as a 'pressure far field' which models the free stream conditions to infinity. This boundary condition requires that the freestream Mach number is defined along with the components of the flow direction.

The inclusion of an Atmospheric Boundary Layer (ABL) was used within the CFD simulations and has been shown to improve the accuracy of the simulations [12]. The ABL profile is modelled using the power law given in the equation:

$$V = V_{ref}\left(\frac{z}{z_{ref}}\right)^{\alpha} \tag{2}$$

where V_{ref} is the velocity at the reference height is, α is a constant dependent on the surface roughness. The following values which were defined for a sea surface were used within the simulations: V_{ref} = 50 knots, Z_{ref} = 200m, α = 0.13 [13]. The freestream wind conditions were set such that 40 knots occurred at the ship's anemometer height.

Computational Methods

Second order-discretisation was used in time and space, and a blended upwind-central differencing scheme was used for the convective terms. Pressure-velocity coupling was resolved through use of the Pressure-Implicit with Splitting of Operators (PISO) scheme.

Turbulence Modeling

Since DES is a 'time accurate' CFD method, having been developed to resolve the flow separation from large bluff-bodies at high Reynolds numbers, it makes an ideal model to simulate the flow around the superstructure of a ship. DES CFD turbulence modelling has the advantages of resolving the medium to large scale turbulent structures explicitly, thereby allowing the unsteady airwake to be captured fully.

General CFD Approach

The approach used to produce time accurate unsteady CFD simulations initially involved the generation of a steady state solution by performing 1000 iterations (i.e. the fluid dynamic equations in the whole domain were iteratively solved 1000 times to converge onto a solution for a steady-state flow field). The results from the steady state flow field were then used as the initial conditions for calculating the unsteady flow field. The unsteady solver was then activated in DES mode and the simulation is carried out at 100Hz. 1500 time steps were then computed to allow the transition from steady state to unsteady to fully develop. These initial time steps were then discarded after which a further 3000 time steps were then computed, while sampling data every fourth time step to produce data for later post processing and use within the flight mechanics modelling software, FLIGHTLAB.

The unsteady flow solutions coupled with the complexity of the ship geometry and the large number of cells used to generate the mesh requires the use of a high performance computing cluster (HPC). The CFD simulations were carried out on a HPC cluster comprising of 2000 nodes, each node having a quad-core processor and 32Gb of Ram. Each simulation was split over 96 nodes, taking around 65 hours to produce the overall 45 seconds of unsteady airwake data required for each run.

Airwake Integration and Rotorcraft Model Analysis

Thirty seconds of unsteady CFD data was generated on a high density, unstructured mesh, due to memory constraints when running real time piloted simulations, the computed airwake data required some post-processing before it could be used within the FLIGHTLAB environment. Reduction of the airwake data size is undertaken by interpolating the unstructured CFD data onto a structured mesh using a grid spacing of 1 metre, covering a region of interest around the flight deck of the ship (see Figure 5).

Once interpolated, the reduced airwake files were re-formatted into a pair of data files containing the airwake data and grid information so that the co-ordinate axes of the CFD data matched those of FLIGHTLAB.

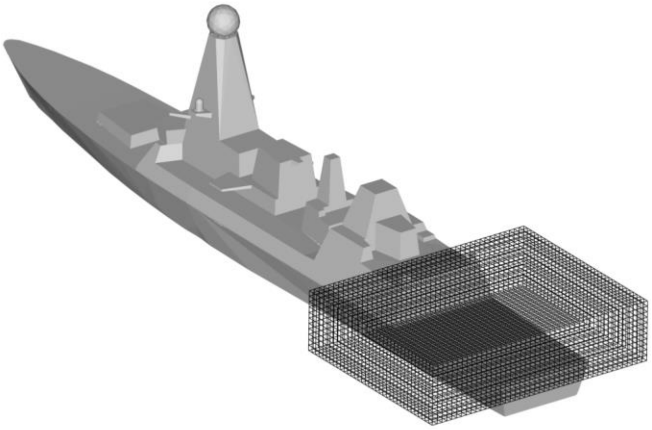

Figure 5. The interpolation grid used to reduce the size of the airwake data set

In order to assess the effect of ship scale airwake on the pilot workload, the University of Liverpool has developed an offline technique known as the Virtual AirDyn (VAD) is an offline analysis tool developed at The University of Liverpool and makes use of the flight dynamic modelling software FLIGHTLAB [14]. The VAD process uses a model helicopter simulation to measure the forces and moments imparted onto the helicopter by the unsteady airwake behind a ship to give a quantitative measure of the impact of the ship design on the aircraft.

The method by which the VAD has been employed to compare ship airwakes is to carry out a translational approach beginning at the ship's hangar height, one beam width from the landing spot, off the port edge of the ship. The helicopter is then held stationary at several positions over the midpoint along the flight deck, with its hub at 100% hangar height, shown in Figure 6.

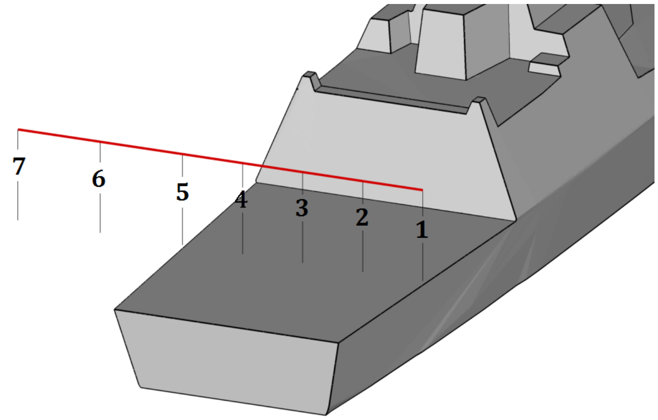

Figure 6. Sampling points used in the VAD and to capture unsteady CFD velocity data

The positions at which the helicopter is placed over the deck of the ship are normalised with the ship's beam width so that each sampling point is at the same position relative to the beam for each ship size tested. Point 3 lies directly over the centre of the deck with Points 1 and 5 over the deck edges, while Points 2 and 4 are equal to 0.25 of the beam width. Point 7 is located 1 beam width away from the centre of the ship, and Point 6 lies halfway between Point 7 and the Port deck edge.

The FLIGHTLAB Generic Rotorcraft model used for this research was configured to be representative of the Sikorsky SH-60B Seahawk, a maritime development of the widely used UH60 Black Hawk. The model is constructed from a set of modular components such as the rotor, fuselage and turbo-shaft engine. The unsteady, interpolated airwake data is integrated into the helicopter via a number of Airload Computation Points (ACP) which are located at various points along each rotor blade, fuselage, tail rotor and empennage, (Figure 7). The helicopter is initially trimmed under the freestream wind conditions away from any influence of the ship airwake. At each of the sampling locations over the ship, the helicopter is held stationary and the time histories of the unsteady moments and forces at the helicopter's centre of gravity are recorded over the full thirty seconds of airwake data. As the trimmed helicopter now experiences out of trim conditions, the forces acting on it are no longer in balance. This data is then time averaged to provide the mean forces and moments acting on the helicopter at each of the seven test Points.

The unsteady RMS forces and moments are produced using a method outlined Wang et al [15], whereby the Power Spectral Densities of the signals are generated from the time histories given by the VAD, and the square root of the integral between the limits 0.2 to 2Hz is used to represent the Root Mean Square (RMS) loadings on the helicopter. The frequency range of 0.2 to 2 Hz was chosen as this has the greatest influence on pilot workload [3]. Frequencies higher than this do not impact on the pilot workload due to the inertia on the helicopter, while lower frequencies can be compensated with control inputs by the pilot. The RMS loading is responsible for the pilot workload while the mean loads will influence the control margins. This method is discussed in further detail by Forrest et al [14].

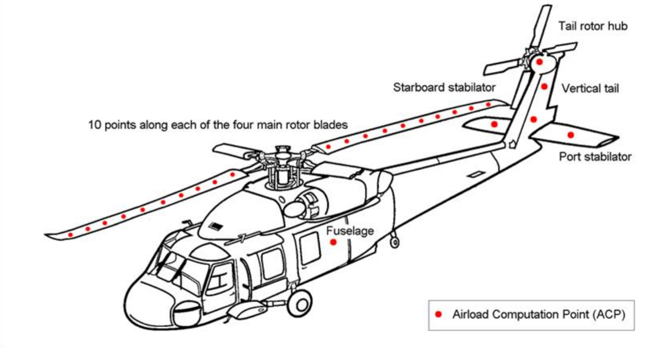

Figure 7. Location of the forty-six Airload Computation Points on the SH60 FLIGHTLAB model

RESULTS

Airwake Velocity Magnitude Scaling

For each of the three ship sizes, Headwind and Green 45° WOD cases were computed at a freestream speed of 40 knots. The mid-scale size ship airwake was also computed at 30 knots to allow velocity scaling to be carried out. To provide unsteady airwake data for scaling, sampling points mirroring those used in the VAD process were used during the CFD simulations to record the unsteady velocities. Points 3 and 5 were used to test the scaling hypotheses for the Headwind and Green 45° cases respectively. Strouhal scaling based on ship size uses the hanger height as the characteristic length.

It has been shown that the computed CFD airwake can be scaled based on frequency and velocity magnitude [5,10]. Whilst previous studies have shown that velocity scaling was viable for a Simple Frigate Shape (SFS) [16], the geometry for the ship model used in this study has an increased level of complexity over that of the SFS used previously. Therefore, a validation of the Strouhal scaling method was first carried out using the mid-scale ship geometry at freestream wind speeds of 40 knots and 30 knots in a headwind WOD. The computed 40 knot data was then scaled down to 30 knots in both velocity magnitude and frequency.

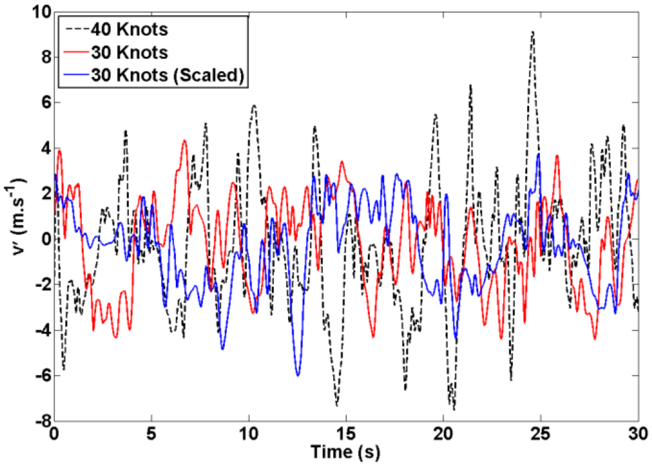

Figure 8. Normalised unsteady total velocity data at Point 3 for the computed 40 and 30 knot data and the scaled 30 knot case

The resulting normalised, unsteady velocity fluctuations at Point 3 can be seen in Figure 8. The scaled 30 knot case shows similar overall magnitudes to the computed 30 knot data with similar peak values. However, the resulting unsteady data in this form makes it difficult to draw any meaningful comparisons, thus the power spectral densities for each of the three cases for the headwind WOD at Point-3 are shown in Figure 9 to allow a more comprehensive comparison between the airwake data sets.

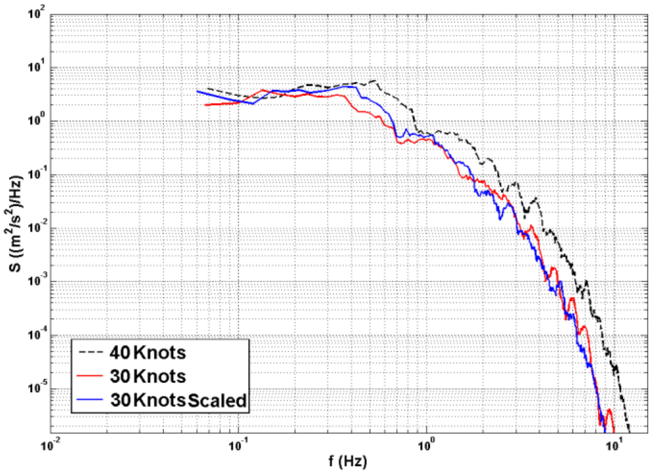

Figure 9. Power spectral densities of the total velocity at point 3 for the computed 40 and 30 knot data and the scaled 30 knot case

At the lower end of the frequency range, between 0 and 0.2Hz, the 40 knot data shows an increase in turbulent energy over the computed and scaled 30 knot cases, as indicated by the increased RMS value of 11.42 m.s^{-1} for the 40 knot case, in comparison to the values of 8.80 m.s^{-1}, 8.79 m.s^{-1} for the 30 knot and scaled 30 knot cases respectively. However due to the reduction in freestream speed, there is a frequency shift of approximately 2.5 Hz in the higher end of the spectrum. This shift is likely to occur in both axes from a combination of a change in both frequency and power. Overall the scaled 30 knot data shows good agreement with the computed 30 knot CFD data, showing that for complex ship geometries Strouhal scaling still holds.

Airwake Characteristic Length Scaling

The unsteady mid-scale ship airwake captured at point 3 was then scaled based on the change in hangar height as a characteristic length to represent the small-scale and large-scale ships, the resulting unsteady data for the small-scale results for the headwind WOD are shown in Figures 10a and 10b. The scaled down airwake data shows a marked increase in the frequency of the fluctuations in comparison with the mid-scale signal, although again the data in this form is difficult to interpret.

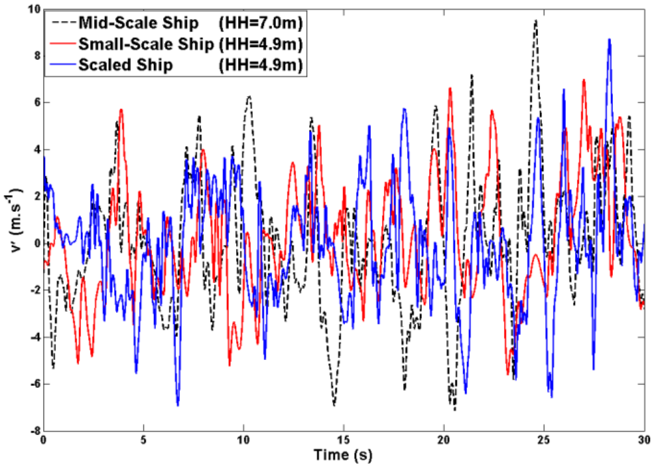

Figure 10a. Normalised, unsteady velocity fluctuations for the mid-scale, small-scale and scaled down airwake data at Point 3

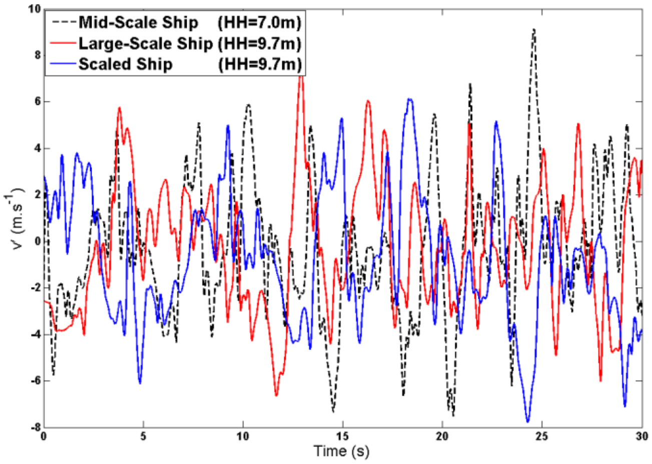

Figure 10b. Normalised, unsteady velocity fluctuations for the mid-scale, large-scale, scaled up airwake data at Point 3

The power spectral densities of the two computed ship airwakes at Point 3 along with the reduced scale data are shown in Figure 11a. The plot shows that between the range of 0.3 and 0.9 Hz the scaled data slightly over estimates the power and thus the turbulent energy within the airwake. However, as the frequency increases beyond this there appears to be a good correlation between the scaled and computed small scale data, capturing the increase in frequency shift of approximately 0.5 Hz exhibited by the small-scale ship data.

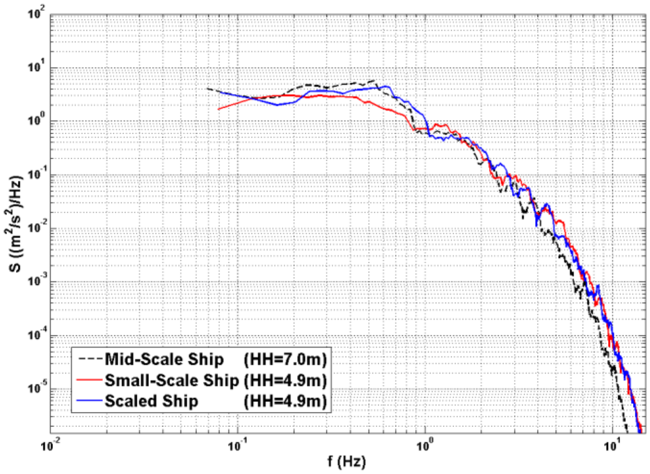

Figure 11a. Power spectral densities of the total velocity for a headwind WOD showing computed small-scale and un-scaled data and the scaled down data at Point 3

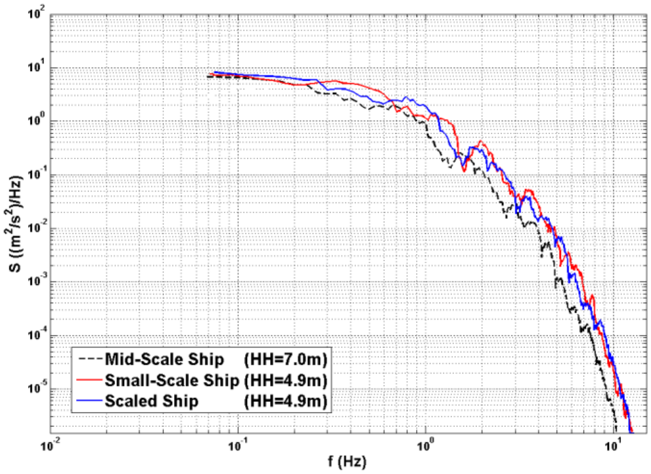

Figure 11b. Power spectral density of the total velocity for a Green 45 WOD showing computed small-scale and un-scaled data and the scaled down data at Point 5

The RMS values for the scaled down airwake in the Headwind case was found to be 10.35 m.s^{-1} which compares favourably with the computed small-scale RMS value of 10.31 m.s^{-1}.

Repeating the comparison for the Green 45° case, this time at Point 5, similar comparisons can be made between the small-scale ship and the scaled down airwake data. The results of which can be seen in Figure 11b. Again the frequency shift of 0.5 Hz occurs due to the increase in vortex shedding in response to the reduction on ship size.

Scaling the airwake to be representative of the larger scale ship is shown in the unsteady velocity fluctuations in Figure 10b. Plots of the power spectral density for the Headwind case, shown in Figures 12a and 12b, show there is again a small over-prediction in the turbulent energy between the frequency range of 0.1 to 0.4 Hz in the scaled flow as was seen in the reduced-scale results. In comparison to the small-scale power spectral density plots and the un-scaled ship, there is now a negative frequency shift of 3 Hz as the vortex shedding occurs at a lower frequency than the mid-scale ship. However, as the frequency exceeds 0.4 Hz the scaled data shows a good agreement with the computed large-scale data. The corresponding RMS values for the Large-scale and

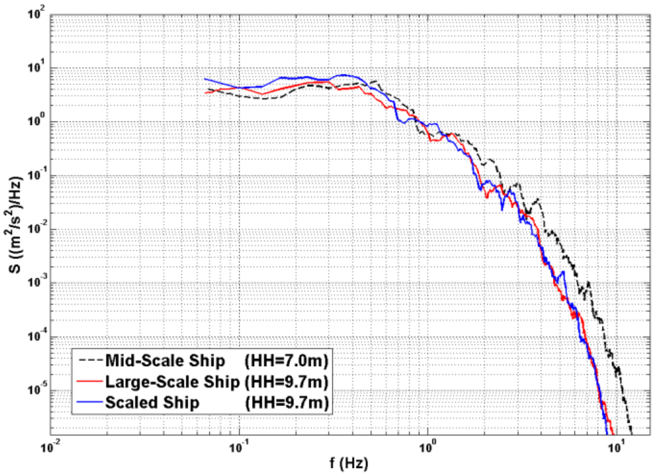

Figure 12a. Power spectral densities of the total velocity for a headwind WOD showing computed large-scale and un-scaled data and the scaled up data at Point 5

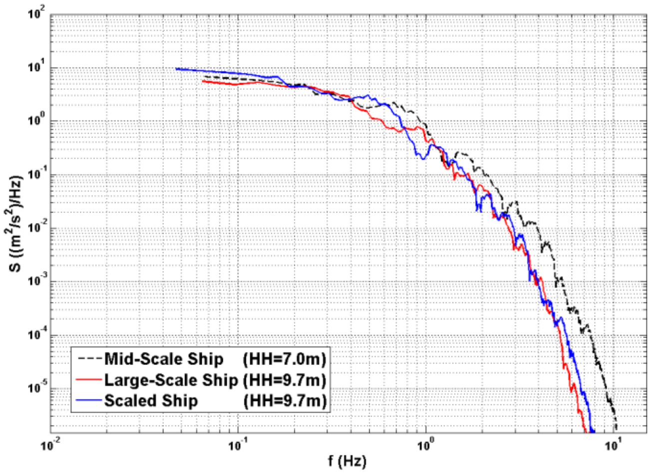

Figure 12b. Power spectral density of the total velocity for a Green 45 WOD showing computed large-scale and un-scaled data and the scaled up data at Point 5

scaled-up ship airwakes were found to be 11.96 m.s^{-1} and 11.98 m.s^{-1}.

Figure 12b shows the power spectral density plot of the scaled-up, large-scale and mid-scale airwake data at Point 5 for the Green 45° case. Once again, the scaled airwake captures the frequency shift exhibited by the Large-scale ship data.

Overall the data suggests that Strouhal scaling is a feasible method for scaling airwakes both in terms of velocity magnitude and ship size. The results of the testing show that in the relatively complex flow field of the Green 45° WOD case, that the airwake can still be scaled to produce data that emulates the computed data well.

CFD and Offline Rotorcraft Analysis

The airwake that occurs over the flight deck for the Headwind case is dominated by the separation that occurs from the hangar edges with a subsequent reattachment point approximately halfway along the deck. This occurs for all three ship scales due to the insensitivity of the flow over sharp edged bluff bodies to the change in Reynolds Number. Figure 13 shows cross sectional contours of the mean, streamwise velocity around the flight deck for both the small-scale and large scale mean CFD data, showing the similarity of the flow between the two ship scales.

As the helicopter size is fixed and the aircraft follows the same translational path for each ship in terms of hangar height and distance from the hangar, the helicopter will be progressively shielded from the increasing freestream velocity away from the ship as the geometric scale size increases. Due to the helicopter being initially trimmed in a 40 knot freestream wind under ‘clean’ conditions, removed from the ship airwake, the rotor disc, empennage and tail rotor will be providing the necessary forces to remain stationary. However once the helicopter comes within the influence of the airwake, those forces are no longer in balance due to changes within the inflow angle of the rotor, the change in the fuselage drag and the flow through the tail rotor for example. These changes can in turn affect the torque required to hold the helicopter in position and the thrust required to maintain altitude. Figure 15a shows a comparison of the mean forces generated by the VAD analysis for the Headwind WOD case. While all three ship scales show broadly similar behavior as the helicopter passes through the airwake, the unbalanced longitudinal force (F_x) on the helicopter can be seen to rise with a decrease in ship scale. This is due to the influence of the airwake through the rotor as the helicopter gets proportionally smaller with the increase in ship size. At Point 7 for the small ship size, some of the SH60B’s rotor disc will be passing over the flight deck; the scale of the rotor disc with each ship size is shown in Figure 14.

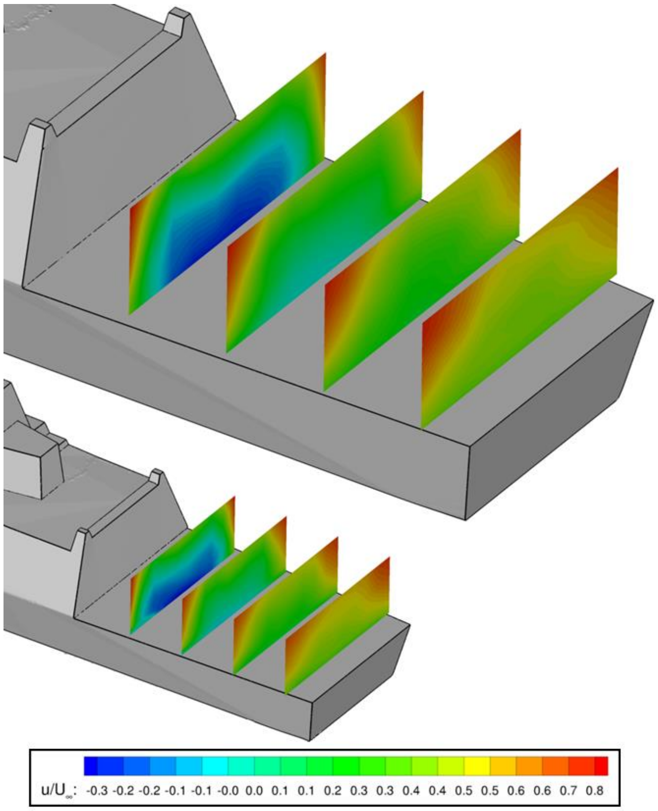

Figure 13. Normalised longitudinal velocity contours over the flight decks of the small and large scale ships for the Headwind case.

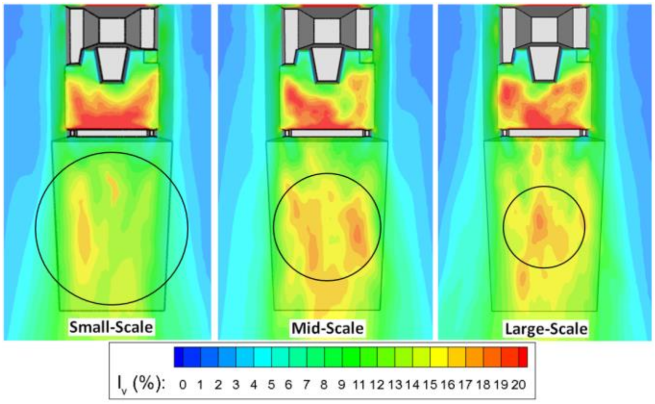

Figure 14. Comparisons of lateral turbulence intensity at 100 % hangar height showing the change in scale of the SH60B rotor disc over the deck

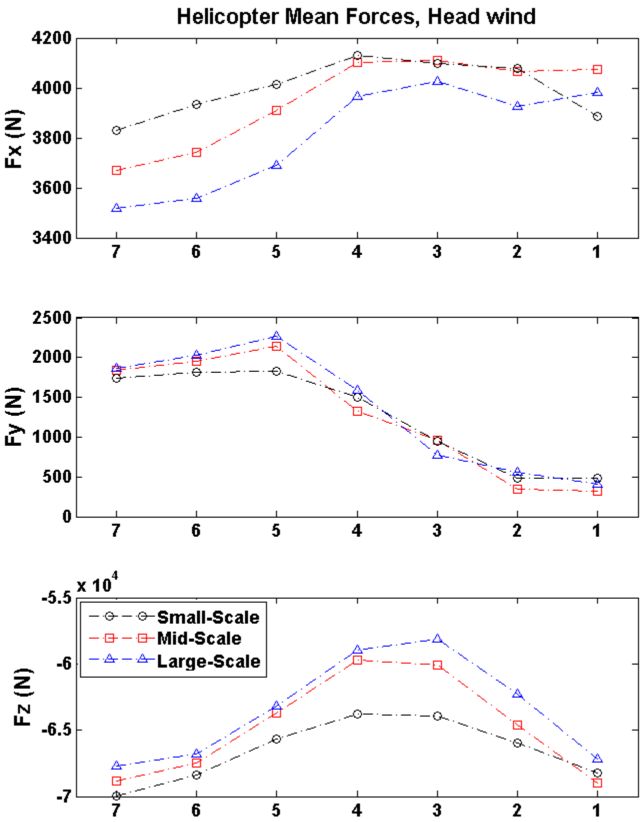

Helicopter Mean Forces, Head wind

Figure 15a. VAD comparison of mean forces

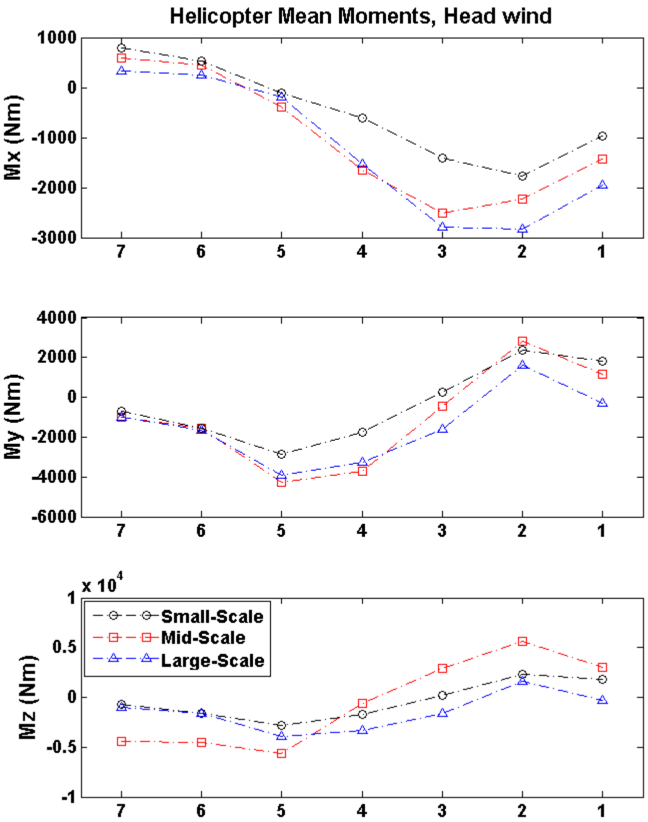

Helicopter Mean Moments, Head wind

Figure 15b. VAD comparison of mean moments

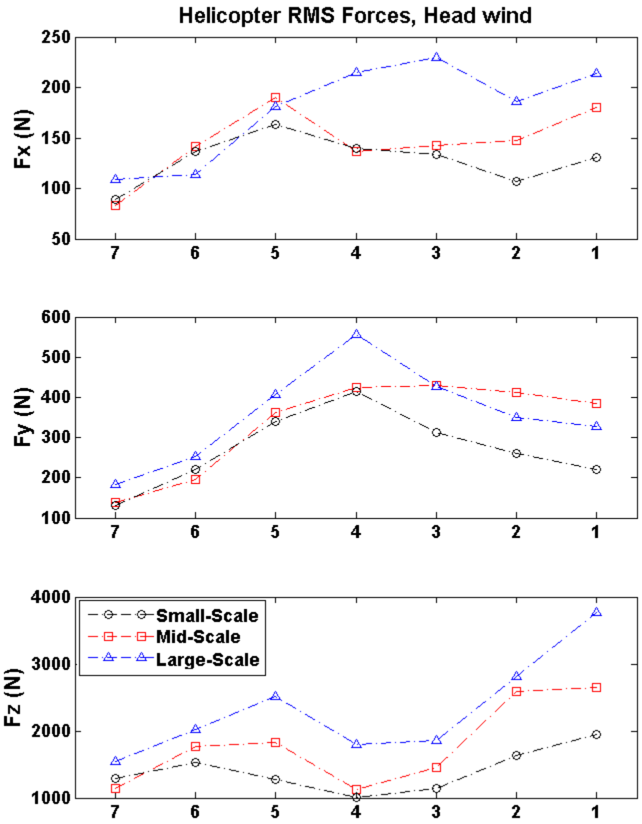

Helicopter RMS Forces, Head wind

Figure 15c. VAD comparison of RMS forces

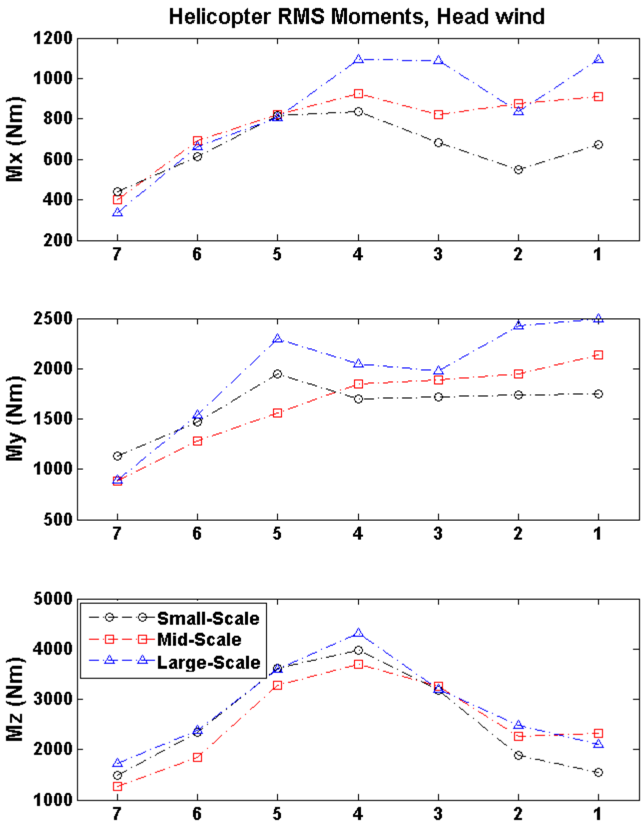

Helicopter RMS Moments, Head wind

Figure 15d. VAD comparison of RMS moments

The flow behind the hangar in a Headwind can be considered as a three-dimensional backward facing step, where the longitudinal component of the flow is reduced in the lee of the hangar. The rise in the longitudinal F_x component of the mean VAD force, Figure 15a, is a reaction from the helicopter to this reduction in flow, as the force produced to keep the helicopter in trim in a 40 knot wind now exceeds the required trim condition in the lower flow speeds.

Over the landing spot, at Point 3, the mean forces generated along the vertical axis (F_z) shown in Figure 15a suggest that as the ship scale increases, the thrust deficit increases due to the larger downwash from the large ships hangar affecting a larger portion of the rotor disc.

The lateral turbulence intensity contours at 100% hangar height for all three ship scales, Figure 14, show that although the areas of turbulence occur over the same regions of the deck, the total turbulence seen at the rotor disc will vary greatly along with that experienced by the fuselage and tail rotor. Looking at Figures 15c and 15d, showing the comparison of RMS forces and moments generated by the turbulent flow, each ship size show similar trends in the longitudinal and lateral components up until Point 5, which lies over the Port edge of the ship. At this point, half of the rotor disc lies directly within the lee of the hangar where the difference in the magnitude of the vortices created by the change in ship size gives rise to the change in RMS forces. As expected, the larger vertical structures of the larger ship contain more energy and although shed at a reduced frequency, do influence the aerodynamic loading of the aircraft more so than the small-scale ship.

So far only an offline rotorcraft analysis has been performed on the computed data. Scaling the airwake to be representative of a smaller and larger ship and implementing the new airwake data into FLIGHTLAB to compare the aerodynamic loadings generated on the aircraft would provide a further insight into the accuracy of the scaling methods.

CONCLUSIONS

A ship geometry was created based on modern, helicopter operating ships, in order to represent the modern trend of naval ships with clean, sharp edges. This geometry was then scaled to represent both the small and large scale helicopter operating ships to assess the effects on ship size on pilot workload.

A series of CFD simulations were carried out and data was sampled at seven points around the flight deck during the simulations. This data was then processed using numerical scaling methods based on the Strouhal number to show the feasibility of scaling based on velocity magnitude. The scaled data showed a good agreement with the computed data. Going further, the airwake was scaled based on an increase and decrease in ship size, using the hangar as a characteristic length. Comparisons were made against the computed data and shown that in each case and again the scaled data showed good agreement to the computed data.

An offline flight mechanics modeling analysis was performed using a model of the SH60B helicopter. The aircraft was placed at seven test points over the deck of each ship to determine the effects of ship size on the aerodynamic loadings.

ACKNOWLEDGEMENTS

The authors are grateful to Dr David Roper at Ansys Inc for his continued support in the ongoing research at the University of Liverpool.

REFERENCES

[1] Lumsden, B. and Padfield, G.D., “Challenges at the Helicopter-Ship Dynamic Interface”, *Military Aerospace Technologies – Fitec ’98*, IMechE Conference Transactions, Institution of Mechanical Engineers, Wiley, 1998, pp 89 - 122

[2] Newman, S., “The Safety of Shipbourne Helicopter Operations”, *Aircraft Engineering and Aerospace Technology*, Vol. 76, No 5, 2004, pp 487 - 501

[3] McRuer, D.T., “Interdisciplinary Interactions and Dynamic Systems Integration”, *Internation Journal of Control*, Vol 59, 1994, pp 3 – 12

[4] Kääriä, C.H., Forrest, J.S., Owen, I., “Determing the Impact of Hangar Edge Modifications on Ship-Helicopter Operations Using Offline and Piloted Flight Simulation”, *American Helicopter Society 66th Annual Forum and Technology Display*, Phoenix, USA, April 29 – May , 2008

[5] Hodge, S.J., Forrest, J.S., Padfield, G.D. and Owen, I., “Simulating the Environment at the Helicopter-Ship Dynamic Interface: Research, development and application”, *The Aeronautical Journal*, Vol 116, No 1185, pp 1155 – 1184

[6] Kääriä, C.H., Forrest, J.S., Owen, I. and Padfield, G.D., “Simulated Aerodynamic Loading of an SH-60B Helicopter in a Ship’s Airwake”, *35th European Rotorcraft Forum*, Hamburg, Germany 21 – 25 Sept, 2009

[7] Forrest, J.S., Hodge, S.J., Owen, I., and Padfield, G.D., “Towards the Fully Simulated Ship-Helicopter Operating Limits: The Importance of Ship-Airwake Fidelity”, *American Helicopter Society 64th Annual Forum*, Montreal, Canada, April 29 – May , 2008

[8] Kääriä, C.H., Forrest, J.S., Owen, I., “Assessing the Suitability of Ship Designs for Helicopter Operations Using Piloted Flight Simulation”, *37th European Rotorcraft Forum*,

Milano, Italy, 13 – 15 Sept, 2011

[9] Prism Defence Ltd, http://www.prismdefence.com.au, accessed March 2014

[10] Polsky, S.A and Bruner, W.W., "A Computational Study of Unsteady Ship Airwake", *RTO AVT Symposium on "Advanced Flow Management: Part A – Vortex Flows and High Angle of Attack for Military Vehicles*, Loen, Norway, 7 – 11 May, 2001

[11] Zan, S.J., "On Aerodynamic Modeling and Simulation of the Dynamic Interface", *Proceedings of the Institute of Mechanical Engineers, Part G*, Journal of Aerospace Engineering, Vol 219 (5), 2005

[12] Forrest, J.S., Owen, I., "An Investigation of Ship Airwakes Using Detached-Eddy Simulation" *Computers and Fluids 39(2010)*, 2009

[13] Counihan, J., "Adiabatic Atmospheric Boundary Layers: A Review and Analysis of Data from the Period 1880 – 1972", *Atmospheric Environment*, Vol 9, No 10, 1975, pp 871 – 905

[14] Forrest, J.S., Kääriä, C.H. and Owen, I., "The virtual AirDyn: a simulation technique for evaluating the aerodynamic impact of ship superstructures on helicopter operations", *The Royal Aeronautical Society*, Vol 117, No 1198, December 2013

[15] Wang, Y., Curran, J., Padfield, G.D. and Owen, I., "AirDyn: An Instrumented Model-Scale Helicopter For Measuring Unsteady Aerodynamic Loading in Airwakes", *Measurement Science and Technology*, Vol 22, pp 1 – 12, March 2011

[16] Kääriä, C.H., Wang. Y., White. M.D. and Owen. I., "An Experimental Technique for Evaluating the Aerodynamic Impact of Ship Superstructures on Helicopter Operations", *Ocean Engineering*, Vol 61, pp 97 – 108 , 2013

[17] Forrest, J.S., "Predicting Ship-Helicopter Operating Limits Using Time-Accurate CFD Ship Airwakes and Piloted Flight Simulation", *PhD Thesis, Dept of Engineering, University of Liverpool*, 2009.

Rebecca Mateer
Paul Scott, Mark White, & Ieuan Owen
University of Liverpool, UK.

The Aerodynamics of a Bulky Mast

ABSTRACT

Many modern warships have enclosed main masts that are bulky and very different to the lattice or pole masts of earlier ships. While the newer masts are carefully designed to reduce radar cross section, and provide a weather tight enclosure for sensors and systems, they also significantly affect the air flow over the ship. This paper reports some results from a CFD study of the air flow over a generic ship representative of a modern frigate with an enclosed mast. Specific attention has been paid to the unsteady velocities at locations around the mast where a ship's anemometer might typically be placed. The flow is seen to be highly disturbed and both the wind strength and angle are significantly different to those of the free stream, hence making a true wind over deck measurement difficult. In the context of helicopter launch and recovery this makes it difficult to specify the helicopter's operational limits which can restrict operational capability. The study has also quantified the temperature field due to the ship's exhaust gas, and shows how vortex shedding from the mast mixes the exhaust gas with the airwake, so quenching the hot gases and reducing temperatures over the flight deck.

INTRODUCTION

Many designs of modern warships have masts that are more solid and bulky than the traditional lattice or tripod masts. Figure 1, for example, shows the mast structures for a US Arleigh-Burke class destroyer and a UK Daring class Type 45 destroyer. The images of the two ships are approximately scaled and it can be seen how the mast of the American ship has a taller and more open structure. The British Type 45 is an enclosed mast which contains a variety of equipment and systems in a watertight enclosure. In this case the outer surface of the mast is constructed from steel, but an enclosed mast could also be made from composite materials which allow antennae to be contained within the mast and to operate effectively as they can 'see' through the composite material. A further evolution of the enclosed mast concept is the integrated mast in which many of the antennae and sensors are not so much contained within the mast, but are themselves part of the outer surface of the mast. An example of a ship that operates with an integrated mast is the Dutch Holland class offshore patrol vessel which carries a Thales integrated mast. The geometry of the enclosed masts also lend them to reduced radar cross section, particularly for the integrated mast which does not have external sensors and equipment, such as those seen on the Type 45 in Fig. 1.

Figure 1: Mast profiles of a US Arleigh-Burke class and a UK Daring class destroyer

A review of integrated masts and their implications for ship design is given by Savage & Kimber [1]. There are structural design issues related to the need to align the base of the mast with the under-deck structure and bulkheads, and the additional strength required to withstand the whipping and slamming loads. The increased weight and higher centre of gravity of the mast also has an influence on ship stability. Savage & Kimber also recognise that the bulkier non-aerodynamic profile of the integrated mast has implications for ship airwake and ship engine exhaust gas dispersion, their concern over the latter being related to the heating of surfaces and electronic components.

The purpose of this paper is to consider the aerodynamics of the flow around an enclosed mast with a particular emphasis on how this may affect the positioning of the ship's anemometers, how it affects the engine exhaust gas dispersion, and the implications of both of these for the operation of the ship's helicopter. The study has been carried out using unsteady Computational Fluid Dynamics (CFD). The accuracy of the wind velocity measurements recorded by the ship's anemometers is important because they are used to define the Ship-Helicopter Operating Limits (SHOL) at the outset of the ship's service, and the Wind-Over-Deck conditions for every sortie thereafter; unreliable anemometers lead directly to unnecessarily restricted SHOLs. As for exhaust gases from the ship's engines, if the temperature of the airflow in which the helicopter has to operate is increased, this can adversely affect the helicopter's performance through reduced rotor lift and reduced engine power.

CFD METHODOLOGY

Generic Frigate Model and Meshing

Figure 2 shows the generic ship model that has been created for this study and which has many of the characteristics of a modern frigate, such as a large bulky main mast similar to that seen on the Type 45, a large rectangular funnel with a main gas turbine (GT) exhaust amidships immediately behind the mast, and four Diesel generator (DG) exhausts – two placed amidships adjacent to the GT and two situated on a starboard rear funnel, above the hangar and immediately in front of the flight deck. The superstructure also has sloping smooth sides to minimise radar cross section reduction.

To illustrate the aerodynamic issues for this ship should its anemometers be mounted off the main mast (as they are on the Type 45), the velocities of the air flow at typical port and starboard positions have been studied in detail. The positions are half-way up the mast and at port and starboard locations equivalent to being at the end of 6m long yardarms attached to the front corners of the mast and angled 60° forward. The positions will be indicated on the relevant figures later in the paper (yardarms can be seen on the mast in Fig. 2, but these are not at mast half-height).

For the exhausts, both the GT and DG's uptakes are cylindrical and have exit planes flush to their funnel top surfaces. The GT exhaust has a diameter of 2.8m whilst the DG exhausts have diameters of 0.5m. The length of the generic frigate is 150m with a beam of 20m.

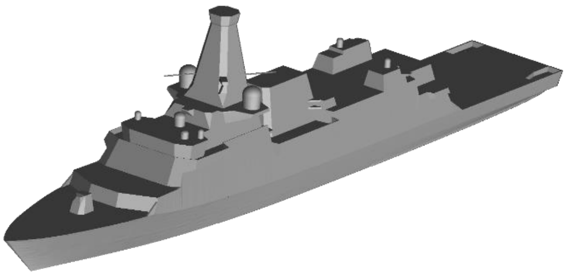

Figure 2: Generic Frigate Model

The CFD analysis was carried out using the commercial code Ansys Fluent. The ship CAD model was imported into the Ansys ICEM mesh generation software for an initial 'clean-up' process to remove any unnecessary clutter and to ensure that the geometry was 'sealed' ready for meshing. The removal of clutter was based upon recommendations by Forrest & Owen [2] where objects less than 0.3m in diameter can be neglected as they have little effect on the airwake but will increase cell count and therefore computational time.

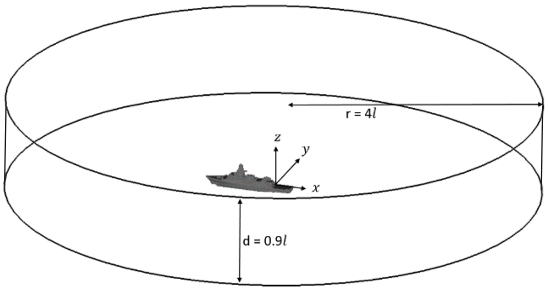

Figure 3: Computational domain

The prepared ship geometry was enclosed in a large cylindrical domain, Fig. 3, of radius, r = 4l and depth, d = 0.9l, where l=ship's length; this ensures that the boundaries are far enough away from the ship model to negate any blockage effects during the simulation. Using a cylindrical domain allows multiple Wind-Over-Deck (WOD) simulations to be run through 360° from a single mesh by altering the x and y velocity components of the oncoming flow. In this instance, the ship was placed in the domain for the positive x-direction to run through the longitudinal axis from bow to stern and positive y-direction to run through the lateral axis toward starboard.

Detached Eddy Simulation (DES) was used for turbulence modelling and an unstructured meshing technique was used which suits the turbulence modelling due to the isotropic nature of the tetrahedra away from the walls [2]. An Octree volume mesh was first used to produce a good quality triangular surface mesh from which a Delaunay volume mesh was grown, as seen in Fig. 4. A general rule of minimum cell size = 0.05 x hangar height was adhered to and prism layers were included in order to resolve the viscous boundary layer on the ship and representative 'sea-surface'. Mesh growth normal to the geometry walls was controlled using a tetra growth ratio of 1.2 to retain a smooth transition between the prism and tetrahedra cells. The refined region over the flight deck is for future work on the effect of the ship airwake on helicopter flight simulation. The total cell count of the domain is approximately 10.5 million cells.

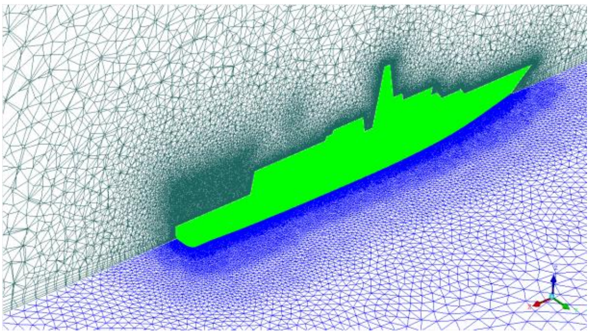

Figure 4: CFD Mesh

Boundary Conditions

Ansys Fluent requires all of the geometry surfaces to have specified boundary conditions. In the case of the cylindrical domain, the upper surface was set as a symmetry condition where there is no flux across the boundary while specifying a zero shear condition. The outer circumference of the domain was set to a 'pressure far field' which allows the freestream conditions to be modelled at infinity. The freestream Mach number must also be specified along with the x, y and z components of the freestream flow velocity for the pressure far field boundary condition.

The ship's surfaces were set as a series of walls with a zero slip condition to allow boundary layers to develop. The sea-surface plane was set as a wall but with a zero shear stress condition to allow the atmospheric boundary layer profile specified at the inlet to propagate through the domain unchanged.

The atmospheric boundary layer (ABL) profile was included to increase the accuracy of the CFD simulations as there can be a significant velocity change between the sea surface and the ship's anemometer height. The following power law was used to model the ABL:

$$V = V_{ref}\left(\frac{z}{z_{ref}}\right)^{\alpha} \qquad (1)$$

Where, V_{ref}, is the velocity at reference height, z_{ref}, and, α, is a constant dependent on the surface roughness. The following values were used: V_{ref} = 50 knots, z_{ref} = 200m, α = 0.13 (as recommended in [2]). At the ship's anemometer height, approximately 27 metres above sea level, this equates to an approximate 20 m/s freestream velocity (~38.5 kts).

For the CFD simulations inclusive of exhaust gas effects, the energy equation within Ansys Fluent was activated, as well as the solution of additional transport equations to account for the buoyancy of the plume. The exhaust efflux has both momentum and buoyancy, however in the near field where this study is concerned the exhaust gases are ejected at high speed (~ 100 m/s) into highly disturbed air therefore the plume is momentum dominated and not buoyancy dominated [3].

The boundaries of both the GT and DG exhausts were specified as mass flow inlets in order to model the exhaust efflux. The GT boundary condition was set with a mass flow rate of 106 kg/s and temperature of 445°C while the DG boundary conditions were set with mass flow rates of 5.6 kg/s and temperatures of 430°C. These values were chosen to be representative of typical engines used in frigates that do not have waste heat recovery systems. In this instance, the exhaust gas species were not modelled with the gas being defined as air for simplicity. The ambient temperature was set to 38°C, which represents a demanding condition for helicopter launch and recovery and is representative of what might be encountered, for example, in the Arabian Gulf.

Computational Modelling

Second-order discretisation was used in time and space, and a blended upwind central-differencing scheme was used for the convective terms.

Pressure-velocity coupling was resolved through use of the Pressure-Implicit with Splitting of Operators (PISO) scheme. As DES is a time-accurate CFD method, and having been originally developed to resolve the flow separation from large bluff-bodies at high Reynolds numbers, it is an appropriate model to simulate the flow around the superstructure of a ship. DES was originally a modification to the Spalart-Allmaras turbulence model [4] such that the distance to the wall, d, is replaced as shown in equation (2):

$$\tilde{d} = \min(d, C_{DES}\,\Delta) \qquad (2)$$

In the unmodified Spalart-Allmaras model the length scale d is used to drive the turbulent viscosity. By linking the length scale to the local grid spacing (Δ), the new modified length scale ($\tilde{d}$) means that turbulent viscosity production is limited away from the walls, allowing the DES model to fully resolve the medium to large scale turbulence. The constant (C_{DES}) has the default value of 0.65 which was retained for this study.

To produce the unsteady CFD solutions, the fluid dynamic equations in the whole domain were first solved iteratively 1000 times to converge onto a steady-state solution. The steady-state flow field was then used as the initial conditions for calculating the unsteady flow field by activating the unsteady solver in DES mode with the simulation carried out at 100Hz. An initial 1500 time steps were computed to allow the transition from steady to unsteady to develop fully; this data was then discarded and a further 3000 time steps were computed to create 30 seconds of unsteady airwake data.

The computational methodology outlined above is based on that reported by Forrest & Owen [2], who included validation against experimental ship airwake data from wind tunnel testing and at-sea measurements taken over the deck of a frigate.

MAST AERODYNAMICS

As can be seen in Fig. 2, the main mast is a tapered structure that has a square cross section with chamfered corners. It has a width at its base of 9m, a height of 14.8m and a width at the top of 3.2m; the surface slope is 11°. The mast clearly does not have an aerodynamic geometry and as such it will have a large and unsteady wake as can be seen in Figs. 5 to 7. For a bluff body with a square cross section and a uniform cross-flow the wake will shed a Von-Karman vortex sheet at a regular frequency described by the Strouhal number St:

$$St = \frac{f\,D}{V} \qquad (3)$$

Where f is the shedding frequency, D is the characteristic diameter, and V is the incident velocity.

For a square cylinder the values of St at high Reynolds number is 0.13 [5]. However the mast does not have a constant or a square cross section. Tamura & Miyagi [6] showed that the Strouhal number (St) can increase to about 0.17 for a square cylinder with chamfered corners, and that for incident angles between 0 and 30° the value of St reduced to 0.14. The effect of the mast taper will also alter the vortex shedding frequency because, as it narrows, Eq.3 shows that the frequency can be expected to increase. This fact is sometimes used to reduce the wind loading on tall buildings since in a tapered building the change in the natural frequency of shedding up the height of the building prevents coherent vortex shedding and reduces the likelihood of resonant unsteady wind loads. Kim & Kanda [7] have shown that for a tall building with a taper on the side of about 3° the value of St decreases from 0.13 to 0.09 at increased height up the structure, and that the spectrum of the unsteady loads on the building become weaker and broader.

It is clear from the discussion above that the wake being shed from the ship's mast will be affected by its geometry and it will be further affected by the fact that the approaching air flow is not orthogonal to the mast, neither is it uniform and it is also unsteady. Figure 5 shows the ship's airwake in a headwind as longitudinal mean velocity contours together with the position of the ship's anemometer in the ABL (indicated by the red arrow). The air flow approaching the mast is rising as it flows over the forward superstructure, and Fig. 6 shows the general turbulence intensity on the centreline plane of the ship created by the flow separating from the non-aerodynamic mast and other geometric features. Figure 7 shows both velocity vectors and contours of general turbulence intensity in a Green 45 WOD at 20 m/s with a plan view of the velocity field in a horizontal plane at 50% mast height. The wake is clearly visible and within the intensely turbulent regions is the unsteady vortex shedding from the edge of the mast. The vectors on the plot are scaled according to velocity magnitude and show clearly the abrupt change in velocity across the shear layer as well as the flow recirculation occurring in the lee of the mast structure. Also shown in Fig. 7 are the locations where anemometers might be placed, as discussed earlier.

Through examining a Fast Fourier Transform (FFT) of the lateral velocity at the starboard anemometer location when it is positioned directly in the lee of the mast wake (Red 150 WOD), it can be seen in Fig. 8 that there is no single dominant vortex shedding frequency. Returning to the previous discussion about the range of shedding frequencies that can be expected from a modified square cylinder, if the ideal St value of 0.13 is adopted then at this location a shedding frequency of 0.43 Hz is obtained, which is in the middle of the spread of dominant frequencies shown in Fig. 8, indicating that the vortex shedding is highly irregular, but within a range that can be expected for a mast of this size and shape.

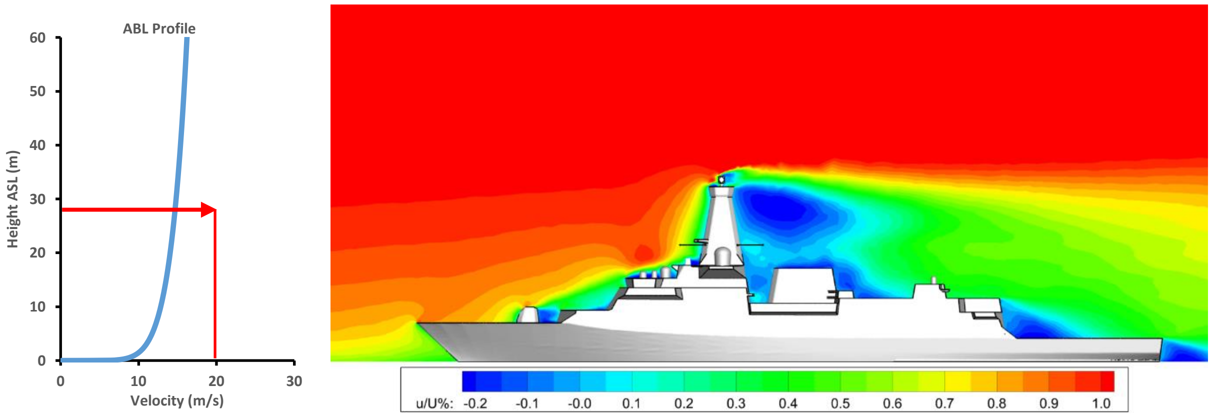

(a) (b)

Figure 5: Atmospheric Boundary Layer profile (a) with reference to a longitudinal view of the ship's airwake showing contours of normalised longitudinal mean velocity (b)

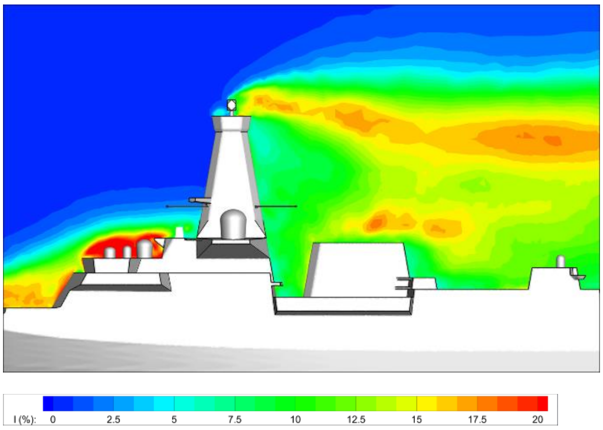

Figure 6: Contours of turbulence intensity in the longitudinal vertical plane in a 20 m/s headwind

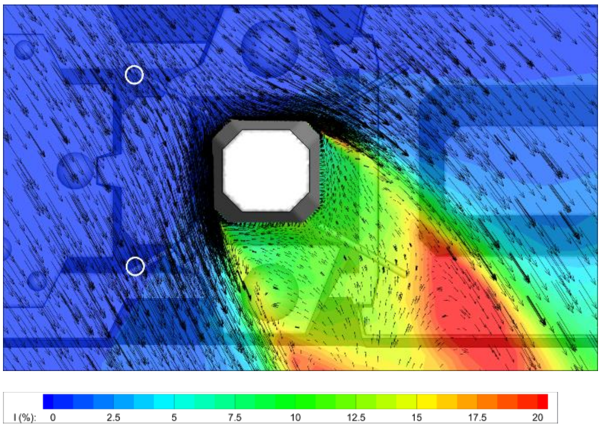

Figure 7: Contours of turbulence intensity with vectors of mean velocity magnitude in the horizontal plane for a 20 m/s Green 45 WOD

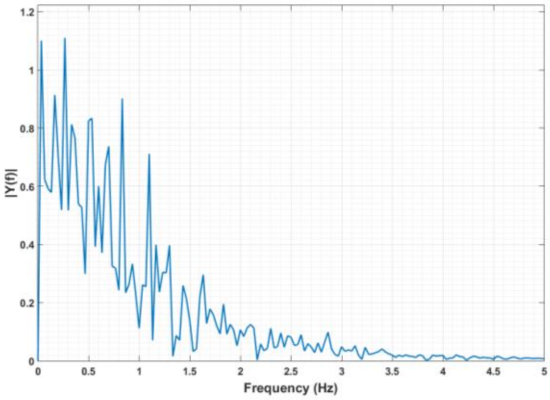

Figure 8: FFT of the lateral velocities at the starboard anemometer in a Red 150 WOD – representative of the anemometer being in the centre of the wake of the mast

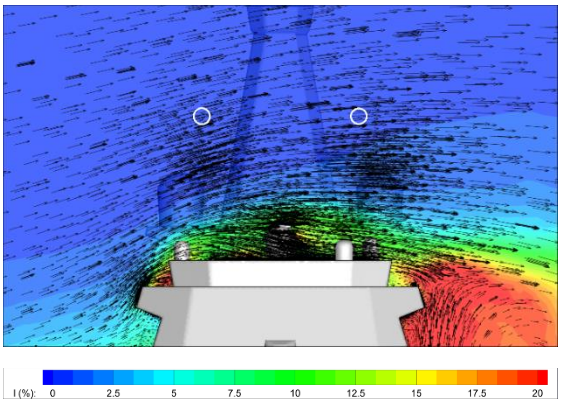

Figure 9: Contours of turbulence intensity with vectors of mean velocity magnitude in transverse vertical plane ahead of the mast in a 20 m/s Green 45 WOD

A ship's anemometers usually only take account of the horizontal components of velocity, although modern ultrasonic anemometers are capable of measuring all three components. The vector sum of the two horizontal components yields both the wind strength and direction with the vertical component being seen as less useful, although it is a measure of the local flow distortion. Figure 10 shows the vertical velocity component, w, calculated for the two assumed anemometer locations, and for a 20 m/s wind for all directions; for an undisturbed wind the vertical velocity would be zero, as indicated by the blue line in Fig. 10. It can be seen that there are vertical (upward) velocities of up to 6 m/s, and on average about 3 m/s; the exception is the tailwind where the air flow is coming from the stern and after the main mast the air flows downwards towards the bow. The magnitude of the vertical component should be seen against the oncoming wind speed of 20 m/s, so this is another indication of the distorted air flow in which the anemometers would have to operate.

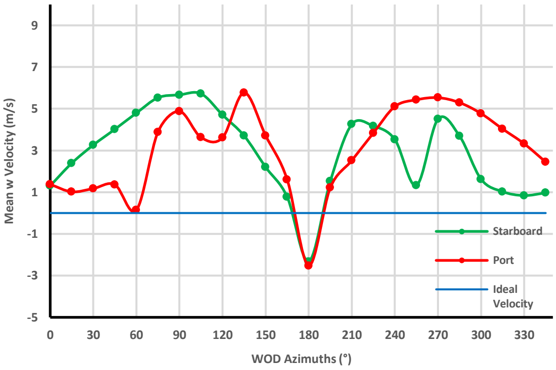

Figure 10: Variation in mean vertical flow velocity for different wind angles

Figures 11 & 12 show the computed air velocity and direction, respectively, for a 20 m/s oncoming wind, for all wind angles. In Fig. 11 the undisturbed wind speed at approximate anemometer height is 20 m/s, as marked on the graph (blue line). The red and green curves represent the port and starboard positions where the velocities are recorded and they can be seen to be very nearly mirror images of each other, reflecting the relatively symmetrical geometry of the ship and of the assumed anemometer positions. Errors in the velocity readings can be seen in the context of UK military defence standards, DEFSTAN 08-133 Part 2 [8], which require an error in velocity readings no greater than 10% of the true wind speed and an error in angular deviation no greater than 5°. As can be seen in Fig. 11, the computed wind speed at the assumed anemometer positions deviate by more than 2 m/s for the majority of wind angles. Between approximately 105° and 195° for the port position, and 165° and 255° for the starboard position, the respective anemometers are in the lee of the mast and would be significantly in error and inoperable for those wind directions.

Referring now to Fig. 12, the true wind direction is indicated by the blue straight line, and again it can be seen that when the anemometer positions are immersed in the mast wake the direction of the flow in the horizontal plane is significantly in error.

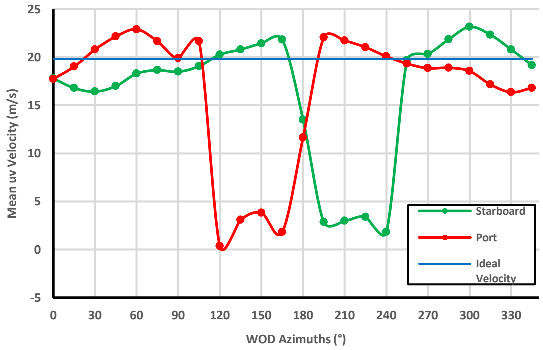

Figure 11: Variation in mean anemometer flow velocity in the horizontal plane (true wind 20 m/s)

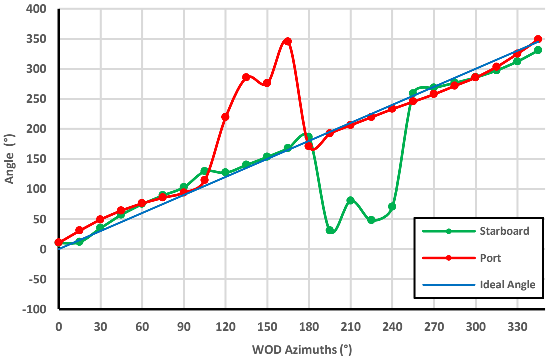

Figure 12: Variation in mean anemometer flow angle in the horizontal plane compared to true wind angle

Finally, on the anemometer positions, Fig. 13 shows the turbulent RMS values in *u*, *v*, *w* in the *x*, *y*, *z* (longitudinal, transverse, vertical) directions respectively. The wind angles that are problematic in Figs, 11 & 12 are also those that have significant unsteadiness, again due to the unsteady and irregular vortex shedding.

It is not unusual for a ship's two main (port & starboard) anemometers to have useable and non-useable wind angles. It is also possible that anemometers which have repeatable errors in wind strength and direction can be calibrated during at-sea trials (or possibly against wind tunnel or CFD data). However, for the bulky mast considered in this study it can be seen that the wind directions where one or both of the anemometers provide accurate readings is limited, and that the significant range of wind angles when the flow is unsteady and irregular makes anemometer calibration more difficult.

The data presented above has been for a potential anemometer position that is half way up the mast. Looking at the disturbed flow near the base of the mast in Fig. 9 shows that if the anemometers can be placed higher up the mast, where its cross-section is smaller and the flow distortion from the superstructure is less, then the better it is for the anemometer.

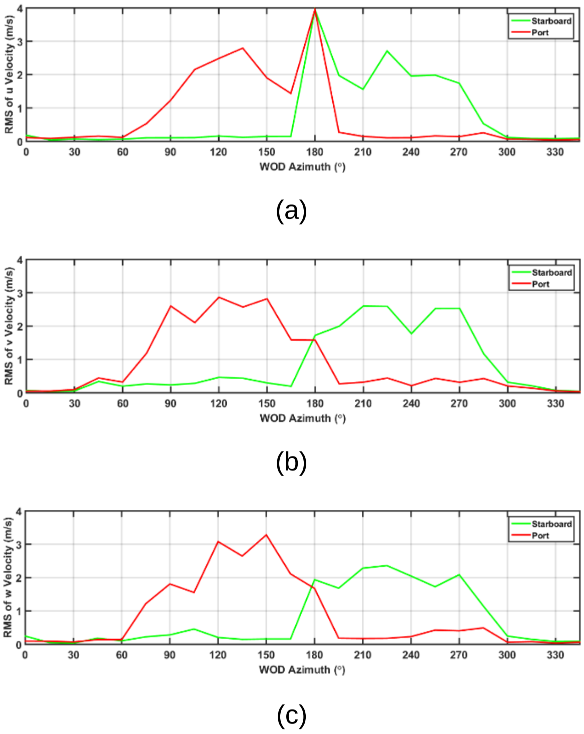

(a)

(b)

(c)

Figure 13: RMS of u (a), v (b), w (c) components of velocity about the mean velocity

EFFECT OF MAST WAKE ON EXHAUST GAS DISPERSION

The large bulky shape of the main mast structure and the relative positioning of the GT exhaust, amidships and directly in the lee of the mast in acute WOD conditions can cause the exhaust gases to be entrained into the mast wake. The unsteadiness of the ship airwake as a result of the vortex shedding from the mast promotes the mixing of the exhaust efflux with the airwake and will enhance its dilution and dispersion.

Figure 14 shows air temperature in a vertical plane through the centre of the GT exhaust for a headwind condition; in this case the wind speed is lower at 14 m/s (~27 kts). As mentioned earlier, the ambient temperature is 38°C. It can be seen how the recirculation zone in the lee of the mast causes the exhaust gases to be entrained into the wake. Adjacent to the mast, air temperatures can reach 26°C above ambient (64°C), shown by the green region against the rear surface of the mast, which may affect sensitive equipment and systems at that location. Figure 15 shows a plan view of the mean velocity vectors and mean temperatures in a horizontal plane at half-mast height; again the entrainment of the hot exhaust gases into the mast wake can be seen with temperatures of the air surrounding the mast in that plane of approximately 20° above ambient. In Fig. 16, which shows mean velocity vectors and air temperatures in a transverse vertical plane through the centre of the flight deck, it can be seen that the hot exhaust has been cooled to about 15°C above ambient. The core of the GT exhaust is high above the deck and is unlikely therefore to interact with the helicopter under normal launch & recovery operations. Also visible in Fig. 16 is an area of raised temperature at around 6°C above ambient at about hangar height which is due to the rear Diesel exhaust.

It is known that elevated air temperatures will reduce the thrust of the main rotor, and the power output of the helicopter engine(s). While these adverse effects are not large, they are sufficient for users of offshore oil/gas platforms to issue guidelines to their helicopter operators that ambient air temperature rises greater than 2°C require some form of action [9]. Somewhat surprisingly there is no similar recommendation for naval operations, a topic that was discussed at some length by Scott et al [10]. Data presented in Fig. 17 shows unsteady temperatures at 200% and 250% hangar height above the landing spot (16m and 20m above the deck respectively). There is an irregular periodicity in the temperature fluctuations that are consistent with the frequencies of the shedding from the mast. In this instance where the WOD condition is a headwind, the higher temperatures in the core of the GT exhaust plume are higher than the standard hover position of a helicopter and therefore may not be of great concern to launch and recovery operations. Acute angle WOD conditions, such as Green/Red 30, do present potential issues as the core of the GT exhaust plume is entrained down into the helicopters operational area on the lee side of the ship, as discussed by Scott et al [10].

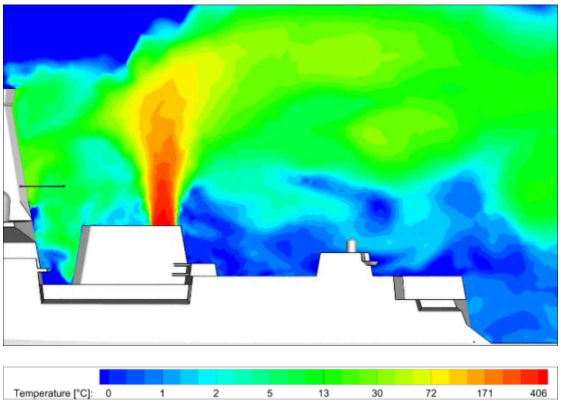

Figure 14: Contours of temperature above ambient along the ship centreline in a 14 m/s headwind (logarithmic scale)

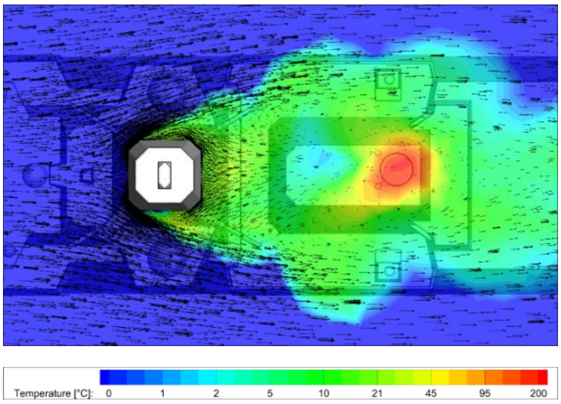

Figure 15: Contours of mean temperature above ambient with vectors of velocity magnitude at 50% mast height in a 14 m/s headwind (logarithmic scale)

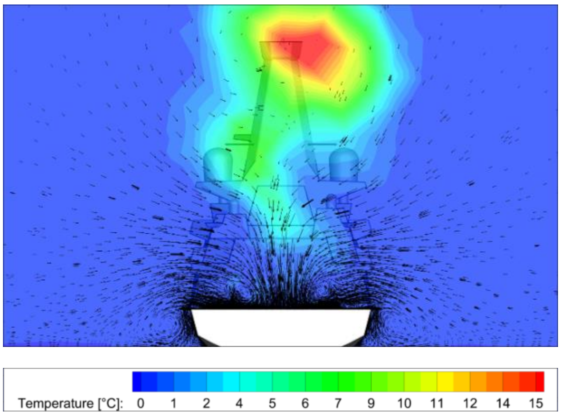

Figure 16: Contours of mean temperature above ambient with vectors of velocity magnitude across the centre of the flight deck in a 14 m/s headwind

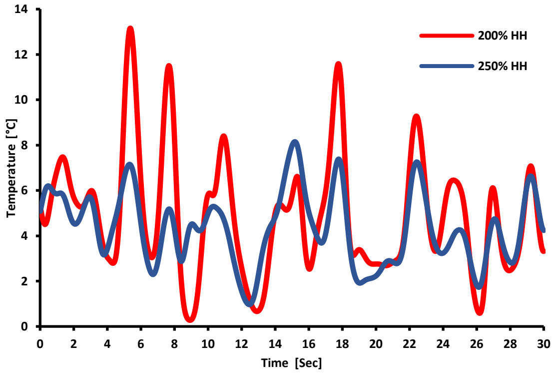

Figure 17: Temperatures above ambient over the landing spot on the flight deck according to hangar height (HH) in a 14 m/s headwind

CONCLUSIONS

The air flow over and around a generic frigate with a bulky enclosed mast has been investigated using unsteady CFD.

The bluff geometry of the mast significantly distorts the air flow and leads to a large and unsteady wake in the lee of the mast.

Mounting the ship's anemometers on the main mast, as is traditional, means that the anemometers could well be in serious error in both speed and direction for a considerable range of wind directions. Furthermore, the unsteady and irregular nature of the mast wake will make it difficult to obtain repeatable readings from the anemometer, which means that corrective calibration would also be problematic. Unsteady anemometers will lead to unnecessarily restricted SHOLs.

The large and unsteady wake from the mast will also interact with the ship's engine exhaust gases. In the case of the generic ship considered in this paper, with a gas turbine exhaust directly behind the main mast, the interaction of the hot exhaust with the unsteady wake appears to be beneficial in that the hot exhaust gases are significantly cooled by the time the pass over the helicopter landing deck. Notwithstanding the cooling of the ship's exhaust, there is still a significant uncertainty over what are acceptable air temperatures for safe helicopter operations.

REFERENCES

[1] C. Savage and A. Kimber, "When is a mast a mast? The impact of integrated masts on platform design and classification," in *RINA Warship 2010: Advanced Technlogies in Naval Design and Construction*, London, 2010.

[2] J. Forrest and I. Owen, "An investigation of ship airwakes using Detached-Eddy Simulation," *Computers and Fluids*, vol. 39, no. 4, pp. 656-673, 2010.

[3] S. Ergin and E. Dobrucali, "Numerical Modelling of Exhaust Smoke Dispersion for a Generic Frigate and Comparison with Experiments," *Journal of Marine Science and Application*, vol. 13, pp. 206-211, 2014.

[4] P. R. Spalart, W. H. Jou, M. Strelets and S. R. Allarmas, "Comments on the feasibility of LES for wings and on a hybrid RANS/LES Approach," in *1st AFOSR International Conference on DNS/LES*, Ruston, LA, 1997.

[5] C. Norberg, "Flow around regular cylinders: pressure forces and wake frequencies," *Journal of Wind Engineering and Industrial Aerodynamics*, pp. 187-196, 1993.

[6] T. Tamura and T. Miyagi, "The effect of turbulence on aerodynamic forces on a square cylinder with various corner shapes," *Journal of Wind Engineering and Industrial Aerodynamics*, pp. 135-145, 1999.

[7] Y. C. Kim and J. Kanda, "Wind pressures on tapered and set back tall buildings," *Journal of Fluids and Structures*, vol. 39, pp. 306-321, 2013.

[8] Ministry of Defence, "Requirements and Guidance for the Aviation Arrangements in Surface Ships: Part 2 - Guidance for the Design and Construction of Aviation Requirements," UK, 2008.

[9] Civil Aviation Authority, “CAP 437: Standards for Offshore Helicopter Landing Areas,” CAA, London, 2013.

[10] P. Scott, M. White and I. Owen, “Unsteady CFD Modelling of Ship Engine Exhausts and Over-Deck Air Temperatures and the Implications for Helicopter Operations,” in *American Helicopter Society 71st Annual Forum and Technology Display*, Virginia Beach, Virginia, USA, 2015.

ACKNOWLEDGEMENTS

The authors are grateful to BAE Systems and to Ansys Inc for their continued support of the ongoing research at the University of Liverpool.

AUTHOR BIOGRAPHIES

Rebecca Mateer is a PhD Student at the University of Liverpool. She received her BEng (Hons) in Aerospace Engineering with Pilot Studies from Liverpool in 2014. Rebecca was awarded the prize for best Individual Project from the Association of Aerospace Universities at their Annual Student Conference in 2014.

Paul Scott is a PhD student at the University of Liverpool; his research is into the effect of ship superstructure aerodynamics on helicopter operations. Paul received his MEng degree in Aerospace Engineering from Liverpool in 2012.

Mark White is a Senior Lecturer at the University of Liverpool. He has over 25 years of research experience including the last 15 years in the area of real-time piloted simulation. He received his bachelors and doctoral degrees from the University of Liverpool.

Ieuan Owen is emeritus professor of Mechanical Engineering and currently visiting professor at the University of Liverpool. He has some 40 years of experience in industrial fluid mechanics and has been working on ship superstructure aerodynamics and their effect on aircraft operations for the past fifteen years. He received his bachelor and doctoral degrees from the University of Wales, Cardiff.

American Society of Naval Engineers Launch & Recovery Symposium,
MITAGS, Linthicum Heights, MD USA, Nov 16-17 2016

Ieuan Owen, Mark White, Paul Scott, Rebecca Mateer & Michael Kelly
University of Liverpool, UK.

Modelling and Simulation at The University of Liverpool in Support of UK Naval Aviation

ABSTRACT

The operation of maritime helicopters to naval vessels at sea is often a difficult and dangerous task. Along with the restricted landing area and the rolling, pitching and heaving of the ship's deck, the pilot also needs to contend with the turbulent wake produced by the air flow over the ship's superstructure. There has been significant research in the past decade or more to better understand the flying environment around the ship and how it impacts the helicopter’s handling qualities and pilot workload. Central to this research has been the use of modelling and simulation, with a particular emphasis on understanding the unsteady airflow over the ship and how this is affected by the superstructure geometry.

In the UK, this flight simulation research has been led by the Flight Science and Technology Research Group at the University of Liverpool. This paper reviews the research that has been carried out at Liverpool, and how this has led to simulated flight trials to establish a simulated Ship-Helicopter Operating Limits envelope and how modelling and simulation is being used to assess the aerodynamic characteristics of the ship while it is still in the design phase, and to inform at-sea first of class flight trials..

1. INTRODUCTION

Modern combat ships, e.g. frigates and destroyers, routinely operate with maritime helicopters. The challenge of landing the helicopter in bad weather is acknowledged as being both demanding and dangerous; moreover, if the flying conditions are too difficult the helicopter will not be cleared to take off, and an important component of the ship’s capability will be lost. The maritime helicopter is often regarded as one of the most important tactical systems on the ship and is used to perform a variety of different roles, including anti-submarine warfare, surveillance, troop transfer and supply replenishment at sea. While these operations are now considered routine, the ship-helicopter dynamic interface presents one of the most challenging environments in which a helicopter pilot will operate. As well as a restricted landing area and a pitching, rolling and heaving deck, the pilot must also contend with the presence of a highly unsteady airflow over the flight deck. This phenomenon, known as the ship’s “airwake”, is caused by the air flowing over and around the ship’s superstructure as a result of the combined effect of the prevailing wind and the forward motion of the ship.

There has been considerable research into understanding the ship’s airwake and how it affects a helicopter’s handling qualities. There has also been research into the use of flight simulation with the aim of creating a high-fidelity simulation of helicopter launch and recovery that includes the impact of the unsteady air flow on the aircraft. Observations of the airwake characteristics and their effects on flying difficulty and pilot workload have also led to research into how a ship’s superstructure affects the airwake. Other aerodynamic factors which affect helicopter operations are the accuracy of the ship’s anemometers when they are immersed in the ship’s airwake, and the dispersion of the ship’s exhaust gases through mixing with the turbulent airwake. The accuracy of the ship’s anemometers is important because they both define the Ship-Helicopter Operating Limits (SHOL) at the outset of the ship’s service, and the wind-over-deck conditions for every sortie thereafter; unreliable anemometers lead directly to unnecessarily restricted SHOLs. As for exhaust gases from the ship’s engines, if the temperature of the airflow in which the helicopter has to operate is increased, this too can adversely affect the helicopter's performance. It is clear therefore that the ship's aerodynamics are important for helicopter operations and should be addressed during the ship's design.

The great majority of the research into understanding ship airwakes and how they affect a helicopter has been conducted through modelling and simulation; both computer-based and experimental. The main purpose of this paper is to describe the contribution that the Flight Science and Technology Research Group at the University of Liverpool has made to the UK's development of modelling and simulation of helicopter-ship operations, while also acknowledging the significant contributions of others.

2. BACKGROUND

As outlined above, the task of landing a helicopter to a ship in bad weather is both dangerous and difficult. SHOLs for a given ship and helicopter combination are normally determined during the ship's First of Class Flight Trials (FOCFT) in which the ship and the helicopter are put to sea and test pilots perform numerous launch and recovery tasks for winds of different strength and direction. Figure 1 shows an example SHOL diagram where the limits of wind strength and direction, relative to the deck, are indicated on a polar chart.

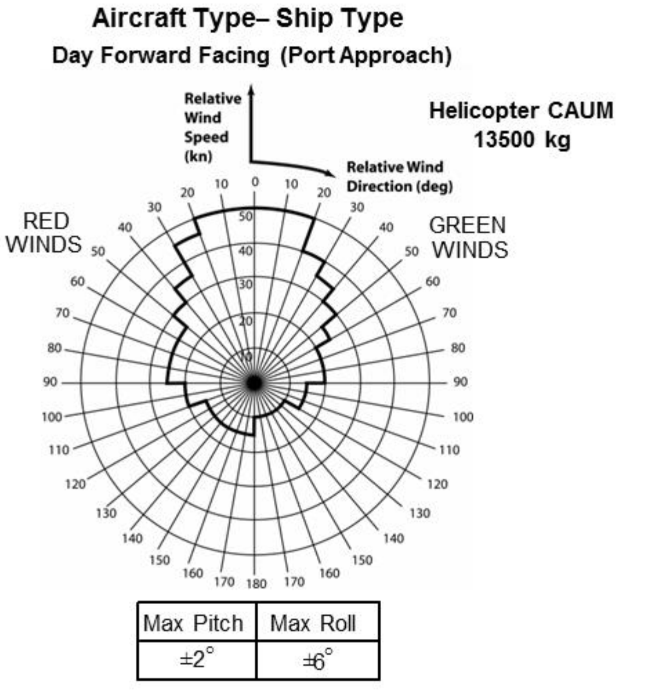

Figure 1 Example SHOL showing wind over deck envelope for a UK port-side landing manoeuvre

The chart is for a UK standard port-side landing manoeuvre, Fig. 2, where the pilot first positions the helicopter alongside the port side of the ship and facing forward in the same direction as the ship's heading. The pilot then translates the aircraft sideways, with the eye-line at about hangar height until positioned above the landing spot; at a quiescent period in the ship's motion the pilot will descend to the deck and land. It can be seen in Fig. 1, for example, that for a headwind the helicopter is still able to operate with a relative wind speed up to 50 knots, while this reduces to some 20/30 knots for oblique winds, partly because of the complex unsteady flows being shed from the ship's superstructure and partly because of the lateral authority required to overcome the side winds. The lower permissible winds from astern are because they push the helicopter towards the hangar and they also reduce the effectiveness of the tail rotor, while the asymmetry in the SHOL is due to the fact the translation is from the port side regardless of whether the winds are from the starboard (Green) or port (Red). In practice it is very difficult in a FOCFT to obtain a full range of wind over deck (WOD) conditions and the costly and time-consuming trails are often incomplete, and while various techniques can be used to fill the gaps in the SHOLs, these normally err on the conservative side and lead to a restricted SHOL. More recently, a method of using shore-based hover trials and ship airwake data to construct a "candidate flight envelope" that can be assessed in shorter at-sea trials has been developed to support the Dutch navy [1].

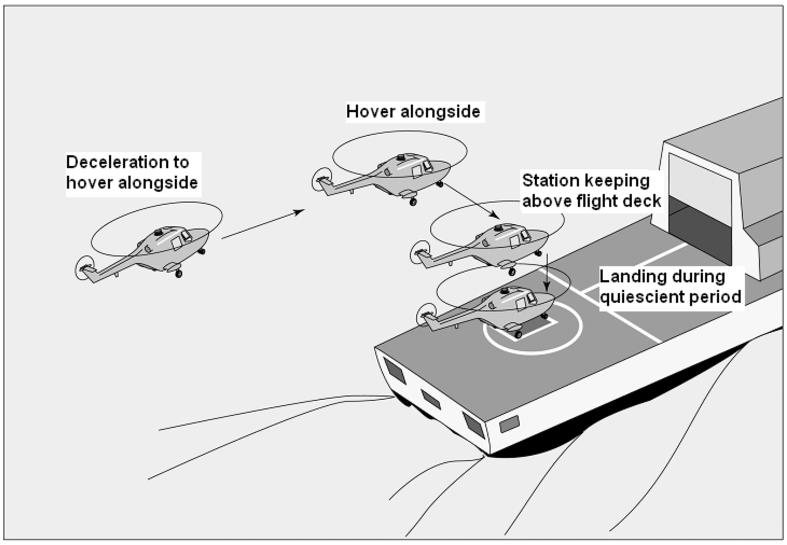

Figure 2 Final stages of the recovery of a Royal Navy helicopter to a single spot frigate.

Significant research into the air flow over ship superstructures and the effect on maritime helicopter operations began to emerge in the mid-1990s, e.g. [2]. In the US, the Joint Shipboard Helicopter Integration Process (JSHIP) was established to support the interoperability of helicopters from the US Navy, Army and Air Force with a range of ships. Conducting the required at-sea trials for the multiplicity of possible ship/helicopter combinations is expensive and time consuming, so a major task of JSHIP was to develop a high-fidelity simulation capability in the NASA Ames Vertical Motion Simulator to demonstrate that realistic piloted launch and recovery missions could be conducted for different aircraft and ship combinations and simulated SHOLs could be determined. The various sub-systems (e.g. flight model, ship model, airwake, cockpit, visuals, motion) that are required to create the simulation environment were integrated within the Dynamic Interface Modelling and Simulation System (DIMSS); see, for example Advani & Wilkinson [3] and Roscoe & Wilkinson [4]. Recognizing the need for higher fidelity modelling of ship airwake effects on rotary wing and fixed wing maritime aircraft, the US Naval Air Systems Command (NAVAIR) and the Office of Naval Research (ONR) initiated the SAFEDI program [5]. SAFEDI developed three levels of analysis: characterisation of unsteady ship airwakes; a desktop simulation in which the unsteady velocity components of the airwake were integrated with an aircraft flight model and the aircraft was 'flown' to the ship on a predetermined flight path by a pilot model; and piloted motion-base flight simulation.

Meanwhile, in 2003 the UK the Ministry of Defence began funding a project to develop a simulation capability for predicting SHOLs using the Merlin helicopter training simulator at the Royal Navy Air Station in Culdrose, Cornwall [6]. The Ship/Air Interface Framework (SAIF) project, as it is called, has created a federated computer architecture where the different elements specific to ship operations (e.g. motion, visuals and airwake for different ships, and different aircraft types) could be flexibly used with the Merlin simulator. Having created the computer architecture with the ability to implement different flight models, this made it possible to include the simulation of maritime unmanned vehicles that did not require the use of the motion base [6]. The SAIF project has conducted simulated SHOL trials for a Merlin operating to a Type 23 frigate and a Type 45 Destroyer [7].

Separately, within the UK, the Flight Science & Technology Research Group at The University of Liverpool was established in 2000, central to which was research into rotorcraft flight dynamics and control, including flight simulation using a motion-base. Flight simulation research began with a single-seat, full motion flight simulator, HELIFLIGHT [8] which was built with a technical and functional specification that would allow research into flight handling qualities, flight mechanics, flight control system design, aircraft design concepts and cockpit technologies. As a research simulator it provided greater availability and flexibility than a fully-utilised naval training simulator and also allowed free access to the simulator's motion controllers. In 2008 a second, larger and more capable simulator, HELIFLIGHT-R, was installed [9] by Advanced Rotorcraft Technology (ART), shown in Fig. 3 (the smaller single-seat HELIFLIGHT simulator can be seen in the background).

Figure 3 HELIFLIGHT-R simulator – internal and external views

HELIFLIGHT-R is a full-motion research flight simulator which has a three channel 220 x 70 degree field of view visual system, a 6 degree of freedom motion platform, a four axis force feedback control loading system and an interchangeable crew station. Flight mechanics models are developed in either FLIGHTLAB or Matlab/Simulink and the current aircraft library features a range of fixed wing, rotary wing and tilt-rotor aircraft. The outside world imagery is generated using Presagis' Creator Pro software to produce either geo-specific or custom visual databases. Using Presagis' VEGA Prime software, the Liverpool group has generated its own run-time environment, LIVE, which allows the simulator operator to change environmental effects such as daylight, cloud, rain and fog along with maritime effects such as sea state, ship's exhaust and rotor downwash on the sea's surface. A heads-up display can either be generated using an LCD screen with a beam splitter located above the instrument panel or projected directly onto the dome. The motion and visual cues, together with realistic audio cues, provide an immersive environment for a pilot. Data from the flight models, e.g. aircraft accelerations, attitudes etc., together with pilot control inputs can be monitored in real-time and recorded for post-flight data analysis.

Amongst the flight simulation projects that were initiated at Liverpool in the early 2000's was research into the ship-helicopter dynamic interface. As well as developing the flight simulation capability, the research was also concerned with the effect of the ship superstructure geometry on the airwake, and hence on the potential flight envelope of the helicopter. Figure 4 shows the mean air flows over three ship geometries for a headwind. The ships are a Type 23 frigate (133m long), a Type 45 destroyer (152m) and a Wave Class Tanker (197m). For each ship the path lines show the chaotic air flow over the aft landing deck and it should also be noted that these flows are highly unsteady.

It is this research capability and experience that has enabled The University of Liverpool to support the UK's SAIF project and current and future FOCFTs, as well as providing ship design guidance. The following sections will describe aspects of this research, particularly those that relate to ship design.

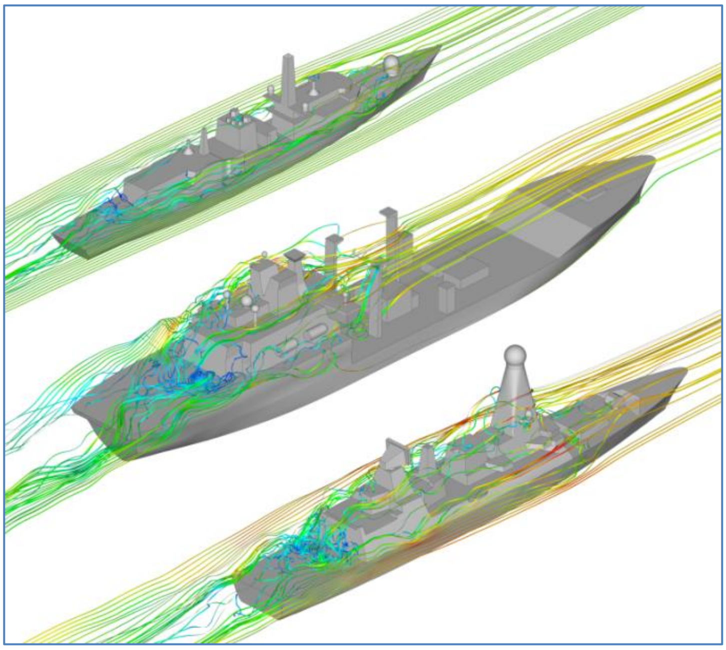

Figure 4 Mean pathlines over (from top) Type 23 Frigate, Wave Class Tanker, Type 45 Destroyer.

3. HELICOPTER FLIGHT SIMULATION AT THE SHIP-HELICOPTER DYNAMIC INTERFACE

The creation of a full-motion flight simulation environment for a helicopter operating to a ship requires: a simulator, in this case the HELIFLIGHT-R shown in Fig. 3; a helicopter flight dynamics model; a ship visual model, such as those shown in Fig. 4; a CFD-generated airwake; a ship motion model and a visual scene.

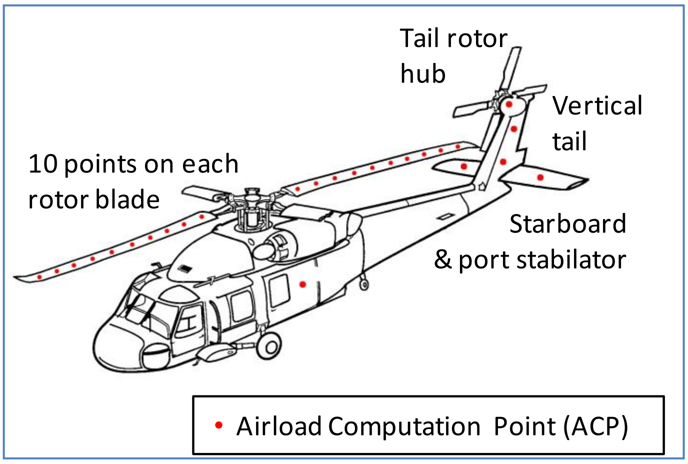

Figure 5 Seahawk helicopter model showing location of Airload Computation Points

The FLIGHLTAB modelling and simulation software has a library with a number of flight models for both rotary and fixed wing aircraft. Figure 5 shows the FLIGHTLAB Generic Rotorcraft, which has been configured to be a Sikorsky SH-60B Seahawk "like" helicopter model and that was used, for example, by Hodge et al [10]. The FLIGHTLAB Generic Rotorcraft model comprises the following major subsystem components: (1) individual blade-element main-rotor model including look-up tables of non-linear lift, drag and pitching moment coefficients stored as functions of incidence and Mach number; (2) a Bailey disk tail-rotor model, (3) finite-state Peters-He dynamic inflow model; (4) separate aerodynamic look-up tables for the fuselage, vertical tail and the port and starboard stabilator forces and moments stored as nonlinear functions of incidence and sideslip; (5) turbo-shaft engine model with a rotor-speed governor; (6) primary mechanical flight control system and Stability Augmentation System (SAS) models including sensor and actuator dynamics; and (7) a landing gear model to provide deck reactions cues on touchdown.

The Airload Computation Points indicated in Fig. 5 are where the unsteady three-dimensional velocity components of the air flow are applied to the helicopter model to create the unsteady forces and moments that are imposed on the aircraft. The velocity components (u,v,w) created by the CFD are stored in a lookup table at fixed positions in space (x,y,z) and at different times (t). The x,y,z locations in the lookup table have to be translated to the locations of the ACPs shown in Fig. 5, including those along the rotating blades of the main rotor.

The unsteady airwake is created using Ansys Fluent, a commercial CFD code. A ship model, such as those shown in Fig. 4, is imported into the Ansys ICEM mesh generation software, so that it can be 'cleaned' to repair any erroneous surfaces and to remove small features to create geometry suitable for meshing. Features such as small antennae, railings and other small deck clutter have little effect on the airwake but if not removed will increase the complexity and hence the run-time of the CFD. Generally, objects that are less than 0.3m in diameter are removed. A surface mesh is then applied to the ship geometry and this is ‘grown’ away from the ship into the computational domain which surrounds the ship; the surface and volume mesh for the Type 23 frigate can be seen in Figure 6.

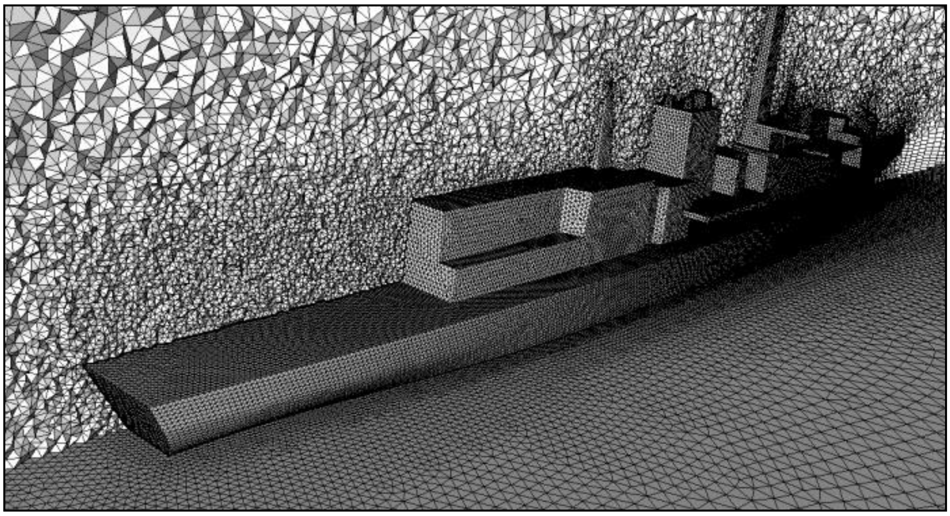

Figure 6 Unstructured CFD mesh for Type 23 frigate

The unsteady CFD airwake is computed using Detached Eddy Simulation (DES) turbulence modelling. The solution is created at 100 Hz, i.e. u,v,w velocity components are calculated every 0.01 seconds, but for implementation within FLIGHTLAB the solution is down-sampled to 0.04 seconds. The u,v,w,t data of the airwake is then stored in a lookup table that coincides with the volume within which the helicopter will fly; Figure 7 shows the domain around the flight deck of the Type 23 frigate in which a helicopter will fly when executing the port-side landing manoeuvre illustrated earlier in Fig. 2. A more detailed account of how the airwakes are produced and validated against experimental data is given in [11]. For simulated SHOLs, where winds of different directions and strengths are required, it is possible to scale the velocities from one wind speed to another using Reynolds and Strouhal scaling, as demonstrated by Scott et al [12], but a separate airwake has to be computed for each wind direction.

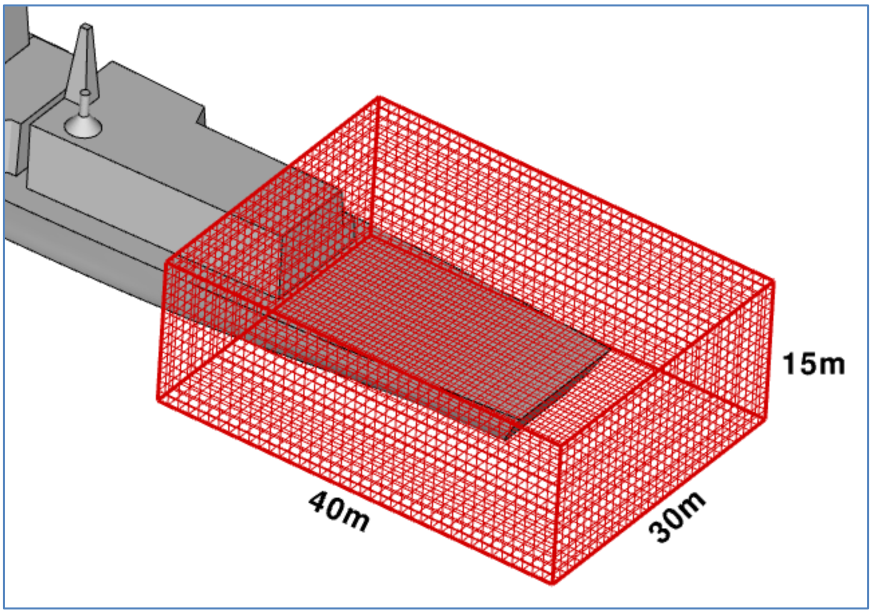

Figure 7 Structured grid for airwake lookup table

4. SIMULATED SHIP-HELICOPTER OPERATIONAL LIMITS

Having created a simulation environment, a programme of research was conducted at Liverpool to establish a simulated SHOL, initially for simplified ship and airwake models [13], and then with a Type 23 frigate and a detailed time-accurate unsteady airwake [10]. For each ship, airwakes were computed for a 40 kt wind coming from different angles relative to the ship around the 360° azimuth; the wind strength was then scaled up and down to create a set of airwakes for wind speeds from 20 to 50 kts.

The simulated flight test programme typically consisted of a series of deck landing tasks for different winds over deck, usually in increments of 15° and 5 kts. During each experiment a highly experienced former Royal Navy (RN) test pilot was instructed to fly the deck landing task using the standard RN technique shown in Fig. 2. This involves flying the helicopter to a stabilised hover on the port side of the ship, then manoeuvring sideways across the deck to a position above the landing spot and waiting there for a quiescent period in the ship's motion before executing a vertical landing. Three Mission task Elements (MTEs) were identified from this description of the deck landing mission: (i) Sidestep manoeuvre; (ii) Station keeping (precision hover) above the flight deck; and (iii) Vertical landing.

Conducting the deck landings in a controlled simulation environment allows test points to be well defined and to be repeated. As well as recording the difficulty of the landing task, either on the Deck Interface Pilot Effort Scale (DIPES) or the Bedford Workload rating scale, it is also possible to record pilot comments, as well as pilot control inputs, helicopter flight dynamics and motion platform dynamics. It is also possible to later interrogate the CFD flow field when airwake disturbances are of interest. More detail of simulated SHOL testing can be found in [10].

The previous paragraph refers to two rating scales that are used to quantify the pilot workload. The Bedford scale is a 10-point scale [14]; 1 indicating insignificant workload, 10 indicating that the pilot had to abandon the task. In the Bedford scale the pilot is asked to consider how much spare capacity they have while performing the assigned task, spare capacity being defined as the pilot's ability to perform secondary tasks, such as maintaining mission awareness, monitoring aircraft systems or listening to radio communications; the primary task being to fly the aircraft through a particular manoeuvre or mission. The higher the workload generated by the primary task, the less spare capacity there is for attention to these secondary tasks. The Bedford scale is applicable to any task, but the DIPES, as its name suggests, was designed specifically for deck landings. The DIPES scale, Fig. 8, requires the test pilot to rate each landing based on workload, performance, accuracy and consistency. On the DIPES scale a numerical rating of 3 or less indicates that deck landings can be repeatedly achieved with precision and safety, under the conditions being tested. A rating of 4 or 5 indicates the contrary and places that condition outside of the SHOL, thus prohibiting deck landings under those conditions. In addition to the detailed comments given by the pilot, a number of letter suffixes can also be assigned to each rating, to describe the cause of increased workload (e.g. 'T' for turbulence or 'D' for deck motion).

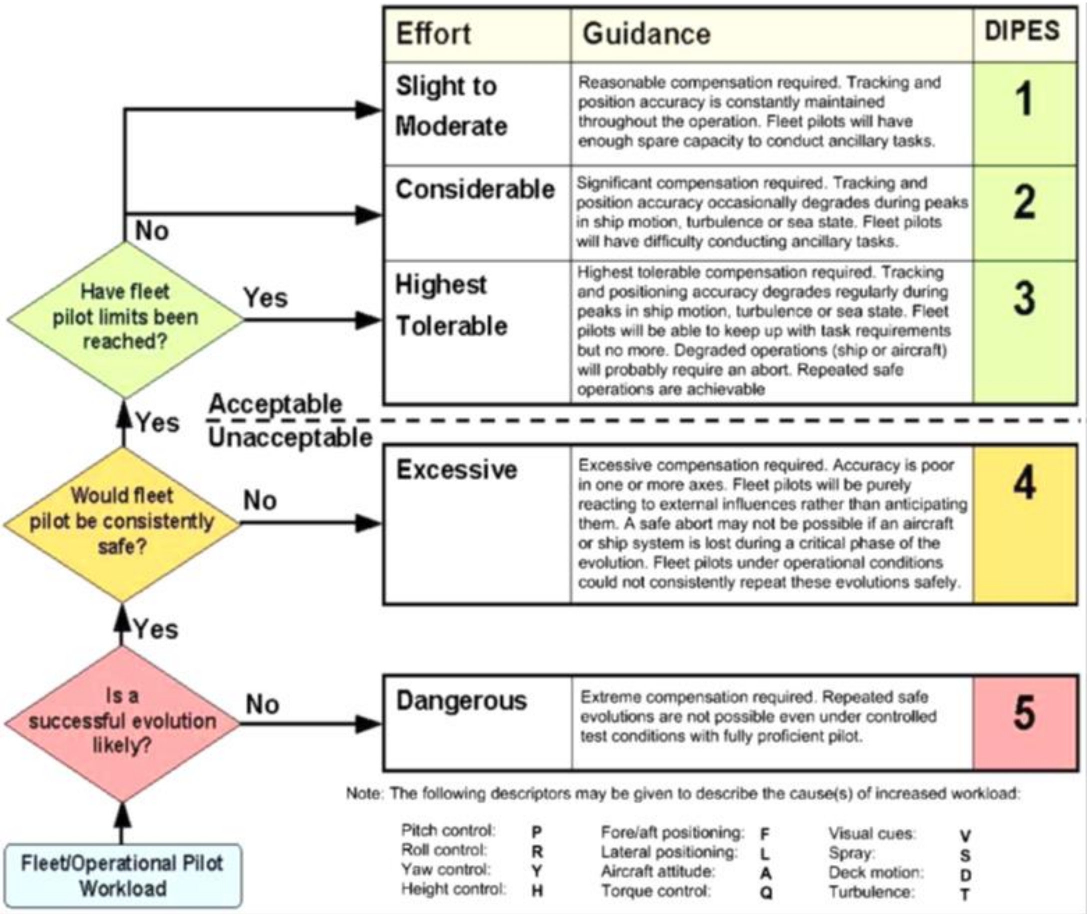

Effort	Guidance	DIPES
Slight to Moderate	Reasonable compensation required. Tracking and position accuracy is constantly maintained throughout the operation. Fleet pilots will have enough spare capacity to conduct ancillary tasks.	1
Considerable	Significant compensation required. Tracking and position accuracy occasionally degrades during peaks in ship motion, turbulence or sea state. Fleet pilots will have difficulty conducting ancillary tasks.	2
Highest Tolerable	Highest tolerable compensation required. Tracking and positioning accuracy degrades regularly during peaks in ship motion, turbulence or sea state. Fleet pilots will be able to keep up with task requirements but no more. Degraded operations (ship or aircraft) will probably require an abort. Repeated safe operations are achievable	3
Excessive	Excessive compensation required. Accuracy is poor in one or more axes. Fleet pilots will be purely reacting to external influences rather than anticipating them. A safe abort may not be possible if an aircraft or ship system is lost during a critical phase of the evolution. Fleet pilots under operational conditions could not consistently repeat these evolutions safely.	4
Dangerous	Extreme compensation required. Repeated safe evolutions are not possible even under controlled test conditions with fully proficient pilot.	5

Note: The following descriptors may be given to describe the cause(s) of increased workload:

Pitch control:	P	Fore/aft positioning:	F	Visual cues:	V
Roll control:	R	Lateral positioning:	L	Spray:	S
Yaw control:	Y	Aircraft attitude:	A	Deck motion:	D
Height control:	H	Torque control:	Q	Turbulence:	T

Figure 8 Deck Interface Pilot Effort Scale (DIPES)

The DIPES scale is used by many navies to construct SHOLs; an example of a simulated SHOL based on DIPES will be discussed in the next section. The Bedford scale is used to assess how difficult a particular MTE is, e.g. hovering over the port-edge of the ship, and can be used to quantify the difficulty caused by the airwake at a particular location; a process that has been useful in assessing the effect a particular feature on the ship's superstructure may have on the helicopter, as will be discussed later.

5. USING FLIGHT SIMULATION TO ASSESS THE EFFECT OF SHIP SUPERSTRUCTURE DESIGN ON HELICOPTER FLYING QUALITIES

To illustrate how flight simulation has been used to quantify the effect that a ship's design can have on a helicopter's operational envelope we shall present two cases: one for ship size, and the other for particular features of the ship superstructure. Flight simulation can also be used to assess the effect of ship motion, landing aids, etc. but these aspects are not included in this paper.

5.1. Ship Size

Figure 9 shows the simulated SHOL diagrams for +/- 90° winds for a SH-60B Seahawk conducting a RN port-side landing on a) a Type 23 frigate and b) a Wave Class Tanker, which were illustrated earlier in Fig. 4. The left hand diagrams show the pilot's DIPES ratings translated onto a polar diagram of wind speed and direction, while the right hand diagrams show the safe boundary drawn through the points. The solid line represents the limits defined by the DIPES ratings, while the dotted lines represent a boundary due to the limits of the tail rotor authority in a side wind.

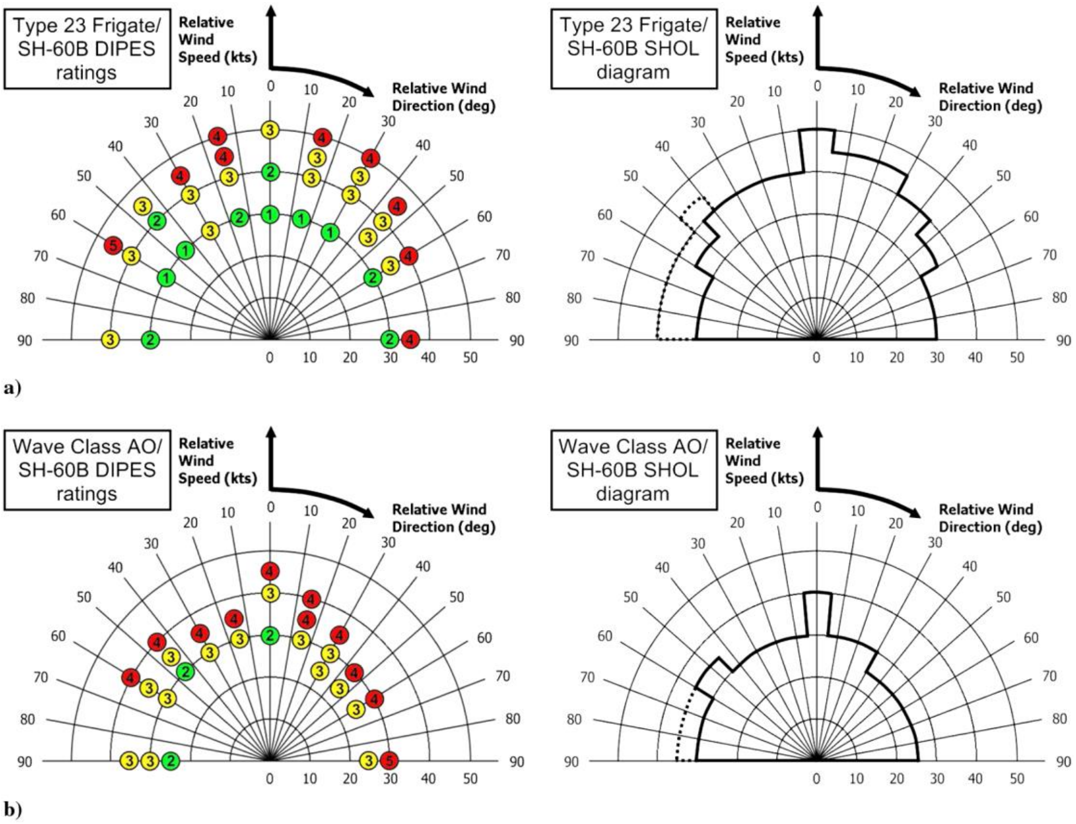

Figure 9 DIPES Ratings and SHOL Diagrams for a Type 23 Frigate and Wave Class tanker.

There is a lot of detail that can be drawn out of these diagrams, and this is supplemented by the recorded pilot control activity and commentary, as reported by Forrest et al [15]. The main observation from Fig. 9 is that the SHOL for the larger Wave Class ship is significantly more restricted than the smaller frigate, despite it having a larger deck to land on. The reason for this is that the air flow over the ships creates unsteady vortical structures that are shed from the sharp edges of the superstructure, and the bigger the ship the bigger and slower the vortices. The vortices are of a similar size to the helicopter main rotor, thereby creating unsteady moments on the helicopter, and of a frequency that can lead to pilot induced oscillations as the pilot tries to hold position by counteracting the unsteady loads on the aircraft.

The data in Fig. 10 is an example of how the pilot's control activity yields further information about the effect of ship size on the helicopter. Figure 10 shows a time-history of the pilot's inputs to the pedal control while trying to hold a hover position over the landing spot. The wind direction is 45° off the starboard (Green 45) and so the pilot is applying a biased input to the tail rotor to maintain heading. In the larger ship's airwake it can be seen that there is more activity, shown by a higher number of pedal reversals being applied, and this represents greater pilot workload.

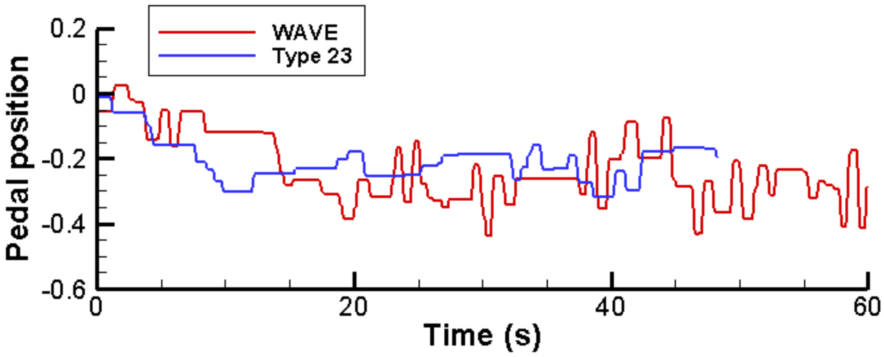

Figure 10 Pilot pedal activity in the simulator while station-keeping above the landing spot of a Wave Class Tanker and a Type 23 frigate in a Green 45 wind

5.2. Superstructure Features

As mentioned earlier, oblique winds produce more challenging airwakes, and Green winds in particular are problematic during a port-side landing approach. Figure 11 shows the air flow, as surfaces of iso-vorticity, over a simplified ship geometry in an oblique 45° wind. The fluctuating shear layer caused by the flow separating from the hangar vertical edge and referred to above can be clearly seen. The other dominant features in the figure are the many vortical structures caused by the flow 'rolling up' and shedding from the sharp edges, for example at the horizontal leading edge of the hangar. More importantly for the helicopter, particularly while off the port side and translating across the deck, are the large vortex structures being shed from the upper horizontal edges on the starboard side of the hangar; the significance of these is that they pass across and above the path taken by the helicopter and get drawn into the helicopter's main rotor, causing significant unsteady moments. These flow features contribute significantly to the high pilot workload in Green winds.

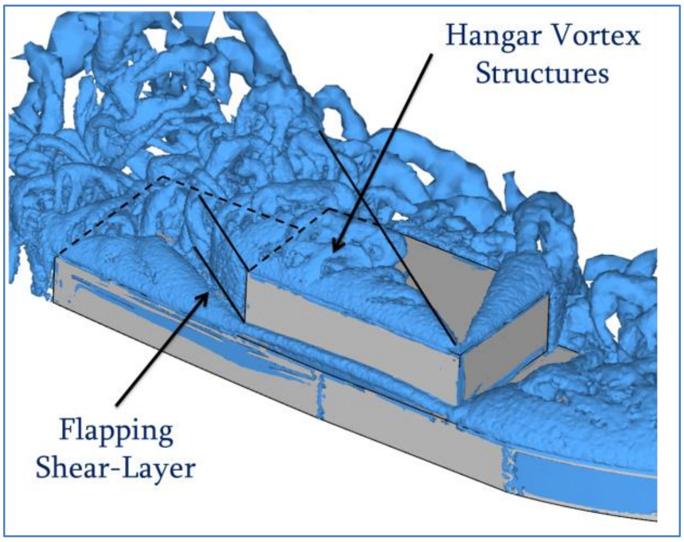

Figure 11 Visualisation of air flow over a simplified ship in oblique 45°winds by surfaces of iso-vorticity

Kääriä et al modified the horizontal hangar edge to interfere with the vortex shedding and then used piloted flight simulation to determine how this would affect helicopter loading and pilot workload [16]. Figure 12 show three different modifications: a cut-out or notch, and two different side flaps. Figure 13 shows pilot workload ratings for the original geometry and the three modifications; these were recorded in the simulator while the pilot maintained the helicopter in a stable hover above the landing spot for 30 seconds in Green winds. The first thing to note in Fig. 13 is that the pilot has to work harder to maintain the helicopter over the landing spot as the wind speed increases, as might be expected. More importantly, the three modifications have significantly reduced pilot workload, particularly the Notch modification with up to a 3-workload-rating reduction, while the side flaps typically show a reduction of one workload-rating. Further understanding of the mechanisms responsible for the improvements are provided by examining the CFD and the various inputs to the pilot's controls. It is understood that ship geometry modifications may also affect other important characteristic such as radar cross section, but the significance of the work is that ship superstructure geometry can improve the flying environment for the helicopter and the pilot.

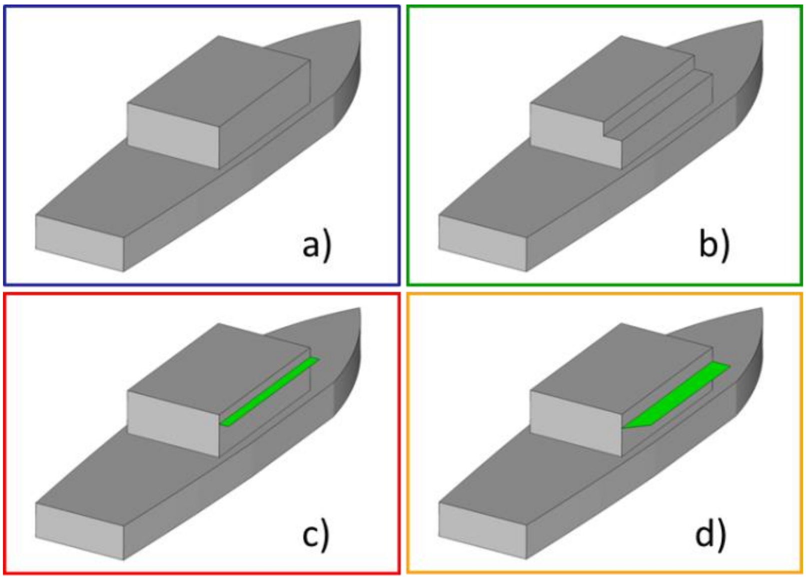

Figure 12 Simplified ship; a) Baseline; b) Notch; c) Side-Flap1; d) Side-Flap 2

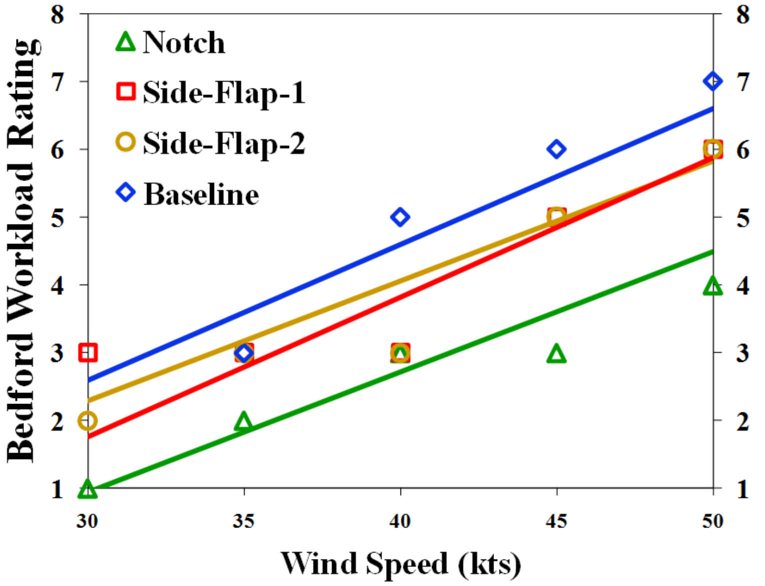

Figure 13 Pilot workload ratings for 30 second hover over landing spot in Green 45° winds

6. NON-PILOTED FLIGHT ASSESSMENT OF SHIP SUPERSTRUCTURE DESIGN ON HELICOPTER LOADING

At the core of the piloted motion-base flight simulation described above is the flight model, which is provided by FLIGHTLAB, and the CFD-generated unsteady airwake; these two elements have been used together, without the motion simulator, to create a computer-based simulation tool that can also be used to assess the impact of ship superstructure designs on a helicopter. The Virtual Airwake Dynamometer, or Virtual AirDyn (VAD), as it is known, is a software analysis tool developed at the University of Liverpool [17]. During piloted real-time simulations, unsteady forces are generated on the aircraft causing it to move away from the trim condition and requiring the pilot to counteract the movement through the aircraft's controls. In the VAD the helicopter is trimmed in the prevailing freestream conditions and is then placed at a selected point in the airwake and is fixed in that position. Because the helicopter is no longer trimmed for the conditions within the airwake it experiences non-zero forces and moments imposed by the unsteady air flow, and it is these values that are recorded by the VAD. Therefore, using the VAD technique, the helicopter model becomes an instrument that measures the unsteady forces and moments imparted by the unsteady CFD airwake, providing a quantitative measure of the relative impact on the helicopter of the airwakes created by the different ship geometries. The helicopter model used in the VAD is again FLIGHTLAB's Generic Rotorcraft configured to represent a Sikorsky SH-60B Seahawk and was chosen because it has been extensively validated.

Typically, as for the piloted simulation described above, the unsteady airwake is computed for 30 seconds and is interpolated onto a structured rectangular grid, as seen earlier in Fig. 7. The airwakes are calculated for a single wind speed, but for a range of wind angles. The method by which the VAD has been employed to compare ship airwakes is to carry out a translational approach beginning with the helicopter's rotor hub located at the ship's hangar height, one beam width from the landing spot, off the port edge of the ship. The helicopter is then held stationary with the rotor hub at several positions over the flight deck as shown in Figure 14.

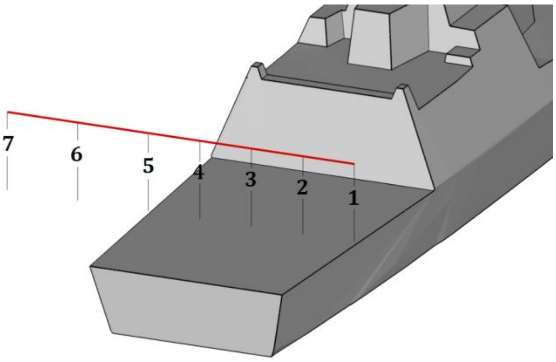

Figure 14 Rotor Hub Fixed Positions Used to Investigate Ship Airwakes with the Virtual AirDyn

As with the application of FLIGHTLAB within the HELIFLIGHT-R flight simulator, the unsteady CFD airwake velocities are imposed onto the helicopter model at the ACPs shown earlier in Fig. 4. At each of the sampling locations over the ship, Fig. 14, the helicopter is held stationary and the time histories of the unsteady forces and moments at the helicopter's centre of gravity are recorded over the full 30 seconds of airwake data. The unsteady loads are then time-averaged to provide the mean forces and moments acting on the helicopter at each of the test points.

A measure of the unsteady forces and moments is produced using a method in which Power Spectral Density (PSD) plots are generated from the time histories given by the VAD, and the square root of the integral between the limits 0.2 to 2Hz is used to represent the RMS loadings on the helicopter [17]. This analysis technique takes account of the fact that although the unsteady loads are imposed over a very wide frequency range, the high-frequency loads (>2 Hz) are less important because the inertia of the aircraft means it does not respond significantly, while the lower frequency loads (<0.2Hz) can be counteracted by the pilot through the helicopter's controls. Loads in the frequency range 0.2 to 2 Hz are said to be in the closed-loop pilot response frequency range and have the greatest influence on pilot workload. In general terms, the RMS loading is responsible for the pilot workload while the mean loads will influence the control margins.

As an illustration of the VAD technique, Fig. 15, extracted from [18], shows the mean and unsteady (RMS) thrust force on the helicopter as it is placed in positions 7 to 1 on Fig. 14. This particular set of data is using the VAD to quantify the effect of ship size on a helicopter's loading. Looking first at the mean loads, off the ship and out of the airwake the rotor thrust equals the weight of the helicopter, 70 kN. As the helicopter moves through the airwake, the thrust generated by the main rotor reduces as the air velocities at various points on the rotor change in magnitude and direction; in practice the pilot would counteract this by increasing the power to the rotor to compensate for the thrust deficit. The mean loads are therefore a measure of the amount of control the pilot has to apply or, more importantly, how much control margin is remaining. The pilot is expected to have a minimum of 10% control margin in all inceptors and if one falls below this the task may have to be aborted.

The RMS loads in Fig. 15 are a measure of the unsteady forces in the 0.2-2.0 Hz frequency range that contributes to pilot workload, again in the vertical direction. The greater the RMS value the greater the unsteadiness that the pilot has to counteract through the controls, and hence the greater the workload. In the figure it can be seen how the unsteady loads increase as the helicopter moves into the airwake, and also how the bigger ship causes the higher RMS, consistent with comments in 5.1 above.

Figure 15 shows mean and unsteady data for only the vertical axis; mean and unsteady data are also acquired for the forward and side forces, and for the pitch, roll and yaw moments.

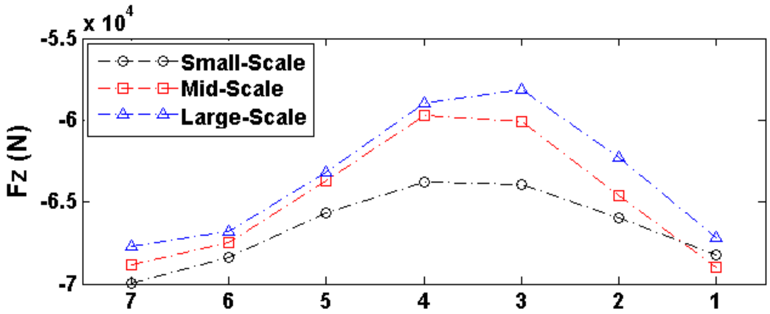

a) Mean loads

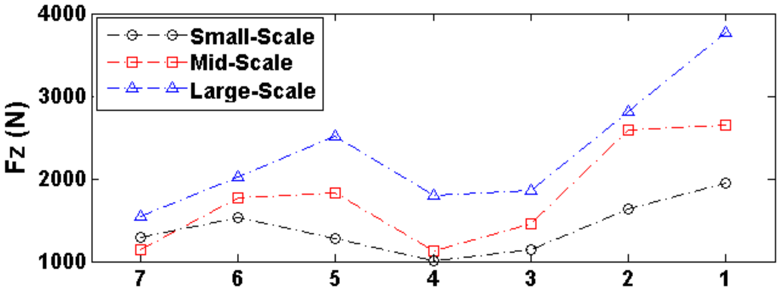

b) Unsteady (RMS) loads

Figure 15 Mean and RMS helicopter loads in ship airwakes measured by the Virtual AirDyn

7. SHIP ANEMOMETERS AND ENGINE EXHAUSTS

The main focus of this paper is the application of modelling and simulation to evaluate the effect of ship superstructure designs on the flight dynamics and handling qualities of a maritime helicopter. However, as discussed in the Introduction, the air flow over the ship also affects the ship's anemometers and the dispersion of the ship's engine exhausts, both of which have consequences for the ship's helicopter, and both of which can be investigated as part of the ship's design. Therefore, for completeness, this section comments briefly on the effect of ship design on the air flow in the vicinity of the ship's anemometers and on the mixing of the ship's engine exhaust with the airwake; more detail of the latter issues can be found in [19].

The accuracy of the ship's anemometers is important because they both define the Ship-Helicopter Operating Limits (SHOL) at the outset of the ship's service, and the wind-over-deck conditions for every sortie thereafter; unreliable anemometers lead directly to unnecessarily restricted SHOLs. Figure 16 shows the mean velocity vectors, coloured by magnitude, in the vicinity of the forward island of a model of the UK's Queen Elizabeth Class aircraft carrier. It can be seen that the air flow is highly disturbed and the placement of the anemometers is therefore critical. CFD analysis at the design stage is capable of evaluating various candidate positions. Furthermore, in preparation for calibration of ship's anemometers during the at-sea Air Flow Air Pattern (AFAP) trials, CFD is being used to inform the positioning of ship-deck and reference anemometers, further improving the accuracy of the ship's anemometers and thereby helping to maximise operational SHOL envelopes.

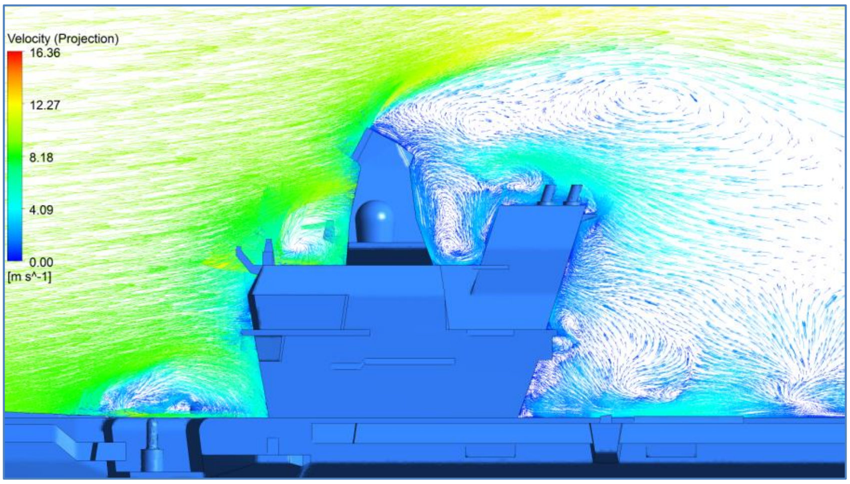

Figure 16 Mean velocity field around aircraft carrier island

The issue for ship engine exhaust gas dispersion, which can either be gas turbine or Diesel exhaust, is partly due to concern over crew comfort and surface heating, but in the context of this paper the main concern is that if the helicopter is immersed in the exhaust plume the heated ambient air will have a lower density and this will reduce the lift generated by the main rotor; elevated and unsteady air temperatures can also have an effect on the helicopter's engine power. Figure 17 shows a snapshot of an unsteady airwake over a ship with a superimposed image of a helicopter over the deck; the ship is in a headwind and, as can be seen, the air temperatures above the deck are about 5°C above ambient. These over-deck temperatures result from engine exhaust temperatures of the order of 500°C and while 5°C above ambient does not seem particularly high, it does exceed the 2°C limit recommended for helicopters operating to offshore oil/gas platforms, as discussed in [19].

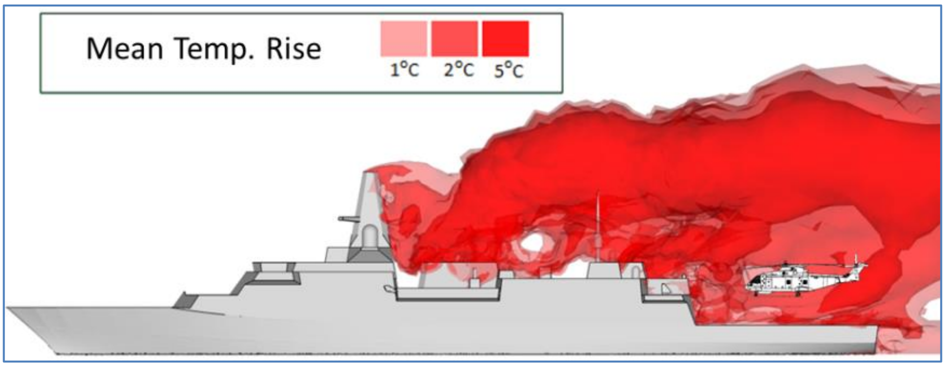

Figure 17 Instantaneous iso-surfaces of unsteady ship exhaust plume temperatures

8. CONCLUDING COMMENTS

This paper has given a very brief overview of the research into ship-helicopter flight simulation that has been conducted at the University of Liverpool. The research has made considerable progress, and has often been undertaken in collaboration with international research groups as well as with the UK's ship designers & builders and naval helicopter community. Simulated SHOL testing to replace at-sea trials is still a long way off, but it is now possible to explore the limits of the helicopter's operational envelope so, when SHOL trials are conducted, priority can be given to properly determining the limits for the more restrictive wind conditions.

The piloted and-non-piloted simulation is being used to inform the design stage of a real ship, and the research into simplified ship geometries has given very useful insight into the kinds of superstructure features that create adverse flying conditions. The creation of the CFD airwakes is still expensive and time-consuming, even with modern computing resources, so while the techniques can be deployed during a ship's design, they should be used carefully at key stages in the design cycle.

Modern developments in ship design, such as radar cross section reduction, large integrated masts, and gas turbine engines are significantly affecting the ship's aerodynamics and will have consequences for the helicopter's operational envelope, so their development should be taken forward with the helicopter in mind.

Acknowledgements

The authors are grateful to Ansys Inc for their continued support, and to BAE Systems.

References

1. Hoenkamp, A., Lee, D., Pavel, M.D. & Stapersma, D., "Lessons learned from NH90 NFH helicopter-ship ineterface: testing across the complete Dutch fleet", 40th European Rotorcraft Forum, Southampton, 2-4 September 2014.
2. Tai, T. & Carico, D., "Simulation of DD-963 ship airwake by Navier-Stokes method", 23rd Fluid Dynamics, Plasmadynamics, and Lasers Conference, Orlando, FL, 6-9 July 1993.
3. Advani, S.K. and Wilkinson, C.H. "Dynamic interface modelling and simulation – a unique challenge", RAeS Flight Simulation Group Conference on The Challenge in Achieving Realistic Training in Advanced Rotorcraft Simulators, London, UK, November 2001.
4. Roscoe, M. & Wilkinson, C.H., "DIMSS – JSHIP's modelling and simulation process for ship/helicopter testing & training", Proc. AIAA Modelling & Simulation Technologies Conference, Monterey, CA, AIAA 2002-4597.

5. Polsky, S.A., Wilkinson, C.H., Nichols, J., Ayers, D., Mercado-Perez, J. & and Scott Davis, T. "Development and Application of the SAFEDI Tool for Virtual Dynamic Interface Ship Airwake Analysis", 54th AIAA Aerospace Sciences Meeting, San Diego, CA, 4-8 January 2016.
6. Cox, I., Turner, G., Finlay, B. & Duncan, J., "The ship/air interface framework (SAIF) project: dynamic challenges", Maritime Operations of Rotorcraft, RAeS Conference, London, UK 11-12 June 2008.
7. Turner, G., Clark, W., Cox, I., Finlay, B. & Duncan, J., " Project SAIF – assessment of ship helicopter operating limits using the Merlin helicopter simulator", AHS 62nd Annual Forum, Phoenix, AZ, 9-11 May 2006.
8. Padfield, G.D. & White, M.D., "Flight simulation in academia: HELIFLIGHT in its first year of operation at the University of Liverpool", Aeronautical J., 2003, 107 (1075), 529-538.
9. White, M.D., Perfect, P., Padfield, G.D., Gubbels, A.W. & Berryman, A.C., "Acceptance testing and commissioning of a flight simulator for rotorcraft simulation fidelity research", Proc. IMechE Part G: J Aerospace Engineering, 2012, 226(4), 638-686.
10. Hodge, S.J., Forrest, J.S., Padfield, G.D. & Owen I., "Simulating the Environment at the Helicopter-Ship Dynamic Interface: Research, development and Application", Aeronautical J., 2012, 116 (1185), 2012, 1155-1184.
11. Forrest, J. S. & Owen, I., "An Investigation of Ship Airwakes Using Detached-Eddy Simulation," Computers & Fluids, 2010, 39 (4), 656–673.
12. Scott, P., White, M.D. & Owen, I., "The effect of ship size on airwake aerodynamics and maritime helicopter operations", 41st European Rotorcraft Forum, Munich, 1-4 September 2014.
13. Roper, D., Owen, I., Padfield, G.D. & Hodge, S. J., "Integrating CFD and piloted simulation to quantify ship-helicopter operating limits", Aeronautical J, 2006, 110 (1109), 419-428.
14. Roscoe, A., & Ellis, G., "A subjective rating scale for assessing pilot workload in flight", RAE report TR90019. Farnborough, UK 1990.
15. Forrest, S.J., Owen, I., Padfield, G.D. & Hodge, S.J., "Ship-helicopter operating limits prediction using piloted flight simulation and time-accurate airwakes", J. Aircraft, 49 (4), 2012, 1020-1031.
16. Kääriä, C.H., Forrest, J.S. & Owen, I., "Using flight simulation to improve ship designs for helicopter operations", RINA-ICCAS 2011, Trieste, Italy, 20 – 22 September 2011.
17. Kääriä, C.H., Forrest, J.S. & Owen, I., "The Virtual AirDyn: a simulation technique for evaluating the aerodynamic impact of ship superstructures on helicopter operations", Aeronautical J., 2013, 117 (1198), 1233-1248.
18. Scott, P., Owen, I. & White, M.D., "The Effect of ship size on the flying qualities of maritime helicopters", American Helicopter Society 70th Annual Forum, Montreal, Canada, May 20-22, 2014.
19. Scott, P., White, M.D. & Owen, I., "Unsteady CFD modelling of ship engine exhaust gases and over-deck air temperatures, and the implications for maritime helicopter operations", American Helicopter Society 71st Annual Forum, Virginia Beach, VA, May 5-7, 2015.

USING PILOTED SIMULATION TO MEASURE PILOT WORKLOAD OF LANDING A HELICOPTER ON A SMALL SHIP

Paul Scott, Michael F Kelly, Mark D White, Ieuan Owen

School of Engineering
University of Liverpool
Liverpool, UK

Abstract

When conducting landings to a ship's deck in strong winds, helicopter pilot workload is often dominated by the turbulence within the ship's airwake. Previous studies have shown that larger ships create more aggressive airwakes and simulated flight trials had shown that it can be easier to land to a smaller ship than a large one. However, there are helicopter-enabled ships that are less than 100m in length and these will have significantly greater ship motion in rough seas than a large ship. The study reported in this paper has used a motion-base flight simulator to evaluate the pilot workload when landing to three geometrically similar ships of lengths 100m, 150m and 200m. Ship motion software has been used to create realistic deck displacements for sea states 4, 5 and 6, which are consistent with the increasing wind speed over the deck. It has been shown that the 100m ship was the most difficult to land to, with deck motion being the limiting factor. The next most difficult ship to land to was the 200m ship, with airwake turbulence being the limiting factor. The 150m ship generated the lowest pilot workload. The study has demonstrated that when ship motion is excessive, as it will be with small ships in rough seas, pilot workload will be dominated by deck motion during a landing task, but as the ship gets larger and more stable, airwake disturbances will dominate. It is clear from this study that realistic ship motion is essential when using piloted flight simulation to conduct simulated ship-helicopter operations.

1. INTRODUCTION

It is now commonplace for helicopters to operate to naval ships such as frigates and destroyers and there are increasing applications of helicopters operating to smaller patrol vessels. While a destroyer may have a typical length of 150m, the length of a helicopter-enabled patrol vessel may only be half of that. For example, HMS Clyde, a UK River-class patrol vessel is 82m long, and its helicopter deck, which is just 24m in length and 13m wide is designed to accommodate a 23m long AW 101 Merlin helicopter. A graphic of HMS Clyde with a Merlin Helicopter on the flight deck is shown in Fig. 1 [1].

Figure 1 Graphic of HMS Clyde, a River-class Patrol vessel with a Merlin helicopter on the flight deck

The next generation UK frigate will be the City class Type 26, an early design version of which is illustrated in Fig. 2 [2]. The helicopter shown in Fig. 2 is again a Merlin so the relative proportions of the landing deck to the helicopter can be seen. It is expected that the ship will be 150m in length and its landing deck will be about 31m long and 20m wide, so providing the pilot a significantly larger deck than in Fig.1.

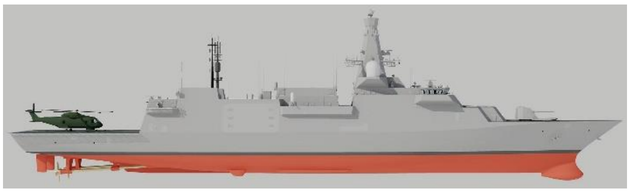

Figure 2 Future UK City class Type 26 frigate with a Merlin helicopter on the flight deck

The difficulty of flying a helicopter to the moving deck of a ship in adverse weather conditions is well documented, e.g. [3]. The main challenges to the pilot come from the small landing area that has considerable movement in heave, pitch and roll in rough seas; from the highly unsteady turbulent air flow over and around the flight deck; and from the close proximity of the ship's superstructure. While there are other adverse effects, such as poor visibility and hot exhaust gases from the ship's engines, the three main effects are those listed above with pilots usually commenting that turbulent air flow is the primary limiting factor for a safe landing in rough weather. The turbulent air flow over the ship is known as the ship airwake, and its characteristics are governed by the ship topside geometry, and the speed and the angle of the wind relative to the ship. The aerodynamics of ship airwakes have been extensively studied through both wind tunnel testing and Computational Fluid Dynamics (CFD), e.g. [4,5].

The demanding nature of ship-helicopter operations means that each ship and helicopter combination is subject to its own specific Ship-Helicopter Operating Limits (SHOL) which specifies the limiting wind strength and direction for which it is safe to launch the helicopter [6]. SHOLs are normally determined during the ship's First of Class Flight Trials (FOCFT) which are inherently costly and dangerous to carry out, requiring aircraft to be flown to the limits of what is considered safe, and often beyond the capabilities of the average fleet pilot. Due to these shortcomings associated with the FOCFTs, considerable research has been conducted, at the University of Liverpool (UoL) and elsewhere, into using flight simulation to support, or possibly replace, SHOL testing [7,8,9].

The Flight Science and Technology Research Group at the UoL has developed rotorcraft flight simulation research facilities with the over-arching aim of improving the fidelity of flight simulation, with particular attention being paid to the helicopter-ship dynamic interface. Much of this work has involved the use of the HELIFLIGHT-R motion-base flight simulator, shown in Fig. 3 [10]. The simulator features a three-channel 220° x 70° field of view visual system, a six degree of freedom motion platform, a four axis control loading system and has an interchangeable crew station. As well as the usual simulation environment, i.e. visual and aural cues, full motion, and aircraft flight mechanics models, an unsteady CFD-generated airwake is also provided to disturb the aircraft when it is within the ship's airwake [8,9].

Using piloted flight simulation, Forrest et al. [8] compared the simulated SHOLs of the UK's Type 23 naval frigate and the larger Wave class tanker. It was found that although the tanker has a much larger deck area, it had a more restricted SHOL than the Type 23 frigate due to the larger turbulent flow structures shed by the larger superstructure. The increased energy contained within the turbulent flow over the tanker in turn increased the level of pilot workload. Although the two ships were substantially different in shape, the conclusion was that larger ships created more problematic airwakes. Considering the relative difficulty of landing a helicopter to the 24m x 13m deck of the patrol vessel in Fig. 1 compared with the 31m x 20m deck of the frigate in Fig. 2 it is not therefore necessarily the case that the smaller landing deck will pose the greatest challenge to the pilot.

Figure 3 The University of Liverpool HELIFLIGHT-R motion base research simulator

To explore further the effect of ship size on the airwake and on the helicopter, Scott et al. [11] used CFD-generated airwakes coupled with a helicopter flight model to show that, as the ship gets smaller, the airwake becomes less aggressive for the helicopter compared with the airwake from a larger ship. This is because the ship superstructure is an assembly of bluff bodies (e.g. mast, funnel, bridge, hangar) that shed unsteady wakes. As the bluff bodies get smaller the size of the shed vortices become proportionally smaller and their frequency of shedding becomes proportionally higher. The net result is that the smaller, higher frequency aerodynamic disturbances contribute less to pilot workload [12]. However, while the study showed that the airwake is less challenging for the helicopter pilot as the ship gets smaller, the landing deck also becomes smaller and the proximity of the superstructure becomes more threatening. It was still not immediately obvious from this study therefore, whether smaller ships are easier for a pilot to land a helicopter to, or harder.

To examine further the effect of ship size on the difficulty of landing to the ship, Scott et al. [13] went on to conduct simulated flight trials in the HELIFLIGHT-R motion simulator in which a pilot carried our deck landings to the three geometrically similar ships shown in Fig. 4. The ships have a generic geometry that is typical of modern warships and the lengths of the three ships are 100m, 150m and 200m. The helicopter model used in the flight tests was representative of a SH-60B Seahawk. Figure 5 shows the size of the helicopter rotor relative to the 100m and 200m ships; also shown in this figure is the turbulence intensity in the ships' airwakes for a head wind. It can be seen that the helicopter rotor is exposed to more turbulent flow over the larger ship.

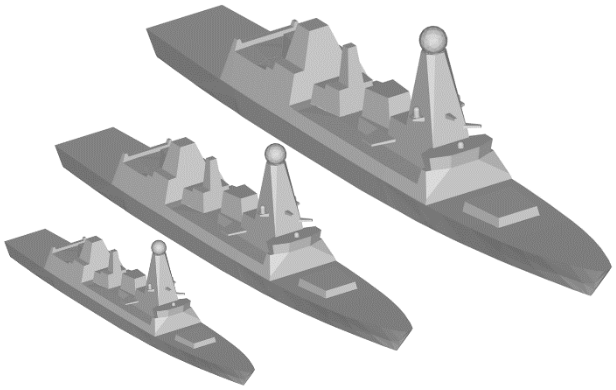

Figure 4 The generic naval frigate geometry and the range of ship sizes used for this study (lengths 100m, 150m, 200m).

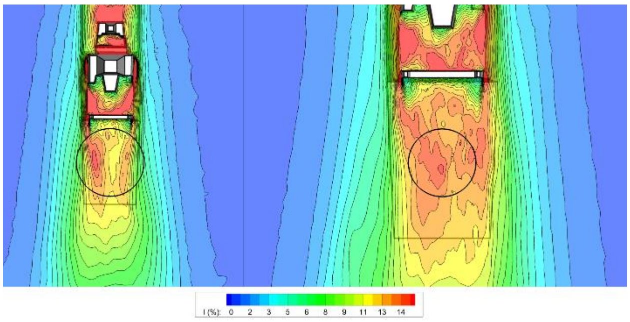

Figure 5 Relative size of 100m and 200m ship flight decks showing SH60-B rotor diameter and CFD-generated turbulence intensity at hangar heights.

In the flight tests reported in [13] the three ships had the same deck motion and while it was recognised that different size ships will have different dynamic responses to a given sea state, it was decided to use the same deck motion for each ship size so that the flight tests were able to distinguish the pilot workload required to land to a small and large ship due only to their airwakes and to the size of their landing decks. The results from the flight trials showed that pilot workload generally increases with ship size and that, despite the landing area being larger and the superstructure proximity being less threatening, the more aggressive airwake still makes the aircraft more difficult to control over the larger ship. During the flight trials, however, the pilot commented that the same ship motion for the different size ships while in the same sea state was unrealistic. Therefore, a new set of flight trials was planned in which the sea state was different for different wind strengths, and the ship motion for each ship size shown in Fig. 4 was used in the simulations. The purpose of this paper is to report a selection of the results of the simulated flight trials for the three ships shown in Fig. 4 in a headwind with different wind strengths and ship motions.

2. CREATING SHIP AIRWAKES IN CFD

To produce the flight simulation environment a generic ship model was created to represent a modern, single-spot naval frigate with a beam of 20m and a length of 150m. This geometry was then scaled to produce two ship models of 100m and 200m in length, creating the ships shown in Fig. 4 and which span the size range of single-spot combat ships that operate with maritime helicopters.

The unsteady airwake was created using ANSYS Fluent, a commercial CFD code. The ship model was imported into the ANSYS ICEM mesh generation software, so that it could be 'cleaned' to repair any erroneous surfaces and to remove small features to create geometry suitable for meshing. Features such as small antennae, railings and other small deck clutter have little effect on the airwake but if not removed will increase the complexity and hence the run-time of the CFD. Generally, objects that are less than 0.3m in diameter were removed. A surface mesh was then applied to the ship geometry and this was 'grown' away from the ship into the computational domain which surrounds the ship. Figure 6 shows a cross-sectional view of the mesh close to the ship.

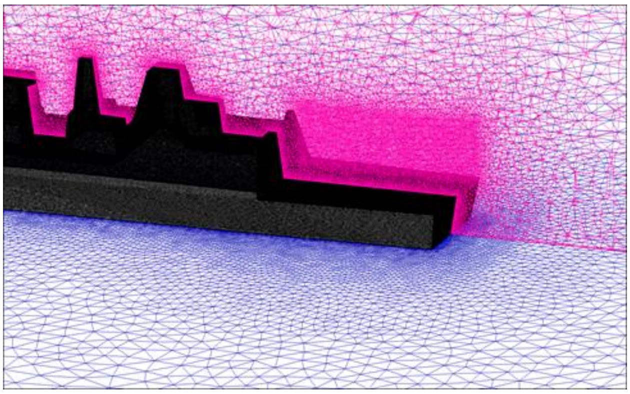

Figure 6 Computational mesh used to produce the CFD simulations, note the refinement region over the flight deck

Areas of particular interest within the volume mesh, such as the flow aft of the hangar and the area adjacent to the flight deck, were further refined using regions of high density mesh to increase the resolution of turbulence within the airwake, the total cell counts were in the region of 15 million cells. The unsteady CFD airwake was computed using Detached Eddy Simulation (DES) turbulence modelling. Thirty seconds of unsteady airwake were computed at 100 Hz for the 150m ship at a 40 knots wind speed for different wind angles. Further details of the CFD methodology and experimental validation has been described by Forrest and Owen [5].

Having created the three-dimensional unsteady velocity components at every 0.01 seconds, the velocity components can then be scaled for different ship sizes and wind speeds, so saving substantial computing time and resources. Scott et al. demonstrated the validity of the scaling process in [13]; for the present study ship size was scaled from the 150m ship to the 100m and 200m ships, and the wind speed from 40 knots to velocities between 15 knots and 60 knots. The vortices shed from bluff bodies within a flow are created at distinct frequencies which can be described by the Strouhal Number (Reynolds number dependence is acknowledged, but is known to be less important at high values and for sharp-edged bodies). Strouhal number relates the characteristic length of a bluff body, l, the flow speed v, and the frequency, f, of the vortices shed from the body ($St = f\ l/v$) This simple relationship shows that for an increase in free stream flow speed there will be a proportional increase in shedding frequency, and for an increase in length scale there will be a proportional decrease in frequency. While this may be obvious for vortex shedding at a single frequency, the principle can also be extended to more complex shedding from the multiple bluff bodies that make up a ship's superstructure. Therefore, the airwake velocity components for the different wind speeds and ship sizes were scaled from the 40 knot airwake for the 150m ship. Note that separate airwakes were computed for different wind angles. The airwake was 'connected' to the ship geometry so that it moves with the ship.

3. SHIP MOTION

The motions of the three ships at sea were simulated using ShipMo3D, a well-validated ship motion potential-flow code developed at Defence Research and Development Canada (DRDC) – Atlantic, and made available to the UoL. ShipMo3D predicts ship motion based on the Green function for zero forward speed, and was selected due to its well-documented validation for vessels travelling at moderate speed (i.e. Froude numbers below 0.4), via both model testing and full-scale at-sea trials [14]. Further, ShipMo3D has been designed to facilitate interoperability with other software, lending itself well to use in a distributed simulation environment such as is used in this study [15]. Validation has shown ShipMo3D can predict RMS motions to typically be within 10 to 30 percent of observed values, with heave predictions being the most accurate and roll predictions being the least accurate.

3.1. Ship Geometry

Geometry representative of the hull of the 150 m long ship was input into ShipMo3D as a set of hull surface coordinates. Ship appendages were also included, with the hull featuring a bulbous bow, two rudders, two propellers, two bilge keels, two roll stabilisers, and a skeg. The hulls and their appendages were linearly scaled in size to match the 100 m and 200 m ships, and while it is acknowledged that hull appendages will not necessarily be linearly scaled with ship length, appendages were scaled in this manner to maintain a better comparison between the three ships. The draught, height of centre of gravity above baseline (KG), and thus metacentric height (GM) were also scaled; these values are given for each ship in Table 1. Roll gyradius was assumed to be 35% beam, while pitch and yaw gyradii were taken as 25% ship length.

Table 1 Scaled ship properties

Length (m)	**100**	**150**	**200**
Beam (m)	11.7	17.6	23.4
Displacement (t)	2,380	8,040	19,057
Draught (m)	4.0	6.0	8.0
GM (m)	1.2	1.8	2.4
No. Panels (wetted hull)	1192	1342	1382
Prop. Dia. (m)	2.67	4.0	5.33
Prop. RPM (@ 12kts)	162.3	106.5	79.2

Once input into ShipMo3D, the hull surface coordinates were panelled as a solid surface using triangular and quadrilateral panels, with a minimum 1000 panels representing the wetted hull to ensure grid independence; the number of panels used on each of the three ships is given in Table 1. The panelled geometries are shown in Fig. 7. The wet and dry hull panels are shown as yellow and green, respectively, with the hydrostatic waterline located at the interface between these surfaces.

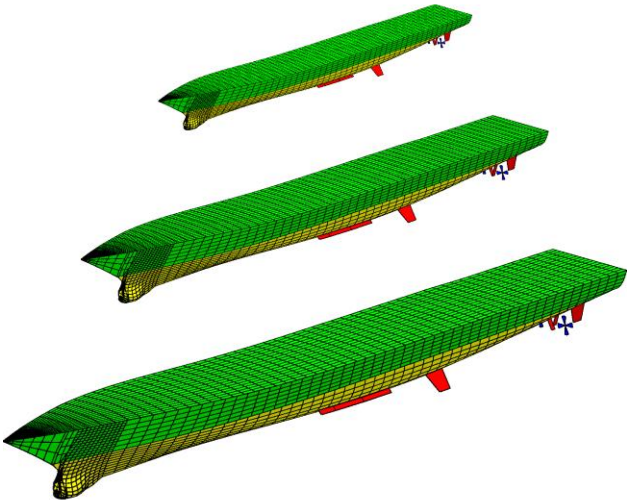

Figure 7 Panelled hulls, with appendages

3.2. Seaway Generation

For the piloted flight trials, three random seaways were generated representing sea states 4, 5, and 6, using the Bretschneider spectrum [16], which is widely used to model point wave spectra in the open ocean. Significant wave heights ($H_{1/3}$) and peak wave periods (T_p) used for each sea state are given in Table 2. For a 12 knot ahead ship speed, sea states 4, 5, and 6 were taken as representative of conditions encountered in the North Atlantic for the Wind Over Deck headwinds tested in this study.

Table 2 Conditions for sea states 4-6

WOD (kts)	Sea State	T_p (s)	$H_{1/3}$ (m)
15, 25	4	8.8	1.9
35, 40	5	9.7	3.3
45, 50	6	12.4	5.0

While a unidirectional Bretschneider spectrum can be used to approximate long-crested oceanic waves, lateral motion (roll, sway, and yaw) will be absent due to the symmetry of the ship geometry travelling directly into two-dimensional waves, and so a cosine-squared spreading function was implemented with a 90° spreading angle and 15° heading interval, as supported by trials evidence for typically occurring conditions in the open ocean [17]. In this way a more representative short-crested wave spectrum was generated, represented by eleven reduced Bretschneider spectra distributed around the dominant ahead wave direction; this has the advantage of imposing realistic lateral forces upon the symmetrical ships in the ahead case that cause the ships to roll, which they would not do in a unidirectional wave spectrum.

3.3. Ship Motion Computations

Once the ship geometries had been successfully panelled and all load condition data specified, the three differently sized ships were placed into the same three simulated head waves at 12 knots ship speed for a total time period of 180 seconds, with the first 60 seconds discarded as a settling period to allow ramping up of ship motions from rest.

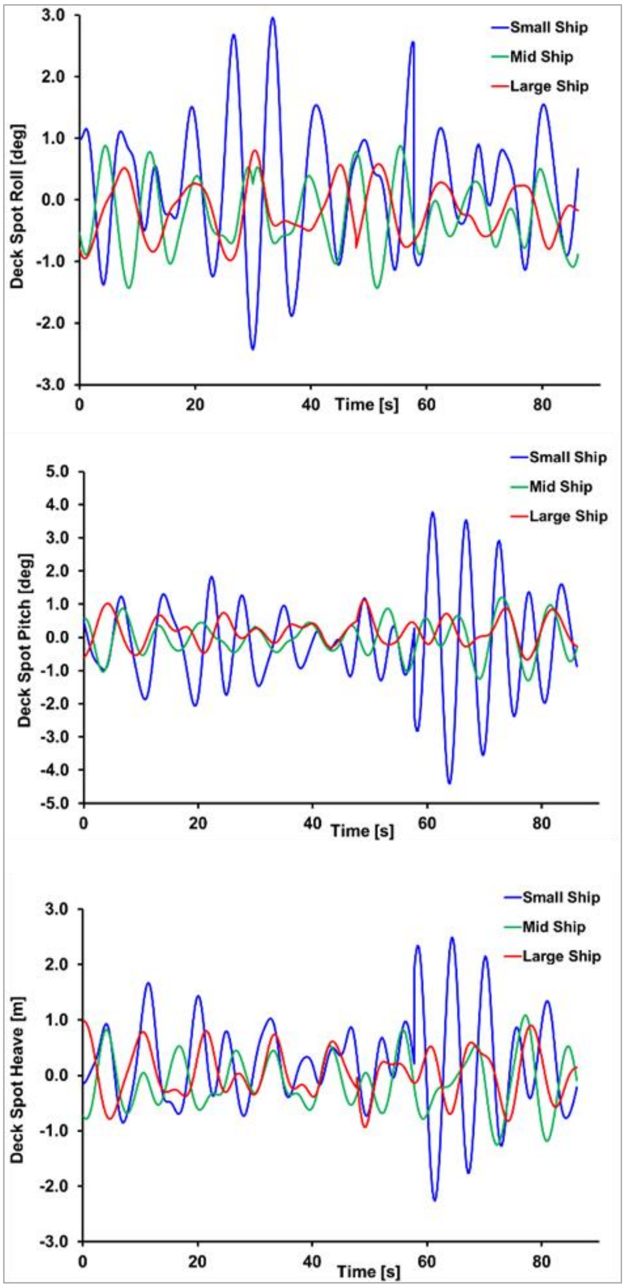

Figure 8 Computed displacements of the landing spot for the three ships travelling at 12 knots through sea state 5 with waves coming from ahead

The ship motion was calculated as roll, pitch and heave at the ship's centre of gravity. These were then imported into UoL's flight modelling and simulation environment, FLIGHTLAB, which creates a deck contact area for launch and recovery operations. The ship motion data is broadcast across a local network to drive a visual model of the ship in UoL's run-time environment, LIVE. Landing spot state information i.e. attitudes, velocities and accelerations, are recorded in FLIGHTLAB during piloted simulation trials. Figure 8 shows an example of the deck motion (roll, pitch and heave) at the landing spot for the three ships travelling at 12 knots through sea state 5, with the waves coming from ahead. Looking at the small ship data, maximum roll and pitch are about ±3˚, and maximum heave is about ±2m, compared with less than ±1˚ pitch and roll, and about ±1m for the large ship. It can also be seen in Fig. 8 that there are periods in the ship motion that are less violent than others and it is these naturally occurring quiescent periods that the pilot waits for when executing a landing.

4. PILOTED FLIGHT SIMULATION

The creation of a full-motion flight simulation environment for a helicopter operating to a ship requires: a simulator, in this case the HELIFLIGHT-R shown in Fig. 3; a ship visual model, such as in Fig. 4, suitably rendered; a CFD-generated airwake; a ship motion model; a visual scene; and a helicopter flight dynamics model.

The helicopter flight dynamics model was provided by Advanced Rotorcraft Technology's (ART's) FLIGHTLAB software [18]. Motion base acceleration commands to the HELIFLIGHT-R simulator are provided as outputs from the aircraft flight dynamics model through a motion drive algorithm. A fully programmable control loading system provides force-feedback through the aircraft cyclic, collective, and pedal inceptors. CFD airwakes can be integrated with FLIGHTLAB, enabling unsteady airwake velocities to be imposed upon the aircraft flight model. During testing, FLIGHTLAB allows real-time data monitoring and recording which, together with in-cockpit video and audio recordings, are used for post-trial analysis.

The FLIGHTLAB Generic Rotorcraft model used for this research was configured to be representative of the Sikorsky SH-60B Seahawk, a maritime development of the widely used UH60 Black Hawk. The model is constructed from a set of modular components such as the rotor, fuselage and turbo-shaft engine. The unsteady airwake data is integrated into the helicopter flight dynamics model by applying the time varying velocity components to the aircraft via a number of Airload Computation Points (ACPs) which are located at various points along each rotor blade, fuselage, tail rotor and empennage, as shown in Fig. 9.

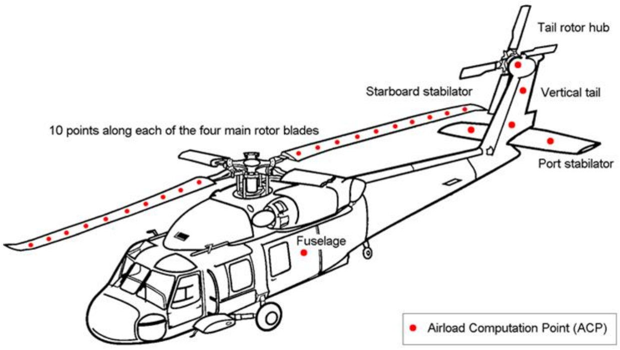

Figure 9 Location of the ACP's used on the SH60-B helicopter flight dynamics model in FLIGHTLAB

Each CFD simulation produces thirty seconds of unsteady CFD data, generated on a high density, unstructured mesh. Due to memory constraints when running real-time piloted simulations, the computed airwake data requires post-processing before it can be used within FLIGHTLAB. Reduction of the airwake data size is undertaken by first sampling the 100Hz data at every fourth time step and then by interpolating the unstructured CFD data onto a structured mesh using a grid spacing of 1 metre, covering a region of interest around the flight deck of the ship. The 30 second airwake data was looped smoothly for the duration of the flight test.

FLIGHTLAB includes a dynamic inflow model and also accounts for the downwash from the rotor. However, the interaction between the airwake and the rotor model is not fully coupled, i.e. it is 'one-way', such that the helicopter is affected by the airwake, but the rotor downwash does not interact with the airwake.

A comprehensive description of the simulated SHOL testing process can be found in [9].

4.1. Test Procedure

The flight tests were conducted by a former UK Royal Navy helicopter test pilot. The landing tasks were based on the Royal Navy port-side approach where the pilot brings the helicopter to a forward-facing hover position alongside the landing deck, approximately one beam width off the port side of the ship, matching the speed of the ship. The pilot then conducts a lateral translation to a hover over the deck landing spot before descending to land on the flight deck. During the tests, the pilot was asked to hold a hover position over the port edge of the flight deck at approximately hangar height for thirty seconds and to provide a rating of the workload experienced; this was followed by a thirty second hover over the flight deck, again with an evaluation of the workload. During the testing, the pilot was given the flexibility to adjust altitude as deemed fit to accommodate the ships' deck motions.

The pilot was asked to provide workload ratings for the individual hover tasks using the Bedford workload ratings scale [19]. The Bedford workload rating scale is a 10-point scale used by evaluation pilots to assess the workload required (by an 'average' pilot) to successfully complete a given task. Ratings 1-3 are awarded when the workload is considered to be satisfactory without reduction and does not prevent the pilot from performing additional tasks (e.g. monitoring aircraft systems or radio communications). Ratings of 4-6 are awarded where workload is deemed to be tolerable for the task, while a rating of 7-9 is awarded where the task can be performed successfully, yet the workload is not tolerable for the task. Finally, a rating of 10 is awarded in situations where the pilot is unable to complete the task, and so must abandon it.

The pilot was also required to provide a rating from the Deck Interface Pilot Effort Scale (DIPES) [20] for the overall difficulty of the complete landing task. The DIPES scale requires the test pilot to give a rating of 1-5 for any given launch/recovery task. A rating of 1-3 is considered to be acceptable, with the task considered to be within the abilities of an average fleet pilot. Conversely, a rating of 4 is deemed to be unacceptable on the basis that an average fleet pilot would not be able to complete the task in a consistently safe manner, while a rating of 5 indicates that the task cannot be safely completed by the test pilot even under controlled test conditions. Additionally, the test pilot can apply one or more letter suffixes to a DIPES rating which describe the cause(s) of the increased workload e.g. T for turbulence.

More complete descriptions of the Bedford and DIPES workload rating scale and their use in flight simulation can be found in [9].

Flight tests were conducted for each ship size and for a number of wind conditions. The results presented in this paper are for the headwind condition with wind speeds from 15 to 50 knots.

4.2. Results

The Bedford workload ratings for each of the three ships for the headwind case are given in Fig. 10, for the thirty second, deck spot hover task. As the wind speed over the sea increases, so the sea state can be expected to increase. In this case the expected sea state for the wind speed is shown on the graph, and the motion of each ship was computed, as described in Section 3, for that sea state and a ship forward speed of 12 knots.

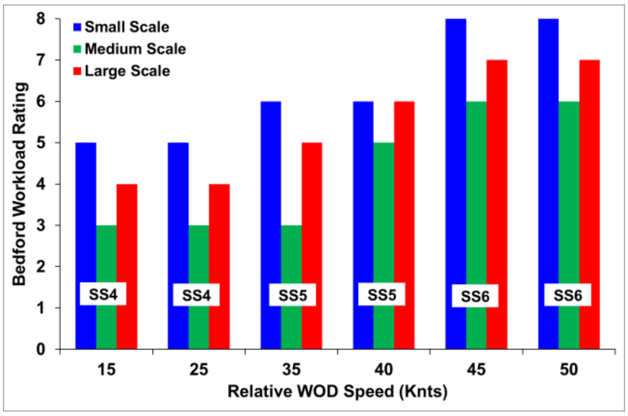

Figure 10 Bedford workload ratings awarded in current tests by pilot for the hover task above the deck spot, headwind, realistic ship motion, 12 knots ship speed.

It can be seen in Fig. 10 that, for all three ships, the workload required to maintain the hover over the moving deck increased as the wind strength increased. This is because the helicopter is immersed within the turbulent airwake and the unsteady loads being imposed on the aircraft will increase as wind speed increases. Also, as the wind speed increases so too does the sea state and the displacement of the ships' deck. It can also be seen that the workload required to hold the hover position over the small ship is higher than for the medium and large ship. This is despite the fact that the small ship's airwake is the least aggressive, and the higher workload must therefore be due to the large displacements of the small ship's deck with some additional workload arising from the airwake disturbances. It can also be seen in Fig. 10 that the large ship has generated workload ratings that are generally one rating less than those awarded for the hover task over the small ship and one rating higher than those awarded for the medium size ship. In each case the minimum workload rating is awarded for the medium size ship. The pilot is having to contend with both the deck motion and the airwake and it appears that the 150m ship (which is typical of a single-spot frigate) has the best combination of moderate deck motion and airwake. The small ship has the least aggressive airwake, but the greatest deck motion, and the large ship has the most aggressive airwake and least deck motion.

These results can be compared with similar tests reported in [13] where the same ships and airwakes were used, but the ship motion was the same for all three ships so that the airwake effect could be seen in isolation. In [13] the ship motion was representative of the medium ship in a sea state 3. The results of the workload ratings awarded for the hover task can be seen in Fig. 11 below; again workload can be seen to increase with wind speed, but with much lower values than in Fig. 10, and in the case where the pilot does award higher ratings for a given wind speed it is for the smaller ship, where the pilot reported the close proximity of the hangar as an issue. It is clear from comparing Figs. 10 and 11 that realistic ship motion is essential for simulated landings of a helicopter to a ship.

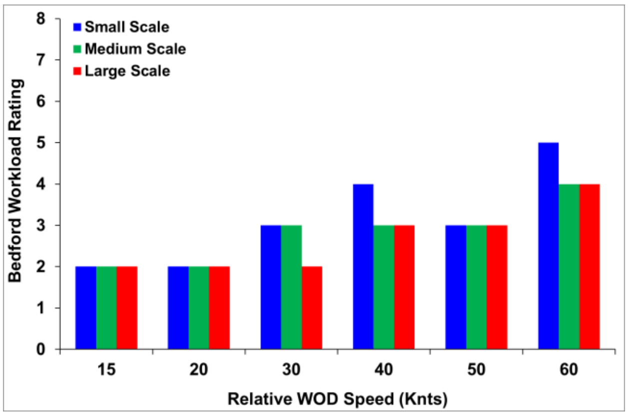

Figure 11 Bedford workload ratings awarded in previous tests [13] by pilot for the hover task above the deck spot, headwind, with equal and limited ship motion.

Further insight into the difficulty of holding the helicopter in a stable hover over the landing spot can be gained by looking at the control activity of the pilot during the hover task. Figure 12 shows the pilot's cyclic control inputs, which are used for lateral and longitudinal positional control during the 30 second hover over the landing spot. The largest excursions are for the large ship and will be due to the larger, slower moving vortices being shed from the ship superstructure. The smaller ship shows the smallest excursions while the control activity for the medium ship lies between the two.

The data in Fig. 12 does not explain why the pilot awarded the greatest workload ratings to the hover task over the smallest ship. However, Fig.13 shows the pilot's control inputs to the collective, which provides power and thrust to main rotor (and which then also interacts with the pedal control as the aircraft changes attitude in yaw). It can be seen in Fig. 13 that the greatest activity in the collective control is for the hover task over the small ship, while the lowest is for the large ship. As the small ship's airwake is the least disruptive the pilot is therefore having to work hard to hold vertical position over the landing spot as the ship moves about violently, as seen earlier in Fig. 8. The same situation is seen in the pedal control activity in Fig. 14 where the largest excursions are seen over the small ship.

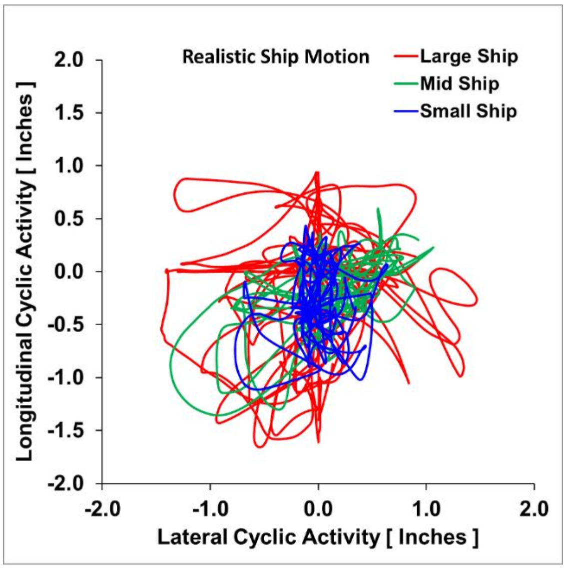

Figure 12 Cyclic control activity during hover task over landing spot for a 40 knot headwind, sea state 5.

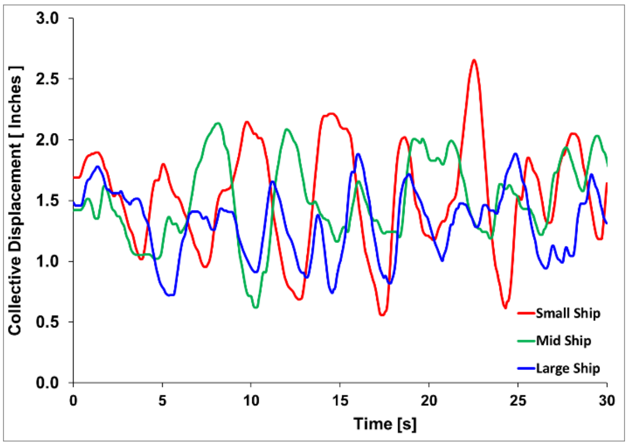

Figure 13 Collective control activity during hover task over landing spot for a 40 knot headwind, sea state 5.

Bearing in mind that while holding position over the landing spot the pilot is also being exposed to visual cues with the smaller ship moving in significant roll, pitch and heave, especially when compared with the slower motion of the larger ship. The combination of control activity and cueing information the pilot is contending with means that, as Fig. 10 shows, the workload is highest for the smaller ship and is lowest for the medium ship.

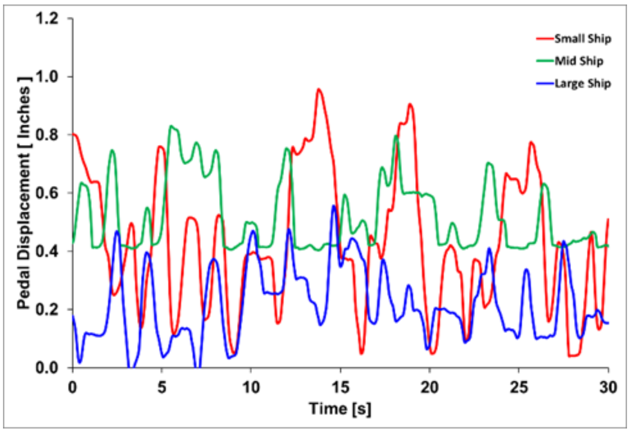

Figure 14 Pedal control activity during hover task over landing spot for a 40 knot headwind, sea state 5.

Finally, the pilot was also asked to rate the difficulty of the whole landing task using the DIPES scale. In this task the pilot began with the helicopter alongside the ship, off the port side; the helicopter was then translated across the deck and held in the hover position over the spot until the pilot deemed it appropriate to land. The DIPES ratings awarded by the pilot for headwind speeds from 15 to 50 knots and for the three ship sizes with appropriate sea-state motion are shown in Fig. 15. Again, it can be seen that in general the pilot's workload increase as the wind speed increases, and the greatest effort is required for the landing to the smaller ship. It should also be noted that the safe limit for the landing task is 3 so that for a headwind of 45 knots it is unsafe to land to the small ship, and for a headwind of 50 knots it is unsafe to land to the small and medium ships.

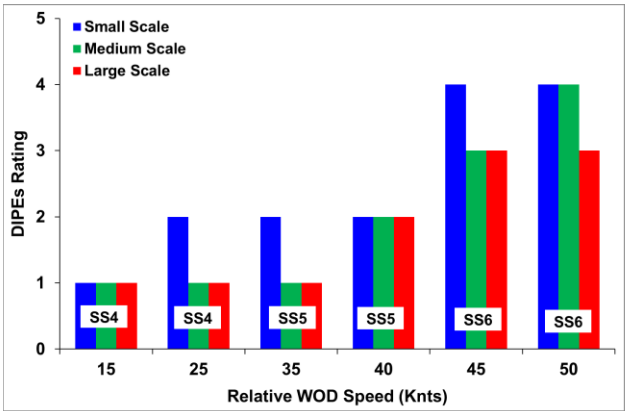

Figure 15 DIPES ratings awarded in current tests by pilot for the landing task. Headwind, with realistic ship motion.

As well as awarding the DIPES ratings in Fig. 15, at higher workload the pilot also identified the causes. For the large ship the pilot indicated that fore-aft positioning and turbulence were the limiting factors. For the smaller ship the limiting factors were difficulty of ship tracking and positional accuracy as well as torque limit while trying to track the deck vertically; i.e. ship motion was the determining factor. For the medium ship the pilot reported that a combination of turbulence and ship motion made it difficult to hold position.

Figure 16, extracted from the earlier study reported in [13], shows the DIPES ratings awarded to the landing task when the ship motion was the same for all three ships, i.e. a relatively low motion corresponding to that of the medium ship in a sea-state 3. As reported in [13], the pilot awarded the lowest DIPES rating of 1 for all three ships up to a headwind speed of 40 knots, and at wind speeds above this the greatest effort was awarded for the deck landings to the larger ships confirming that when ship motion is not an issue it is the unsteady aerodynamic loads on the aircraft due to the airwake that dominates the pilot's workload.

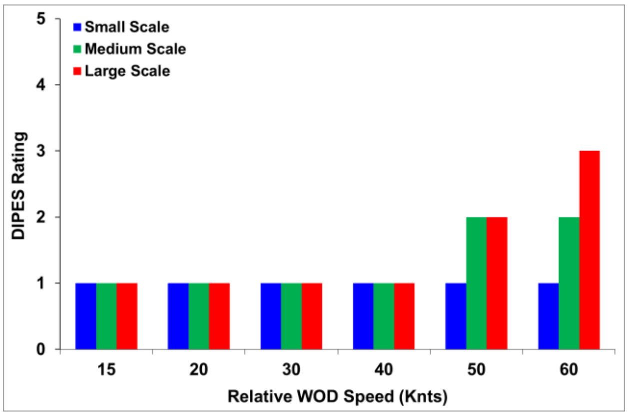

Figure 16 DIPES ratings awarded in previous tests [13] by pilot for the landing task. Headwind, with equal and limited ship motion.

5. CONCLUSIONS

Previous studies have shown that larger ships create more aggressive airwakes and simulated flight trials had shown that it can be more difficult to land to a large ship than a smaller one, even though it had a bigger landing deck; i.e. the landing task was dominated by the ship airwake. In those tests, however, the deck motions of the large and small ships were the same. In the study reported in this paper, realistic ship motion for three different size ships has been computed for sea states that are consistent with the relative wind over the ship.

Three geometrically similar ships of length 100m, 150m and 200m have been considered. With the realistic ship motion included, flight simulation showed that workload was highest when landing to the smaller ship and lowest when landing to the medium size ship. It cannot be said therefore that as the ship gets larger the landing gets more difficult, but when ship motion is significant the moving deck provides a greater challenge to the pilot than does the airwake. With larger ships, the deck motion presents less of a challenge, while the unsteady loads from the airwake dominate the pilot's workload.

It is clear from this study that realistic ship motion is essential when using piloted flight simulation to conduct simulated ship-helicopter operations.

References

1. Royal Navy website, accessed July 2017, http://www.royalnavy.mod.uk/our-organisation/the-fighting-arms/surface-fleet/patrol/river-class/hms-clyde
2. Royal Navy website, accessed July 2017, http://www.royalnavy.mod.uk/the-equipment/ships/future-ships/type-26
3. Lumsden, B. and Padfield, G.D. "Challenges at the Helicopter-Ship Dynamic Interface", Military Aerospace Technologies - Fitec ' 98, IMechE Conference Transactions, Institute of Mechanical Engineers, Wiley, UK, 1998.
4. Polsky, S.A. and Bruner, C.W.S. "Time-Accurate Computational Simulation of an LHA Ship Airwake", AIAA Paper No. 2000-4126, 18th Applied Aerodynamics Conference, Denver, Colorado, USA, August 2000.
5. Forrest, J. S. and Owen, I., "An Investigation of Ship Airwakes Using Detached-Eddy Simulation," Computers & Fluids, 2010, 39 (4), 656–673.
6. Carico, G.D., Fang, R., Finch, R.S., Geyer Jr, W.P., Krijins, H.W. and Long, K. "Helicopter/Ship Qualification Testing". NATO SCI-055 Task Group, RTO-AG-300 Vol 22, February 2003.
7. Roscoe, M. and Wilkinson, C.H., "DIMSS – JSHIP's modelling and simulation process for ship/helicopter testing & training", Proc. AIAA Modelling & Simulation Technologies Conference, Monterey, CA, AIAA 2002-4597.
8. Forrest, S.J., Owen, I., Padfield, G.D. and Hodge, S.J., "Ship-helicopter operating limits prediction using piloted flight simulation and time-accurate airwakes", J. Aircraft, 2012, 49 (4), 1020-1031.
9. Hodge, S.J., Forrest, J.S., Padfield, G.D. and Owen I., "Simulating the Environment at the Helicopter-Ship Dynamic Interface: Research, development and Application", Aeronautical J., 2012, 116 (1185), 2012, 1155-1184.
10. White, M.D., Perfect, P., Padfield, G.D., Gubbels, A.W. and Berryman, A.C., "Acceptance testing and commissioning of a flight simulator for rotorcraft simulation fidelity research", Proc. IMechE Part G: J Aerospace Engineering, 2012, 226(4), 638-686.
11. Scott, P., White, M.D. and Owen, I., "The effect of ship size on airwake aerodynamics and maritime helicopter operations", 41st European Rotorcraft Forum, Munich, 1-4 September 2014.
12. McRuer, D.T. "Interdisciplinary interactions and dynamic systems integration", Int J Control, 1994, Vol. 59, 3-12.
13. Scott, P., Owen, I. and White, M.D., "The Effect of ship size on the flying qualities of maritime helicopters", American Helicopter Society 70th Annual Forum, Montreal, Canada, May 20-22, 2014.
14. McTaggart, K., "Validation of ShipMo3D Version 1.0 User Applications for Simulation of Ship Motion", Technical Memorandum, DRDC Atlantic TM 2007-173, August 2007.
15. McTaggart, K.A. and Langlois, R.G., "Physics-Based Modelling of Ship Replenishment at Sea Using Distributed Simulation", Society of Naval Architects and Marine Engineers Annual Meeting and Expo, Providence, Rhode Island, USA, 20-23 October 2009.
16. ITTC Seakeeping Committee Report. In 15th International Towing Tank Conference, Vol. 1, pp. 55–114. The Hague, 1978.
17. Cummins, W.E. and Bales, S.L., "Extreme value and rare occurrence statistics for Northern Hemisphere shipping lanes", 1980 SNAME Spring Meeting and STAR Symposium, California, USA, 3-7 June 1980.
18. Duval, R.W. "A real-time multi-body dynamics architecture for rotorcraft simulation," in RAeS Proceedings of the challenge of realistic rotorcraft simulation, London, UK, 7-8 November, 2001.
19. Roscoe, A. H., and Ellis, G. A., "A Subjective Ratings Scale for Assessing Pilot Workload in Flight: A Decade of Practical Use," RAE, TR TR90019, 1990.
20. Finlay, B.A. "Ship Helicopter Operating Limit Testing – Past, Present and Future", RAeS Rotorcraft Group Conference on 'Helicopter Operations in the Maritime Environment', London, UK, March 2001.

41st European Rotorcraft Forum 2015

THE EFFECT OF SHIP SIZE ON AIRWAKE AERODYNAMICS AND MARITIME HELICOPTER OPERATIONS

Paul Scott, Mark White
School of Engineering
University of Liverpool
Liverpool, UK
paul.scott1@liv.ac.uk
mdw@liverpool.ac.uk

Ieuan Owen
School of Engineering
University of Lincoln
Lincoln, UK
iowen@lincoln.ac.uk

Abstract

This paper describes an investigation that has used piloted flight simulation to assess pilot workload while manoeuvring a helicopter over the landing decks of three different size, but similar, ships. Three generic ships with lengths of 100m, 150m and 200m were created to be representative of the range of size of single-spot ships that operate with maritime helicopters. Ship airwakes were produced using unsteady CFD simulations for a range of free stream wind speeds from 20 knots to 50 knots for a headwind and Green 45° Wind Over Deck. To reduce the numbers of expensive and computationally intensive airwakes that have to be produced for simulated deck landings it has been demonstrated that for a given wind angle it is possible to Strouhal-scale the airwake velocities from one representative wind strength to other wind strengths, and from one ship size to another ship size with accuracies which are considered acceptable for their implementation within a flight simulator.

Simulated deck landing trials for each of the three ships were used to provide subjective pilot workload ratings. It was found that the pilot workload generally increases with the ship size and that, despite the landing area being larger and the superstructure proximity being less threatening, the more aggressive airwake from the larger ship still makes the aircraft more difficult to control over the larger ship.

1. INTRODUCTION

The operation of maritime helicopters to naval vessels at sea is often a difficult and dangerous task for the pilot[1,2]. Along with the restricted landing area and the rolling, pitching and heaving of the ship's deck the pilot also needs to contend with the turbulent wake produced by the air flow over the ship's superstructure. This turbulent airwake is a product of both the ship's forward speed and the prevailing wind conditions. In recent years the topside design parameters for modern frigates have been strongly influenced by the requirement to reduce radar cross section, leading to less cluttered 'slab-sided’ ships where the superstructure can be considered to be comprised of a number of bluff bodies. As the air flow separates from the sharp edges of the superstructure it creates a highly complex airwake containing steep velocity gradients and unsteady turbulent structures which can adversely affect the aerodynamic loads on a helicopter operating within the flow. The nature and severity of the airwake will vary with both the speed and azimuth of the Wind Over Deck (WOD). As the relative angle of the wind moves from a headwind towards more oblique angles, the flow becomes increasingly complex with large vortical structures being shed from the windward horizontal upper edges of the hangar and deck, and a strong vertical shear layer forms obliquely across the deck, emanating from the windward vertical hangar edge.

As the pilot manoeuvres through the turbulent airwake during an approach to the flight deck, there will be large perturbations in the aerodynamic loading and response of the rotor due to the highly unsteady velocity fluctuations, particularly those in the closed-loop pilot response frequency range of 0.2 to 2 Hz[3]. Disturbances within this frequency range have been shown to have the greatest impact on the pilot's workload[4].

On encountering a disturbance to the aircraft, the pilot will react by implementing control inputs to correct changes in altitude, attitude and heading. Therefore the geometric design of the ship superstructure can have a significant impact on the pilot workload, particularly when operating in close proximity to the ship during launch and recovery to the flight deck.

The demanding nature of ship-helicopter operations means that each ship and helicopter combination is subject to its own specific Ship-Helicopter Operating Limits (SHOL), as shown in Figure 1. Each SHOL denotes the safe operating conditions based on a

WOD speed and azimuth, with the terminology Red and Green referring to winds approaching from the port and starboard side of the ship respectively.

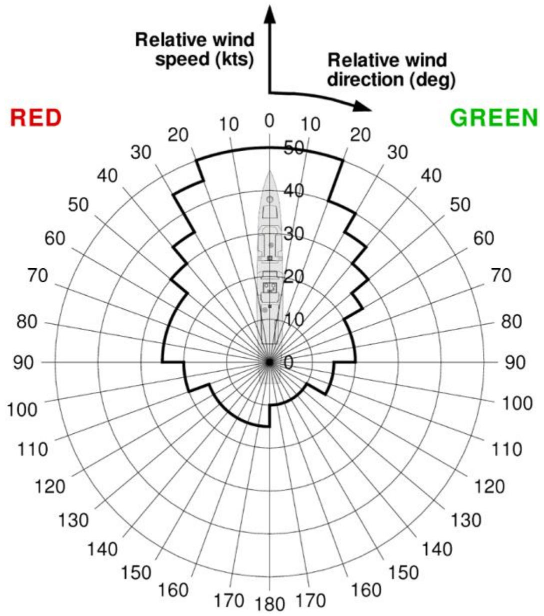

Figure 1 Typical SHOL diagram for a helicopter operating from a frigate

SHOLs are normally determined during the ship's First Of Class Flight Trials (FOCFT) and are inherently costly and dangerous to carry out, requiring aircraft to be flown to the limits of what is considered safe, and often beyond the capabilities of the average fleet pilot. Due to these shortcomings associated with the FOCFTs, considerable research has been conducted, at the University of Liverpool and elsewhere, into using flight simulation to support, or possibly replace, SHOL testing[5,6,7].

Over the past fifteen years the Flight Science and Technology Research Group at the University of Liverpool have developed rotorcraft flight simulation research facilities with the over-arching aim of improving the fidelity of flight simulation, with particular attention being paid to the helicopter-ship dynamic interface. Much of this work has involved the use of the HELIFLIGHT-R motion-base flight simulator, shown in Figure 2[8]. The simulator features a three-channel 220° x 70° field of view visual system, a six degree of freedom motion platform, a four axis control loading system and has an interchangeable crew station. As well as the usual simulation environment, i.e. visual and aural cues, full motion, and aircraft flight mechanics models, an unsteady CFD-generated airwake is also provided to disturb the aircraft when it is within the ship's airwake[7-10].

Figure 2 The HELIFLIGHT-R motion base simulator as used at the University of Liverpool

Using piloted flight simulation, Forrest et al[11] compared the simulated SHOLs of the UK's Type 23 naval frigate and the Wave Class oiler. It was found that although the oiler has a much larger deck area it had a more restricted SHOL than the Type 23 frigate due to the larger turbulent flow structures shed by the larger superstructure. The increased energy contained within the turbulent flow of the oiler in turn increased the level of pilot workload. Although the two ships were substantially different in shape, the conclusion was that larger ships created more problematic airwakes.

Building on this conclusion, the current study has investigated the effect of ship size on the airwake over the deck, and its impact on the helicopter and on pilot workload during a landing task; three geometrically similar ships of different sizes have been used. As indicated above, the airwake from the larger ship can be expected to provide greater disturbances to the aircraft, but the larger deck may be easier to land to. Current naval ships routinely operating helicopters can be as small as half the size of a conventional frigate, for example the Knud-Rasmussen class patrol vessel operated by the Royal Danish Navy with a length of 71m, Figure 3, and the similarly sized River Class patrol vessel in service with the UK Royal Navy. The small size introduces further challenges to pilots in that they are often asked to operate much closer to the superstructure of the ship during launch and recovery than they would be expected to on a larger ship.

Producing unsteady full-scale CFD simulations of the ship airwake is extremely computationally expensive and time consuming, taking several days to compute the unsteady data required for implementation within the flight simulator. The present study has therefore also explored the feasibility of computing an airwake, for a given WOD, for one ship size, and scaling it to another ship size using Strouhal scaling.

Figure 3 Knud-Rasmussen Class Patrol vessel[12]

2. SHIP AIRWAKE SCALING

To investigate the effect that ship size has on the level of pilot workload during a deck landing, a generic ship model was created to be representative of a modern, single-spot naval frigate of 150m length and 20m beam. This ship model was then scaled up and down to create two further ship models that were 200m and 100m in length, Figure 4. The airwakes for each of these three ship sizes were used to provide comparative data to (i) demonstrate the feasibility of Strouhal-scaling the airwake, and (ii) to investigate the consequences of a change in size on helicopter operations and pilot workload.

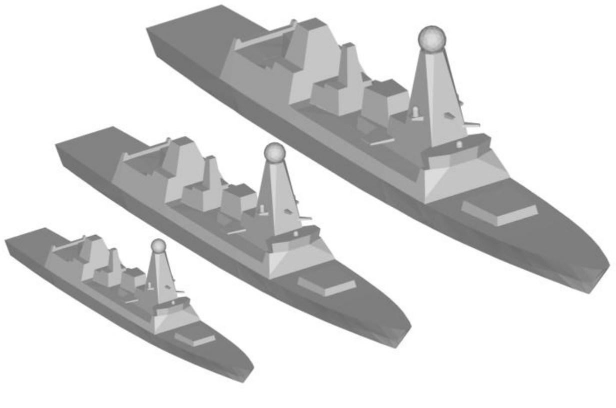

Figure 4 The generic naval frigate geometry and the range of ship sizes used for this study

The scaling of airwake data involves the use of the Strouhal number, shown below in Equation 1. The vortices shed from bluff bodies within a flow are created at distinct frequencies which can be described by the Strouhal Number (Reynolds number dependence is acknowledged, but is known to be less important at high values and for sharp-edged bodies). Strouhal number relates the characteristic length of a bluff body, l, the flow speed v, and the frequency f of the vortices shed from the body. This simple relationship shows that for an increase in free stream speed there will be a proportional increase in shedding frequency, and for an increase in length scale there will be a proportional decrease in frequency. While this may be obvious for vortex shedding at a single frequency, the principle can also be extended to more complex shedding from the multiple bluff bodies that make up a ship's superstructure.

$$St = \frac{fl}{v} \tag{1}$$

The scaling of airwakes in terms of velocity magnitude has been previously carried out by Polsky[13] who showed that the linear scaling of the airwake magnitude was possible. Further observations by Zan[14] "noted that the airwake should be shifted in frequency content as well as the velocity magnitude due to the large scale turbulent structures within the ship airwake which are the result of flow separation. In order to use Strouhal scaling to modify the airwake data, for example to change the airwake in terms of velocity magnitude from a free stream of 40 knots to 20 knots, the velocity components and frequency spectra are simply halved. Using this approach, Hodge et al[8] showed that the Strouhal scaling of CFD airwake data from 40 to 30 knots, in both frequency and velocity magnitude, gave good results when compared to a computed 30 knot airwake.

3. CFD METHODOLOGY

Ansys Fluent CFD software with Detached Eddy Simulation turbulence modelling was used throughout this study.

3.1. Geometry and Meshing

The ship models were imported into the mesh generation software Ansys ICEM, so that it could be 'cleaned' to repair unsuitable surfaces and to remove small features to create geometries suitable for meshing. Features such as small antennae, railings and other small deck clutter would have little effect on the airwake but if not removed would increase the cell count and hence the run time of the CFD; generally objects less than 0.3m in diameter were removed.

The final 'cleaned' ship model was then placed within a cylindrical flow domain, shown in Figure 5; this style of domain allows the relative WOD angle to be varied through 360° by changing the magnitudes of the x and y free stream velocity components of the flow, without having to change the computational domain. The orientation of the domain is such that the x-direction is in line with the longitudinal axis of the ship, while y is the lateral direction.

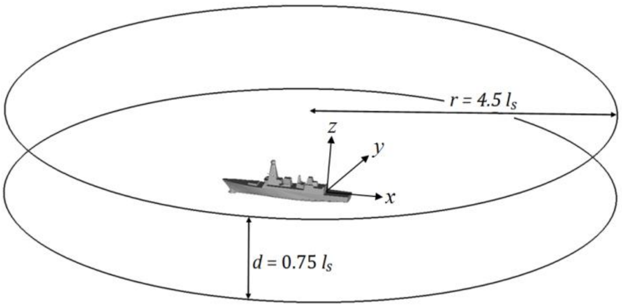

Figure 5 Computational flow domain for a ship of length l_s

An unstructured meshing approach was used for this study, which suits the Detached Eddy Simulation turbulence model (DES) well due to the near isotropic nature of the tetrahedra away from the walls[15]. The mesh was generated by first creating a surface mesh, from which a Delauney volume mesh was then grown. The surface mesh size on the ships was set to 0.05 times the hangar height and the growth of the volume mesh was controlled using an expansion ratio of 1.2 so that a smooth transition occurred away from the ship's surfaces.

Areas of particular interest within the volume mesh, such as immediately above the flight deck, were refined using regions of dense mesh within the volume to control the cell size and provide better resolution of the turbulent structures within the wake. Several layers of prism cells were grown from both the ground plane and the ship's surface into the volume mesh to resolve the boundary layers. These techniques allow better resolution of the vortical features shed from the ship and ensure the velocity distribution within the atmospheric boundary layer profile was modelled correctly. The surface mesh over the sea can be seen in Figure 6. The number of cells for each volume mesh was typically around 15 million.

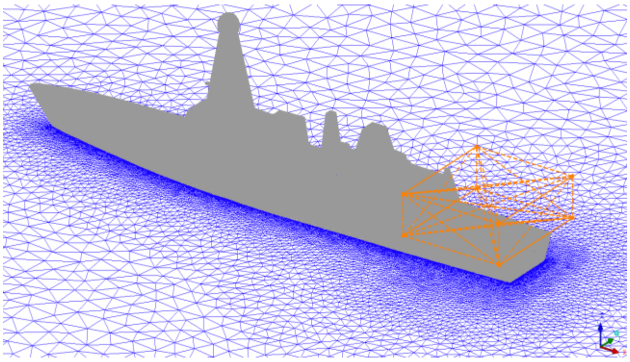

Figure 6 Surface mesh, note the region of dense mesh over the flight deck

3.2. Boundary Conditions

The surface of the ship was modelled as a series of walls with a zero-slip condition so allowing for boundary layer formation. The sea surface was also set as a wall but with zero shear stress, as this allows the specified atmospheric velocity profile to propagate unchanged through the domain. The top of the computational domain was set to a symmetry condition, which assumes there is zero flux across the boundary while specifying a zero shear condition.

The outer circumference of the domain was set as a 'pressure far field' which models the free stream conditions to infinity. This boundary condition requires that the free stream Mach number is defined along with the components of the flow direction.

An Atmospheric Boundary Layer (ABL) was applied within the CFD using the power law given in equation 2.

$$\boldsymbol{V = V_{ref}\left(\frac{z}{z_{ref}}\right)^{\alpha}} \qquad (2)$$

Where V_{ref} is the velocity at the reference height z_{ref}, and α is a constant dependent on the surface roughness. The following values, defined for a sea surface, were used within the simulations: $V_{\text{ref}} = 50$ knots, $z_{\text{ref}} = 200$m, $\alpha = 0.13$[16]. The free stream wind conditions led to a nominal 40 kt wind speed at the ships' anemometer height.

Adding an ABL has been shown to be essential to creating the correct airwake, but it should also be noted that to obtain complete dynamic similarity between the flows over the three ship sizes, the inlet velocity profile should also be scaled. However, scaling the ABL is not realistic as it does not change with ship size. Therefore, to explore the effect of applying the same ABL to the three ship sizes, airwakes were also computed for a uniform inflow (i.e. no ABL) so achieving the correct conditions for dynamic similarity between the three cases.

3.3. Computational Methods

Second order-discretisation was used in time and space, and a blended upwind-central differencing scheme was used for the convective terms. Pressure-velocity coupling was resolved through use of the Pressure-Implicit with Splitting of Operators (PISO) scheme.

3.4. Turbulence Modelling

Since DES is a 'time accurate' CFD method, having been developed to resolve the flow separation from large bluff-bodies at high Reynolds numbers, it is very well suited to computing the flow around the superstructure of a ship. DES CFD turbulence modelling has the advantage of resolving the medium to large scale turbulent structures explicitly, thereby allowing the unsteady airwake to be captured fully.

3.5. General CFD Approach

The approach used to produce the time-accurate unsteady CFD simulations initially involved the generation of a steady-state solution by performing 1000 iterations. The results from the steady-state flow field were then used as the initial conditions for calculating the unsteady flow field. The unsteady solver was activated in DES mode and the simulation was carried out at 100Hz. First, 1500 time steps were computed to allow the transition from steady state to unsteady to develop fully. These initial time steps were then discarded after which a further 3000 time steps were computed, while sampling data every fourth time step to produce data for later post-processing and use within the flight mechanics modelling software, FLIGHTLAB. The development of the CFD technique and its validation against experimental data has been reported by Forrest & Owen[15].

3.6. Airwake Processing for Flight Simulation

Each CFD simulation produces thirty seconds of unsteady CFD data, generated on a high density, unstructured mesh. Due to memory constraints when running real-time piloted simulations the computed airwake data requires post-processing before it can be used within FLIGHTLAB. Reduction of the airwake data size is undertaken by first sampling the 100Hz data at every fourth time step and then by interpolating the unstructured CFD data onto a structured mesh using a grid spacing of 1 metre, covering a region of interest around the flight deck of the ship. Once interpolated, the individual airwake files are re-formatted into a pair of data files containing the airwake data and grid information so that the co-ordinate axes of the CFD data match those of FLIGHTLAB. The 30 second airwake data was looped smoothly for the duration of the flight test.

The FLIGHTLAB Generic Rotorcraft model used for this research was configured to be representative of the Sikorsky SH-60B Seahawk, a maritime development of the widely used UH60 Black Hawk. The model is constructed from a set of modular components such as the rotor, fuselage and turbo-shaft engine. The unsteady, interpolated airwake data is integrated into the helicopter flight mechanics model by applying the time varying velocity components to the aircraft via a number of Airload Computation Points (ACP) which are located at various points along each rotor blade, fuselage, tail rotor and empennage, Figure 7.

FLIGHTLAB includes a dynamic inflow model and also accounts for the downwash from the rotor. However, the interaction between the airwake and the rotor model is not fully coupled, i.e. it is 'one-way', such that the helicopter is affected by the airwake, but the rotor downwash does not interact with the airwake.

A comprehensive description of the simulated SHOL testing process can be found in Reference 9.

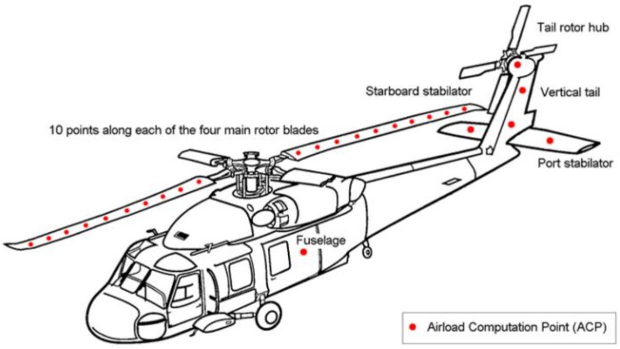

Figure 7 Location of the ACP's used on the SH60-B helicopter model in FLIGHTLAB

4. RESULTS

4.1. Airwake Scaling on Velocity Magnitude

For the medium sized ship, headwind WOD cases were computed at free stream speeds (V_{ref}) of 50 and 20 knots to allow velocity scaling to be carried out and compared.

Figure 8 shows the results of scaling unsteady velocity data from 50 knots to be representative of 20 knot data, alongside the computed 20 knot data, using power spectral density (PSD) plots. The point in the flow field at which the velocities were extracted from the CFD is at hangar height above the landing spot. While the data do not exactly overlie in the central region of the PSD, the scaling can be seen to be reasonably good, capturing the shift in both frequency and power. The scaled velocities are considered suitable for representing the airwake in the FLIGHTLAB flight simulation software, thus confirming the observation of Hodge et al[8] that it is not necessary to compute airwakes for all free stream velocities; for a given wind direction they can instead be computed for one velocity and scaled in magnitude and frequency for other free stream velocities.

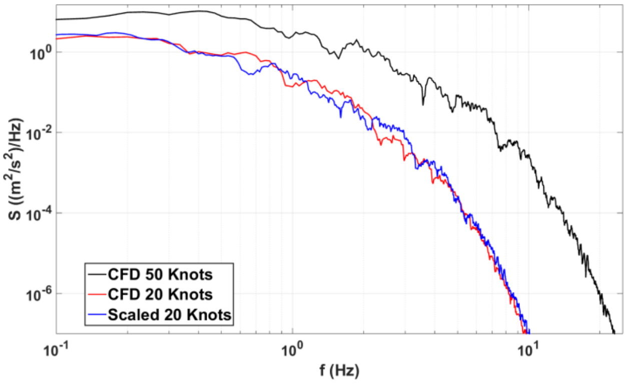

Figure 8 Power spectral densities of the total velocity for the computed 50 and 20 knot data and the scaled 20 knot case

4.2. Airwake Scaling on Characteristic Length

Having confirmed the velocity spectra scaling based on a characteristic velocity, the next step was to demonstrate the scaling of velocity spectra based on characteristic length, or ship size. As before, the velocity PSD was extracted from the CFD at a point above the landing spot at hangar height, in a headwind. The airwakes were computed for the large and small ship, and then the velocity PSD for the large ship was scaled to represent the small ship, and the computed and scaled PSDs were then compared to judge the effectiveness of the scaling.

Figure 9 shows the velocity data and scaling comparison for the case when the ABL was applied; the free stream velocity was 50 kts, which is equivalent to 40 kts at the anemometer height. Despite the lack of dynamic similarity due to the ABL not being scaled, the scaling of the velocities from the large ship to the size of the small one does produce a reasonably representative velocity PSD.

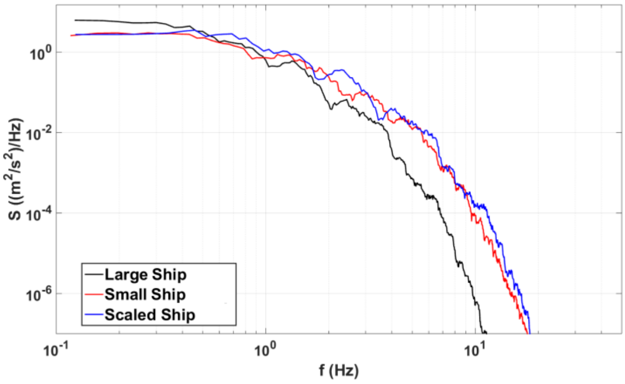

Figure 9 Power spectral densities of the total velocity for a headwind WOD using an ABL, showing computed data for the small ship compared with the data scaled from the large ship

In Figure 10, the same comparison is made but this time with a uniform inlet velocity profile (UBL) of 40 kts, so that it matches the previous inlet velocity at anemometer height. It can be seen that there are differences in the comparisons for the uniform and atmospheric profiles, but the magnitudes of the differences between the computed and scaled PSDs are similar. At this stage in the research it is not certain that airwakes can be simply scaled between similar ships of different sizes to be used in flight simulation, but it looks promising.

Although not reported in this paper, similar PSD comparisons have been made at different locations within the airwake, and for different wind angles; equally good comparisons between scaled and computed data were found for both velocity-based and size-based scaling.

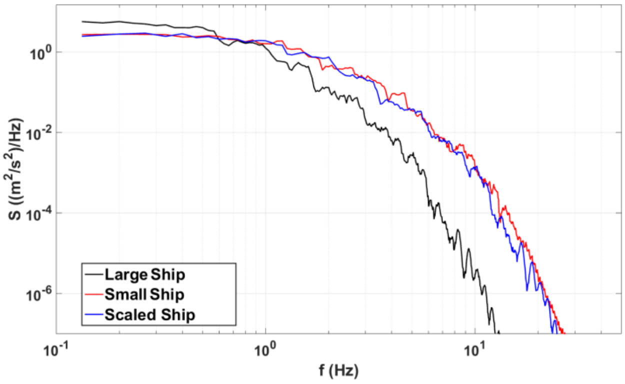

Figure 10 Power spectral densities of the total velocity for a headwind WOD using a UBL, showing computed data for the small ship compared with the data scaled from the large ship

Overall this data suggests that Strouhal scaling is a feasible method to scale airwakes to account for changes in both ship size and velocity magnitude. The use of an ABL profile during the CFD simulation does not appear to preclude the use of airwake scaling.

4.3. Piloted Flight Simulation

Having demonstrated the airwake scaling process, the investigation then went on to consider the effect of ship size on pilot workload, with a point of interest being whether the more benign airwake of the small ship would be negated by the smaller deck and reduced space for manoeuvre. To illustrate the space restriction in the horizontal plane the rotor disc diameter is superimposed on some CFD data in Figure 11. As can be seen, the shear layer that is formed across the deck is larger and more turbulent for the larger ship, which can be expected to affect the unsteady loading on the helicopter.

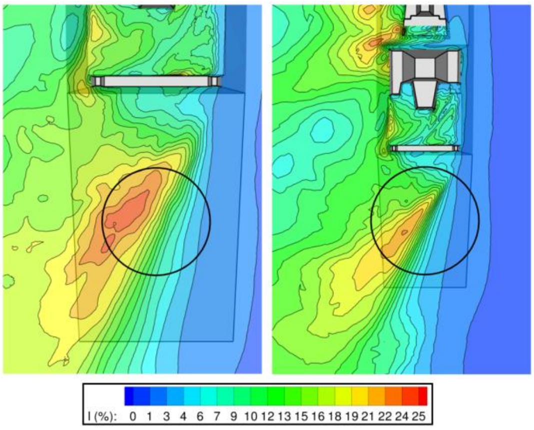

Figure 11 Comparisons of turbulence intensity contours at 100 % hangar height showing the relative size of the SH60-B rotor disc over the large and small flight decks

As part of the scaling investigation described in the previous sections, the airwakes had been computed separately for each size of ship, and they were then scaled up and down from the computed velocity of 40kts at the anemometer height to produce airwakes for a range of wind speeds. The wind directions were restricted to a headwind and a Green 45°.

While the focus of the study being reported in this paper was the effect of ship size on the airwake and on pilot workload, it is also recognised that ships of different size will have different motion, for a given sea state. Therefore, to avoid too many variables being changed, the ship motion (heave, roll, pitch) used in the flight simulation, and applied to the ships' centres of gravity, was the same for each ship. Future work will involve scaling the ship motion (frequency and amplitude) to provide the pilot with another challenge that will vary with ship size.

The unsteady airwakes for each of the three ship sizes were therefore formatted and integrated into the FLIGHTLAB software, as described in the previous sections and more comprehensively in Reference 9. An experienced test pilot was tasked with conducting approaches to each of the ships using the HELIFLIGHT-R motion base flight simulator. The piloted flight testing consisted of a series of approaches to each of the three ships for the headwind and Green 45° WOD conditions while subjected to a range of wind speeds. The pilot was asked to give an assessment of the difficulty of the task using the Bedford Workload Rating Scale as shown in Figure 12.

The task was based on the standard approach to a ship as used by the Royal Navy, shown in Figure 13. This technique involves an approach to a hover, approximately one beam width off the port side of the ship, followed by a lateral translation to a hover over the deck spot before descending to land on the flight deck. During the manoeuvre, the pilot was asked to hold a hover position over the port edge of the flight deck at approximately hangar height for

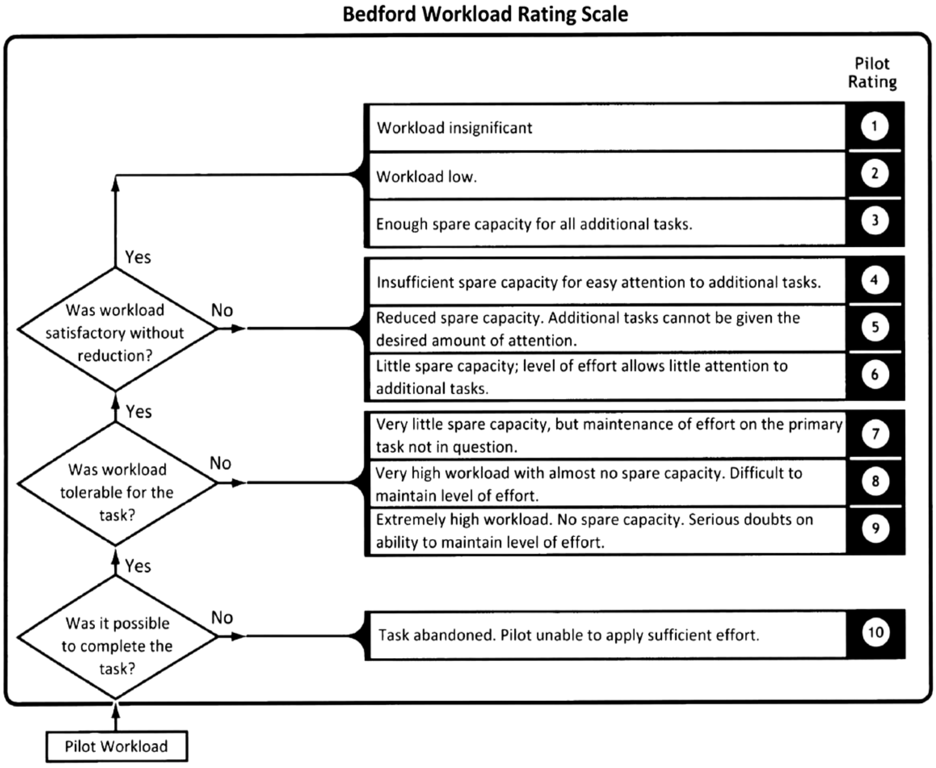

Workload insignificant 1
Workload low. 2
Enough spare capacity for all additional tasks. 3
Insufficient spare capacity for easy attention to additional tasks. 4
Reduced spare capacity. Additional tasks cannot be given the desired amount of attention. 5
Little spare capacity; level of effort allows little attention to additional tasks. 6
Very little spare capacity, but maintenance of effort on the primary task not in question. 7
Very high workload with almost no spare capacity. Difficult to maintain level of effort. 8
Extremely high workload. No spare capacity. Serious doubts on ability to maintain level of effort. 9
Task abandoned. Pilot unable to apply sufficient effort. 10

Figure 12 The Bedford Workload Rating scale thirty seconds and provide a rating of the workload experienced, followed by a thirty second hover over the flight deck, again with an evaluation of the workload.

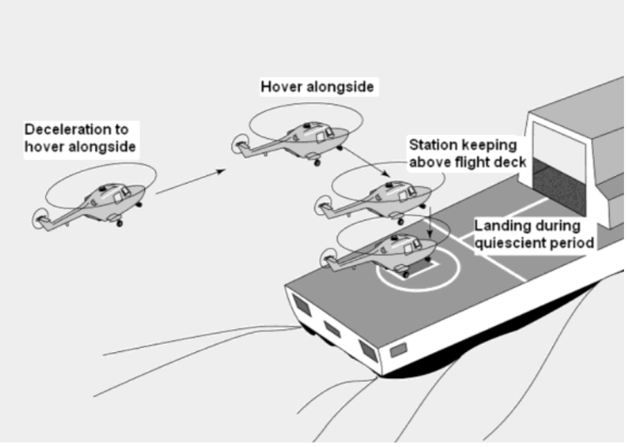

Figure 13 The Royal Navy UK standard approach to a deck landing

Figure 14 shows the Bedford workload ratings given by the pilot for the headwind WOD when asked to maintain a hover position over the flight deck landing spot for each of the three ships. The wind speeds relate to those that would be measured at the height of the anemometer. As is usually the case, the workload in a headwind case is less than that in a green wind so for that reason the maximum wind speed in the headwind was 60 kts, while it was 40 kts in the Green 45° wind.

Pilot assessment of their workload is a subjective process and, although guided by the methodology of the rating scale, each workload rating will have an uncertainty attached to it. Also, the rating scale is not linear, i.e. a rating of 4 does not reflect twice as much work as a rating of 2. To add further complexity, the reasons for the workload will also vary between test points; for example the effort being expended could be in the cyclic controls, or in a combination of collective and pedal controls.

Bearing in mind the previous comments, the workload ratings in Figure 14 show that the effort required by the pilot to hold position over the landing spot, while in a headwind, was low for wind speeds up to 30 kts, and the ship size did not seem to matter. However, as the wind speed increases the workload also increases, as the airwake becomes more aggressive, and also the increase in workload is greater for the larger ship. The pilot comments also revealed that the reason for the workload ratings changed between ships from being due to difficulty in holding position due to the severity of the fluctuating airwake loads over the large ship, to difficulty in holding position while so close to the superstructure of the small ship.

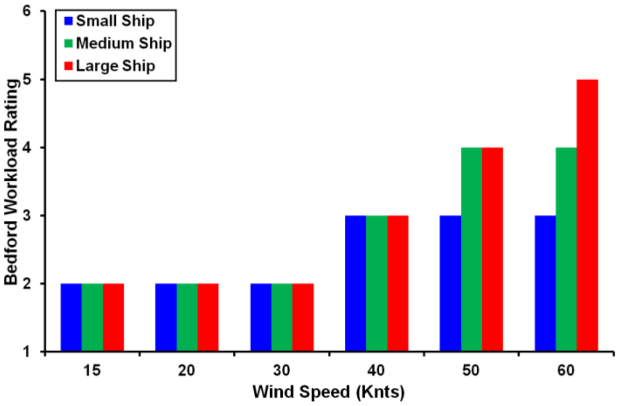

Figure 14 Bedford Workload Ratings for the hover postion over the flight deck for the headwind case

Figure 15 shows the trace history of the cyclic control inceptor for the hover task over the flight deck of both the large and small ships for a 40 knot wind speed. The control activity for the large ship shows larger control inputs were required to maintain position than was seen for the small scale ship.

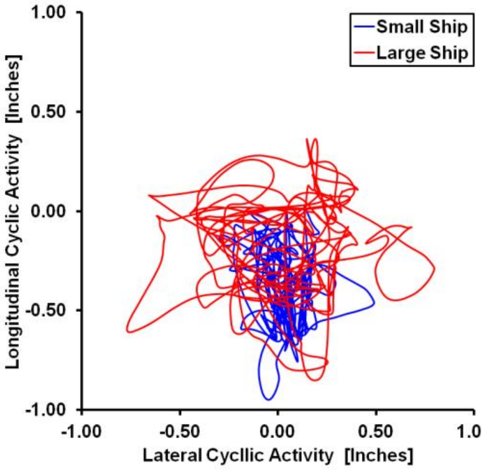

Figure 15 Cyclic control activity for a 40 knot Headwind WOD case

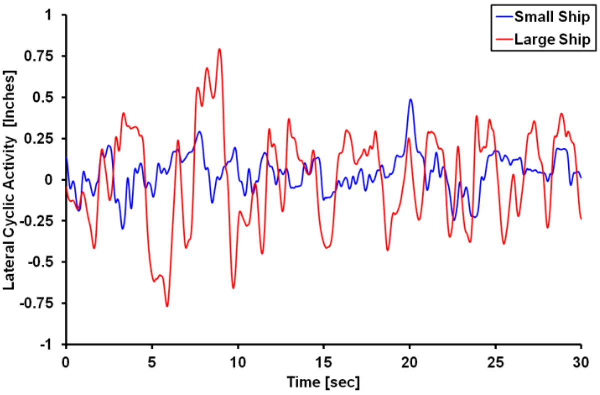

Figure 16 Time histories of lateral cyclic activity for a 40 knot Headwind WOD case

The time histories of the lateral cyclic activity for both the large and small ships for a 40 knot headwind, shown in Figure 16, also demonstrate the larger displacements applied by the pilot to the cyclic when holding position over the landing spot for the larger ship, and also the lower frequency.

Considering the Green 45° WOD condition, the workload ratings for the station-keeping task above the port edge of each ship are given in Figure 17. In this case the hover is over the deck edge, as opposed to over the spot as in Figure 14, because in the oblique wind this position provided more energetic airwake disturbances. Despite the scatter in the data, the trend is the same, i.e. workload increases with wind speed and is greater for the larger ship. The pilot comments about the reasons for the workload ratings, i.e. aerodynamic perturbations versus superstructure proximity were consistent with those for the headwind tests.

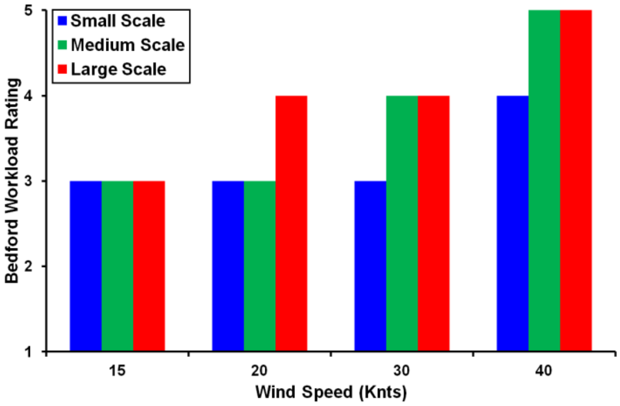

Figure 17 Bedford Workload Ratings for the hover position over the port edge for the Green 45° case

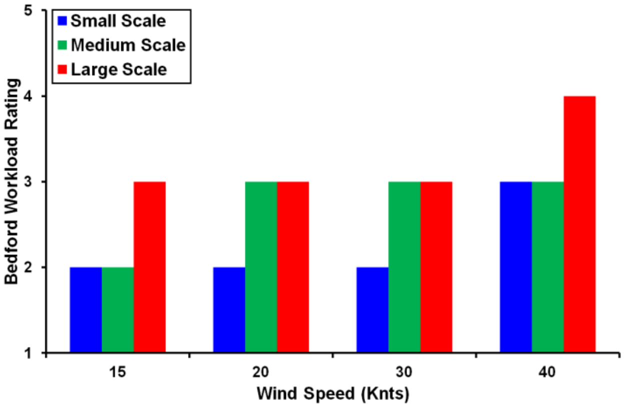

Figure 18 Bedford Workload Ratings for the hover position over the flight deck for the Green 45° case

The ratings given by the pilot for the thirty second hover above the landing spot of each ship, for a Green 45° WOD are shown in Figure 18. The overall ratings were lower than those given when station keeping over the port edge of the ships. Comments made by the pilot during the tasks indicated that the aerodynamic perturbations and subsequent upset on the aircraft were reduced as the helicopter translated across the deck.

The path followed by the helicopter's rotor hub while the pilot translates the aircraft from off the port side to over the landing spot, including holding the positions over the port deck edge and the landing spot for 30 seconds each, are shown in Figure 19. The WOD is a 40kt Green 45°. At the beginning of the flight test the control of the aircraft is handed over to the pilot while the aircraft is hovering off the port side of the ship. Therefore at the start of each trace an initial vertical displacement is seen where the pilot takes control and adjusts to the task in hand. Despite the size of the ship, and the different airwake characteristics, the trajectory followed by the pilot is relative consistent for the two ship sizes (and noting that the helicopter size is the same for each ship). The 30 second station-keeping task over the port edge shows greater vertical displacement for the smaller ship, although the pilot did not report greater workload for the smaller ship at that position and wind strength.

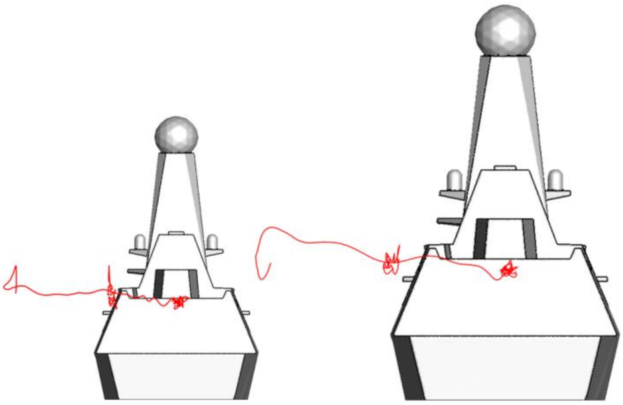

Figure 19 Trajectory of the path taken by the helicopter during the approach and station keeping to both the large and small scale ships for a 40 knot wind, Green 45 WOD case

The contours of turbluence intensity, shown previously in Figure 11, highlight that for this WOD the proportion of the helicopter's rotor disc operating in turbulent flow is greater for the larger ship, which is reflected in the greater excursion in the cyclic activity recorded in Figure 20.

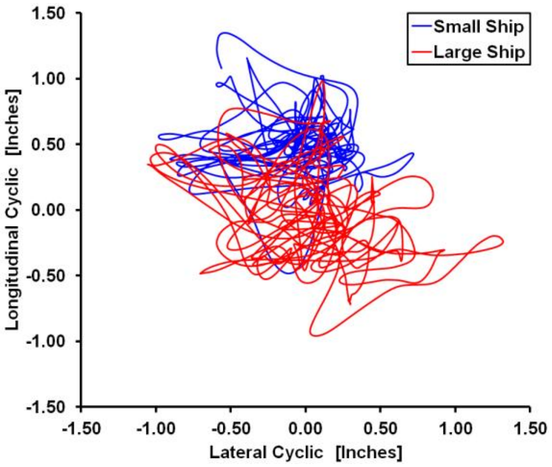

Figure 20 Cyclic control activity for a 40 knot, Green 45° WOD case

However, another intesting observation from Figure 20 is that for the smaller ship the cyclic activity has moved forward. An explanation for this can be found in Figure 21 which shows contours of mean vertical wind velocity at the rotor during the hover task. For the smaller ship, the rotor is placed into a region of flow where there is an updraft of 2.5 - 3 $m.s^{-1}$ passing through the starboard edge of the rotor, as the flow passes over the starboard edge of the ship and flight deck. This updraft results in a change in the aerodyanmic loading of the rotor and, due to the 90° phase delay, the rotor disc will pitch backwards requiring the pilot to maintain a constant correction with forward cyclic to maintain position over the deck. This behaviour was also observed by Forrest et al[6] when conducting simulated deck landings to a Type 23 frigate and shows that a pilot's control strategy must account for both the mean and unsteady velocity components of the flow.

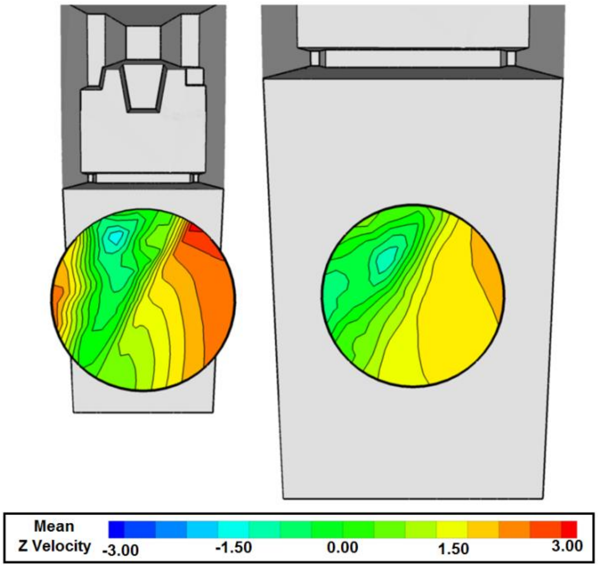

Figure 21 Contours of mean, vertical wind velocities shown at the rotor disc during the hover task.

5. CONCLUSIONS

Three ships with similar geometries but with lengths of 100m, 150m and 200m have been used to investigate the effect of ship size on airwake characteristics and on pilot workload during a simulated landing manoeuvre.

Creating unsteady airwakes for different ships, and at different wind speeds and directions is very time consuming and computationally expensive. It has been shown that for a given wind angle it is possible to Strouhal-scale the airwake velocities from one representative wind strength to other wind strengths with an accuracy that is acceptable for their implementation within a flight simulator. It has also been shown that it is possible to Strouhal-scale the airwake from one ship size to another ship size, again with an accuracy that could be acceptable for flight simulation. Both of these techniques will be very useful for creating flight simulation capability for helicopter launch and recovery to ships.

Piloted flight simulation in which a maritime helicopter was flown to the deck of each of the three ships has shown that the pilot workload generally increases with the ship size and that, despite the landing area being larger and the superstructure proximity being less threatening, the more aggressive airwake from the larger ship still makes the aircraft more difficult to control over the larger ship.

6. ACKNOWLEDGEMENTS

The authors are grateful to Dr David Roper at Ansys Inc for his continued support in the ongoing research at the University of Liverpool.

7. REFERENCES

[1]Lumsden, B. and Padfield, G.D., “Challenges at the Helicopter-Ship Dynamic Interface”, *Military Aerospace Technologies – Fitec ’98*, IMechE Conference Transactions, Institution of Mechanical Engineers, Wiley, 1998, pp 89 - 122

[2]Newman, S., “The Safety of Shipbourne Helicopter Operations”, *Aircraft Engineering and Aerospace Technology*, Vol. 76, No 5, 2004, pp 487 - 501

[3]McRuer, D.T., “Interdisciplinary Interactions and Dynamic Systems Integration”, *Internation Journal of Control*, Vol 59, 1994, pp 3 – 12

[4] Kääriä, C.H., Forrest, J.S., Owen, I.,

"Determining the Impact of Hangar Edge Modifications on Ship-Helicopter Operations Using Offline and Piloted Flight Simulation", *American Helicopter Society 66th Annual Forum and Technology Display*, Phoenix, USA, April 29 – May , 2008

[5]Hodge, S.J., Padfield, G.D., and Southworth, M.R., "Helicopter-ship dynamic interface simulation: Fidelity at low-cost, Cutting Costs in Flight Simulation - Balancing Quality and Capability", *RAeS Conference*, London, UK, 2006

[6]Forrest, J.S., Hodge, S.J., Owen, I., and Padfield, G.D., "An investigation of ship airwake phenomena using time-accurate CFD and piloted helicopter flight simulation", *34th European Rotorcraft Forum*, Liverpool, UK, September 16-19, 2008

[7]Forrest, J.S., Hodge, S.J., Owen, I., and Padfield, G.D., "Towards the Fully Simulated Ship-Helicopter Operating Limits: The Importance of Ship-Airwake Fidelity", *American Helicopter Society 64th Annual Forum*, Montreal, Canada, April 29 – May , 2008

[8] White MD, Perfect P, Padfield GD, Gubbels AW and Berryman AC, "Acceptance testing and commissioning of a flight simulator for rotorcraft simulation fidelity research" in Proceedings of the Institution of Mechanical Engineers, Part G: Journal of Aerospace Engineering, Volume 227 Issue 4, pp. 663 – 686, April 2013

[8]Hodge, S.J., Forrest, J.S., Padfield, G.D. and Owen, I., "Simulating the Environment at the Helicopter-Ship Dynamic Interface: Research, development and application", *The Aeronautical Journal*, Vol 116, No 1185, pp 1155 – 1184

[9]Kääriä, C.H., Forrest, J.S., Owen, I. and Padfield, G.D., "Simulated Aerodynamic Loading of an SH-60B Helicopter in a Ship's Airwake", *35th European Rotorcraft Forum*, Hamburg, Germany 21 – 25 Sept, 2009

[10]Kääriä, C.H., Forrest, J.S., Owen, I., "Assessing the Suitability of Ship Designs for Helicopter Operations Using Piloted Flight Simulation", *37th European Rotorcraft Forum*, Milano, Italy, 13 – 15 Sept, 201

[11]Forrest, J.S., Owen, I., Padfield, G.D. and Hodge, S.J. "Ship-helicopter operating limits using piloted flight simulation and time-accurate airwakes", *Journal of Aircraft*, 2012, Vol. 49, No. 4, pp. 1020-1031.

[12]Prism Defence Ltd, www.prismdefence.com.au, accessed March 2014

[13]Polsky, S.A and Bruner, W.W., "A Computational Study of Unsteady Ship Airwake", *RTO AVT Symposium on "Advanced Flow Management: Part A – Vortex Flows and High Angle of Attack for Military Vehicles*, Loen, Norway, 7 – 11 May, 2001

[14]Zan, S.J., "On Aerodynamic Modeling and Simulation of the Dynamic Interface", *Proceedings of the Institute of Mechanical Engineers, Part G*, Journal of Aerospace Engineering, Vol 219 (5), 2005

[15]Forrest, J.S., Owen, I., "An Investigation of Ship Airwakes Using Detached-Eddy Simulation" *Computers and Fluids 39(2010)*, 2009

[16]Counihan, J., "Adiabatic Atmospheric Boundary Layers: A Review and Analysis of Data from the Period 1880 – 1972", *Atmospheric Environment*, Vol 9, No 10, 1975, pp 871 – 905

[17]Forrest, J.S., Kääriä, C.H. and Owen, I., "The virtual AirDyn: a simulation technique for evaluating the aerodynamic impact of ship superstructures on helicopter operations", *The Royal Aeronautical Society*, Vol 117, No 1198, December 2013

[18]Wang, Y., Curran, J., Padfield, G.D. and Owen, I., "AirDyn: An Instrumented Model-Scale Helicopter For Measuring Unsteady Aerodynamic Loading in Airwakes", *Measurement Science and Technology*, Vol 22, pp 1 – 12, March 2011

[19]Scott, P., Owen, I. and White, M.D., "The Effect of ship size on the flying qualities of maritime helicopters", *American Helicopter Society 70th Annual Forum*, Montreal, Canada, May 20-22, 2014

UNSTEADY CFD MODELLING OF SHIP ENGINE EXHAUST GASES AND OVER-DECK AIR TEMPERATURES, AND THE IMPLICATIONS FOR MARITIME HELICOPTER OPERATIONS

Paul Scott
p.m.scott1@liv.ac.uk
University of Liverpool
Liverpool, UK

Mark White
mdw@liv.ac.uk
University of Liverpool
Liverpool, UK

Ieuan Owen
iowen@lincoln.ac.uk
University of Lincoln
Lincoln, UK

ABSTRACT

This paper describes the results of a Computational Fluid Dynamics (CFD) study into the modelling of unsteady ship airwakes and their interaction with a ship's exhaust efflux. The fluctuating temperatures in the air flow above the flight deck were assessed to determine potential impacts on maritime helicopter operations. A generic ship model was created that is representative of a modern naval single-spot frigate. Included in the simulation was the hot exhaust efflux from three exhaust uptakes representing a ship operating combined gas turbine and Diesel engines, typically found in modern frigates. The unsteady airwake was computed at 40 knots for a Headwind, Green 30° and Green 45° Wind Over Deck (WOD) conditions and the unsteady temperatures were sampled at various locations around the flight deck. The temperature rise limits over the deck as specified in CAP 437 were found to be exceeded for the Headwind and Green 30° cases. The trajectory of the plumes for the Green 30° and Green 45° WOD cases showed that although the over-deck temperatures were within limits, the exhaust gases were entrained in the downwash in the lee of the ship causing the air temperatures to increase in the region where a helicopter would operate for a port-side approach. The resulting air temperatures over and around the flight deck are discussed in relation to helicopter performance and safety, drawing on the experience and practices in the offshore oil industry.

INTRODUCTION

There has been considerable research into understanding the unsteady airwake produced by a ship and its interaction with a maritime helicopter, including the subsequent impact on pilot workload [1-6]. The airwake is the turbulent air flow that occurs over and around a ship due to the combined effects of the prevailing wind and the ship's forward speed. Modern, single-spot naval vessels often rely on combinations of both Diesel and gas turbine engines to provide power for propulsion, and in doing so emit large volumes of hot exhaust gases which will mix with the airwake and be carried over the flight deck. The air flow over and around the ship's landing deck will therefore have elevated temperatures that may affect the helicopter's performance; the effect of air temperatures over and around the flight deck on helicopter operations has so far received little attention.

The exhaust gases can potentially impact on a helicopter when they are drawn into and through the rotor, creating changes in lift due to the reduction in air density. In addition, the helicopter engine intakes are often situated directly beneath the main rotor, so any hot gas passing through the rotor is likely to be ingested by the engines, possibly leading to a loss of power, compressor surge or even flame-out [e.g.7,8]. While there is also a potential problem for the helicopter engine if it ingests oxygen-depleted air, this problem does not arise from the ship's gas turbine exhausts which operate with considerable excess air, and neither is there believed to be a problem from the ship's Diesel exhausts.

Figure 1 Ship exhaust discharging over helicopter deck. Photo by Courtesy of Lt Cdr RN L S Evans

---

Presented at the AHS 71st Annual Forum, Virginia Beach, Virginia, May 5–7, 2015.

Notwithstanding these potential issues, there appears to be little evidence from naval helicopter pilots that ship exhaust gases give rise to problems, except for complaints that fumes in the cockpit can be unpleasant. Figure 1 shows a Chinook over the landing deck of a RN Fleet Auxiliary vessel, directly in line with an exhaust vent. It could be that the transient disturbances caused by the unsteady air temperatures due to the exhaust plume are indistinguishable from the more general transient disturbances due to the ship's airwake.

However, in contrast there has been significant concern, research and guidance in relation to gas turbine exhausts on offshore oil rigs and their effect on the helideck environment and helicopter operations. In 2000 the UK Civil Aviation Authority (CAA) and the Health and Safety Executive (HSE) published a report into research on offshore helideck environmental issues [7]. The research was in response to concerns in the UK offshore industry about the threat to helicopter safety from structure-induced turbulence, down-draughting and hot gas plumes generated by gas turbine exhausts and flarestacks. Setting the scene for the research, the report includes the results of a survey of offshore helicopter pilots; one question was “does turbulence around the platforms cause you a high workload or a safety hazard?” Of the 145 respondents the answer was an overwhelming ‘yes’ with many of the comments referring to turbine exhausts on the platform.

Also included in [7] are summaries of 18 incident reports published between 1976 and 1998; eight of these reports cited gas turbine or flarestack plumes as primary or secondary causes of the incident. A particular incident that caused concern occurred in 1995 on the Claymore accommodation platform, 94 nm northeast of Aberdeen, where a Sea King helicopter suffered an uncontrolled rapid descent to the helideck. During the approach to the platform, the crew reported that they were aware of the helicopter becoming engulfed in the plume from the smell. The hard landing caused the main rotor to deflect downwards so that it impacted the tail boom and severed the tail rotor drive shaft. In 1998, on the Ravenspurn North platform in the southern North Sea, a Eurocopter AS365 suffered compressor surge when applying take-off power from the hover position 10 ft above the deck, during which the crew reported audible 'popping' noises. The platform at the time was operating two gas turbine generators rather than the usual single engine and both exhausts were positioned in close proximity to the deck. Furthermore in 2002 a civil Jet Ranger helicopter was operating close to the chimneys of a power station in Ireland, as the helicopter passed through the plume of the chimney efflux the engine lost power and ran down. The pilot reported that the entire windscreen had misted over and that no plume was visible at the time of the incident [8]. The reports for these incidents highlighted that high temperature exhaust plumes were significant contributing factors in each case.

Gas turbines are used on offshore platforms for power generation. The exhaust gases are usually (although not always) discharged vertically upwards, and temperatures in excess of 400°C are common. The scenario is similar to that on a ship, except the rig exhausts are generally higher above the deck, and the wind over deck is that due to the prevailing wind alone. The environmental research described in [7] is reflected in CAP 437 “Standards for Offshore Helicopter Landing Areas” [9] which sets limits for the air temperatures over platform helidecks. As far back as 1981, when little research had been carried out and helicopter operator experience was limited, CAP 437 was advocating a temperature rise limit of 2 or 3 degrees. The origin of this criterion is not clear but it is believed to relate to the loss of lift equivalent to one passenger; it may also relate to the resolution of the Weight Altitude and Temperature (WAT) charts used by pilots to determine the payload for a given set of environmental factors. CAP 437 has had numerous revisions and the 2013 version still contains the temperature criterion, but it has now been sharpened so that the limit is 2°C above ambient, averaged over 3 seconds. The 3 second period is representative of the response time of helicopter engine to a sudden temperature change. The volume of airspace to which the criterion applies is up to a height above the deck of 30 ft plus wheels-to-rotor height plus one rotor diameter; typically around 30 m for a medium-weight helicopter.

The statement of the temperature criterion in CAP 437 includes: “when the results of wind tunnel or CFD modelling indicate a temperature rise of more than 2°C, averaged over a 3 second period, the helicopter operator should be consulted at the earliest opportunity so that appropriate operational restrictions may be applied”. This statement recognises that there will be occasions when the criterion cannot be met, so pilots may be required to take measures such as avoiding the exhaust plume when close to the rig, adjusting the payload accordingly, and generally exercising care.

The NORSTOCK Standard [10], developed by the Norwegian petroleum industry for the offshore helicopter industry, is aligned with the UK standard CAP 437, although it discusses air temperatures in terms of mean values and does not mention the 3-second time interval. At the design stage the Standard makes recommendation for stack exhaust height and distance from the landing deck. The Standard also outlines a CFD method for determining acceptable risk for helicopter operations in relation to air temperature rises over the landing deck. The methodology uses CFD to evaluate mean temperatures in the exhaust plumes from gas turbines. The method discusses RANS analysis, and requires that the CFD be carried out for a wind direction which takes the plume over the centre of the landing deck, and for different wind speeds. The computed average air temperatures at different heights above the deck are then compared with the Temperature Gradient Matrix shown in Figure 2. Depending on where the temperature/height data point falls, the Matrix then recommends normal operations, caution, or no operation, corresponding to the green, amber and red sections of the Matrix. It can be seen that caution is triggered by a 2°C temperature rise, and no operation by a 30°C rise. The cautionary measures will be similar to those in CAP 437, i.e. avoid the exhaust plume when close to the rig, adjust payload accordingly, and exercise care.

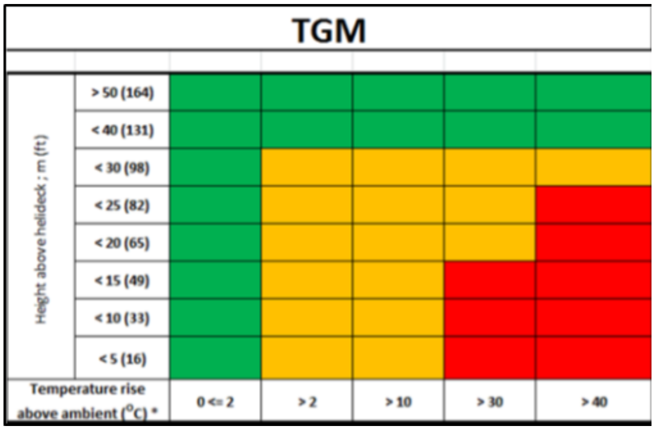

TGM						
Height above helideck ; m (ft)	> 50 (164)	🟩	🟩	🟩	🟩	🟩
	< 40 (131)	🟩	🟩	🟩	🟩	🟩
	< 30 (98)	🟩	🟨	🟨	🟨	🟨
	< 25 (82)	🟩	🟨	🟨	🟨	🟥
	< 20 (65)	🟩	🟨	🟨	🟨	🟥
	< 15 (49)	🟩	🟨	🟨	🟥	🟥
	< 10 (33)	🟩	🟨	🟨	🟥	🟥
	< 5 (16)	🟩	🟨	🟨	🟥	🟥
Temperature rise above ambient (°C) *		0 <= 2	> 2	> 10	> 30	> 40

Figure 2 A sample NORSOK chart [10] showing acceptable levels of temperature rise over the flight deck

Within reference 7 there is some simple analysis of the adverse effects of temperature gradients due to hot plumes on a helicopter. If the air temperature passing through the rotor increases then lift is reduced. Therefore to support the weight of the helicopter the power to the main rotor needs to be increased, which means that the margin of thrust control left to the pilot is reduced. The 2°C threshold in CAP 437 requires an increase in power of 0.24% which equates to a loss of thrust margin of 0.17%. The corresponding figures for a 10°C rise in air temperature are 1.22% and 0.86%.

Reference 7 also discusses the effect of temperature change on helicopter engine performance and shows that a 10°C rise in temperature is estimated to result in a transient loss of power of 1.65%, and a loss of control margin of 1.1%. Graphs of simulated engine response are shown in Figure 3.

Another concern of rapid temperature rise highlighted in [7] is that of engine surge, which is a concern if temperature increases at a rate approaching 1000°C/s. The situation can be further complicated if the air temperature is different across the face of the engine, which it could well be due to the discrete turbulent structures that form within the airwake carrying the exhaust plume over the flight deck.

From the discussion above it is clear that the ship exhaust gases could have a negative effect on the helicopter, particularly while it is immersed in the unsteady airwake and flying in close proximity to the moving deck and superstructure of the ship. The purpose of this paper is to present the results of a CFD study of the unsteady air flow over a naval ship, including the ship's engine exhaust gases, and to consider the results in the light of their potential effect on a maritime helicopter.

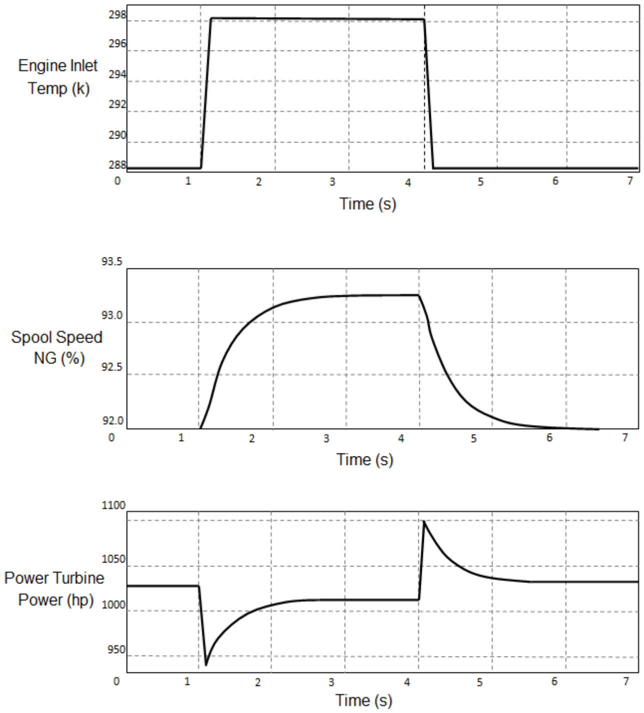

Figure 3 Simulated response of a typical helicopter engine to a 10°C change in bulk inlet temperature over a three second period [7]

The ship airwake, including the exhaust plumes, has been created for a typical naval ship operating combined gas turbine and Diesel engines. The CFD analysis has enabled the unsteady temperatures over the flight deck to be determined. Previous research in this area has focused primarily on the interaction of the exhaust plume with the ship's superstructure to determine potential problems with weapon placements, to satisfy personnel issues or to highlight concerns with sensitive equipment [11-16]. There appears to be no published research on the effect of ship exhaust gases on helicopter operations.

CFD METHODOLOGY

Generic Frigate Model and CFD Meshing

The ship model used for this study, shown in Figure 4, was created to be representative of a frigate with a length and beam of 148m and 20m respectively. The model represents a modern naval vessel having multiple Diesel uptakes and a main gas turbine stack. The Diesel exhaust uptakes are placed at the rear of the starboard funnel, while the gas turbine exhaust uptake is located amidships on the superstructure, behind the main mast. Each exhaust uptake consists of a simple cylindrical duct with a length of five duct diameters, emanating from within the model and emerging flush with the superstructure, with diameters of 0.5m and 2.5m for the Diesel and gas turbine uptakes respectively. The duct lengths of 5 diameters is to allow a representative profile for the exit velocity from the stack to develop.

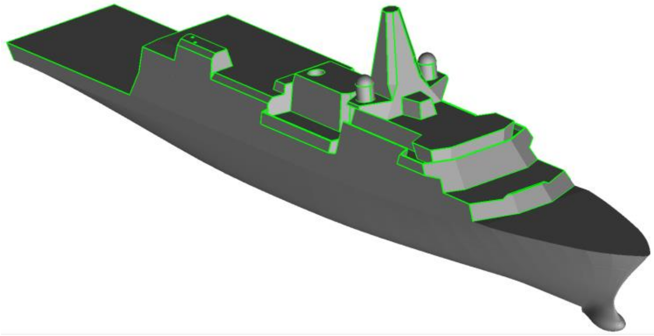

Figure 4 CAD model of the generic frigate

The ship model was imported into the Ansys ICEM mesh generation software so that that it could undergo a process to 'clean' the model to render it suitable for the process of meshing. Small features such as antennae, pole masts and other assorted small deck clutter were removed as these have little effect on the airwake but would otherwise increase the overall cell count and thus the computational time taken to produce the CFD simulation. Typically, objects less than 0.3m in diameter were neglected, as recommended by Forrest & Owen [3].

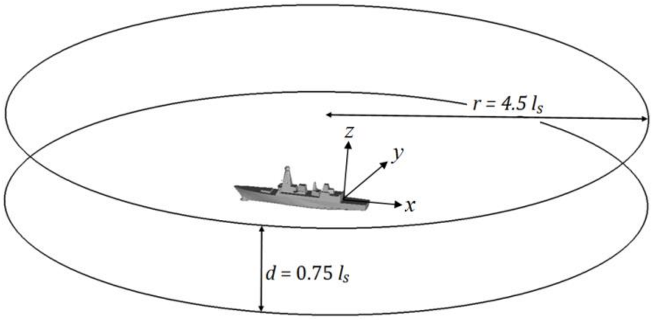

Figure 5 Computational CFD domain

The finished ship model was placed within a cylindrical domain, shown in Figure 5, whose size (given in terms of ship lengths) is such that the boundaries of the domain are sufficiently far from the ship that blockage effects do not occur. The use of a cylindrical domain allows the relative Wind Over Deck (WOD) angle to be varied through 360° by varying the x and y components of the freestream velocity without having to alter the computational domain. The ship was placed within the domain so that the positive x-direction runs along the longitudinal axis of the ship, towards the bow, while the positive y-direction passes through the lateral plane, towards the starboard side of the ship.

An unstructured meshing approach was used, which suits the Detached Eddy Simulation turbulence model (DES) due to the near isotropic nature of the tetrahedra away from the walls [3]. An initial triangular surface mesh was generated from which a Delauney volume mesh was then grown, Figure 6. The cell size used to mesh the ship's surfaces was set to 0.05 times the hangar height and 15 layers of prism cells were used to resolve the viscous boundary layer on both the ship and ground plane surfaces. The growth of the volume mesh, normal to the walls, was controlled using an expansion ratio of 1.2 to ensure a smooth transition between the tetrahedra and prism cells. Areas of particular interest within the volume mesh, for example the region over the flight deck, were refined by controlling the growth of the volume cells. These regions of dense mesh provide better resolution of turbulent structures within the ship's airwake. The total cell count of the domain is approximately 10 million cells.

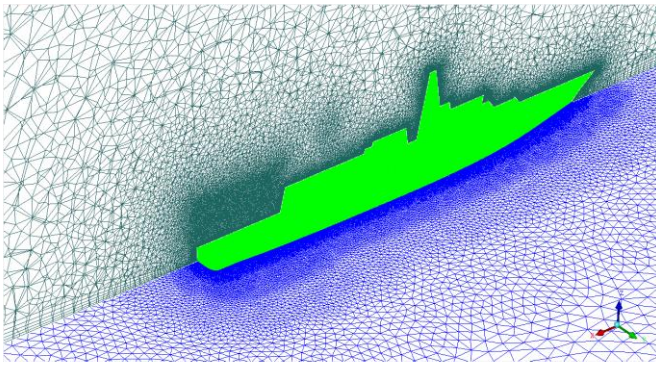

Figure 6 Cross sectional view of the volume mesh, (note region of dense mesh over the flight deck)

Boundary Conditions

The flow solver, Ansys Fluent, requires that all surfaces within the mesh are specified. The upper surface of the cylindrical flow domain was set as a symmetry boundary condition, which assumes there is no flux across the boundary while specifying a zero shear condition. The outer circumference of the flow domain was set to a 'pressure far field' to allow modelling of the freestream conditions at infinity. The pressure far field boundary condition requires that the freestream Mach number is specified along with the components of the flow direction.

The boundary condition for the ship's superstructure was set as a series of walls with a zero slip condition where the velocity at the surface was set to zero to allow the formation of a boundary layer. The ground plane (sea surface) was also set as a wall but with zero shear stress, allowing the specified boundary layer profile used as the input condition for the pressure far field to propagate unchanged through the domain.

The inclusion of an atmospheric boundary layer profile (ABL) was used to increase the accuracy of the CFD simulations as there is a significant difference between the air velocity at the sea surface and at the ship's anemometer. The ABL was modelled using the power law given in equation (1):

$$V = V_{ref}\left(\frac{z}{z_{ref}}\right)^{\alpha} \quad (1)$$

where V_{ref} is the velocity at the reference height z_{ref}, and α is a constant dependent on the surface roughness. The following values for a sea surface were used: $V_{ref} = 50$ knots, $z_{ref} = 200$m, $\alpha = 0.13$, as recommended in [3]. The freestream wind conditions coincided with a 40 knot wind speed at a height equivalent to the ship's anemometer.

Exhaust Plume Boundary Conditions

To model the transport of the hot exhaust gases from the ship into the airwake, the energy equation was activated within Ansys Fluent, along with the solution of additional transport equations to account for the buoyancy of the plume. Although the efflux has both momentum and buoyancy, in the near field where the exhaust is injected into highly disturbed air the plume is momentum-dominated rather than buoyancy-dominated as observed by Ergin et al [12], amongst others.

To model the exhaust flows, the boundaries of both the Diesel and gas turbine exhausts, shown in Figure 7, were designated as mass flow inlets. However, to give a representation of the velocity profile of the exhaust flow, the exhaust ducting was also included within the model so that the injected mass flow was allowed to develop from a uniform velocity profile for 5 duct diameters. The gas turbine boundary was specified with a mass flow rate of 131 $kg.s^{-1}$ and a temperature of 565°C, while the Diesel exhaust boundaries were both given a mass flow rate of 5.5 $kg.s^{-1}$ at a temperature of 400°C. These figures are typical for ship engines used in frigates that do not utilise waste heat recovery systems. The individual exhaust gas species were not specified and the exhaust was simply defined as air. The ambient temperature was set to ISA standard day conditions of 15°C. For the purposes of this study, the Diesel and gas turbine engines were considered to be operating simultaneously.

Computational Modelling

Second-order discretisation was used in time and space, and a blended upwind central-differencing scheme was used for the convective terms. Pressure-velocity coupling was resolved through use of the Pressure-Implicit with Splitting of Operators (PISO) scheme.

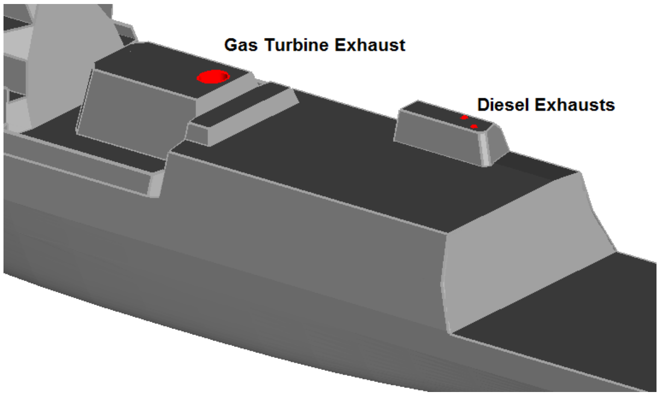

Figure 7 Detail showing the location of the Diesel and gas turbine uptakes

As DES is a time-accurate CFD method, and having been originally developed to resolve the flow separation from large bluff-bodies at high Reynolds numbers, it is an appropriate model to simulate the flow around the superstructure of a ship. DES was originally a modification to the Spalart-Allmaras turbulence model [17] such that the distance to the wall, d, is replaced as shown in equation (2):

$$\tilde{d} = \min(d, C_{DES}\,\Delta) \quad (2)$$

In the unmodified Spalart-Allmaras model the length scale d is used to drive the turbulent viscosity. By linking the length scale to the local grid spacing (Δ), the new modified length scale ($\tilde{d}$) means that turbulent viscosity production is limited away from the walls, allowing the DES model to fully resolve the medium to large scale turbulence. The constant (C_{DES}) has the default value of 0.65 which was retained for this study.

General CFD Approach

To produce the unsteady CFD solutions, the fluid dynamic equations in the whole domain were first solved iteratively 1000 times to converge onto a steady-state solution. The steady-state flow field was then used as the initial conditions for calculating the unsteady flow field, by activating the unsteady solver in DES mode with the simulation carried out at 100Hz. An initial 1500 time steps were computed to allow the transition from steady to unsteady to develop fully; this data was then discarded and a further 3000 time steps were computed to create 30 seconds of unsteady airwake data. For this study, three different WOD cases were simulated, a headwind, Green 30° and Green 45° (i.e. WOD of 30° and 45° from the starboard side, relative to the ship). To record the instantaneous temperatures, data were sampled at a number of discrete points around the flight deck at different hangar heights (HH), as shown in Figure 8.

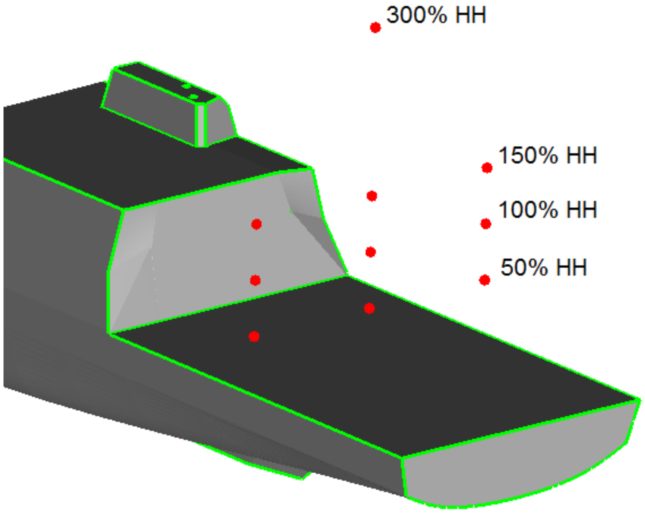

Figure 8 Location of points used to sample unsteady data during the CFD computation

RESULTS

Headwind WOD Case

The structure of the plume for the headwind WOD case, shown in Figure 9, highlights the differences between the mean and unsteady exhaust plumes in the wake of the ship's superstructure. Although the mean temperature flow field suggest that there is little mixing of the gas turbine and Diesel plumes with few vortical structures present, viewing the data for a single time step shows the chaotic turbulent structures that mix and advect the hot exhaust over the flight deck.

The magnitude of these unsteady temperature fluctuations obtained from the CFD simulation can be seen in Figure 10. The unsteady temperatures sampled at three heights over the landing spot can approach 10°C above ambient. To assess the unsteady temperature variations in accordance with the limits set out by CAP 437, the data shown in Figure 10 was then modified to give the three-second moving average temperatures shown in Figure 11. The moving average temperatures show that the 2°C limit is exceeded for significant periods of time at each of the heights sampled with the largest excursions generated at 100% and 150% hangar heights. The lower helicopter image shown in Figure 9 indicates the height of the helicopter in a normal hover position over the deck. The main rotor and the engine intake will typically be at about hangar height and will be exposed to the air temperatures shown in Figures 10 and 11.

The unsteady temperatures over the starboard edges of the deck, Figure 12, show that the temperature rise is negligible at the three hangar heights as neither the Diesel or the gas turbine plumes extend over the full beam of the ship; the temperatures will be similar over the port edge.

Figure 13 shows the unsteady and three-second mean temperatures at 300% hangar height, corresponding to the upper bound over the flight deck specified in CAP 437 (30 ft plus wheels-to-rotor height plus one rotor diameter) as shown by the box in Figure 9. At this location a helicopter would be operating almost entirely within the gas turbine plume with air temperatures in excess of 10°C above ambient, and a three-second average of about of 10°C above ambient. This condition relates directly to the engine data in Figure 3, and the associated discussion.

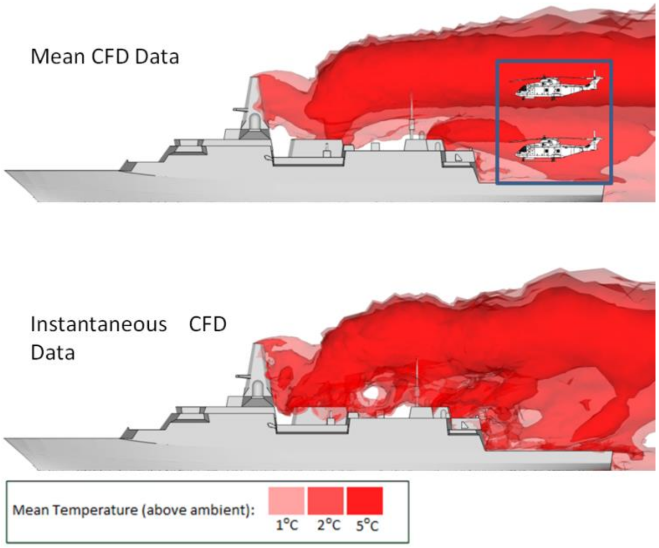

Figure 9 Iso-surfaces of temperature for a Headwind WOD for both mean and unsteady flow fields. Also showing helicopter positions in low and high hover, and volume specified for temperature limits in CAP 437

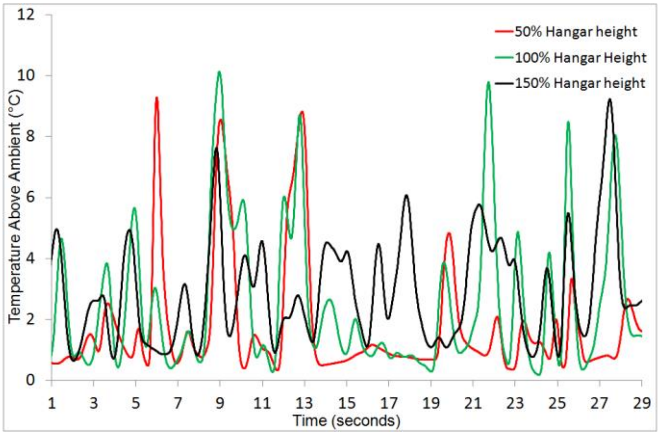

Figure 10 Unsteady temperature variation over the landing spot for the Headwind WOD

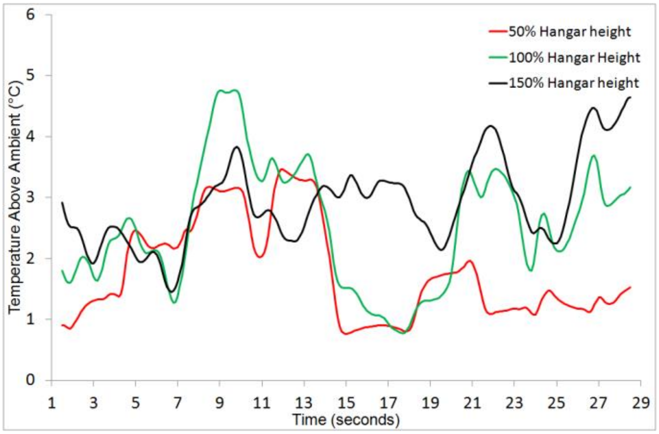

Figure 11 Three-second moving average of the unsteady temperatures over the landing spot for the Headwind WOD

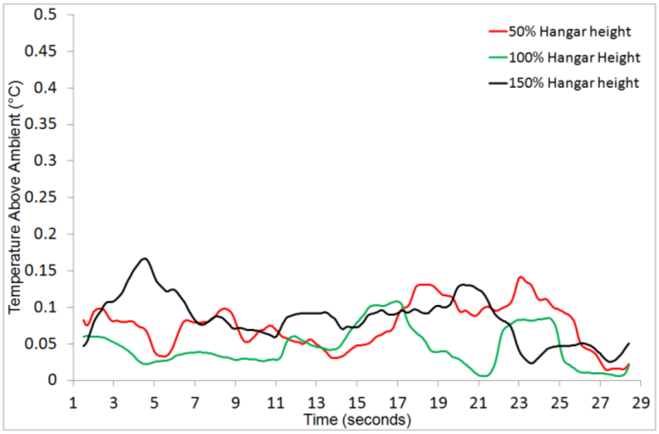

Figure 12 Three-second moving average of the unsteady temperatures over the starboard edge for the Headwind WOD

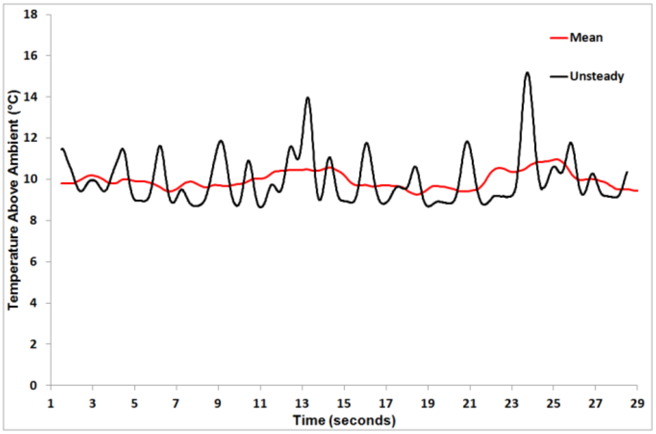

Figure 13 The unsteady and corresponding three-second moving average at 300% hangar height above the landing spot for the Headwind WOD

Green 30° WOD Case

As can be seen in Figure 14, unlike the headwind case there appears to be little interaction between the gas turbine and Diesel exhaust plumes for this WOD. The Diesel exhaust gases are now recirculated within the wake of the hangar while the gas turbine plume is angled away from the flight deck, off the port edge of the ship. Here the plume trajectory exhibits a downwash in the lee of the ship's superstructure and puts the plume into the flight path of an approaching helicopter during a port-side landing approach (as used by the UK Royal Navy, and others). As the gas turbine plume no longer passes over the flight deck there is a corresponding decrease in the unsteady temperatures in that region.

Figures 15 & 16 show the three-second average temperatures sampled above the landing spot and the port edge of the flight deck respectively. Above the landing spot, the temperature is higher closer to the flight deck due to the entrainment of the Diesel efflux into the hangar wake and it can be seen that the 2°C limit is not exceeded. Above the port edge of the flight deck the core of the Diesel plumes are found in the region of 100% and 150% hangar heights and the 2°C limit is marginally exceeded at the higher sampling point.

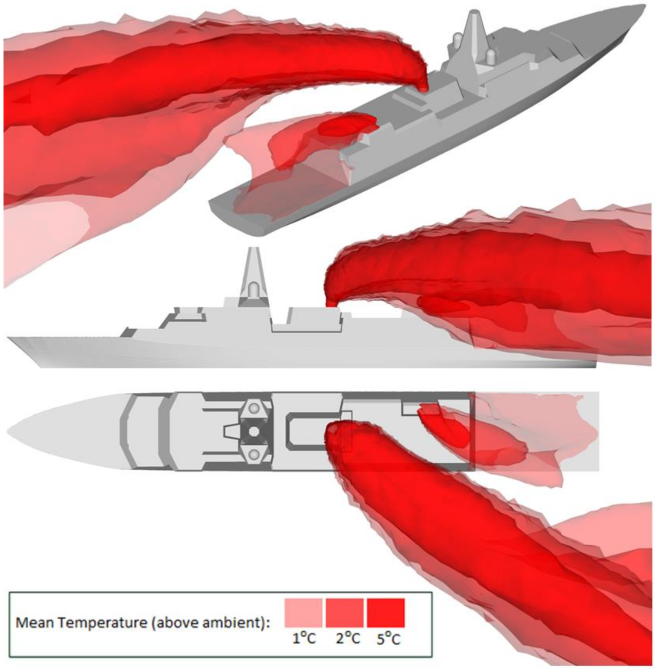

Figure 14 Iso-surfaces of mean temperature of the mean flow field for the Green 30° WOD case.

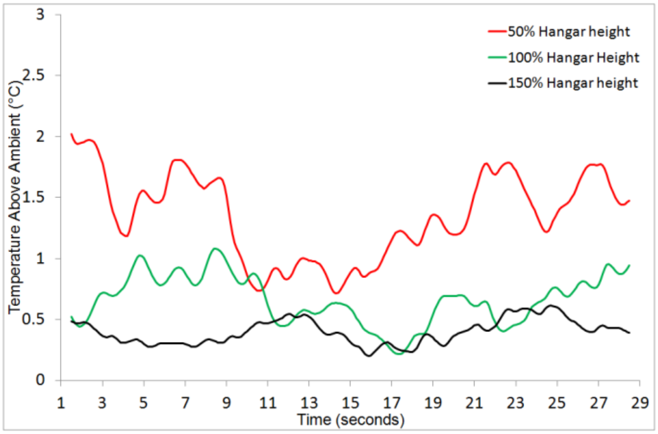

Figure 15 Three-second moving average of the unsteady temperatures over the landing spot for the Green 30° WOD

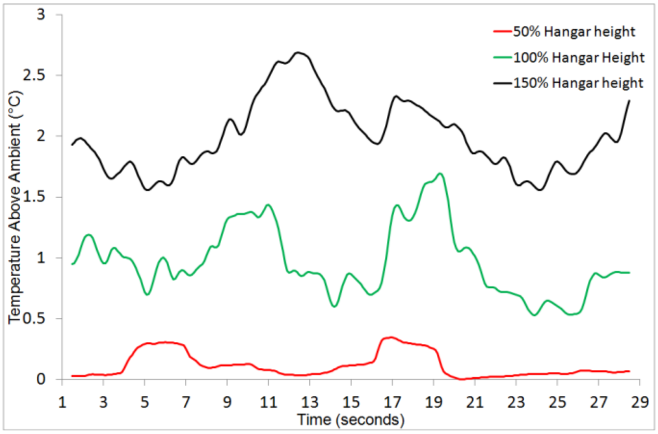

Figure 16 Three-second moving average of the unsteady temperatures over the port deck edge for the Green 30° WOD

Green 45° WOD Case

With the increase in wind angle to 45°, the efflux from both the gas turbine and Diesel uptakes do not appear to encroach the flight-critical regions over the deck, as shown in Figure 17. As such, the temperature changes over the deck are not significant for helicopter operations. The downwash of the plume that occurred for the Green 30° WOD case is also present in the Green 45° WOD case, so that one beam width off the port edge of the ship, average temperatures were seen to be 2°C above ambient. Nevertheless, at this distance the gas turbine exhaust has been diluted and the temperature rise is not excessive.

Discussion

The temperatures sampled for the headwind case show, that for the conditions applied in this test case, the 2°C limit as defined in CAP 437 is generally exceeded for locations over the central area of the flight deck with the recirculation behind the hangar serving to transport the hot exhaust gases down towards the deck surface. The magnitude of the temperature rise increases with height above the deck as the gas turbine plume becomes more influential. Helicopters operating in this region would likely see an increase in the temperature rise due to the rotor drawing in air, particularly if the helicopter is in the high hover position shown in Figure 9.

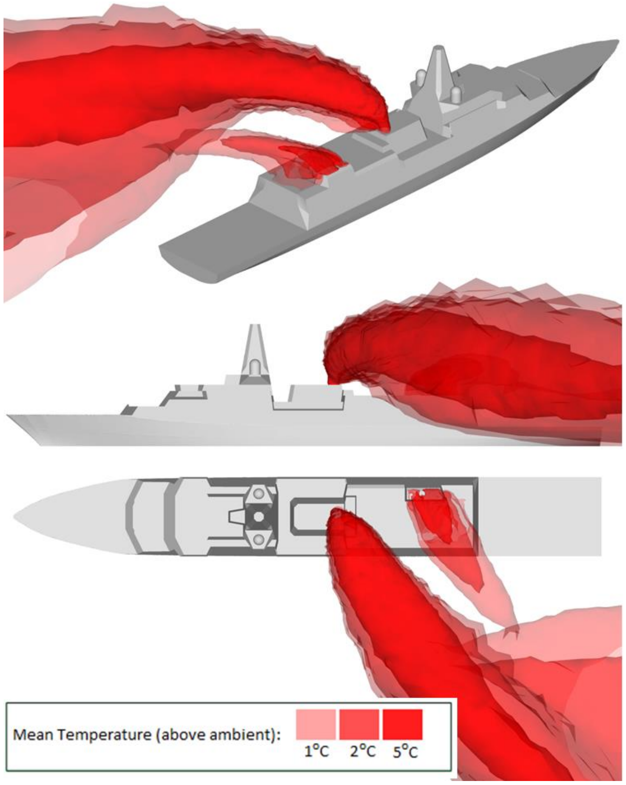

Figure 17 Iso-surfaces of mean temperature of the mean flow field for the Green 45° WOD case.

Closer to the deck, the turbulence generated by the superstructure leads to greater fluctuations in temperature which could impact on the helicopter's engine performance, particularly as the turbulent structures will be carrying discrete masses of hot gas, therefore presenting the face of the engine intake with temperatures that vary in both time and space.

For the Green 30° and Green 45° WOD cases the unsteady temperature rise over the deck is reduced in comparison to the headwind case. However the exhaust efflux in the lee of the ship exhibits a downwash, bringing the Diesel and gas turbine plumes to levels approaching hangar height, which may impact on helicopters operating off the port side of the ship. This can be seen in the moving three-second average temperatures sampled over the port deck edge for the Green 30° WOD and as the height above deck increases, so does the temperature.

The CFD simulations were carried out for an ambient temperature of 15°C, however maritime operations are also carried out in parts of the world where the ambient temperature can approach 50°C. Therefore temperature fluctuations of 10°C above ambient could have a marked impact on the flight performance of a helicopter already operating with reduced engine power. This highlights some of the issues regarding CAP 437 when applying a single temperature rise over the flight deck of a ship without taking into account the ambient temperature or the WOD conditions. The NORSOK C-004 Standard goes into further detail to try to address some of the issues regarding the variables involved in over-deck temperatures. However both of the Standards, if applied to naval frigates, only apply temperature limits to the region immediately above the flight deck while neglecting the flight-critical areas off the ship. As well as the issue of where the criteria should be applied, there is also significant uncertainty about what is an acceptable temperature rise limit.

CONCLUSIONS

There has been a concerted effort to define a safe operational environment governing the operation of civilian maritime helicopters to offshore oil and gas rigs, particularly in relation to air temperature rise due to gas turbine exhausts. Following a number of incidents on offshore platforms, specific temperature rise criteria have been developed. The same concerns have not been expressed for maritime helicopters operating to naval ships, and there appear to be no specific regulations or operational guidelines.

The CFD study reported in this paper has shown that high temperature exhausts from a ship's engines can lead to unsteady air temperatures that would cause significant concern for offshore platform operators. In a headwind the concerns would be the air temperatures over the landing deck, while in oblique winds the concern is for the flying area alongside the deck where the exhaust gases become entrained into a downwash in the lee of the ship. Consideration should be given to what are the acceptable temperature rise limits over and around the ship's landing deck.

ACKNOWLEDGEMENTS

The authors are grateful to Ansys Inc for their continued support of the ongoing research at the University of Liverpool.

REFERENCES

[1] Lumsden, B. and Padfield, G.D., "*Challenges at the Helicopter-Ship Dynamic Interface*", Military Aerospace Technologies – Fitec '98, IMechE Conference Transactions, Institution of Mechanical Engineers, Wiley, 1998, pp 89 - 122

[2] Hodge, S.J., Zan, S.J., Roper, D.M., Padfield, G.D. and Owen, I., *"Time-Accurate Ship Airwake and Unsteady Aerodynamic Loads Modeling for Maritime Helicopter Simulation*", Journal of the American Helicopter Society, 2009, Vol 54, 22005, 1-16.

[3] Forrest, J.S, and Owen, I., "*An Investigation of Ship Airwakes Using Detached-Eddy Simulation*", Computers & Fluids, 2010, Vol 39, pp 656-673.

[4] Hodge, S.J., Forrest, J.S., Padfield, G.D. and Owen, I., "*Simulating the Environment at the Helicopter-Ship Dynamic Interface: Research, Development and Application*", The Aeronautical Journal, 2012, Vol 116, No 1185, pp 1155 – 1184

[5] Kääriä, C.H., Forrest, J.S., and Owen, I., "*Assessing the Suitability of Ship Designs for Helicopter Operations Using Piloted Flight Simulation*", 37th European Rotorcraft Forum, Milano, Italy, 13–15 Sept, 2011.

[6] Forrest, J.S., Hodge, S.J., Owen, I., and Padfield, G.D., "*Towards the Fully Simulated Ship-Helicopter Operating Limits: The Importance of Ship-Airwake Fidelity*", American Helicopter Society 64th Annual Forum, Montreal, Canada, April 29 – May , 2008

[7] Civil Aviation Authority. *'Research On Offshore Helideck Environmental Issues'.* London: Civil Aviation Authority. CAA Paper 99004, 2000.

[8] Liddy, G. (2004). *AAIU Synoptic Report No: 2004-001.* Shannon: Irish Aviation Authority.

[9] Civil Aviation Authority. *"Standards for Offshore Helicopter Landing Areas".* CAP 437, ondon, 2013.

[10] Norweigian Oil and Gas Association, *"Helicopter Deck On Offshore Installation".* NORSOK Standard C-004, 2013.

[11] Camelli, F., Soto, O., Lohner, R., Sandberg, W. C., and Ramamurti, R., "*Topside LPD17 Flow and Temperature Study with an Implicit Monolithic Scheme*". 41st Aerospace Science Meeting and Exhibit, Reno, Nevada, 6-9 January 2003, AIAA 2003-969.

[12] Ergin, S. and Dobrucali, E., *"Numerical modelling of exhaust smoke dispersion for a generic frigate and comparison with experiments"*, J. Marine Sci. Appl., 2014, Vol. 13, 206-211.

[13] Kulkarni, P.R., Singh, S.N. and Seshadri, V., "*Parametric studies of exhaust smoke – superstructure on a naval ship using CFD*", Computers & Fluids, 2007, Vol. 36, 794-816.

[14] 5. Kulkarni, P.R., Singh, S.N. and Seshadri, V., "*The smoke nuisance problem on ships – a review*", Int. J. Maritime Eng., 2005, Vol. 147, Part A2, 27-50.

[15] Park, S., Heo, J., YU, B.S. and Rhee S.H., "*Computational analysis of ship's exhaust-gas flow and its application for antenna location*", Applied Thermal Engineering, 2011, Vol. 31, 1689-1702.

[16] Vijayakumar, R., Singh, S.N. & Seshadri, V., "*CFD prediction of the trajectory of hot exhaust from the funnel of a naval ship in the presence of ship superstructure*", Intl. J. Maritime Eng., Vol. 156, Part A1, 2014, A1-A23.

[17] Spalart, P. J. "*Comments on the fesibility of LES for Wings and on a Hybrid RANS/LES Approach*". 1st AFOSR International Conference on DNS/LES. Ruston, LA: 1997.